ENERGY SYSTEMS RESEARCH UNIT
AEROSPACE AND MECHANICAL ENGINEERING DEPARTMENT
UNIVERSITY OF LIÈGE

Sustainable Energy Conversion Through the Use of Organic Rankine Cycles for Waste Heat Recovery and Solar Applications.

in Partial Fulfillment of the Requirements for the Degree of
Doctor of Applied Sciences

Presented to the Faculty of Applied Science
of the University of Liège (Belgium) by

Sylvain Quoilin

Liège, October 2011

Introductory remarks

Version 1.3, published in October 2011

The importance of the glossary. It is strongly recommended to read the glossary in full before starting with the first chapter.

Hints for screen use. This work is optimized for both screen and paper use. It is recommended to use the digital version where applicable. It is a file in Portable Document Format (PDF) with hyperlinks for convenient navigation. All hyperlinks are marked with link flags (►). Hyperlinks in diagrams might be marked with colored borders instead.

Navigation aid for bibliographic references. Bibliographic references to works which are publicly available as PDF files mention the logical page number and an offset (if non-zero) to calculate the physical page number. For example, to look up [Example :a01, p. 100_{-80}] jump to physical page 20 in your PDF viewer.

Abstract

This thesis contributes to the knowledge and the characterization of small-scale Organic Rankine Cycles (ORC). It is based on experimental data, thermodynamic models and case studies.

The experimental studies include:

1. A prototype of small-scale waste heat recovery ORC using an open-drive oil-free scroll expander, declined in two successive versions with major improvements.
2. A prototype of hermetic scroll expander tested on vapor test rig designed for that purpose.

The achieved performance are promising, with expander overall isentropic effectivenesses higher than 70% and cycle efficiencies comparable or higher than the typical efficiencies reported in the scientific literature for the considered temperature range.

New *steady-state semi-empirical models* of each component are developed and validated with the experimental data. The global model of the ORC prototype allows predicting its performance with a good accuracy and can be exploited to simulate possible improvements or alternative cycle configurations.

Dynamic models of the cycle are also developed for the purpose of evaluating the system's reaction to transient conditions. These models are used to define and compare different control strategies.

The issues of cycle optimization and fluid selection are treated using the steady-state semi-empirical models. The thermodynamic optimization of such cycles is first demonstrated by practical examples. Furthermore, three different methods for fluid selection are proposed, investigated and compared. Their respective advantages and fields of application are described.

Finally, two prospective studies of small-scale ORC systems are proposed. The first one is a solar ORC designed for the rural electrification of remote regions in Africa. This prototype aims at competing with the photovoltaic technology, with the advantage of generating hot water as by-product.

The second prospective study deals with the recovery of highly transient heat sources. Advanced regulation strategies are proposed to address the practical issues of such systems. These strategies are compared with the state-of-the-art strategies and show a non-negligible potential of performance improvement.

Acknowledgments

I would like to thank Professor Vincent Lemort for his trust and his support during the whole period of this work. I wish to thank him for the numerous moments spent working together on practical and theoretical issues as well as for countless valuable discussions.

I am also grateful to professor Jean Lebrun, who gave me the opportunity to start this thesis and provided constructive advices along the work.

Thank you to the members of the Thesis Committee, Piero Colonna, Assaad Zoughaib, Georges Heyen, Philippe Ngendakumana and Pierre Duysinx for their valuable comments and constructive criticism.

A large part of this work would not have been possible without the trust of colleagues from foreign laboratories, namely Matthew Orosz, Andreas Schuster, Richard Aumann and their respective teams. They allowed me to gain valuable experience and know-how and warmly welcomed me to stay in their labs.

Special thanks goes to Stéphane Bertagnolio and all the members of the Thermodynamics Laboratory for their help and availability, but above all for their friendship and the great moments spent together during these four years.

Furthermore, I want to thank my family and my friends for their support and encouragements throughout my studies.

Last but not least, special thanks to Jessica Schrouff for her unwavering support, for the proofreading and for the multiple comments and advices to improve this thesis.

Table of contents

Table of contents

Table of contents

Table of contents

Nomenclature

A	area, m²
AU	heat transfer conductance, W/K
b	corrugation depth, m
Bo	boiling number, $Bo = \dot{Q}/(A G i_{fg})$
c	specific heat, J/(kg K)
Co	convection number, $Co = \rho_g/\rho_l((1-x)/x)^{0.5}$
d	diameter, m
D_h	hydraulic diameter, m
Fr	froude number $Fr = G^2/(\rho \cdot g \cdot D_h)$
G	mass velocity, kg/m²s
h	heat transfer coefficient, W/m²K
h	specific enthalpy, J/(kg K)
i_{fg}	enthalpy of vaporization, J/kg
k	conductivity, W/m K
K_p	proportional gain, -
L	length, m
M	mass, kg
$\dot{M}$	mass flow rate, kg/s
N	number of nodes, -
N_s	specific speed, rad
N_p	number of plates, -
N_{rot}	rotating speed, rpm
Nu	Nusselt number, $\mathrm{Nu} = h D_h/k$
p	pressure, Pa
P_r	Prandtl number, $Pr = \mu Cp/k$
$pinch$	pinch point value, K
$\dot{Q}$	Heat power, W
$\dot{q}$	linear heat flux, W/m
r	ratio, -

Nomenclature

$r_{v,\text{in}}$	internal built-in volume ratio, -
s	specific entropy, J/(kg K)
S_{beam}	beam solar insolation, W/m²
t	time, s
T	temperature, °C
T	torque, N m
U	heat transfer coefficient, W/(m² K)
U	tip speed, m/s
v	specific volume, m³/kg
V	velocity, m/s
V	volume, m³
V_s	swept volume, m³
$\dot{V}$	volume flow rate, m³/s
w	specific work, J/kg
W	width, m
W	relative speed, m/s
$\dot{W}$	power, W
x	vapor quality, -
x	axial distance, m
X	capacity fraction, -

Greek symbols

α	absorptivity
α	proportionality factor
ε	effectiveness
ε	emissivity
Δ	differential
η	efficiency
ρ	density, kg/m³
ρ	reflectivity, -
ϕ	filling factor, -
τ	transmittance -

τ	time constant, s
ξ	penalty factor

Subscripts and superscripts

abs	Absorber
ad	Adapted
amb	Ambient
cal	Calorimeter
calc	Calculated
cd	Condenser
cf	Cold fluid
col	Collector
el	Electrical
em	Electromechanical
ev	Evaporator
ex	Exhaust
exp	Expander
f	Working fluid
i	Relative to cell i
in	Internal
hr	Heat recovery
htf	Heat transfer fluid
hx	Heat exchanger
l	Liquid
meas	Measured
n	Nominal
opt	Optical
pp	Pump
pred	Predicted
r	Refrigerant
rec	Recuperator
ref	Reference
s	Isentropic, Swept
sh	Shaft

sf	Secondary fluid
su	Supply
tot	Total
tp	Two-phase
v	Vapor, volume
w	wall
2	turbine nozzle exhaust
3	turbine rotor exhaust

Acronyms

BWR	Back Work Ratio
CHP	Combined Heat and Power
CS	Control Signal
CSP	Concentrating Solar Power
GDP	Gross Domestic Product
GHG	Greenhouse Gases
GWP	Global Warming Potential
HCE	Heat Collection Element
HVAC	Heating, Ventilation, and Air Conditioning
ICE	Internal Combustion Engine
IPCC	Intergovernmental Panel on Climate Change
ODP	Ozone Depleting Potential
ORC	Organic Rankine Cycle
PV	Photovoltaïc
SIC	Specific Investment Cost
TIT	Turbine Inlet Temperature
VC	Volume Coefficient
WHR	Waste Heat Recovery

Chapter 1:

Introduction

Modern technology
Owes ecology
An apology.
Alan M. Eddison

Energy access is a fundamental parameter for human development. Institutions such as the World Bank, the United Nations or the European Union consider energy as a key-element for promoting or improving base services such as lightning, drinking water access, health services, education or communications.

The economic development stated in a number of areas in the world over the last century has involved an important growth in energy consumption. Unfortunately, this growth has been mainly covered by the use of fossil fuels, motivated by economic considerations. Other factors such as atmospheric pollution, limited oil resources and national energy dependence were not properly taken into account.

In its first report in 2007, the IPCC formulated the following statement: "*Most of the observed increase in global average temperatures since the mid-20th century is very likely due to the observed increase in anthropogenic greenhouse gas concentrations.*" According to the different scenarios the average earth temperature should rise between 2 to 4°C before the end of the century, with dramatic consequences such as the rise of sea levels, higher drought occurrences and desertification, higher frequency of natural disasters, negative impact on biodiversity, etc.

84% of the greenhouse gases emissions are attributable to the energy sector, mainly in the form of carbon dioxide emissions (Quadrelli & Peterson, 2007). These emissions are mainly due to industrialized countries: the ten first emitting countries generate two thirds of the world emissions. It can be feared that the actual development of least-industrialized countries will be accompanied by a dramatic increase in CO_2 emissions.

Today, a good correlation exists between gross energy consumption and GDP, literacy rate, infant mortality and fertility (Jones & Thompson, 1996). However, more and more voices are being heard, calling for a decoupling between economic growth and resource consumption (Jackson et al., 2011). This decoupling can only be achieved by massive investments in the R&D effort for sustainable energy conversion technologies and by promoting energy

efficiency policies. Massive technology transfers will also be required to ensure a cleaner development of countries with an emerging economy.

According to the EU 2050 Roadmap (European Climate Foundation, 2010), greenhouse gases emissions could be cut by 80% in 2050. This pathway involves the following modifications of the current energy system:

1. A decrease in the energy intensity of buildings (minus 950 TWh/year by 2050) and industry (minus 450 TWh/year).
2. A shift from fossil fuels towards electricity, e.g. for transportation and space heating.
3. Clean power generation by a massive shift towards renewable energies, among which 25% of wind energy, 19% of PV, 5% of CSP, 12% of biomass, 2% of geothermal, 12% of large hydro.
4. A reinforcement of the grid capacity and inter-regional transmission lines to absorb daily and seasonal fluctuations.

Amongst the proposed solutions to fulfill these objectives, the Organic Rankine Cycle (ORC) technology can play a non-negligible role, in particular for the objectives 1 and 3:

- It can have a beneficial effect on the energy intensity of industrial processes, mainly by recovering waste heat (i.e. heat that is otherwise lost).
- It can have a positive effect on building consumptions, e.g. using CHP systems.
- It can be used to convert renewable heat sources into electricity. This mainly includes geothermal, biomass and solar sources (CSP).
- During the shifting transition towards electric vehicles, it can be used to increase the well-to-wheel efficiency by waste heat recovery on the exhaust gases, on the EGR and on the engine coolant.

The Organic Rankine Cycle involves the same components as a conventional steam power plant (a boiler, a work-producing expansion device, a condenser and a pump). However, the working fluid is an organic component characterized by a lower ebullition temperature than water and allowing power generation from low heat source temperatures.

The success of the ORC technology can be partly explained by its modular feature: a similar ORC system can be used, with little modifications, in conjunction with various heat sources. Moreover, unlike conventional power cycles, this technology allows for local and small scale power generation.

Today, Organic Rankine Cycles are commercially available in the MW power range. However very few solutions are actually suitable for the kW scale.

This work aims at contributing to the development of the ORC technology, mainly in the small-scale power range. It is organized as follows:

Chapter 2 summarizes the state of the art of the ORC technology. The main applications are described, with their practical limitations, the range of competiveness, the practical design of the cycle, the typical efficiencies and temperature levels, etc.

Chapter 3 describes the experimental studies carried out on ORC prototypes and their components. Special attention is paid to the expander technology, since it is a key component for the efficient use of small-scale ORCs.

Chapter 4 describes the sizing and simulation models developed in the scope of this work and required for simulating and optimizing different types of ORC cycles. These models are validated using the experimental results of Chapter 3.

Chapter 5 takes profit of the acquired practical experience (Chapter 3) and of the developed models (Chapter 4) to propose an optimization methodology for such cycles. A thermodynamic optimization method is described and three fluid selection methods are proposed and compared.

Chapter 6 illustrates how the developed steady-state and dynamic models can be used to evaluate the performance of prospective small-scale ORC systems. A transient WHR system and a CSP system are evaluated.

Chapter 2:

The Organic Rankine Cycle

Summary. The Organic Rankine Cycle (ORC) is a well known technology since the early 70's. A large amount of ORC power plants have been built, mainly for geothermal, waste heat recovery and combined heat and power applications. This technology shows a number of advantages over the traditional steam Rankine cycle, making it more profitable for power plants with a limited electrical output power (typically lower than 1 MWe), despite a lower efficiency. The optimization of the ORC is quite different from that of the steam cycle, mainly because of the heat source temperature limitation, and because there is usually no constraint regarding the vapor quality at the end of the expansion. This chapter presents an overview of the current state of the art in the ORC technology and exposes the main target applications.

1 Introduction

The particularity of the Organic Rankine Cycle (ORC) over the traditional Rankine cycle lays in the working fluid: an organic component is used instead of water. This organic compound is typically a refrigerant, a hydrocarbon (butane, pentane, hexane, etc.), a silicon oil, a perfluorocarbon... Its boiling point is lower than that of water, which allows recovering heat at a lower temperature than in the traditional steam Rankine cycle. Its thermophysical properties differ from that of water in a number of aspects (further discussed in section 3), which has practical implications on the design of the Organic Rankine Cycle.

Organic Rankine Cycles have been studied both theoretically (Davidson, 1977, Probert et al., 1983) and experimentally (Monahan, 1976) as early as in the 70s, with reported efficiencies usually below 10% for small-scale systems. Experimental studies generally involved the use of vane expanders (Badr et al., 1990, Davidson, 1977) and high Ozone Depleting Potential (ODP) refrigerants such as R11 or R13.

The first commercial applications appeared in the late 70s and in the 80s with medium-scale power plants developed for geothermal and solar applications.

Nowadays, more than 200 ORC power plants are identified, with over 1800 MWe installed, and this number is growing at a faster pace than ever before. Most of the plants are installed for biomass CHP applications, followed by

geothermal plants and by WHR plants. It should however be noted that the first application in terms of installed power is geothermy (Enertime, 2011).

The layout of the Organic Rankine Cycle is somewhat simpler than that of the steam Rankine cycle: there is no water-steam drum connected to the boiler, and one single heat exchanger can be used to perform the three evaporation phases: preheating, vaporization and superheating. The variations on the cycle architecture are also more limited: reheating and turbine bleeding are generally not suitable for the ORC cycle, but a recuperator can be installed as a liquid preheater between the pump outlet and the expander outlet, as illustrated in Figure 1.

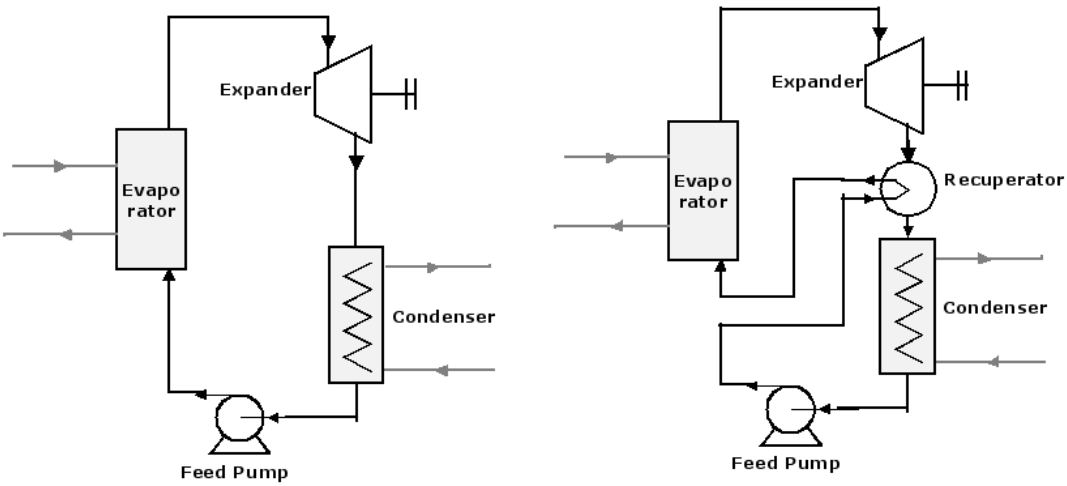

Figure 1: Working principle of an ORC cycle with (right) and without (left) recuperator

The basic cycle is very similar to the traditional steam cycle: the organic working fluid is successively pumped, vaporized, expanded and then condensed. The cycle with recuperator takes profit of the residual heat after the expansion to preheat the liquid after the pump. This operation allows reducing the amount of heat needed to vaporize the fluid in the evaporator.

2 Applications

2.1 Biomass combined heat and power

Biomass is widely available in a number of agricultural or industrial processes such as wood industry or agricultural waste. It is best used locally for two main reasons : (1) the energy density of biomass is low compared to that of fossil fuels, which increases transportation costs; (2) heat and electricity demand are usually available on-site, which makes a biomass plant particularly suitable in the case of off-grid or unreliable grid connection. Local generation leads to smaller scale power plants (<1-2 MWe) which excludes traditional steam cycles that are not cost-effective in this power range.

The working principle of such a cogeneration system is described in Figure 2 and Figure 3: heat from the combustion is transferred from the flue gases to

the heat transfer fluid in two heat exchangers, at a temperature varying between 150 and 320°C. The heat transfer fluid (thermal oil) is then directed to the ORC loop to evaporate the working fluid, at a temperature slightly lower than 300°C. The evaporated fluid is then expanded, passes through the recuperator to preheat the liquid and is then condensed at a temperature around 90°C. The condenser is used for hot water production.

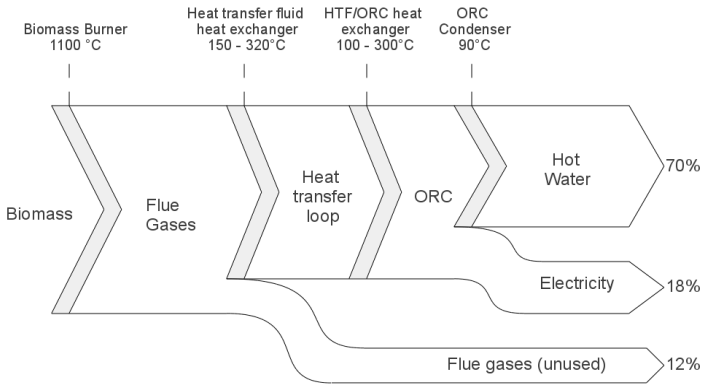

Figure 2: Energy fluxes in a biomass CHP ORC system

The efficiency of power generation with ORCs is lower than that of traditional steam cycles, and generally decreases for small scale units. This is statement is partly explained by their simpler design and lower cost. Heat demand is therefore a prerequisite to increase the overall plant energy conversion efficiency. This heat demand can be fulfilled by industrial processes (such as wood drying) or space heating. Plant load can be controlled either by on-site heat demand, or by maximizing power generation. The latter solution involves wasting the additional heat but has the advantage of increasing the annual full load operating hours.

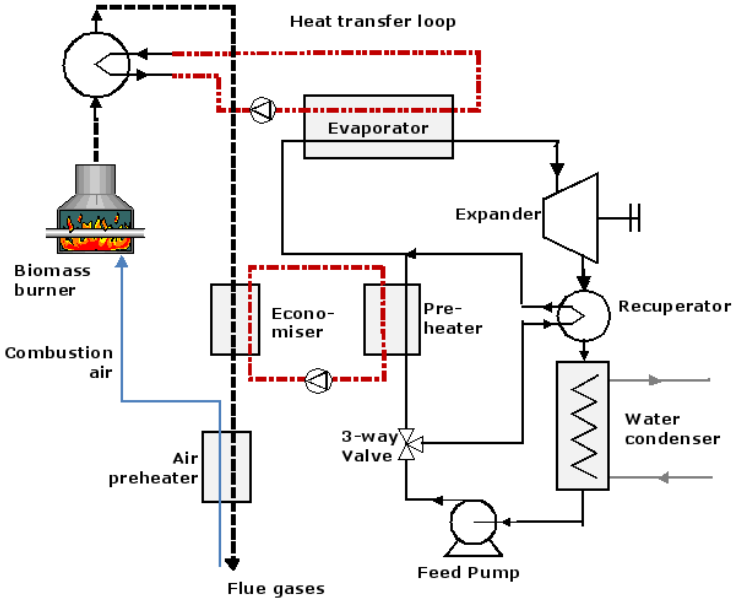

Figure 3: Working principle of a biomass CHP ORC system

For the particular example of Figure 2, although the electrical efficiency of the CHP system is quite low (18%), the overall efficiency of the system is 88% which is much higher than centralized power plants, in which most of the residual heat is lost.

In order to reduce heat losses in the flue gases, these gases must be cooled down to the lowest possible value, as long as the acid dew point is not reached. To achieve this, two heat transfer loops are used: a high temperature loop and a low temperature loop. The low temperature loop is installed after the high temperature one on the flue gases to reduce their outlet temperature (Figure 3).

The main competing technology for electricity generation from solid biofuels is biomass gasification: In this technology, biomass is transformed into a synthetic gas composed mainly of H_2, CO, CO_2, CH_4. This synthetic gas is treated and filtered to eliminate solid particles, and is finally burned in an internal combustion engine or in a gas turbine.

When comparing the technology and the costs of Biomass CHP using an ORC with gasification, it can be showed that gasification yields higher investment costs (about 75%) and higher operation and maintenance costs (about 200%). On the other hand, gasification shows a higher power-to-thermal ratio, which makes its exploitation more profitable (Rentizelas et al., 2009). It should also be noted that ORC is a well-proven technology, while gasification plants actually in operation are mostly prototypes for demonstration purpose.

2.2 Geothermal energy

Geothermal heat sources are available over a broad range of temperatures, from a few tens of degrees up to 300°C. The actual technological lower bound for power generation is about 80°C: below this temperature conversion efficiency becomes too small and geothermal plants are not economical. Table 1 indicates the potential for geothermal energy in Europe and shows that this potential is very high for low temperature sources.

Temperature	MWth	MWe
65-90°C	147736	10462
90-120°C	75421	7503
120-150°C	22819	1268
150-225°C	42703	4745
225-350°C	66897	11150

Table 1: Potential for geothermal energy in Europe for different heat source temperature ranges (Data source: (Karytsas, 2007))

To recover heat at an acceptable temperature, boreholes must generally be drilled in the ground, for the production well and for the injection well (cfr. Figure 4). The hot brine is pumped from the first one and injected in the second one at a lower temperature. Depending on the geological configuration, boreholes can be several thousands meters deep, requiring several months of continuous work. This leads to a high share of the drilling in

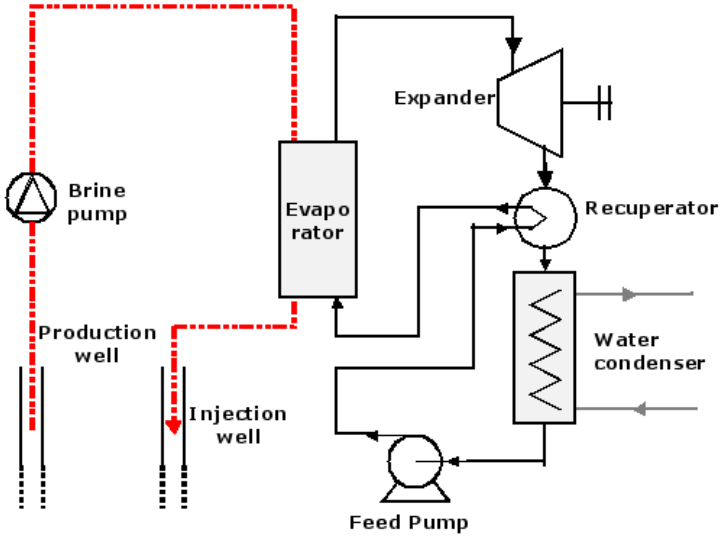

Figure 4: Working principle of a geothermal ORC system

the investment cost (up to 70%) of a geothermal ORC plant (Kranz, 2007).

Low-temperature geothermal ORC plants are also characterized by a relatively high auxiliary consumption: the pumps consume from 30 up to more than 50% of the gross output power (Frick, 2009). The main consumer is the brine pump that has to circulate the brine on large distances and with an important flow rate. The working fluid pump consumption is also higher than in higher temperature cycles, because the ratio between pump consumption and turbine output power ("back work ratio") increases with a decreasing evaporating temperature.

Higher temperature (>150°C) geothermal heat sources enable combined heat and power generation: the condensing temperature is set to a higher temperature (e.g. 60°C), allowing the cooling water to be used for district heating. In this case, the overall energy recovery efficiency is increased, but at the expense of a lower electrical efficiency.

2.3 Solar power plants

Concentrating solar power is a well-proven technology: the sun is tracked and reflected on a linear or on a punctual collector, transferring heat to a fluid at high temperature. The heat is then transferred to a power cycle generating electricity. The three main concentrating technologies are the parabolic dish, the solar tower, and the parabolic trough. Parabolic dishes and solar towers are punctual concentration technologies, leading to a higher concentration

factor and to higher temperatures. The best suited power cycles for these technologies are the Stirling engine (small-scale plants), the steam cycle, or even the combined cycle, for solar towers.

Parabolic troughs work at a lower temperature (300°C to 400°C). Up to now, they were mainly coupled to traditional steam Rankine cycles for power generation (Müller-Steinhagen & Trieb, 2004). The same limitation as in geothermal or biomass power plants remains: steam cycles require high temperatures, high pressures, and therefore high installed power to be profitable.

Organic Rankine cycles seem to be a promising technology to decrease investment costs at small scale: they can work at lower temperatures, and the total installed power can be reduced down to the kW scale. The working principle of such a system is presented in Figure 5. Technologies such as Fresnel linear concentrators (Ford, 2008) are particularly suitable for solar ORCs since they require lower investment cost, but work at a lower temperature.

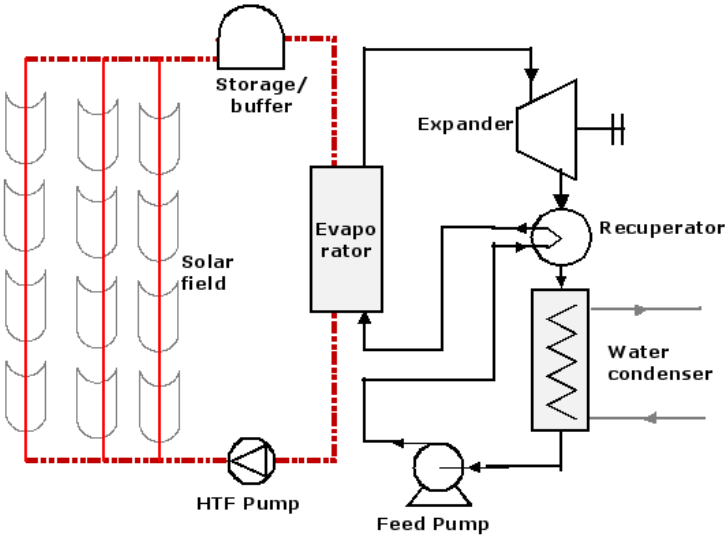

Figure 5: Working principle of a solar ORC system

Up to now, very few CSP plants using ORC are available on the market:

- A 1MWe concentrating solar power ORC plant was completed in 2006 in Arizona. The ORC module uses n-pentane as the working fluid and shows an efficiency of 20 %. The overall solar to electricity efficiency is 12.1% on the design point (Canada, 2004).
- Some very small-scale systems are being studied for remote off-grid applications. The only available proof-of-concept is a 1 KWe system installed in Lesotho by “STG International” for rural electrification. The goal of this project is to develop and implement a small scale solar thermal technology utilizing medium temperature collectors and an ORC to achieve economics analogous to large-scale solar thermal installations. This configuration aims at replacing or supplementing Diesel generators

in off-grid areas of developing countries, by generating clean power at a lower levelized cost.

2.4 Heat recovery on mechanical equipment and industry processes

Many applications in manufacturing industry reject heat at relatively low temperature. In large-scale plants, this heat is usually overabundant and cannot be reused on-site or for applications such as district heating. It is therefore rejected to the atmosphere.

This causes two types of pollution (Bundela & Chawla, 2010):

- The pollutants (CO_2, NO_x, SO_x, HC) contained in the flue gases can generate health or environmental issues.
- The heat rejection can perturb aquatic equilibrium and have a negative effect on biodiversity.

Recovering this waste heat can mitigate these two types of pollution. It can moreover generate electricity to be consumed on-site or sent back to the grid. In such a system, the waste heat is usually recovered by an intermediate heat transfer loop and used to evaporate the working fluid of the ORC cycle. A potential of 750 MWe is estimated for power generation from industrial waste heat source in the US (Bailey & Worrell, 2005).

Some industries present a particularly high potential for waste heat recovery. Among them, the cement industry, in which 40% of the heat is lost in flue gases. These flue gases are located after the limestone preheater or in the clinker cooler, with a temperature varying between 215 and 315 °C (Engin & Ari, 2005). CO_2 emissions from cement industry amount for 5% of the total world CO_2 emissions, and half of it is due to the combustion of fossil fuels in the kilns (Bundela & Chawla, 2010). Other possible industries include the iron and steel industries (10% of the CO_2 emission in China for example), refineries or chemical industries.

Despite their high potential and low cost (1000 to 2000 €/kWe), waste heat recovery organic Rankine cycles only account for 9 to 10% of the installed ORC plants in the world, far behind biomass CHP and geothermal units (Enertime, 2011).

2.5 Heat recovery on internal combustion engines

An Internal Combustion Engine only converts about one third of the fuel energy into mechanical power. For instance, for a typical 1.4 liter Spark Ignition ICE, with a thermal efficiency ranging from 15 to 32%, 1.7 to 45 kW are released through the radiator (at a temperature close to 80 - 100°C) and 4.6 to 120 kW through the exhaust gas (400 - 900°C).

The heat recovery Rankine cycle system is an efficient means for recovering heat (in comparison with other technologies such as thermo-electricity and absorption cycle air-conditioning). The idea of associating a Rankine cycle to

an ICE is not new and the first technical developments followed the 70's energy crisis. For instance, Mack Trucks (Patel & Doyle, 1976) designed and built a prototype of such a system operating on the exhaust gas of a 288 HP truck engine. A 450 km on-road test demonstrated the technical feasibility of the system and its economical interest: an improvement of 12.5% of the fuel consumption was reported. Systems developed today differ from those of the 70's because of the advances in the development of expansion devices and the broader choice of working fluids.

However, at the present time, Rankine cycle systems are under development, but no commercial solution seems to be available yet.

Most of the systems under development recover heat from the exhaust gases and from the cooling circuit (Freymann et al., 2008). By contrast, the system developed by (Oomori & Ogino 1993) only recovers heat from the cooling circuit.

Different architectures can be proposed to recover engine waste heat: The heat recovery system can be a direct evaporation system or a heat transfer loop system. In the first case, the evaporator of the ORC is directly connected to the exhaust gases. The advantage of such a configuration is the high temperature of the heat recovery, allowing higher cycle efficiency. In the second case, thermal oil is used to recover heat on the exhaust gases and is then directed to the evaporator. This second system acts as buffer and reduces the transient character of the ORC heat source, which simplifies its control. It also shows the advantage of avoiding hot spots in the evaporator, which could damage the organic working fluid.

The expander output can be mechanical or electrical. With a mechanical system, the expander shaft is directly connected to the engine drive belt, with a clutch to avoid power losses when the ORC cycle power output is too low. The main drawback of this configuration is the imposed expander speed: this speed is a fixed ratio of the engine speed and is not necessarily the optimal speed for maximizing cycle efficiency. In the case of electricity generation, the expander is coupled to an alternator, used to refill the batteries or supply auxiliary equipments such as the air conditioning. It should be noted that current vehicle alternators show a quite low efficiency (about 50 to 60%), which reduces the ORC output power.

As for the expander, the pump can be directly connected to the drive belt, to the expander shaft, or to an electrical motor. In the latter case, the working fluid flow rate can be independently controlled, which makes the regulation of such a system much easier.

The control of the system is particularly complex due to the (often) transient regime of the heat source. However, optimizing the control is crucial to improve the performance of the system. It is generally necessary to control both the pump speed and the expander speed to maintain the required conditions (temperature, pressure) at the expander inlet.

Performance of the recently developed prototypes of Rankine cycles is promising. For instance, the system designed by Honda (Endo et al., 2007)

showed a maximum cycle thermal efficiency of 13%. At 100 km/h, this yields a cycle output of 2.5 kW (for an engine output of 19.2 kW) and represents an increase of the engine thermal efficiency from 28.9% to 32.7%.

A competing technology under research and development is the thermoelectric generator (TEG), which is based on the Seebeck effect: its main advantages are a substantially lower weight than the ORC system, and the absence of moving parts. Major drawbacks are the cost of materials (they contain rare earths) and the low achieved efficiency.

3 Comparison with the steam Rankine Cycle

Figure 6 shows in the T-s diagram the saturation curves of water and of a few typical organic fluids in ORC applications. Two main differences can be stated:

- The slope of the saturated vapor curve (right curve of the dome) is negative for water, while the curve is much more vertical for organic fluids. As a consequence, the limitation of the vapor quality at the end of the expansion process disappears in an ORC cycle, and there is no need to superheat the vapor before the turbine inlet.
- The entropy difference between saturated liquid and saturated vapor is much smaller for organic fluids. This also involves that the enthalpy of vaporization is smaller. Therefore, for the same thermal power through the evaporator, the organic working fluid mass flow rate must be much higher than that of water, leading to a higher pump consumption.

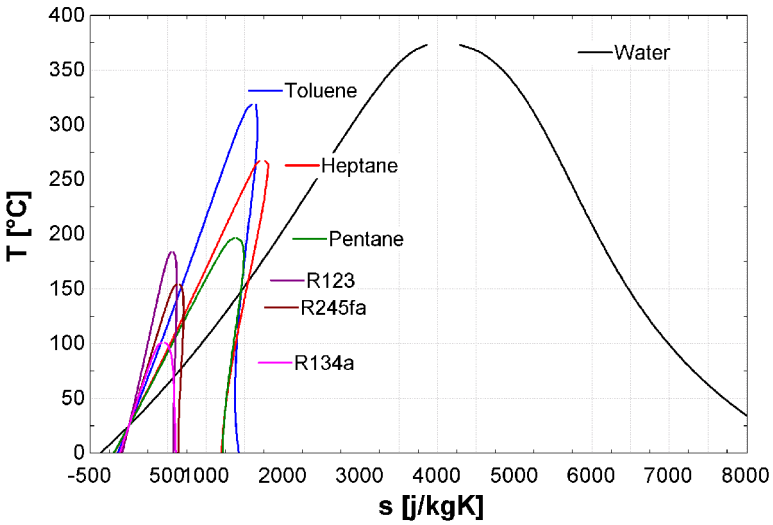

Figure 6: T-s diagram of a few typical organic fluids and of water

Superheating. As previously stated, organic fluids usually remain superheated at the end of the expansion. Therefore, there is no need for superheating in ORC cycles, contrary to steam cycles. The absence of condensation also reduces the risk of corrosion on the turbine blade, and increases its lifetime up to 30 years instead of 15-20 for steam turbines (Bundela & Chawla, 2010).

Low temperature heat recovery. Due to the lower boiling point of the organic working fluids, heat can be recovered at a much lower temperature. This allows for, among others, power generation from geothermal heat sources.

Components size. The size of the components is very dependent on the volume flow rate of the working fluid because pressure drops increase with the square of the fluid velocity. This leads to the necessity of increasing the heat exchangers hydraulic diameter and the pipe diameter to reduce this velocity. The turbine size is roughly proportional to the volume flow rate.

Turbine inlet temperature. In steam Rankine cycles, due to the superheating constraint, a temperature higher than 450°C is required at the turbine inlet to avoid droplets formation during the expansion. This leads to higher thermal stresses in the boiler and on the turbine blades and to higher cost.

Pump consumption. Pump consumption is proportional to the liquid volume flow rate and to the pressure difference between outlet and inlet. It can be evaluated by the Back Work Ratio (BWR), which is defined as the pump consumption divided by the turbine output power. In a steam Rankine cycle, the water flow rate is relatively low and the BWR is typically 0.4%. For a high temperature ORC using toluene, typical value is 2 to 3%. For a low temperature ORC using HFC-134a, values higher than 10% can be stated. Generally speaking, the lower the critical temperature, the higher the BWR.

High pressure. In a steam cycle, pressures of about 60 to 70 bar and thermal stresses increase the complexity and the cost of the steam boiler. In an ORC, pressure generally does not exceed 30 bar. Moreover, the working fluid is not evaporated directly at the heat source (e.g. a biomass burner) but by the intermediary of a heat transfer loop. This makes the heat recovery easier since thermal oil is at ambient pressure, and avoids the necessity of an on-site steam boiler operator.

Condensing pressure. In order to avoid air infiltrations in the cycle, high condensing pressures are advisable. It is not the case for water, whose condensing pressure is generally lower than 100 mbar absolute. Low temperature organic fluids such as HFC-245fa, HCFC-123 or HFC-134a meet this requirement since they condense at a pressure higher than the atmospheric pressure. However, fluids with a higher critical temperature such as hexane or toluene are subatmospheric at ambient temperature.

Fluid characteristics. Water as working fluid is very convenient compared to organic fluids. Its main assets are:

- Cost-effectiveness and availability
- Non-toxicity
- Non-flammability
- Environment friendly: low Global Warming Potential (GWP), null Ozone Depleting Potential (ODP).

- Chemical stability: no working fluid deterioration in case of hot spot in the evaporator
- Low viscosity: lower friction losses, higher heat exchange coefficients

However, steam cycles are generally not fully tight: water is lost as a result of leaks, drainage or boiler blow down. Therefore, a water-treatment system must be integrated to the power plant to feed the cycle with high-purity deionised water.

Turbine design. In steam cycles, the pressure ratio and the enthalpy drop on the turbine are both very high. This involves using turbines with several expansion stages. In ORC cycles the enthalpy drop is much lower, and single or two-stage turbines are usually used, which reduces their cost.

Additional effects of the low enthalpy drop include lower rotating speeds and lower tip speed. The lower rotating speed allows direct drive of the electric generator without reduction gear (this is especially advantageous for low power-range plants), while the low tip speed decreases the stress on the turbine blade and makes their design easier.

Efficiency. The efficiency of current high temperature Organic Rankine Cycles does not exceed 24%. Typical steam Rankine cycles show a thermal efficiency higher than 30%, but with a more complex cycle design (in terms of number of components or size). The same trend is stated for low temperature heat sources: steam Rankine cycles remain more efficient than ORC cycles.

The advantages of each technology are summarized in Table 2.

Advantages of the ORC	Advantages of the steam cycle
No superheating	Fluid characteristics
Lower turbine inlet temperature	High efficiency
Compactness (higher fluid density)	Pump consumption
Lower evaporating pressure	
Higher condensing pressure	
No water-treatment system	
Turbine design	
Low temperature heat recovery	

Table 2: Advantages and drawbacks of each technology

As a consequence, the ORC cycle is more profitable in the low to medium power range (typically less than a few MWe), since small-scale power plants cannot afford an on-site operator, and require simple and easy to manufacture components and design. For high power ranges, the steam cycle is generally preferred, except for low temperature heat sources.

4 Expansion machines

Performance of the ORC system strongly correlates with that of the expander. The choice of the machine depends on the operating conditions and on the size of the system. Two main types of machines can be distinguished: the turbo and positive displacement types. Similarly to refrigeration applications, displacement type machines are more appropriate to the small-scale ORC units, because they are characterized by lower flow rates, higher pressure ratios and much lower rotational speeds than turbo-machines (Persson, 1990).

4.1 Turbomachines

Currently, two main types of turbines are available: the axial turbine and the radial inflow turbine.

Axial turbines show a distinct design when used with high molecular weight working fluids. The main difference between organic fluid and steam is the enthalpy drop during the expansion, much higher for steam. As already mentioned, fewer stages are required when using an organic fluid. Single-stage turbines can even be employed for low or medium temperature ORC cycles.

Another characteristic of organic fluids is the low speed of sound. This speed is reached much faster in an ORC than in a steam cycle and constitutes an important limitation: high Mach number can indeed lead to increased irreversibilities and to decreased turbine efficiencies.

Radial inflow turbines are designed for high pressure ratios and low working fluid flow rates. Their geometry allows higher peripheral speeds than axial turbine, and therefore a higher enthalpy drop per stage. They also show the advantage of conserving an acceptable efficiency for a large range of part-load conditions.

However, unlike the axial turbine, it is uneasy to assemble several stages in series.

Figure 7 shows a typical maximum efficiency curve as a function of the specific speed for a radial turbine. The specific speed is defined by:

$$N_s = \frac{2 \cdot \pi \cdot N \cdot \sqrt{(\dot{V}_{ex})}}{\Delta h_s^{0.75}} \quad (1)$$

This maximum efficiency is the design point efficiency. It is obtained only when speed triangles (i.e. the blade angles) are optimized for the design conditions. If an efficiency of 84% is required, the acceptable specific speed range is comprised between 0.3 and 0.9 for this turbine technology (Figure 7).

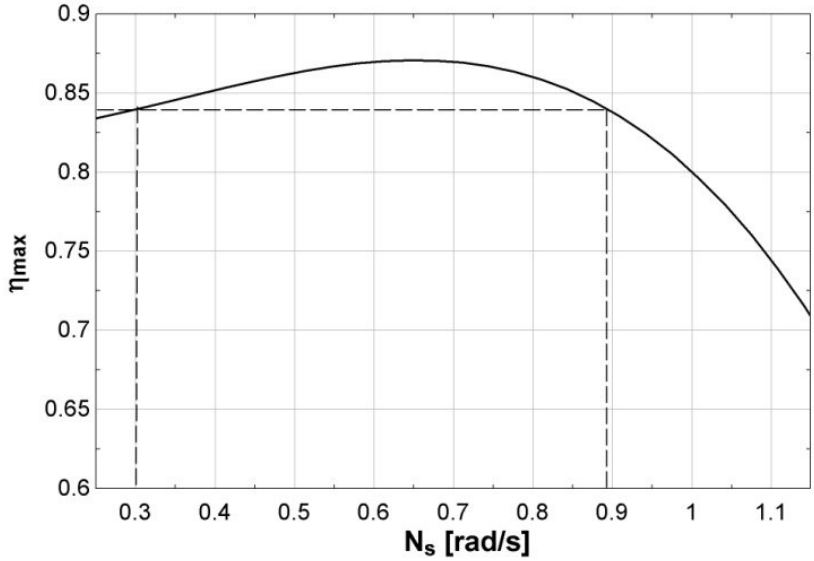

Figure 7: Typical maximum efficiency curve of a radial turbine as a function of its specific speed

Turbomachines are not suitable for very small-scale units, mainly because their rotating speed increases dramatically with a decreasing turbine output power. This is due to a typical characteristic of turbomachines: for a given technology, their tip speed is more or less constant, whatever the turbine size. This tip speed can be written:

$$U_2 = \pi \cdot N \cdot D_2 \tag{2}$$

where U_2 is the tip speed, N is the rotating speed and D_2 is the outer diameter.

As a consequence, when the turbine size (D_2) decreases, the rotating speed increases in the same proportion (Persson, 1990).

4.2 Positive displacement expanders

The major types of positive displacement expanders are the piston, the scroll, the screw and the vane expanders. In piston expanders, the same volume works successively as the suction, expansion and discharge chambers according to the timing of the suction and discharge valves. In rotary expander (scroll, screw, vanes), those chambers co-exist. The suction chamber evolves into one or two expansion chambers (for instance scroll expanders are characterized by two expansion chambers) after one shaft revolution. Similarly, expansion chambers become discharge chambers once they get into contact with the discharge line of the machine.

By contrast with most piston expanders, rotary expanders do not need valves: the timing of suction and discharge processes is imposed by the geometry of the machines. In terms of design, this is a major advantage over piston expanders. Moreover, the fact that suction and discharge do not occur in the same location limits the suction heat transfer, which has a positive impact on the volumetric performance of the machine. On the other hand, piston

expanders typically show lower internal leakage than scroll and screw expanders.

While technically mature turbomachines are available on the market for large ORC units, almost all positive displacement expanders that have been used up to now are prototypes, often derived from existing compressors (Zanelli and Favrat, 1994; Yanagisawa et al., 2001; Aoun and Clodic, 2008; Lemort et al., 2008). Positive displacement expanders are a good substitute to turbomachines for low output powers: their rotating speed is limited (generally 1500 or 3000 rpm on a 50 Hz electrical grid), they are reliable (widely used for compressor applications), they can tolerate the presence of a liquid phase during expansion, and they show a good isentropic efficiency.

In such a machine, the decrease of the pressure is caused by an increase of the volume of the expansion chambers. The ratio between the volume of the expansion chamber(s) at the end of the expansion and that at the beginning is called “built-in volume ratio” ($r_{v,in}$). This expansion is illustrated in Figure 8 in the particular case of a scroll expander: fluid is admitted at the center and trapped in a pocket of fluid that is progressively expanded while traveling to the periphery, where the working fluid is finally discharged.

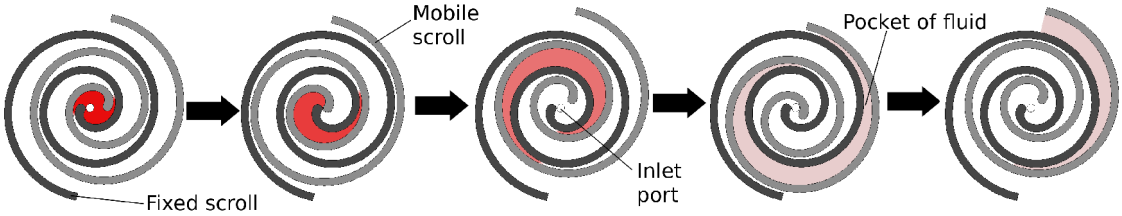

Figure 8: Working principle of a scroll expander

The fixed built-in volume ratio can generate two types of losses if the system specific volume ratio is not equal to the expander nominal volume ratio:

Under-expansion occurs when the internal volume ratio of the expander is lower than the system specific volume ratio. In that case, the specific volume in the expansion chambers at the end of the expansion process (P_{in}) is lower than the specific volume in the discharge line.

Likewise *Over-expansion* occurs when the internal volume ratio imposed by the expander is higher than the system specific volume ratio.

These two effects can considerably reduce the efficiency of the expansion process, the most common being the under-expansion. As a consequence, volumetric expanders are generally less adapted to high expansion ratios than turbomachines. Other sources of losses include friction losses, supply pressure drop, internal leakage and heat transfers (V. Lemort et al., 2009).

To optimize the performance of the expander and minimize under-expansion and over-expansion losses, this built-in volume ratio should match the operating conditions. However, volume expansion ratios achieved in Rankine cycle systems are typically larger than those achieved in vapor compression refrigeration systems, which justifies developing adapted designs of such expanders rather than retrofitting existing compressors. Generally speaking,

piston expanders are more appropriate for applications with large expansion ratio because their design allows for higher internal built-in volume ratios.

A major difficulty associated with the use of a positive displacement machine is its lubrication.

One solution consists in installing an oil separator at the expander exhaust. In this case, unlike with compressors, an oil pump is necessary to drive the separated oil back to the expander suction. Another solution consists in letting the oil travel with the refrigerant through the system and to install an oil separator at the evaporator exhaust. Separated oil is injected into the bearings, while the lubrication of the two spirals (in the case of a scroll expander) relies on the slight inefficiency of the separator. Alternatively, oil-free machines can be used, but generally show lower volumetric performance and high leakage due to larger tolerances between moving parts (V. Lemort et al., 2009, Yanagisawa et al., 2001).

In some operating conditions (wet fluids with limited superheat at the expander supply), liquid may appear at the end of the expansion. This could be a threat of damage for piston expanders but not for scroll and screw expanders, since the latter can generally accept a large mass fraction of liquid.

Chapter 3:

Experimental setups

If you cannot measure it,
You cannot improve it
<Lord Kelvin>

Summary. This chapter presents two experimental studies: the first one is an ORC prototype whose expander is an oil-free scroll expander and the second one is a prototype of a hermetic scroll expander. Both expanders are obtained by adapting a scroll compressor to make it run in reverse. A maximum efficiency of 7.3% is obtained for the ORC prototype, with a very promising expander mechanical isentropic effectiveness of 71%. About the same effectiveness is measured on the hermetic scroll expander but considering the electrical output power instead of shaft power.

1 Introduction

The small-scale Organic Rankine Cycle technology is still at an early stage of development. To understand the behavior of such a cycle under different conditions, practical experience is needed. This experience has at least three objectives:

- Evaluate the performance potential of such a system and point out the main sources of irreversibilities.
- Calibrate a model of the cycle and compare predictions with experimental data.
- Understand and quantify the main physical and thermodynamic processes taking place in the system in order to be able to control them and propose a regulation strategy.

Few studies have provided experimental data from operational small-capacity ORC prototypes. The work on a superposed ORC cycle (i.e. the condenser of the topping cycle is also the evaporator of the bottoming cycle) proposed by (E. H. Kane, 2002) is of particular interest, since the technology is similar to the one proposed in the present work. The fluids of the bottoming and topping cycles (respectively HCFC-123 and HFC-134a) were selected to optimize the overall performance, with a heat source temperature of 165°C. A maximum net efficiency of 12% was reached. (Manolakos et al., 2009) studied a 2kWe low-temperature solar ORC with HFC-134a as working fluid and evacuated tube collectors: an overall efficiency below 4% was obtained. (H. Liu et al.,

2010) studied the coupling of an ORC unit with a biomass boiler for combined heat and power (CHP) applications. They built a test rig and obtained a net ORC efficiency of 1.34%. (R. B. Peterson et al., 2008) evaluated the performance of a micro-scale ORC (about 250 W output power) working with HCFC-123. A maximum efficiency of 7.8% was obtained. (Pei et al., 2011) tested a 1.3 kW ORC with HCFC-123 and a reaction radial inflow turbine as expansion device. They reached a cycle efficiency of 6.8% with an evaporating temperature of about 100°C and a condensing temperature close to 30°C.

Experimental studies of small scale ORC units demonstrated that the scroll expander is a good candidate for small scale power generation, because of its reduced number of moving parts, reliability, wide output power range, and broad availability (Zanelli & Favrat, 1994).

Until now, mainly open-drive scroll expanders have been investigated. (Yanagisawa et al., 2001) carried out an experimental study on an oil-free scroll-type air expander. Measured performance was analyzed by comparison with the prediction of an analytical model of the expander. They observed that the performance is lowered greatly by the mechanical losses accompanying the orbiting motion. Leakage losses become significant as the rotational speed decreases. Mechanical losses result from 1) the main bearing and the auxiliary crank mechanisms that support the revolving motion of the orbiting scroll; 2) friction between the orbiting and the fixed scrolls. They observed that the mechanical loss torque is neither a function of the suction pressure nor of the rotational speed. Volumetric effectiveness of 76% and isentropic effectiveness of 60% were achieved under condition of suction pressure 6.5 bar gauge and rotational speed of 2500 rpm.

(Manzagol et al., 2002) studied a cryogenic scroll expander used for a 10 L/h helium liquefier. The expander was tested on a Brayton cycle refrigerator and reached an isentropic effectiveness of 50 to 60% for inlet gas conditions of 35K and 7.0 bar.

(Xiaojun et al., 2010) investigated the possibility to recover work in a fuel cell by means of a scroll expander. The expander was numerically simulated and a prototype of the expander was tested. It was shown that the leakages strongly impact on the volumetric performance of the machine.

(Aoun & Clodic, 2008) carried out an experimental investigation on an oil-free scroll type vapor expander. Original gasket was replaced by a hand-made polytetrafluoroethylene (PTFE) gasket, more adapted for high temperature applications (about 190°C) and showing lubricating properties. Maximal isentropic effectiveness was 48% at rotation speed of 2000 rpm and pressure ratio of 3.8.

In his experimental study, (R. B. Peterson et al., 2008) tested a kinematically rigid scroll expander with a displacement of 12 cm^3 and a built-in volume ratio of 4.57. The expander was fed in oil by means of an external gear pump coupled to a centrifugal oil separator at the outlet of the expander. They showed that the critical component, in terms of impact on the system efficiency, was the expander, with a measured isentropic effectiveness ranging

between 45 and 50%. Such low performance was due to excessive internal leakages, which is characteristic to this type of expander.

For some applications, such as micro-combined heat and power (CHP), it would be more convenient to have an expander producing directly electrical power, instead of mechanical power. This justifies the interest for better characterizing the performance of a hermetic scroll expander. Such machine is expected to show better volumetric performance than kinematically rigid expanders since the gap between scrolls is smaller and filled by oil. They also show the advantage of being perfectly tight.

Only a few scientific works on this type of machine were found in the open literature. (Zanelli & Favrat, 1994) tested a prototype of hermetic scroll expander-generator fed with refrigerant HFC-134a. The maximal achieved isentropic effectiveness was 65% and the power produced by the machine ranged from 1.0 to 3.5 kW. Within its prototype of hybrid solar thermal power, (E. H. Kane, 2002) tested hermetic scroll expanders and obtained an effectiveness of ranging between 50 and 68% depending on the pressure ratio.

More recently, (H. Wang, Peterson, et al., 2009) measured the performance of a compliant scroll expander derived from an existing compressor and characterized by a displacement of 6.5 cm^3 and a built-in volume ratio of 2.5. The machine was tested in a gas cycle with HFC-134a for different pressure ratios (2.65 to 4.84) and rotational speeds (2005 to 3670 rpm). Their prototype of expander allowed for a control of the sealing pressure, by pressurizing the chamber atop the fixed scroll. They also showed that the scroll sealing pressure was a critical parameter to maximize the expander performance. Maximum mechanical isentropic effectiveness reached 77%. Maximum shaft work was around 1 kW. They observed that the impact of the rotational speed and pressure ratio was limited.

This chapter aims at contributing to the characterization of small-scale ORC units working with scroll expanders. To that end, the experimental results relative to two different test benches are described. The first one is a prototype of small-scale organic Rankine cycle using an oil-free scroll expander and tested with two different refrigerants, namely HCFC-123 and HFC-245fa. The second test bench was built with the objective of testing a hermetic lubricated scroll expander in order to compare its performance with the oil-free expander. The evolution of the performance with main operating parameters is also presented. Among others, the impact of the quantity of lubricating oil is investigated.

2 ORC test bench

2.1 Description

The experimental study was carried out on a prototype of ORC working with HCFC-123. A schematic representation of the first version of the test bench is provided in Figure 9. The scroll expander was originally an oil-free open-drive scroll compressor, adapted to operate in reverse. It drives an asynchronous

machine through two belt-pulley couplings and a torque meter. The latter is used to measure the expander shaft power. The heat source consists of a set of three heat exchangers supplied with two hot air flows. The condenser is cooled by water. A diaphragm piston-type pump drives the liquid fluid from the condenser exhaust to the boiler supply. A pulse damper is installed before the Coriolis flow meter to attenuate the flow rate fluctuations generated by the volumetric pump. All the components are insulated with an elastomeric rubber, with a thickness of 13 mm and a 0°C conductivity of 0.036 W/(mK).

The first version of this test bench was initially designed and operated by V. Lemort, (2009), whose work mainly focused on the characterization of the scroll machine.

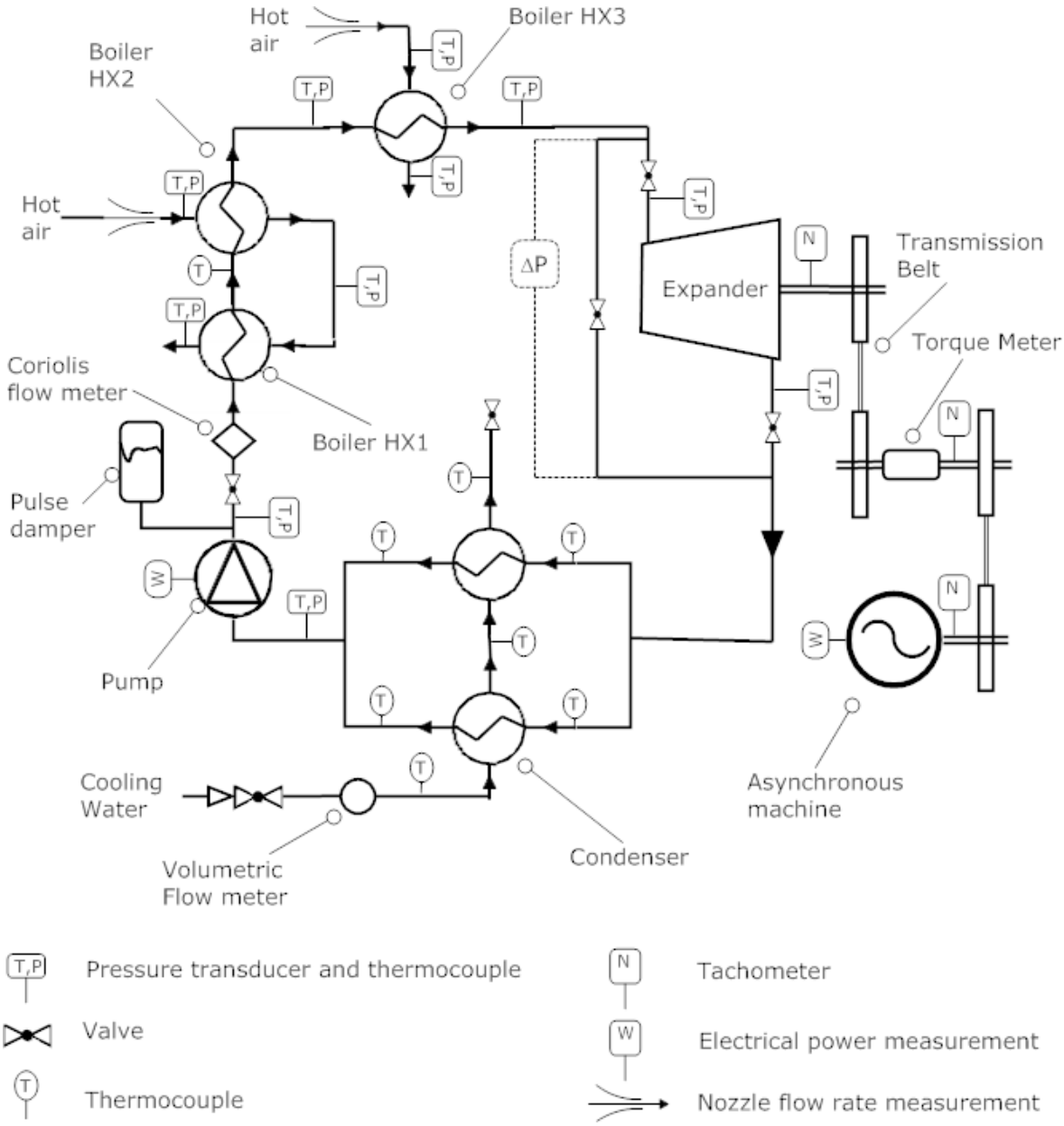

Figure 9: Schematic view of the ORC test bench (first version)

Pump

The pump is a hydraulic diaphragm metering pump. Its characteristics are provided in Table 3.

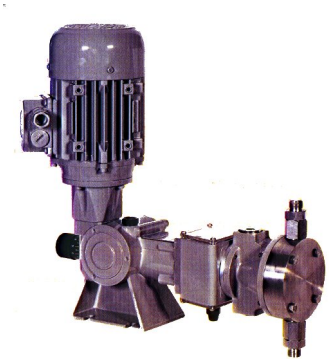

Model	Doseuro B.250N-40
Stroke frequency	112 strokes/min
Maximal flow rate	210 l/h at 50 Hz
Maximal pressure	12 bars
Motor	0.55 kW 1400 rpm
Piston diameter	40 mm
Stroke length	25 mm
Net weight	26 kg

Table 3: Pump characteristics

In this type of pump, there is no contact between the fluid and the piston, which allows for the use of abrasive or corrosive liquids. The flow rate can be adjusted by a manual graduated gearbox at the rear of the pump. It modifies the swept volume and thus the amount of fluid displaced at each stroke.

Heat exchangers

All heat exchangers are single-pass chevron-type brazed plate heat exchangers manufactured by Alfa Laval. The last heat exchanger of the evaporator (HX3) is a CB27-75LC model. All the other heat exchangers are CB27-35MC. Their characteristics are provided in Table 4.

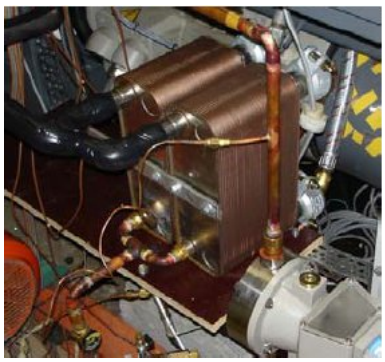

Model	CB27-75LC	CB27-35MC
Number of plates	75	35
Total volume [l]	3,75	1,75
Dimensions [mm]	250x112x189	250x112x93
Chevron angle	60°	30°
Working temperatures [°C]	-160 to 175	-160 to 175
Working pressures [bar]	0 to 32	0 to 32

Table 4: Plate heat exchangers characteristics

Scroll expander

The selected expander is originally an oil-free open-drive air compressor (Figure 10). It is characterized by a high internal built-in volume ratio (close to 4), which is an advantage in ORC cycles, where pressure ratios are generally higher than in refrigeration cycles. The swept volume of the device is 148 cm^3 in compressor mode. A valuable characteristics of this machine is the absence of lubrication, which avoids the need for an external pump and lubrication loop.

The main drawback is the open-drive configuration: in compressor mode, air tightness between the inside and the outside of the compressor is not guaranteed. In the present application, this is not acceptable since a refrigerant is used instead of air.

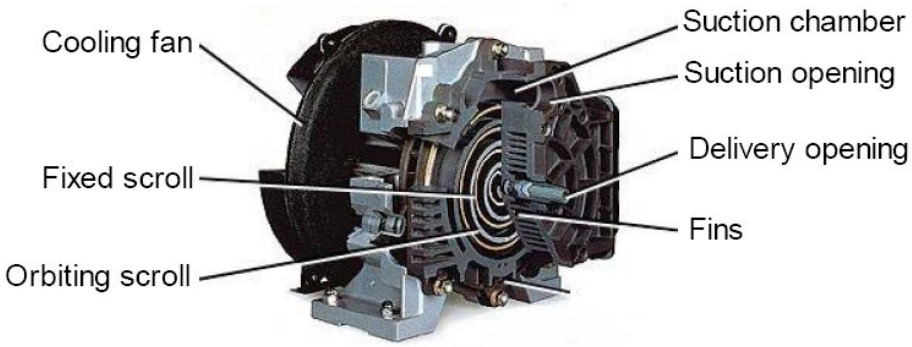

Figure 10: Air scroll compressor

In order to reduce the peripheral leakage, an extra 0.8 mm seal (O-ring) is inserted under the original peripheral dust seal (Figure 11). The contact effort between the fixed and orbiting scroll bodies is also increased, at the expense of increased friction losses.

Another modification brought to the compressor is the obstruction of its air-cooling circuit (air channel along the finned external envelope of the scroll). Cooling the vapor down is indeed advantageous in a compression process, but not in an expansion.

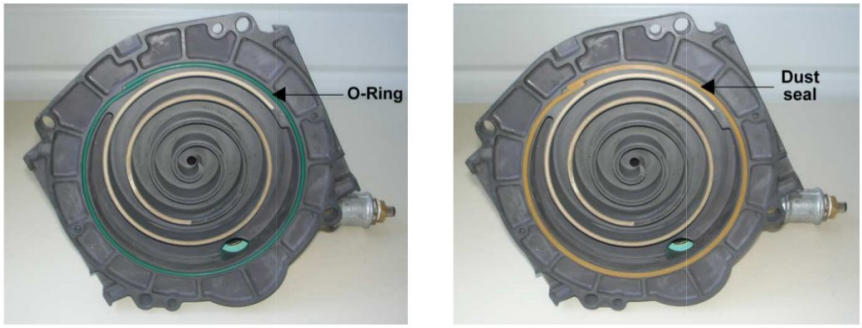

Figure 11: Peripheral seal

Measurement devices

Temperatures are measured using T-type thermocouples. Pressure levels are measured with both absolute and differential pressure sensors. The shaft power is measured with torque and tacho meters and a Coriolis flow meter is installed at the pump outlet to measure the refrigerant flow rate. The different sensors used on the test bench are described in Table 5.

Measurement	Constructor	Range	Accuracy
Absolute Pressures	Keller	0-5 or 0-10 bar	0.5% full scale
Pressure drops	Sensotec	0-500 or 0-1000 mbar	0.5% full scale
Working fluid flow rate	Emerson	0-0.15 kg/s	0.1% full scale
Temperatures	n/a	-200°C to 350°C	0.3 K
Torque	Lebow	max 20Nm 15000 rpm	+- 0.1 Nm
Electrical power	Gossen	0 to 3 kW	0.5% full scale

Table 5: Measurement devices

2.2 Measurements

In total, 39 steady-state performance points were achieved, by varying the operating conditions of the cycle, i.e. the expander speed, the pump swept volume, the heat source/sink flow rate and temperature and the refrigerant charge. The variation range of each parameter is provided in Table 6.

Working condition	Minimum value	Maximum value
First hot air source mean temperature	53.4 °C	86.4 °C
Second hot air source mean temperature	101.0 °C	163.2 °C
Air mass flow rate	0.071 kg/s	0.90 kg/s
Refrigerant flow rate	45 g/s	86 g/s
Condenser water volume flow rate	0.13 l/s	0.70 l/s
Condenser mean water temperature	13.2 °C	15.0 °C
Expander rotation speed	1771 rpm	2660 rpm

Table 6: Range of achieved operating conditions

Cross-checking and redundancies

Experimental research is an open door to many measurement issues, such as sensor malfunction, bad calibration or operating mistakes on the user side. It is therefore very important to install as many redundancies in the measurements as possible to cross-check the results and detect problems at an early stage of the experimental campaign.

On the present test bench, redundancies include secondary fluids flow rate and temperature measurements, redundant pressure sensors (e.g. the use of two absolute and one differential pressure sensors on the expander), and the use of several temperature sensors on the same refrigerant line.

Figure 12 illustrates this with the heat balance across the evaporator: $\dot{Q}_a$ is the heat flow measured on the air side and $\dot{Q}_f$ is the heat flow measured on the refrigerant side. The subscript hx1 refers to the first of the three heat exchanger composing the evaporator. Likewise, hx12 refers to the two first

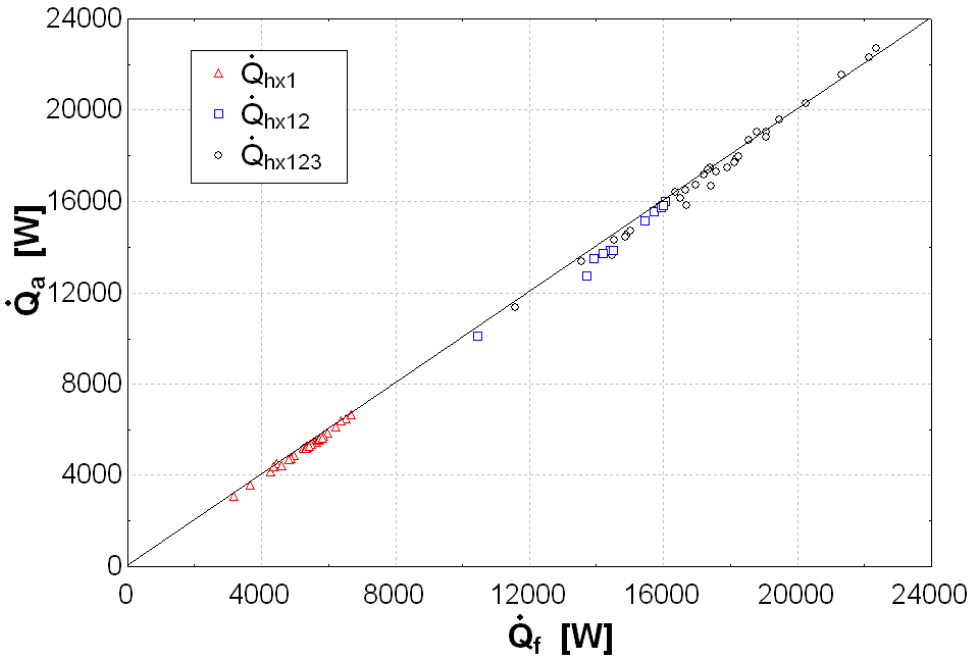

Figure 12: Heat balance over the evaporator

heat exchangers and hx123 to the whole evaporator. The points where a two-phase flow is present between two heat exchangers were excluded since the enthalpy cannot be calculated. An error lower than 4% on the heat balance is stated for all the point except one. The error is relatively low and can be explained by non-considered effects such as ambient heat losses.

The same analysis is performed on the condenser side, and a maximum error of 4.5% is obtained. When cross-checking the additional redundancies, an error lower or slightly higher than the inaccuracy of the considered sensor (Table 5) was obtained for all points.

The flow rate measurement can also be compared to the theoretical flow rate of the pump, given by:

$$\dot{M}_{su,pp,th} = X_{pp} \cdot \rho_{su,pp} \cdot \dot{V}_{pp,max} \quad (3)$$

where X_{pp} is the pump fraction (manually set) and $\dot{V}_{pp,max}$ is the maximum volume flow rate of the pump, namely 210 l/h. This corresponds to a mass flow rate of 85.4 g/s for HCFC-123 at 25°C.

The maximum error between theoretical and measured flow rates in the absence of cavitation is 2.6 g/s.

2.3 Achieved performance

Three performance indicators are taken into account: the expander shaft power, the expander isentropic effectiveness, and the cycle first and second-law efficiencies.

The expander overall isentropic effectiveness is defined by:

$$\varepsilon_s = \frac{\dot{W}_{sh}}{\dot{M}_r \cdot (h_{su,\exp} - h_{ex,\exp,s})} \quad (4)$$

The cycle fist-law efficiency is defined by:

$$\eta_{cycle} = \frac{\dot{W}_{sh} - \dot{W}_{pp}}{\dot{Q}_{ev}} \quad (5)$$

The cycle second-law efficiency is defined by:

$$\eta_{II} = \frac{\dot{W}_{net}}{\dot{I}_{hf}} \quad (6)$$

$\dot{I}_{hf}$ is the heat source exergy flow rate defined by:

$$\dot{I}_{hf} = \dot{M}_{hf} \cdot [(h_{hf,su} - h_{hf,ref}) - T_{cf,su} \cdot (s_{hf,su} - s_{hf,ref})] \quad (7)$$

where the reference state is defined at the inlet temperature of the heat sink.

As shown in Figure 13, an expander isentropic effectiveness ranging from 42 to 68% is reached, corresponding to a maximum cycle efficiency of 6.6%. The pressure ratio over the expander varies from 2.7 to 5.4 and has a clear influence on the system performance. Error bars account for measurement uncertainties: Provided measurements are uncorrelated and random, the uncertainty U_Y on the variable Y is calculated as function of the uncertainties U_{Xi} on each measured variables X_i by (Klein, 2011):

$$U_Y^2 = \sum_i \left(\frac{\partial Y}{\partial X_i} \right)^2 U_{Xi}^2 \quad (8)$$

The efficiency curve plotted as a function of the pressure ratio shows several irregularities, which is explained by the effects of some other working conditions, such as pressure and temperature levels.

The cycle efficiency is mainly limited by a low pump efficiency (about 15%) and by the presence of non-condensing gases, as detailed in the next sections.

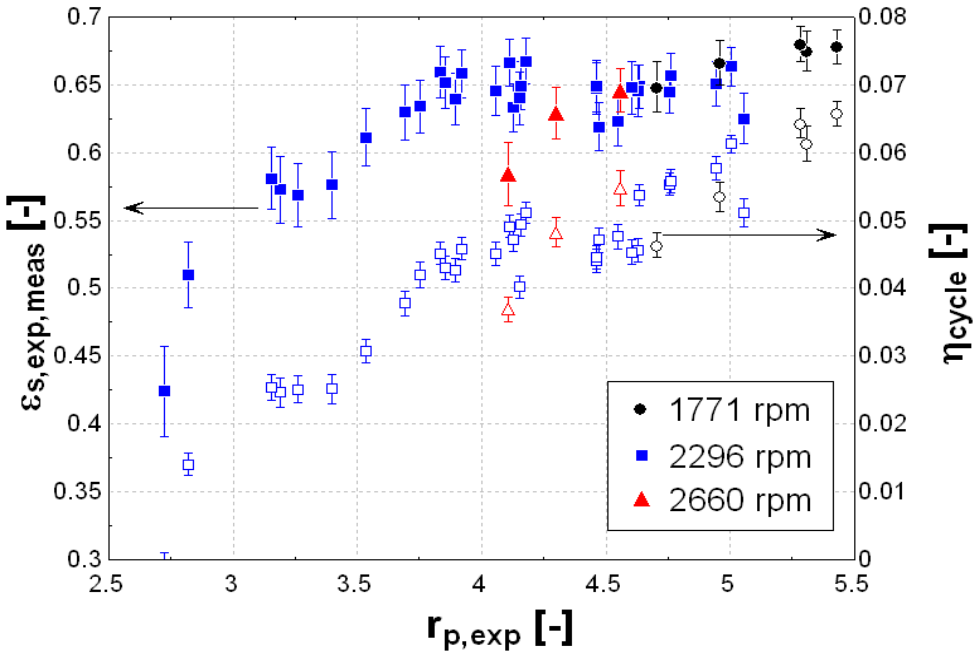

Figure 13: Expander effectiveness and cycle efficiency (Lemort, 2009)

Volumetric performance of the machine is quantified through the filling factor, defined as the ratio of the measured mass flow rate and the mass flow rate theoretically displaced by the expander:

$$\phi_{meas} = \frac{\dot{M}_{meas} \cdot v_{su,\exp}}{\dot{V}_{s,\exp}} \tag{9}$$

where $\dot{V}_s$ is the theoretical "swept" volume flow rate of the expander.

Figure 14 shows that there is a strong dependency between the filling factor and the rotating speed. This can be explained by the residence time of a given fluid particle in the device: the higher the rotation speed, the lower the

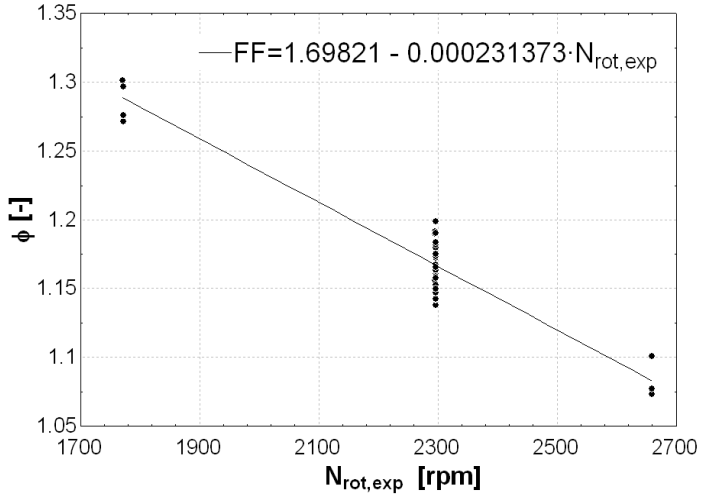

Figure 14: Measured filling factor as a function of the rotating speed

residence time. This decreases the relative leakage flow inside the expander since the fluid has "less time" to leak, and the filling factor is decreased. This phenomenon will be further detailed in the next sections using a semi-empirical model of the expander.

The T-s diagram of the cycle allows pointing out the main sources of irreversibility. The following statements can be formulated:

- The pressure drop over the condenser is very high. This is partly explained by the low density of HCFC-123 at ambient temperature, and by the presence of non-condensable gas in the condenser (see next paragraphs for more details). This pressure drop reduces the pressure difference at the expander boundaries and thus the output power.
- The subcooling is very high at the condenser exhaust. Because of the pinch point limitation, this imposes a high condensing pressure and thus a lower output power.
- The second heat source (on HX3) is poorly utilized. It exits the evaporator at a temperature higher than 120°C, leaving most of the waste heat unrecovered.
- The overheating is too high.

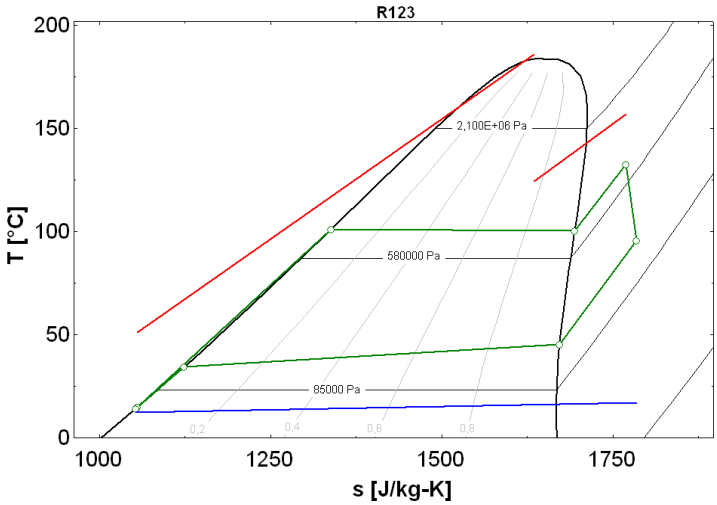

Figure 15: T-s diagram of the best measured performance point

The presence of a non-condensable vapor in the loop is stated: when the cycle is stopped several hours, it is observed that its pressure stabilizes at a mean value of 1.3 to 1.4 bar and at a temperature close to the ambient temperature (around 22°C). The vapor pressure of the working fluid at this temperature is 0.82 bar. It is therefore concluded that a non-condensable gas (most likely air) is present, whose partial vapor pressure in the cycle is around 0.5 bar. The presence of air in the circuit is explained by the negative relative vapor pressure of the refrigerant at low temperatures, and by the imperfect tightness of the open-drive scroll expander.

This statement explains the apparent very high subcooling after the condenser: the measured pressure is actually the sum of two partial pressures (the partial pressure of vapor and that of the air). The "measured" saturation temperature, the one indicated in Figure 15, corresponds to that saturation temperature at the measured pressure:

$$T_{sat,meas} = \boldsymbol{T}_{\boldsymbol{sat}}(p = p_{ex,cd,meas}) \quad (10)$$

However, the real saturation temperature is the one corresponding to the partial pressure of the refrigerant:

$$T_{sat,part} = \boldsymbol{T}_{\boldsymbol{sat}}(p = p_{f,part,ex,cd}) \quad (11)$$

with $p_{ex,cd,meas} = p_{f,part,ex,cd} + p_{air,part,ex,cd}$

For most tests, the partial pressure of air was comprised between 0.5 and 1.1 bar.

This effect was only stated in the condenser, not in the evaporator because non-condensable gases are carried by the main flow to the condenser, where they accumulate because of the condensation of the working fluid. It is therefore in the condenser that the highest concentration of non-condensable gases can be detected.

3 Improved ORC test bench

3.1 Description

To improve the performance of the first prototype described in section 2 , a few modifications are performed on its design. This modified test bench allows testing alternative configurations, new working conditions and working fluids, improving the operational experience gained on such cycles. A schematic representation of the modified test bench is provided in Figure 16.

Working fluid. HCFC-123 is a refrigerant with a non-null Ozone Depleting Potential (ODP). Therefore, it is progressively being phased out on the basis of the Montreal protocol. The definitive phasing out is planned for 2030. In this new test bench, HCFC-123 is replaced by HFC-245fa, which is a very common working fluid in ORC applications.

Liquid receiver. In the same manner as in refrigeration cycles, the refrigerant charge imposes the subcooling at the condenser exhaust: more fluid involves a higher liquid level in the heat exchangers and therefore more space for the subcooling zone. To reduce the subcooling, the refrigerant charge had to be adjusted manually to its minimum value for each new working point of the first version of the test bench. A good solution consists in using a liquid receiver after the condenser: it imposes a saturated liquid state at this point and thus a null subcooling (at least in steady-state). Variations of the liquid level in the heat exchangers are compensated by a variation of the liquid level in the liquid receiver. The installed liquid receiver is a refrigeration

liquid receiver, with a capacity of 8 liters and a maximum pressure of 30 bar. A level indicator is installed on the side (Figure 17).

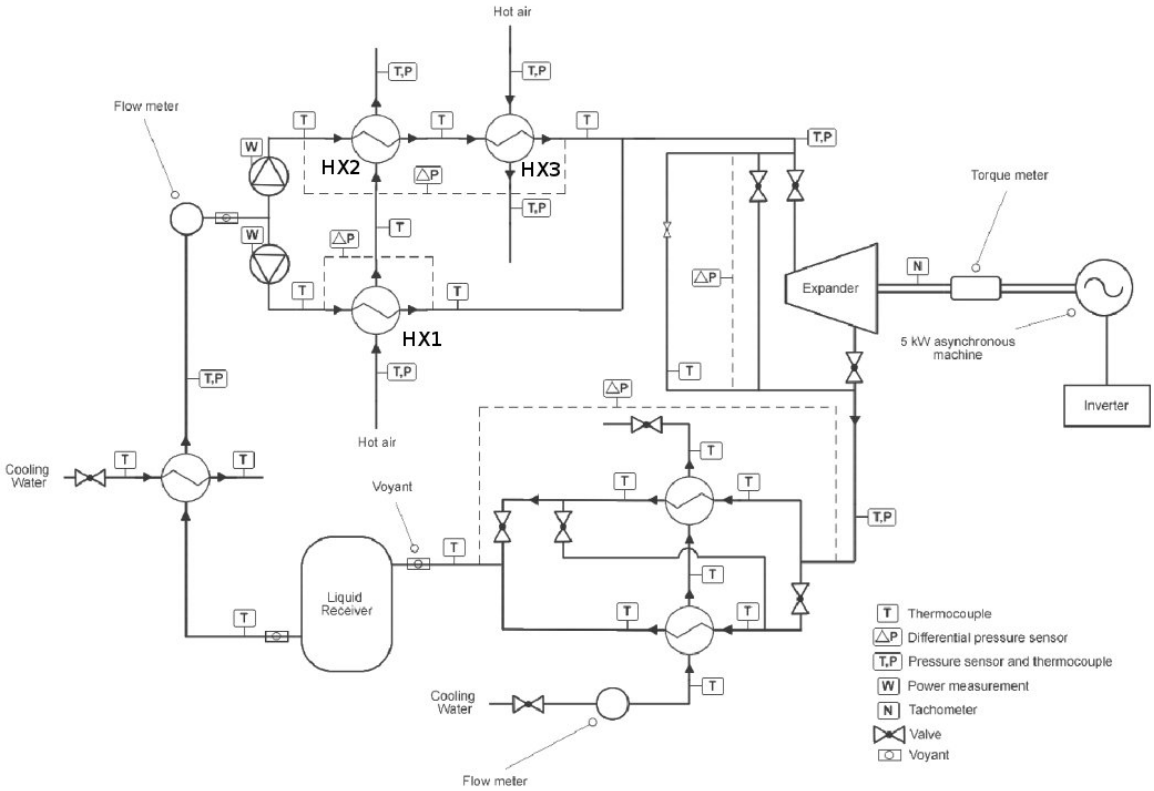

Figure 16: Schematic representation of the improved test bench

Figure 17: Liquid receiver

Evaporator. As previously stated, the second hot air source was poorly recovered by the first ORC setup. A second configuration (Figure 16) is tested in order to maximize the heat recovery on the two heat sources. This configuration is a mixed parallel/series configuration. To impose the working fluid flow rate in both parallel refrigerant lines, a second identical pump is installed next to the first one. This ensures that the fluid enthalpy is more or less equal when both streams are joined to avoid exergy losses.

Expander. The major issue linked to the original open-drive scroll compressor is the air tightness. Leakages have been reduced by installing an

additional seal and by increasing the pressure between both scrolls but the experimental results showed that some leakage remains (cfr. section 2.3). To fix this, the expander is installed in a semi-hermetic container (with only the expander shaft going out), as shown in Figure 18. The expander discharges the vapor in the container, connected to the exhaust pipe at its lowest part in order to avoid accumulation of condensate. The tightness at the shaft level is ensured by a rubber seal.

With such a casing, the necessity to add peripheral seals and increase the pressure between the scrolls disappears. This should reduce the friction losses and increase the expander effectiveness.

A second modification on the expander is linked to the change of working fluid: HFC-245fa in vapor phase is about 1.5 times denser than HCFC-123 at an evaporating temperature of 100°C. Therefore, the swept volume of the expander must be reduced. The expander selected has a compressor swept volume of 122 cm^3 (instead of the former 148 cm^3), with the same internal volume ratio of 4.

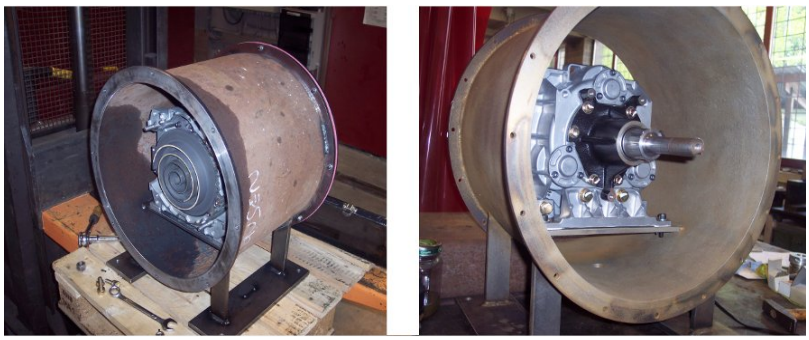

Figure 18: Scroll expander casing

Direct shaft connection. To avoid the uncertainty of the belt transmission efficiency when measuring shaft power, the torque meter is installed directly on the expander-generator shaft (Figure 19).

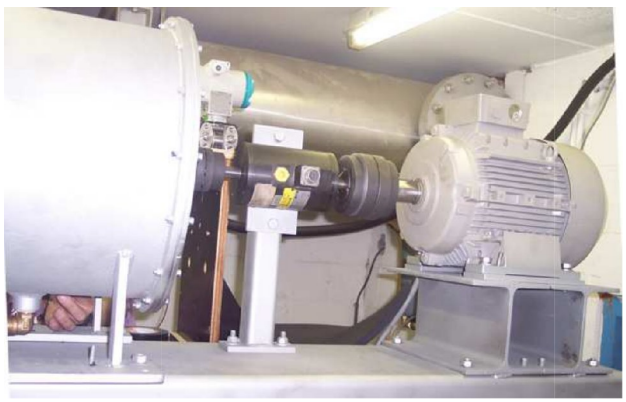

Figure 19: Expander (left), Torque meter (middle) and asynchronous generator (right)

Inverter. On the previous test rig, the expander speed was adjusted by varying the diameter of the transmission pulleys between the expander and

the asynchronous generator. Because of the direct shaft connection, the generator speed must vary on the new test rig: a four-quadrant inverter (i.e. an inverter that can work either in motor or in generator mode) is thus installed between the asynchronous generator and the grid. The inverter model is ABB ACS800.

Measurements. Two additional sensors are installed: the pressure drop over the condenser and the evaporator are measured using Sensotec differential pressure sensors. Moreover, a wattmeter is added to measure the pump consumption.

3.2 Test results

After the same cross-checking of the experimental results as in section 2.2 , 30 steady-state working points are measured by varying the available degrees of freedom of the test rig. Measured performance in terms of expander

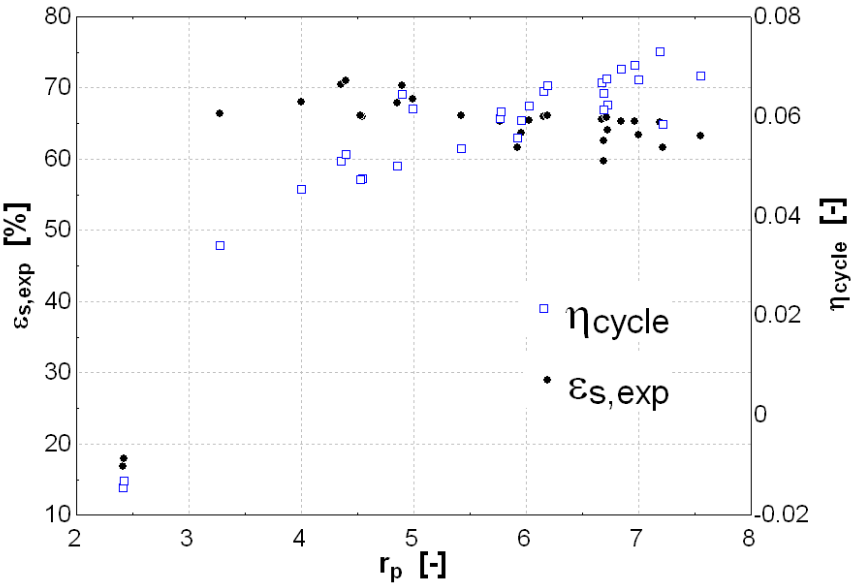

Figure 20: Expander isentropic effectiveness and cycle efficiency as a function of the pressure ratio

effectiveness and cycle efficiency is provided in Figure 20. Maximum measured cycle efficiency is 7.3%, and the maximum isentropic effectiveness is 71.1 %. These values are slightly higher than the values obtained with the first version of the test rig. Moreover, the cycle performance has been tested with much higher pressure ratios: it can be seen that for low (below 3) or high (higher than 5) pressure ratios, the effectiveness decreases. This trend is mainly explained by the under and over-expansion losses.

Figure 21 shows the T-s diagram of the improved cycle. The following improvements can be stated:

- The pressure drops have been decreased dramatically in the condenser, which is explained by a higher working fluid density and a lower partial pressure of non-condensable gas.

- The apparent subcooling is lower, but still too high, which indicates that a non condensable gas is present in the cycle and therefore that the seal on the expander shaft is not fully tight.
- The recovered amount of heat on the second air source has been increased.

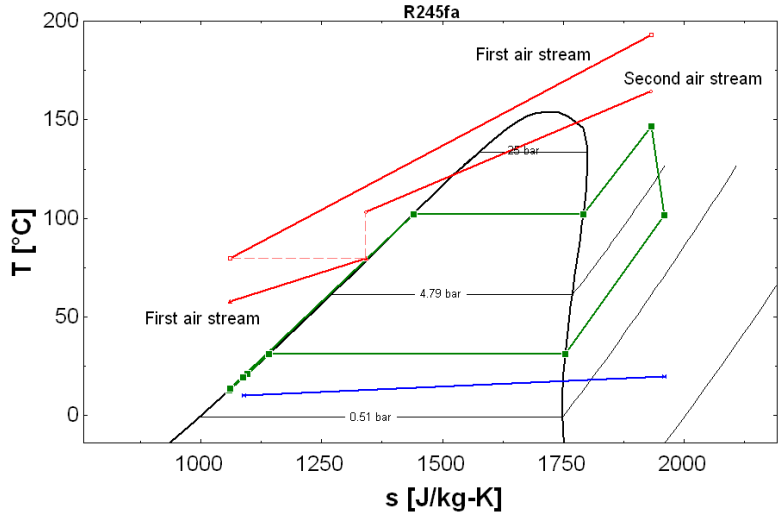

Figure 21: T-s diagram of the measured thermodynamic states with superposed heat source/sink temperature profiles

For theses tests as well as for the previous ones, the cycle efficiency was limited among others by a very low pump effectiveness. Due to high constant electromechanical losses, this effectiveness increases with the isentropic pumping power, but remains limited below 15% (Figure 22).

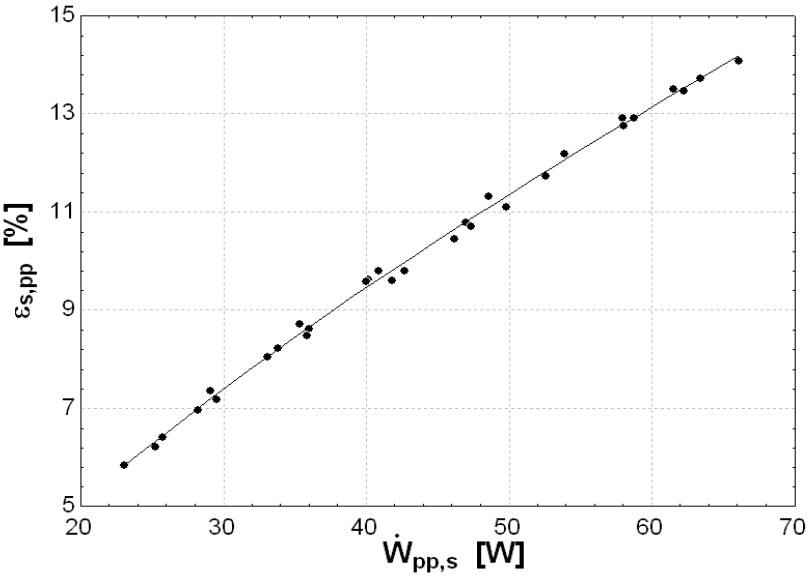

Figure 22: Measured Pump isentropic effectiveness as a function of the isentropic pumping power

Measuring the level in the liquid receiver is also of interest since it allows evaluating the relationship between refrigerant charge and superheating. Figure 23 shows the superheatings at the evaporator exhaust and at the condenser supply as a function of the liquid level in the tank (measured with the pump level as reference level). A clear dependency exists between the measured values: when the liquid level is low in the tank, the size of the vapor zone in the heat exchangers is reduced and the amount of superheating is reduced.

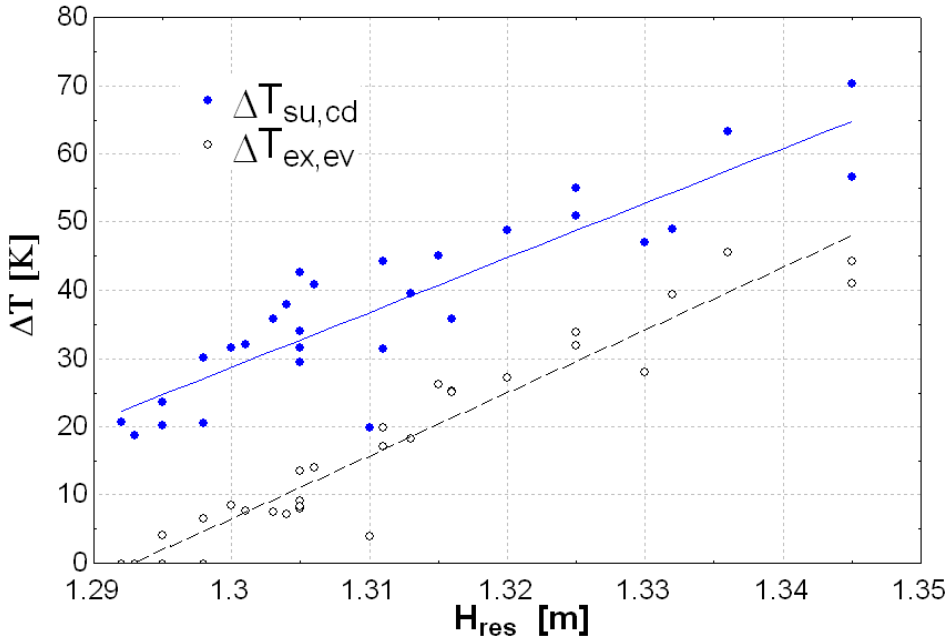

Figure 23: Superheating at the condenser inlet and at the evaporator outlet as a function of the liquid level in the tank

The variation ranges for the main working conditions are summarized in Table 7. The main conclusion of the comparison between former and new test results are:

- Although smaller, the expander delivered a higher shaft power in the modified test rig. This is partly due to the higher density of HFC-245fa in vapor phase.
- The presence of non-condensable gas at the condenser level is stated on the new setup, but its partial pressure is generally smaller. This allowed lowering the condensing pressure 6K below the lowest one obtained on the former test rig.
- The net output power has been increased by 25% on the new test rig. This is explained by a higher cycle performance and by improved temperature profiles in the evaporator.
- The expander isentropic effectiveness has been slightly improved, most likely due to its installation in the container and to lower friction losses.

Variable	Description	Improved test rig	Former results
$\bar{T}_{hf1}$	First hot air source mean temperature	110 - 130°C	53.4 - 86.4 °C
$\bar{T}_{hf2}$	Second hot air source mean temperature	110 - 134°C	101 - 163.2 °C
$\dot{M}_a$	Air mass flow rate	71-126 g/s	71 - 90 g/s
r_p	Pressure ratio	2.42 - 7.44	2.7 - 5.4
$\dot{M}_f$	Mass flow rate	49 - 78 g/s	45 - 86 g/s
N_{rot}	Expander rotating speed	1855 - 3125 rpm	1771 - 2660 rpm
T_{ev}	Evaporating temperature	84.3 - 102.1 °C	83.9 - 116.2
T_{cd}	Condensing temperature	26.5 - 56.5 °C	33.6 - 50.2 °C
$\dot{Q}_{ev}$	Heat transfer at the evaporator	14 - 24 kW	11.6 - 22.35 kW
$\dot{W}_{\exp}$	Shaft power	180.5 - 2164 W	382 - 1820 W
$\dot{W}_{net}$	Net power	-224 - 1709 W	-0.9 - 1421 W
$\varepsilon_{s,\exp}$	Expander effectiveness	16.9 - 71.1 %	42 - 68 %
η_{cycle}	Cycle efficiency	-1.4 - 7.3 %	0 - 6.6 %
η_{II}	Second-law cycle efficiency	-4.1 - 20.2%	0 - 16.5 %
$p_{part,air,cd}$	Partial pressure of non-condensable gases	0.53 - 0.69 bar	0.5 - 1.48 bar

Table 7: Operating parameters and reached performance on the two experimental setups

4 Expander test rig

4.1 Description of the test rig

A “vapor cycle” test rig was built to test the performance of the expander with fluid HFC-245fa. This rig (simpler, less bulky and cheaper to build than the entire Rankine cycle system) is mainly made up of a scroll compressor, a scroll expander, a water-cooled heat exchanger and a by-pass valve. A simplified representation of the cycle described by the working fluid is given in Figure 24: the fluid, in vapor phase, is successively compressed (1-2), expanded (2-3) and cooled-down (3-1). A heat exchanger could have been integrated at the outlet of the compressor to adjust the expander inlet temperature.

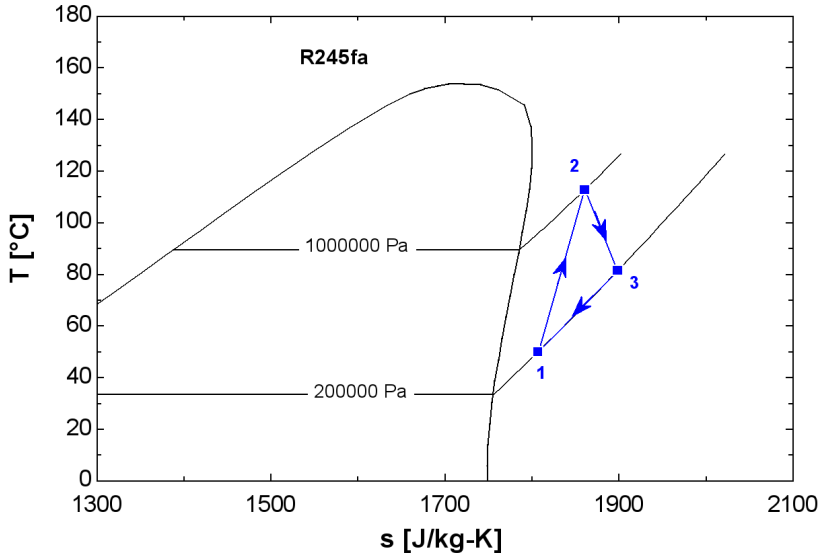

Figure 24: T-s diagram of the proposed gas cycle (assumed adiabatic)

The expander is originally a hermetic compressor designed for heat pump applications and characterized by a maximal electrical consumption of 5.5 kWe. The displacement of the machine in compressor mode is 11.72 m3/h approximately and the built-in volume ratio is close to 3.0 (Table 8).

Brand	Copeland
Type	Scroll
Identification	ZH30K4E-TFD
Swept volume	11.7 m³/h
Max discharge pressure	32 bar
Oil quantity	1.89 l
Max current	8.2 A

Table 8: Scroll compressor/expander characteristics

The details of the conversion of such a scroll machine into an expander are provided in Appendix B.

A detailed representation of the rig is provided in Figure 25. The expander supply and exhaust pressures were regulated by controlling simultaneously the by-pass valve opening and the charge of fluid in the system. Refrigerant could be added or withdrawn by condensation or vaporization inside a tank connected to the main refrigerant circuit and equipped with both a cooling coil and an electrical resistance.

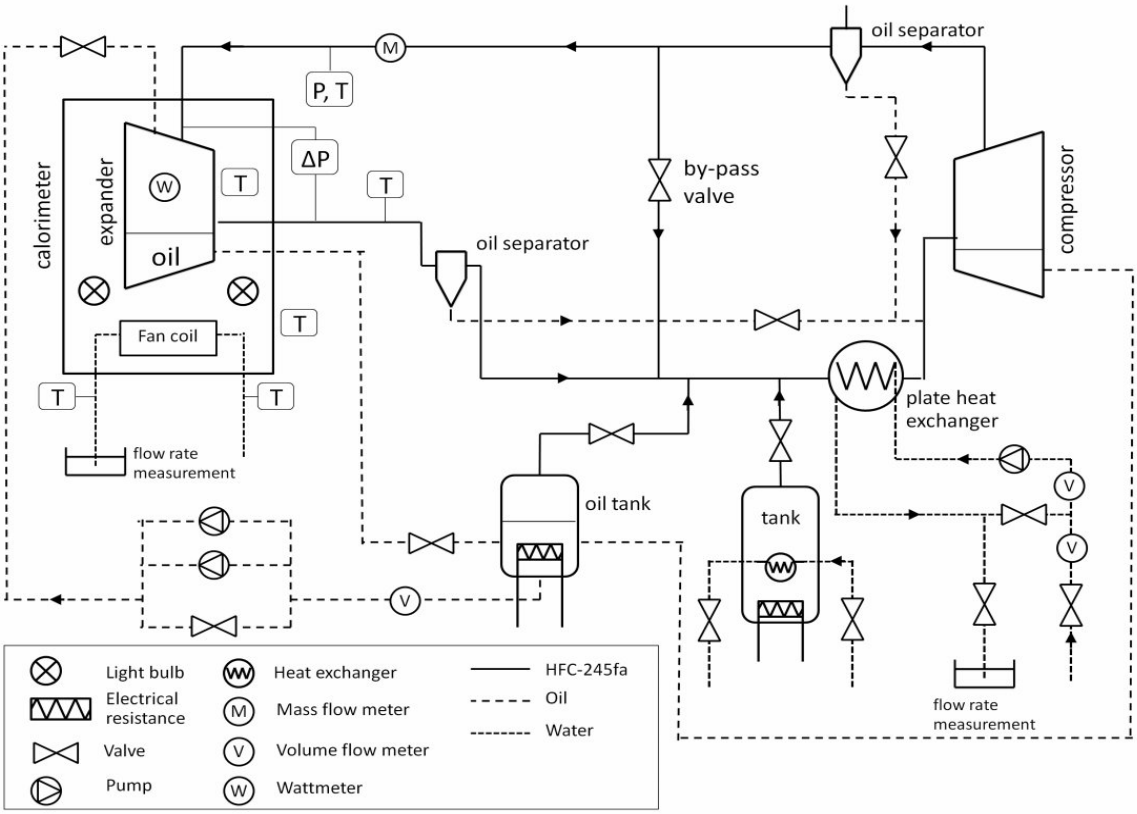

Figure 25: Schematic representation of the test bench

The test rig was designed to have a good control and measurement of the oil mass flow rate at the expander supply. This was achieved by separating the oil from the refrigerant at the compressor exhaust and by sending it back to the expander supply through an external oil circuit. Main components of this circuit are an oil flow meter, 2 gear pumps in parallel arrangement, an oil tank with an electrical heater (used for separating the gas entrained by the oil coming from the compressor oil sump) and a needle valve (used to regulate the oil flow rate supplied to the expander).

The expander was installed inside a calorimeter to determine the heat transfer to the ambient. A constant air temperature is maintained inside the calorimeter by simultaneously controlling the fan coil water flow rate and the power supply of two light bulbs.

The heat balance over the calorimeter box is given by:

$$-\dot{Q}_{cal,amb}+\dot{W}_{fan}+\dot{W}_{bulb}-\dot{H}_{coil}+\dot{Q}_{\exp,amb}=0 \quad (12)$$

With

$\dot{Q}_{cal,amb}$ heat transfer between the calorimeter box and the outside environment, W

$\dot{W}_{fan}$ fan power, W

$\dot{W}_{bulb}$ light bulb power, W

$\dot{H}_{coil}$ enthalpy flow rate of the cooling water, W

$\dot{Q}_{\exp,amb}$	heat transfer between the expander and the environment inside the calorimeter box , W

Calibration of the calorimeter box consisted in developing a given heating power inside the box and measuring the temperature difference between the inside and outside environments. The calibration of the calorimeter box allowed for the determination of the heat transfer coefficient between the box and the outside environment. The identified value was 3.2 W/K. This value will be further used during the tests to estimate the ambient heat losses.

4.2 Measurement devices

Temperatures were measured by T-type thermocouples. The reference temperature was given by a mixture of ice and water. Pocket-mounted thermocouples were used to measure the gas temperatures and contact thermocouples to measure the surface temperatures.

The expander supply pressure was measured by means of an absolute pressure transducer. The expander exhaust pressure was determined by measuring the pressure difference over the expander with a differential pressure transducer. A Coriolis mass flow meter was used to measure the mass flow rate through the expander. Measuring ranges and accuracy of the different sensors are provided in Table 9.

	Temperature			**Pressures**		**Flow rates**		**Power**
Measured variable	$T_{r,su,exp}$	$T_{r,ex,exp}$	$T_{surf,exp}$	$P_{r,su,exp}$	$\Delta P_{r,exp}$	$\dot{M}$	$\dot{V}_{oil}$	$\dot{W}_{\exp}$
Range	-200 - +300°C	-200 - +300°C	-200 - +300°C	0-25 bar	0-20 bar	0.25-13 kg/min	1.25 l/min	0-3 kW
Uncertainty	0.5 K	0.5 K	0.5 K	0.125 bar	0.1 bar	±1%	±0.05 l/min	15 W

Table 9: Measuring ranges and accuracy

4.3 Overall measured performance

In total, a series of 27 performance points were achieved. Several independent variables were available for the control of the system during the experimental campaign: the expander supply and exhaust pressures, the supply temperature and the quantity of circulating oil. Dependent variables resulted from the choice of the independent variables. These variables were the fluid mass flow rate, the electrical power produced by the expander and the exhaust temperature. Minimum and maximum values of all these variables are given in Table 10. To check the accuracy of the measurements, the following heat balance is performed in steady-state on the expander:

$$residue = \dot{M}_{meas} \cdot (h_{su} - h_{ex}) + \dot{M}_{oil} \cdot c_{oil} \cdot (T_{oil,su} - T_{ex}) - \dot{Q}_{\exp,amb} - \dot{W}_{el,meas} \quad (13)$$

For the 27 measurements points the residue is lower than 8.9% of the total enthalpy drop.

	Independent variables				Dependent variables			Performance	
	P_{su}	P_{ex}	T_{su}	x_{oil}	$\dot{M}$	$\dot{W}_{el}$	$T_{ex,meas}$	ε_s	ϕ
	[bar]	[bar]	[°C]	%	[g/s]	[W]	[°C]	[-]	[-]
Min	6.72	1.69	92	0.8	38.35	298	68.4	0.342	1.024
Max	16.06	3.19	139	3.2	121.2	2032	100	0.710	1.101

Table 10: Ranges of measured variables

The overall performance of the expander was evaluated in terms of overall isentropic effectiveness, defined as the ratio between the measured electrical power output and the isentropic expansion power (Eq. (4)). This isentropic effectiveness is an electrical effectiveness (i.e. the electrical output power divided by the isentropic expansion power). Comparison with the isentropic effectivenesses calculated in the previous sections should be conducted with care since these effectivenesses were related to the mechanical output power.

Volumetric performance of the machine was quantified through the filling factor, defined as the ratio of the measured mass flow rate and the mass flow rate theoretically displaced by the expander (Eq. (9)).

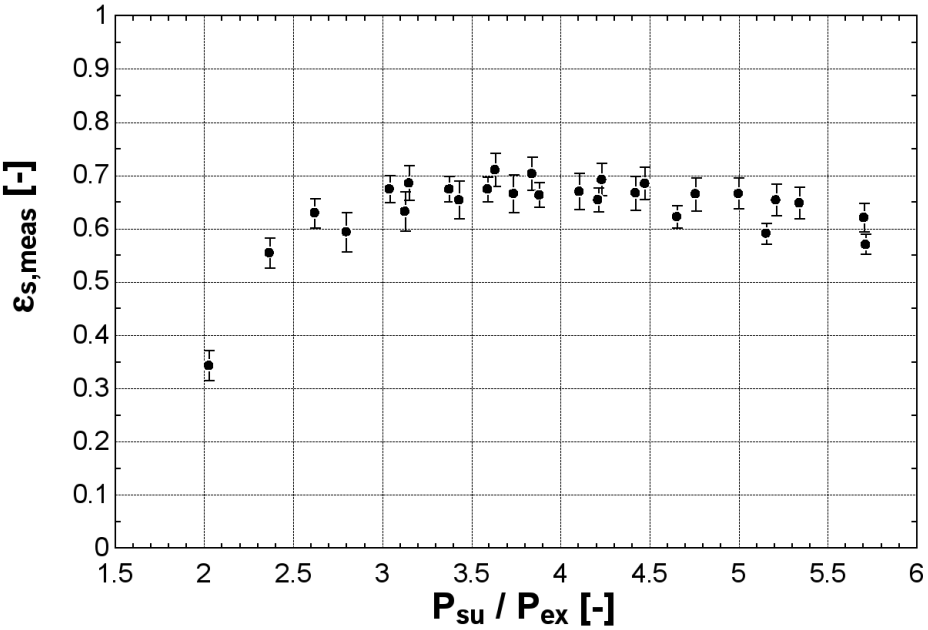

Figure 26: Measured isentropic effectiveness vs. pressure ratio

The evolution of the overall isentropic effectiveness with the pressure ratio is shown in Figure 26, for the whole tests. As already stated with the open-drive expander, this effectiveness sharply decreases for the small pressure ratios due to over-expansion losses and decreases for the larger pressure ratios due to under-expansion losses. In the current tests, a maximum isentropic effectiveness of 71.03% was achieved.

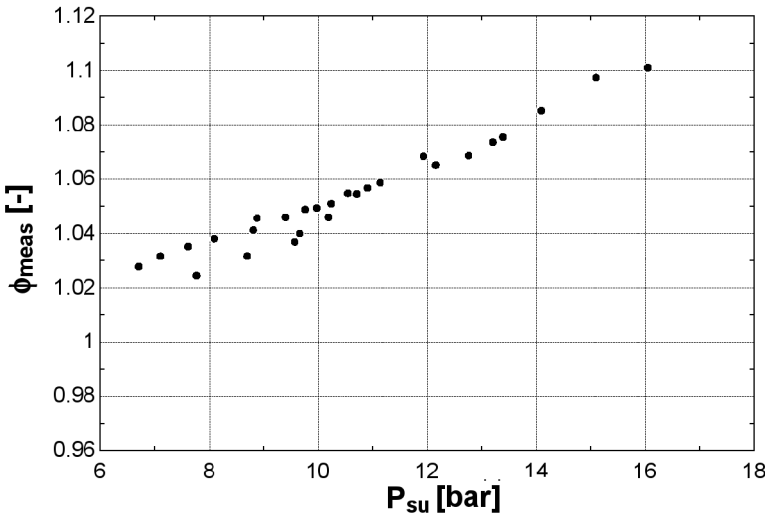

Figure 27: Measured filling factor vs. expander supply pressure

Error bars are associated with calculated uncertainties (Eq. (8)).

The evolution of the filling factor with the supply pressure is given in Figure 27, for a series of points characterized by an exhaust pressure ranging from 1.98 to 3.84 bar and a supply temperature ranging from 92 to 139°C. The slight increase of the filling factor with the pressure might be explained by the increase of internal leakages.

Figure 28 shows that the electrical power developed by the machine monotonically increases with the system pressure ratio. It shows that, although operated higher than its internal pressure ratio (around 3), the discharge process still produces useful work for the expander. Scattering is due to the variation of the other operating conditions, such as the supply pressure and temperature.

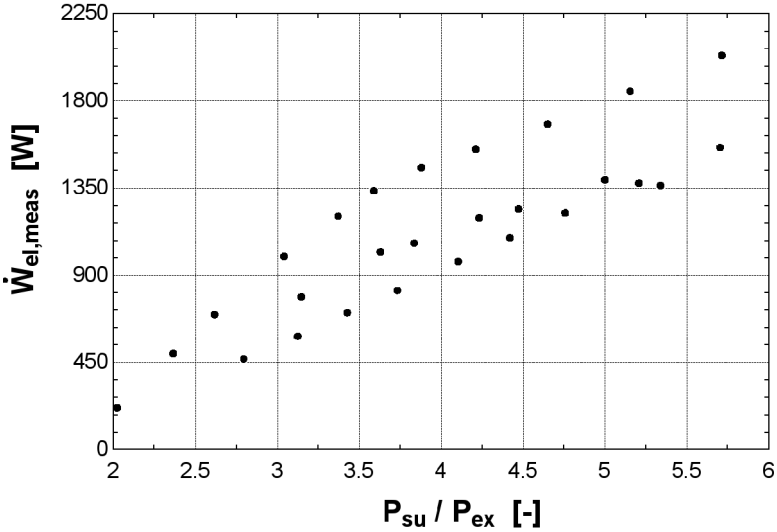

Figure 28: Electrical output power vs. pressure ratio

4.4 Impact of oil mass fraction on performance

In the tests presented previously, the oil mass fraction was maintained between 0.7 and 2.3 %. Additional tests were carried with larger oil mass fractions to investigate the impact of the oil quantity on the expander performance. Figure 29 shows the evolution of the expander overall isentropic

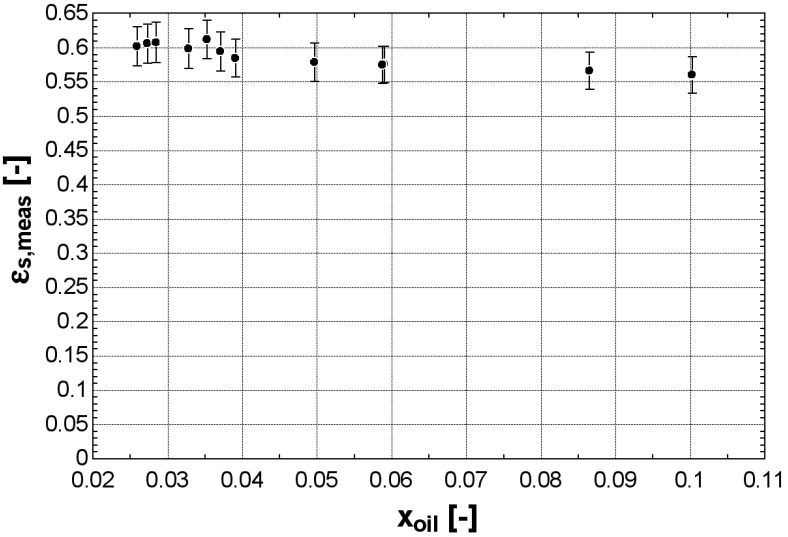

Figure 29: Isentropic effectiveness vs. oil mass fraction

effectiveness with the oil mass fraction (for a pressure ratio of 4.218±0.065 and a supply temperature of 92.0±1.5°C). It can be observed that the isentropic effectiveness decreases with the oil quantity. Further investigation is needed to identify with certainty the underlying reason (among suspects, the increase of the supply pressure drops or viscous losses).

As shown in Figure 30, the filling factor correlates fairly well with the supply pressure and the oil mass fraction. As mentioned previously, the increase of

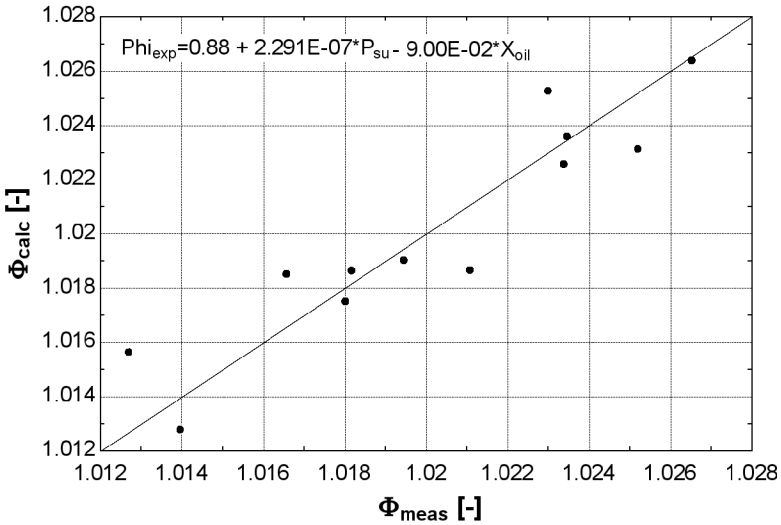

Figure 30: Predicted vs. measured filling factor as a function of the supply pressure and oil fraction

the filling factor with the supply pressure is due to the increasing impact of the leakages. On the contrary, the decrease of this factor with the oil mass fraction can be due to either the better ability of oil to seal the leakage paths or the larger supply pressure drops. It should however be noted that the range of variation of the filling factor is quite limited, making it impossible to draw any accurate conclusion. The polynomial law should therefore be taken as a general trend, not a firm rule.

5 Conclusions

Experimental data is a prerequisite to quantify the physical phenomena occurring in an ORC system. In this chapter, different experimental setups have been presented.

The measurements on the ORC prototypes gave special insight of the studied system. Their accuracy and reliability were cross-checked using the different redundancies and heat balances available on the test bench.

The ORC prototype highlighted the main sources of irreversibility in the cycle, such as pressure drops, subcooling or excessive superheating. It also pointed out the effect of non-condensable gases in the cycle, which is to impose an "artificial" subcooling at the pump inlet, and to prevent the condensing temperature to decrease. The effect of the refrigerant charge was also evaluated and correlates fairly well with the superheating at evaporator exhaust and condenser supply. The low effectiveness of the diaphragm pump was also pointed out.

The final performance of the prototype was 7.3% efficiency, with a net output power of 1709 W.

The experimental investigations allowed better characterizing the performance of two prototypes of scroll expander: a lubricated hermetic expander derived from an existing heat pump compressor, and an oil-free open-drive scroll expander derived from an air compressor.

The tested prototypes achieved an excellent performance, generally higher than the one reported in the scientific literature: a maximum electrical isentropic effectiveness of 71.03% was reached on the hermetic expander, compared to a maximum of 68% in previous scientific works.

The maximum mechanical isentropic effectiveness of the open-drive expander was 71.1%.

It can therefore be concluded that the performance of the oil-free scroll expander is lower than that of the hermetic scroll expander since its effectiveness does not take into account the electromechanical losses of the generator. This lower performance is mainly due to higher internal leakage due to the absence of oil between the scrolls.

Additional tests with larger oil mass fractions indicated that the isentropic effectiveness of the hermetic machine decreases with the quantity of oil. Further investigation must indicate with certainty the underlying reason.

Chapter 4:

Modeling

Essentially, all models are wrong,
But some are useful
George E. P. Box

Summary. This chapter presents two different types of models. These models, although applied to same ORC components, are very different in terms of modeling platform and paradigms. The first group of models is defined for steady-state conditions. These models are suitable for sizing problems, system performance evaluation, or cycle optimization problems. The second group of models is defined for transient conditions. This type of model is suitable for dynamic control issues, or to estimate the cycle performance under transient heat source conditions.

---

1 Introduction

Although many studies showed the influence of the working fluid thermodynamic properties on the ORC performances, only a few papers present detailed simulation models of the ORC, accounting for the characteristics of each component of the cycle: (E. H. Kane, 2002) proposed a semi-empirical model of a small scale ORC with 3-zones heat exchangers, and a scroll expander model accounting for friction losses, intake throttling and internal leakage. This model was used to conduct a thermoeconomic optimization on the system. (McMahan, 2006) proposed a detailed model and an optimization of the ORC cycle for solar applications. (Wei et al., 2008) proposed a dynamic model of a 100 KWe ORC, focusing mainly on the heat exchangers and using empirical laws for the pump and for the expander. (Jing, Gang, & Jie, 2010a) developed a model of an ORC cycle using HCFC-123 as working fluid and coupled to CPC collectors: the predicted overall efficiency was about 7.9% for a solar insolation of 800 W/m^2 and an evaporating temperature of 147°C. They also focused on the ambient heat losses of scroll expanders, and obtained, through simulations and measurements, an ambient heat transfer coefficient of about 15 W/m^2K (Jing et al., 2011).

Most of the above mentioned studies show that the ORC efficiency is significantly improved by inclusion of a recuperator, of cascaded cycles, or of reheating.

However, these models were never fully validated with a detailed set of experimental data. In this work the semi-empirical approach proposed by E. H.

Kane, (2002) is selected, but the model parameters are calibrated with the experimental data, and the final model is validated with the measurements.

The first part of this chapter presents steady-state thermodynamic models the ORC system presented in chapter 3.2. This global cycle model is built by interconnecting the sub-models of the different components: the heat exchangers, the pump and the expander. Each model is validated experimentally. Finally, these validated models are used to investigate, through simulations, the performance of the system and to point out some achievable improvements.

The second part of the chapter presents a dynamic model of the ORC. This kind of model is necessary when transient phenomena such as start or shutting down, dynamic control or variable heat sources are studied. The proposed dynamic model focuses on the heat exchangers, the dynamics of the other components being of minor importance because of lower time constants.

2 Steady-state modeling

This section describes the steady-state models of the different components under investigation. The modeling approach consists in developing semi-empirical models, instead of deterministic models. Semi-empirical models involve a limited number of physically meaningful parameters that can easily be identified from performance measurements, while deterministic models require an exact knowledge of the geometry of all the components. Semi-empirical models are usually numerically more robust than deterministic models and allow a sharp decrease of the computational expenses. They are therefore more appropriate to be interconnected for the simulation model of a larger system.

All the models proposed in this section are developed in the EES environment (Klein, 2011).

2.1 Models

Open-drive scroll expander

In this model, initially proposed by (V. Lemort et al., 2009), the evolution of the refrigerant through the expander is decomposed into the following thermodynamic processes (as shown in Figure 31):

1. Supply pressure drop (su→ su,1)
2. Supply cooling-down (su,1 → su,2)
3. Isentropic expansion to the internal pressure imposed by the built-in volume ratio of the expander (su,2 → in)
4. Expansion at a fixed volume to the exhaust pressure (in → ex,2)
5. Mixing between suction flow and leakage flow (ex,2 → ex,1)
6. Exhaust cooling-down or heating-up (ex,1 → ex)

As shown in Eq. 14, the internal mass flow rate $\dot{M}_{in}$ is the difference between the mass flow rate $\dot{M}$ entering the expander and the leakage mass flow rate $\dot{M}_{leak}$. The internal mass flow rate is the volume flow rate $\dot{V}_{s,\exp}$ divided by the specific volume of the fluid $v_{su,2}$ after entering cooling down and pressure drop. The volume flow rate is defined as the product of the swept volume $V_{s,\exp}$ and the expander rotational speed $N_{\exp}$. The swept volume in expander mode is equal to that in compression mode divided by the built-in volume ratio of the machine $r_{v,\text{in}}$.

$$\dot{M}_{in} = \dot{M} - \dot{M}_{leak} = \frac{V_{s,\exp}}{v_{r,su,2}} = \frac{N_{\exp} \cdot V_{s,cp}}{60 \cdot v_{r,su,2}} = \frac{N_{\exp} \cdot V_{s,\exp}}{60 \cdot v_{r,su,2} \cdot r_{v,\text{in}}} \tag{14}$$

The leakage mass flow rate can be computed by reference to the flow through a simply convergent nozzle. The fictitious leakage area A_{leak} is assimilated to the nozzle throat area and must be experimentally identified.

In the same manner as for the leakage mass flow rate, the pressure drop is computed as the flow through a simply convergent nozzle, whose throat diameter is the equivalent supply port diameter d_{su}.

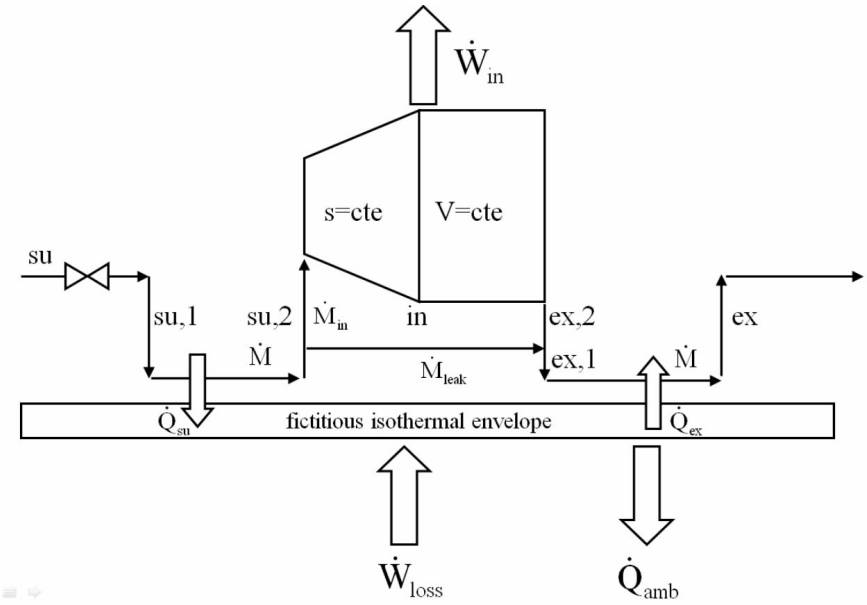

Figure 31: Conceptual scheme of the expander model

The internal expansion power $\dot{W}_{in}$ is obtained by multiplying the internal work w_{in} by the internal mass flow rate. This internal work is the sum of the internal work $w_{in,s}$ associated to the isentropic part of the expansion and the internal work $w_{in,v}$ associated to the constant-volume evolution. In Eq 15, h_{in}, v_{in} and p_{in} are respectively the specific enthalpy, the specific volume and the pressure of the fluid at the end of the isentropic part of the expansion. The specific volume v_{in} is the product of the built-in volume ratio $r_{v,\text{in}}$ with the specific volume $v_{su,2}$.

$$\begin{aligned}\dot{W}_{in} &= \dot{M}_{in}\cdot w_{in} = \dot{M}_{in}\cdot(w_{in,s}+w_{in,v}) \\ &= \dot{M}_{in}\cdot((h_{su,2}-h_{in})+v_{in}\cdot(p_{in}-p_{ex})) \\ &= \dot{M}_{in}\cdot((h_{su,2}-h_{in})+r_{v,\text{in}}\cdot v_{su,2}\cdot(p_{in}-p_{ex}))\end{aligned} \quad (15)$$

The expander mechanical power can be split into the internal expansion power and the mechanical losses $\dot{W}_{loss}$. These losses can be expressed as a function of a mechanical losses torque T_m and the rotational speed of the expander. The expander mechanical power is given by

$$\dot{W}_{sh} = \dot{W}_{in} - \dot{W}_{loss} = \dot{W}_{in} - 2\cdot\pi\cdot N_{\text{exp}}\cdot T_m \quad (16)$$

A fictitious envelope of uniform temperature T_w is assumed to be sufficient to represent the three heat transfer modes. T_w is determined by establishing a steady state energy balance on this envelope, as proposed by (Winandy et al., 2002):

$$\dot{W}_{loss} - \dot{Q}_{ex} + \dot{Q}_{su} - \dot{Q}_{amb} = 0 \quad (17)$$

Supply and exhaust heat transfers are described by introducing fictitious semi-isothermal heat exchangers characterized by global heat transfer conductances AU_{su} and AU_{ex}. The latter can be correlated to the refrigerant mass flow rate according to the following law (suitable for turbulent regime):

$$AU = AU_n\left(\frac{\dot{M}}{\dot{M}_n}\right)^{0.8} \quad (18)$$

The variables involved in the ORC model are of three types: input variables, output variables and parameters. They are summarized in Figure 32. It should

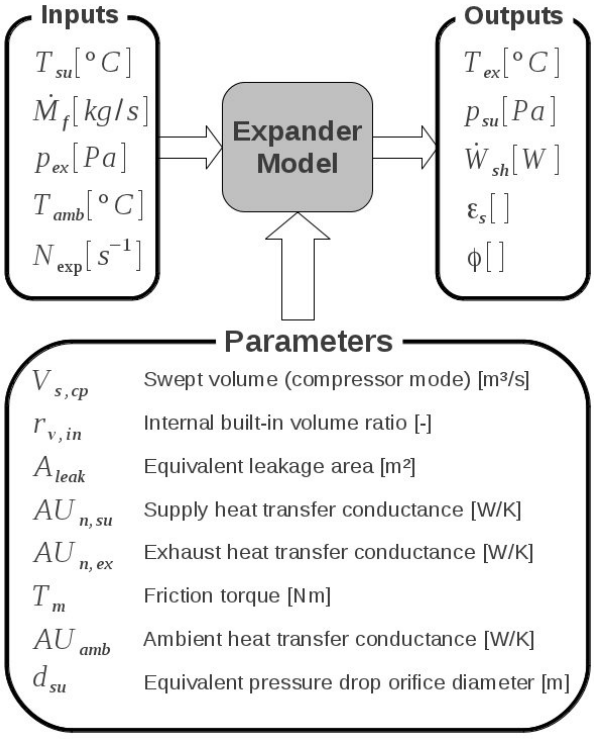

Figure 32: Expander model

be noted that the selection between input and output can be dependent on the target application. For example in Figure 32, the mass flow rate $\dot{M}_f$ and the rotational speed $N_{\exp}$ are imposed to the expander, which imposes the supply pressure p_{su} in return. If the supply pressure and the rotational speed were imposed, the mass flow rate would be recalculated by the expander model.

Model validation

As detailed above, the proposed model is a semi-empirical model, i.e. its parameters must be tuned to fit the measurements. To this end, the measurements on the ORC test bench regarding the open-drive scroll expander working with refrigerant HCFC-123 are used.

The model parameters are tuned to best fit the three model outputs (supply pressure, exhaust temperature, shaft power) to experimental data. The input variables of this calculation are: the expander rotational speed, the refrigerant mass flow rate, the supply temperature and the exhaust pressure. Model parameters can be of two types:

- Some parameters are given by the constructor or can be directly measured in the device. This is the case for $V_{s,cp}$ or $r_{v,in}$. The ambient heat transfer conductance and the friction torque could also be directly measured, but this was not the case with the present test rig.
- Other parameters are not given and cannot be calculated, such as the internal heat transfer conductances or the leakage areas. Those parameters have to be identified from the measurements.

This second type of parameters is identified by minimizing an error-objective function F (using a genetic algorithm) defined as a weighted sum of the errors for each output:

$$F=\sum_{1}^{39}\left[F_1\cdot\left(T_{f,ex,\exp,meas}-T_{f,ex,\exp_{pred}}\right)_i^2+F_2\cdot\left(\frac{p_{f,su,\exp,meas}-p_{f,su,\exp,pred}}{p_{f,su,\exp,meas}}\right)_i^2+F_3\cdot\left(\frac{\dot{W}_{sh,meas}-\dot{W}_{sh,pred}}{\dot{W}_{sh,meas}}\right)_i^2\right] \quad (19)$$

The weighting factors F_1, F_2, and F_3 are selected to give each term the same approximate weight: $F_1=1/\sqrt{(60)}$; $F_2=1$; $F_3=1/\sqrt{(2)}$.

Comparisons between the model predictions and the measurements for the exhaust temperature and the output power are given in Figure 33, Figure 34 and Figure 35. The maximum deviations between the measurements and the predictions of the model are 3 K for the temperature, 6% for the shaft power and 2% for the supply pressure.

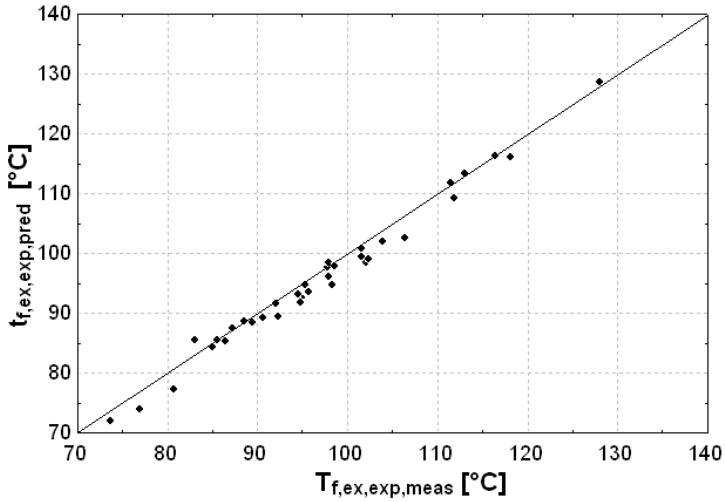

Figure 33: Predicted vs. measured exhaust temperature

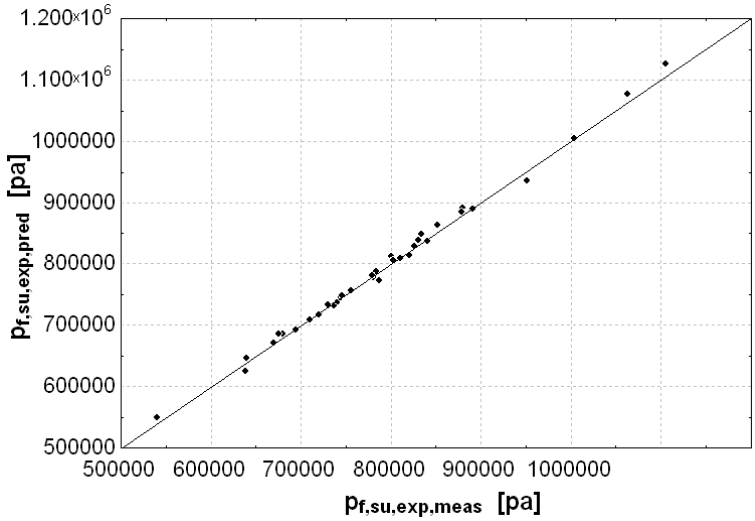

Figure 34: Predicted vs. measured supply pressure

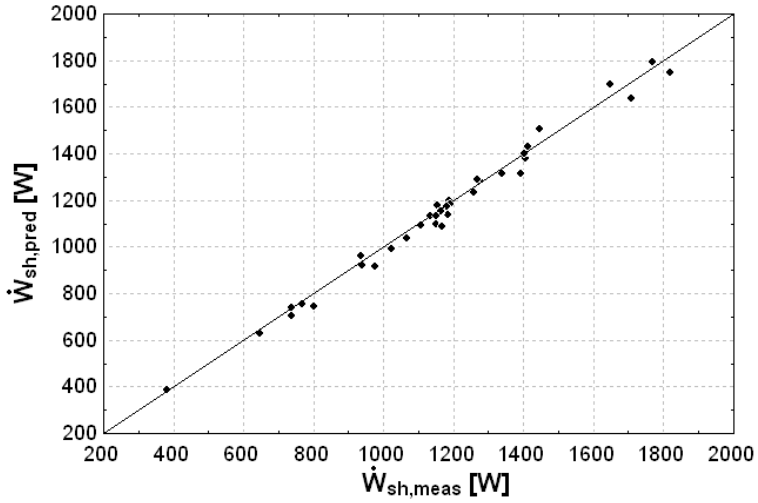

Figure 35: Predicted vs. measured shaft power

The final model parameters are summarized in Table 11.

Parameter	Value	Parameter	Value
AU_{amb}	6.38 W/K	T_m	0.4067 N.m
AU_{su}	21.22 W/K	A_{leak}	4.858 mm²
AU_{ex}	34.2 W/K	r_v	4.05
d_{su}	0.00591 m	$V_{s,cp}$	148 cm³

Table 11: Parameters of open-drive scroll expander model

Polynomial model

A semi-empirical thermodynamic model such as the one proposed in the previous section is well suited for the simulation of one particular machine. However, it cannot be used for bigger or smaller machines since the model parameters would need to be scaled according to a law that cannot be known without testing a large range of expanders with different swept volumes.

To obtain a generic non-dimensional efficiency curve, a polynomial fit of the effectiveness can be defined using carefully selected input variables. If ambient heat losses are neglected, scroll expanders can indeed be modeled by their isentropic effectiveness and filling factor as defined in Eq. (4) and (9).

To simulate realistic performance close to the actual experimental data, $\varepsilon_{s,\exp}$ and $\phi_{\exp}$ are expressed as a polynomial laws of the main working conditions. The three selected working conditions are the fluid inlet density ρ_{su}, the rotational speed N_{rot} and the pressure ratio over the expander r_p since they turned out to be the main representative variables of the working conditions. The polynomial fits are expressed in the following form:

$$\varepsilon = \sum_{[i,j,k]\in\Omega} a_{ijk} \cdot \ln(r_p)^i \cdot \rho_{su}^j \cdot N_{rot}^k = f(r_p, \rho_{su}, N_{rot}) \tag{20}$$

Where Ω is a set defined as a two-by-two combination of the working conditions[1].

The filling factor shows a very limited dependency with the pressure ratio. It can therefore be expressed as a function of the rotating speed and the supply density:

[1] Ω is defined by:

$$\Omega_n = \bigcup_{\alpha\in\{0,1,2\}} \{P \in \mathbb{R}^3 : P = c_1\sigma^\alpha(i) + c_2\sigma^\alpha(j), (c_1, c_2) \in [0, n[\times[0, n[\} \cup \{n\sigma^\alpha(i)\}$$

where $\sigma = (i, j, k)$ is a 3rd order circular permutation defined by:

$$i, j, k = \begin{pmatrix}1\\0\\0\end{pmatrix}, \begin{pmatrix}0\\1\\0\end{pmatrix}, \begin{pmatrix}0\\0\\1\end{pmatrix}$$

$$\phi = \sum_{j=0}^{n-1}\sum_{k=0}^{n-1} a_{jk}\cdot\rho_{su}^{j}\cdot N_{rot}^{k} + a_{0n0}\cdot\rho_{su}^{n} + a_{00n}\cdot N_{rot}^{n} = f(N_{rot},\rho_{su}) \quad (21)$$

It is assumed that, when changing the scale of the expander (and thus the swept volume), the isentropic effectiveness and the filling factor remain comparable if the working conditions are unchanged.

Since the number of parameters in this model is quite important, the 39 measured working points are not sufficient to accurately determine all of them. Therefore, the semi-empirical model developed and validated in the previous sections is used to predict the performance on a wide range of working conditions: 2641 different working points are calculated inside of the following operating conditions: $1000 < N_{rot} < 5000$; $20 < \rho_{su} < 40$; $1.2 < r_p < 20$

The parameters of Eq. 20 and 21 are then determined using these 2641 working points. For ε, a 4th-order (n=4) polynomial fit is used, while for ϕ a second-order (n=2) polynomial fit turned out to be sufficient. Their values were respectively predicted with R^2=99.92% and R^2=99.41%.

The values of parameters a_{ijk} are provided in Appendix C.

Hermetic scroll expander

The hermetic scroll expander model is very similar to that of the open-drive scroll expander. The main difference is related to the particular configuration of a hermetic expander: in such a machine the asynchronous generator in integrated into the expander shell. This involves two differences:

- The expander speed is almost constant since the generator is directly connected to a 50 Hz grid (i.e. 3000 rpm for a one pole-per-phase machine and 1500 rpm for a two poles-per-phase machine)

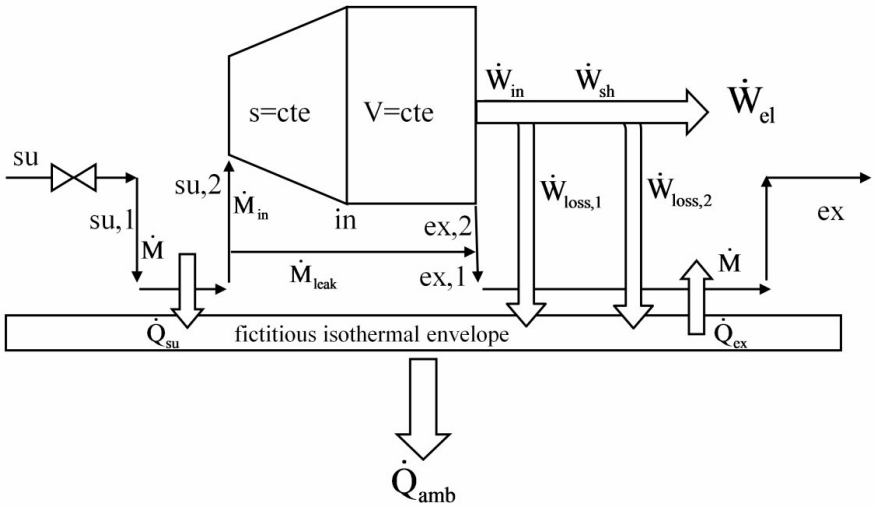

Figure 36: Conceptual scheme of the hermetic scroll expander model

- The additional electromechanical losses of the generator must be taken into account.

The rotational speed of the expander slightly increases with the power it produces, as a result of the slip (difference between synchronous and actual rotational speed) characteristic of the asynchronous machine. The following relationship has been derived from the performance given by the manufacturer:

$$N_{\text{exp}} = 3007 + 0.02155 \cdot \dot{W}_{el} + 2.091 \cdot 10^{-6} \cdot \dot{W}_{el}^2 \quad (22)$$

The modeling assumes that the distinction can be done between mechanical losses $\dot{W}_{loss,1}$ due to friction between moving elements (scrolls, journal bearings, Oldham coupling, thrust surface) and electromechanical losses $\dot{W}_{loss,2}$ in the generator. Equation (16) becomes:

$$\dot{W} = \dot{W}_{sh} - \dot{W}_{loss,2} = \dot{W}_{in} - \dot{W}_{loss,1} - \dot{W}_{loss,2} \quad (23)$$

Mechanical losses are computed on the basis of the mechanical efficiency of the compressor:

$$\dot{W}_{loss,1} = (1 - \eta_{mech}) \cdot \dot{W}_{in} \quad (24)$$

Electromechanical losses were evaluated on the basis of the performance of the asynchronous machine in motor mode given by its manufacturer and can be expressed as a function of the shaft rotational speed:

$$\dot{W}_{loss,2} = 199 - 0.455 \cdot (3002 - N_{\text{exp}}) + 0.037 \cdot (3002 - N_{\text{exp}})^2 \quad (25)$$

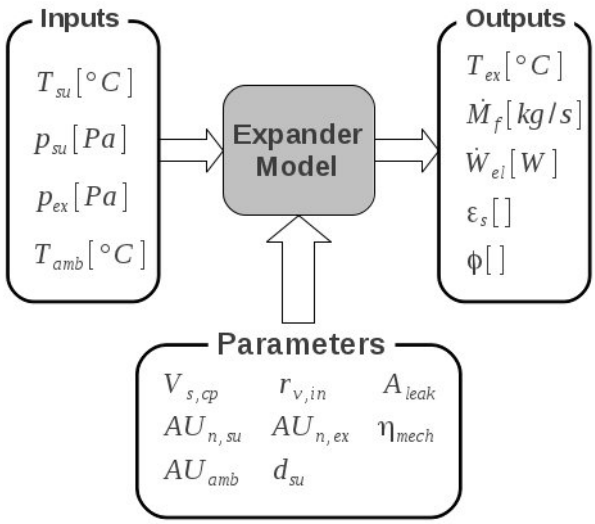

Figure 37: Hermetic scroll expander model

Figure 37 shows the parameters, inputs and outputs of the hermetic scroll expander model. This model computes the electrical output power instead of the shaft power for the open-drive model. The friction torque has been replaced by the mechanical efficiency η_{mech} and the rotational speed is removed from the inputs since it is recalculated by the model. The pressures are considered as inputs and the flow rate as an output since it corresponds

better to the test rig presented in the previous chapter: in this experimental setup, the pressures were imposed by adjusting the by-pass valve opening and the subsequent mass flow rate was measured.

Model validation

The input variables of the expander simulation model are the supply and exhaust pressures and the supply temperature. The output variables are the mass flow rate displaced by the expander, its electrical power production and the exhaust temperature. The model necessitates 8 parameters that are tuned To best match the values of the output variables with the measurements. Parameter values are evaluated following the same methodology as described in the previous section (Eq. 19). They are listed in Table 12.

Parameter	Value	Parameter	Value
AU_{amb}	3.4 W/K	η_{mech}	0.9
AU_{su}	30 W/K	A_{leak}	0.68-0.116(10-P_{su} [bar])
AU_{ex}	30 W/K	r_v	2.85
d_{su}	0.00618 m	$V_{s,cp}$	63.8 cm³

Table 12: Parameters of hermetic scroll expander model

The best agreement between measurement and model predictions was obtained by considering a leakage area varying linearly with the supply pressure. There may be several underlying reasons such as the compliance mechanism.

Predictions of the model are compared to experimental data for the displaced mass flow rate (Figure 38), the exhaust temperature (Figure 39) and the electrical power (Figure 40). For almost all the points, the maximal deviation between the prediction by the model and the measurements is 2% for the mass flow rate, 6% for the shaft power and 2K for the exhaust temperature. The discrepancies between predicted and measured values are most likely due to phenomena that were not taken into account. To take those effects into account, more intrusive measurements should be performed in the scroll pockets in order to accurately validate a model.

As shown in Figure 41, the model also roughly predicts the heat transfer to the ambient. Despite the insulation of the machine, the ratio between ambient losses and the electrical power produced by the machine ranges from 15% to 40%.

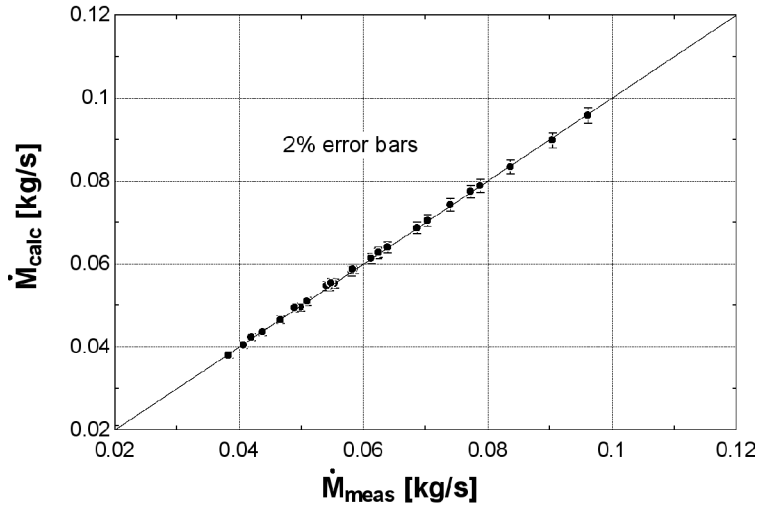

Figure 38: Calculated vs. measured mass flow rate

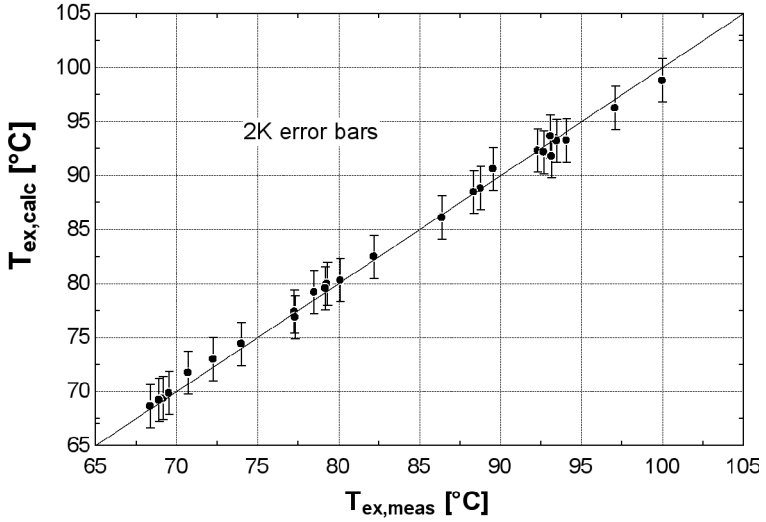

Figure 39: Calculated vs. measured exhaust temperature

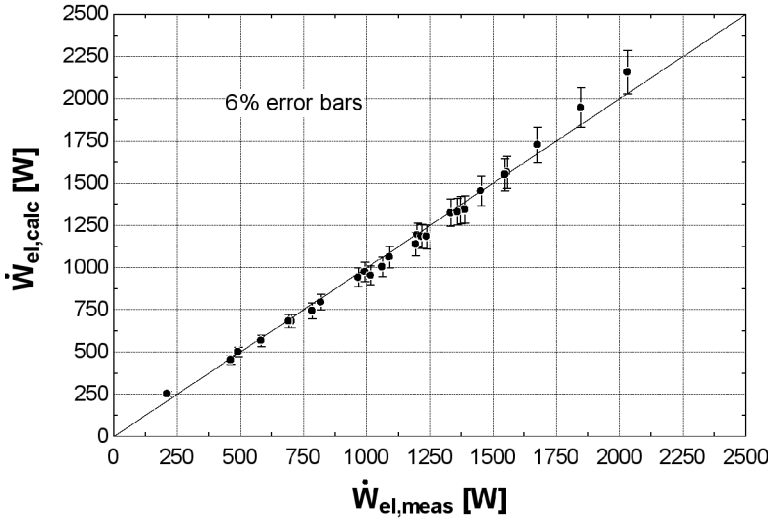

Figure 40: Calculated vs. measured electrical output power

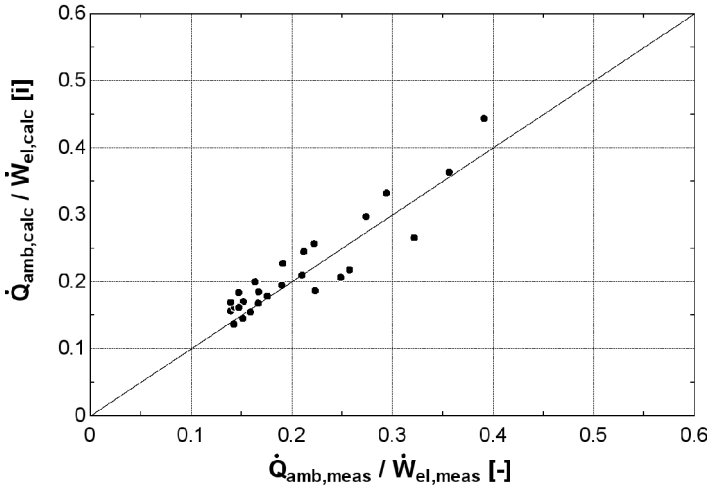

Figure 41: Calculated vs. measured relative ambient heat losses

Polynomial model

In the same manner as for the open-drive expander, a generic efficiency curve can be generated using the model described above. In the hermetic machine, the rotational speed is an output of the model and cannot be considered as an independent variable. Both the isentropic effectiveness and the filling factor can therefore be expressed by:

$$\varepsilon, \phi = \sum_{i=0}^{n-1} \sum_{j=0}^{n-1} a_{ij} \cdot \ln(r_p)^i \cdot \ln(p_{su})^j + a_{n0} \cdot \ln(r_p)^n + a_{0n} \cdot \ln(p_{su})^n = f(r_p, p_{su}) \qquad (26)$$

$\ln(p_{su})$ is here used instead of ρ_{su} because it yields a better accuracy.

The semi-empirical model developed and validated in the previous sections is used to predict the performance over a wide range of working conditions: 1100 different working points are calculated inside of the following operating conditions: $1.8 < p_{su}[bar] < 35.9$; $1.7 < r_p < 20$.

The parameters of Eq. (26) are then determined using these 1100 working points. For ε , a 5th-order (n=5) polynomial fit is used, while for ϕ a second-order (n=2) polynomial fit turned out to be sufficient. Their values were predicted with R^2=99.31% and R^2=99.62% respectively.

The values of parameters a_{ij} are provided in Appendix C.

2.2 Heat exchangers

The plate heat exchangers are modeled by means of the ε-NTU or LMTD methods for counter-flow heat exchangers. In the case of the evaporator and of the condenser, the heat exchanger is subdivided into 3 zones, each of them being characterized by a heat transfer area A and a heat transfer coefficient U. The modeling paradigm is presented in Figure 42 in the case of the evaporator. The practical implementation of such a model, with strategies to ensure the robustness of the solution process, is presented in Appendix D.

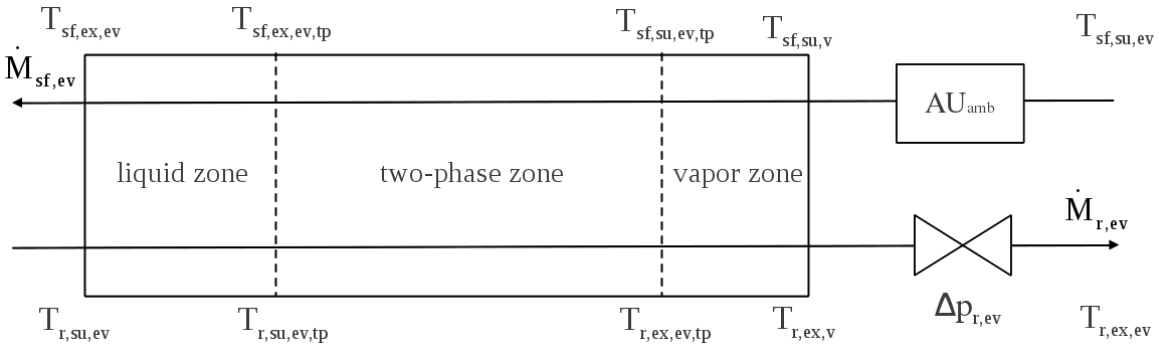

Figure 42: Three zones, moving boundaries heat exchanger evaporator model

Each heat transfer coefficient U is calculated by considering two convective heat transfer resistances in series (secondary fluid and refrigerant sides).

$$\frac{1}{U}=\frac{1}{h_f}+\frac{1}{h_{sf}} \tag{27}$$

The respective heat transfer area of each zone is obtained by imposing the total heat transfer area of the heat exchanger:

$$A_l+A_{tp}+A_v=(N_p-2)\cdot L\cdot W \tag{28}$$

where N_p is the number of plates, L is the plate length between inlet and outlet ports and W is the plate width between gaskets (Figure 43).

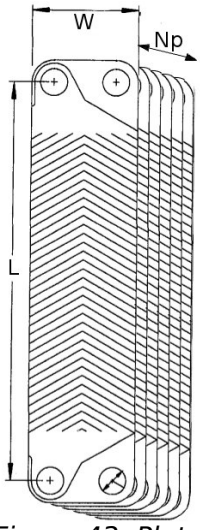

Figure 43: Plate heat exchanger

The heat exchangers considered in the studied applications show relatively low pressure drops (typically not more than 200 mbar). Therefore, to facilitate the convergence of the numerical iteration process, these pressures drops are summed and lumped into one single pressure drop on the vapor exhaust line.

$$\Delta p_{tot}=\Delta p_l+\Delta p_{tp}+\Delta p_v \tag{29}$$

The vapor line is selected because pressure drops in liquid state are relatively smaller in plate heat exchangers.

Single-phase

Forced convection heat transfer coefficients are evaluated by means of the non-dimensional relationship:

$$Nu = C \cdot Re^{n} \cdot Pr^{n} \tag{30}$$

where the influence of temperature-dependent viscosity is neglected.

The exponents m and n are set according to recommendations for corrugated plate heat exchangers. m depends mainly on the flow regime (laminar or turbulent) and ranges between 0.5 and 0.8. n is generally set to 1/3.

The coefficient C can be either identified from scientific literature on plate heat exchangers (e.g. (Muley & Manglik, 1999) (Thonon B., 1995)), or identified with experimental data, by minimizing the difference between predicted and measured values for a set of working points. Because of the large differences between Reynolds numbers, this coefficient is assigned different values for the vapor and liquid zones (refrigerant side) and for the secondary fluid.

Neglecting the port and acceleration pressure drops, the friction pressure drop is computed by:

$$\Delta p = \frac{2 \cdot f \cdot G^{2}}{D_h \cdot \rho} \cdot L \tag{31}$$

where f is the Fanning friction factor (either identified, or calculated with a correlation), G is the mass velocity, D_h is the hydraulic diameter ($=2 \cdot b$ for plates heat exchangers), ρ is density and L is the plate length.

Two-phase

Scientific literature covering two-phase flows in plate heat exchangers is still limited. While a few correlations have been established both for the condensation and evaporation processes, these correlations lead to very high discrepancies in the prediction of the heat transfer coefficient. (García-Cascales et al., 2007) compared 4 boiling heat transfer correlations 5 condensation heat transfer correlations and showed that the predicted coefficients can vary in a ratio as high as 1 to 7.

The Boiling heat transfer Coefficient is estimated with an expression inspired by the Hsieh correlation (Hsieh & Lin, 2002), established for the boiling of refrigerant R410a in a vertical plate heat exchanger. This heat exchange coefficient is assumed to be constant during the whole evaporation process and is calculated by:

$$h_{tp,ev} = C \cdot h_l \cdot Bo^{0.5} \tag{32}$$

where Bo is the boiling number and h_l is the all-liquid non-boiling heat transfer coefficient (Eq. 30).

Two-phase pressure drops strongly depend on the vapor quality. They are generally expressed by:

$$\frac{\Delta p_{tp}}{dL} = \frac{2 \cdot f_{tp} \bar{v} \cdot G^2}{D_h} \tag{33}$$

where the Fanning friction factor f_{tp} depends on the vapor quality and $\bar{v} = x \cdot v_g + (1-x) \cdot v_l$.

The total pressure drop is thus obtained by integrating numerically over the exchanger length and by assuming that the vapor quality evolves linearly in the heat exchanger with axial coordinate:

$$\Delta p_{tp} = \int_0^1 \frac{2 \cdot f_{tp} \bar{v} \cdot G^2}{D_h} dx \cdot L \tag{34}$$

where x is the vapor quality.

The condensation heat transfer coefficient is estimated with an expression derived from the Kuo correlation (Kuo et al., 2005), established in the case of a vertical plate heat exchanger fed with R410A:

$$h_{tp} = C \cdot (0.25 \cdot Co^{-0.45} \cdot FR_l^{0.25} + 75 \cdot Bo^{0.75}) \tag{35}$$

Where Fr_l is the Froude Number in saturated liquid state, Bo the boiling number and Co the convection number.

The heat transfer coefficient correlation is quality-dependent. However, in this model, an average heat transfer coefficient is considered. For this reason, the two-phase heat transfer correlations are integrated by assuming that vapor quality variation is linear with length, the average heat transfer coefficient:

$$\bar{h_{tp}} = \int_0^1 h_{tp} dx \tag{36}$$

Model validation

To calibrate the model described above, the experimental data of the first ORC test bench is used. The proposed model is slightly simplified:

- The ambient heat losses are neglected since the heat exchangers are well insulated. It was shown in Figure 12 that these losses are very low, the energy unbalance between both sides of the heat exchangers being almost negligible.
- The pressure drops are neglected because no accurate pressure drop measurement was installed on the test rig. Experimental results however showed that these pressure drops were very limited in the evaporator.

The parameters of the condenser and of the evaporator models are identified by imposing some input variables and by minimizing the deviation between the measured and predicted output variables. For given refrigerant supply

temperature and exhaust subcooling, the condenser model predicts the condensing pressure with a relative error of about 3% (Figure 44).

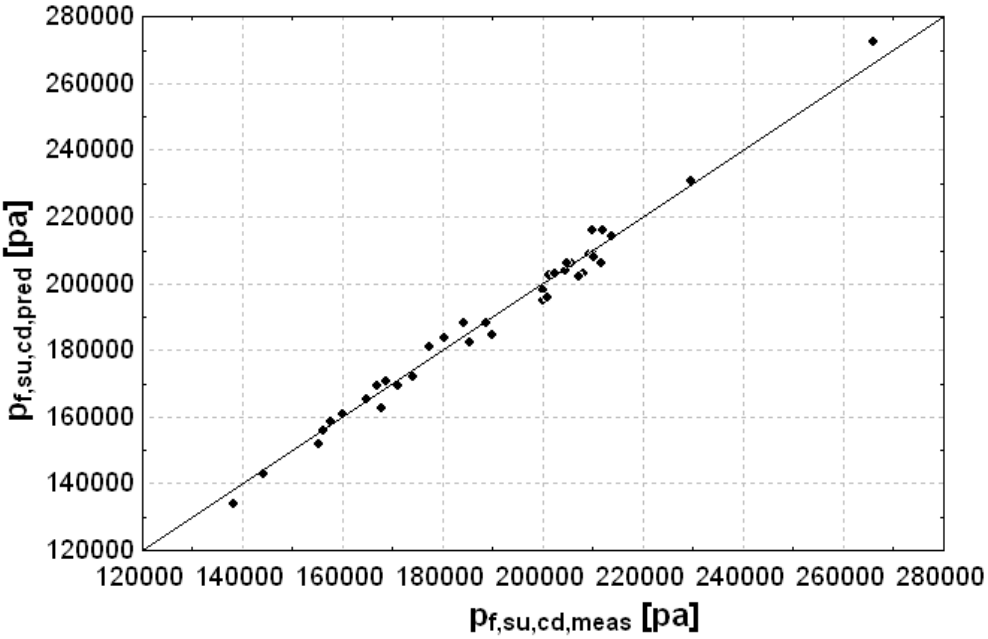

Figure 44: Predicted vs measured condensing pressure

For given refrigerant supply temperature and saturation pressure, the evaporator model predicts the heat flow rate and the exhaust temperature. Figure 45 shows that the exhaust temperature is predicted with a maximum absolute error of 7K, which corresponds to an error of 2.5% in the prediction of the heat flux.

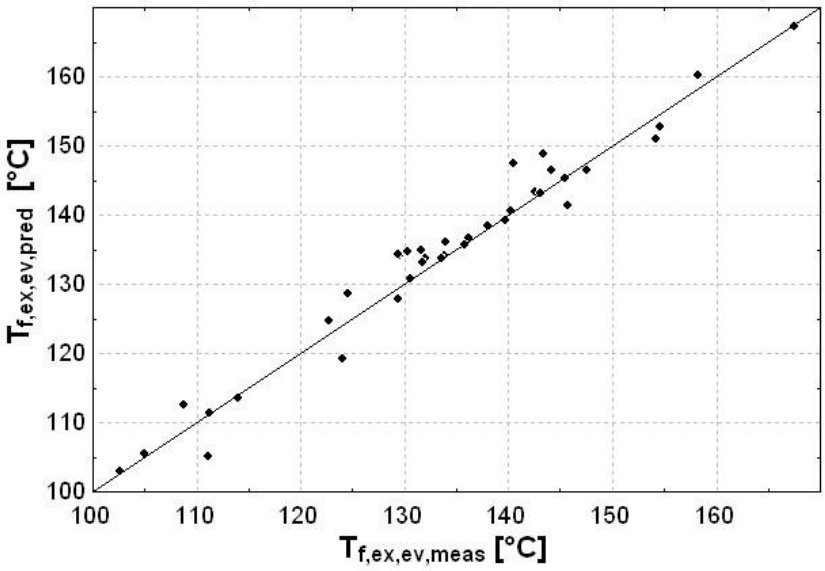

Figure 45: Predicted vs. measured evaporator exhaust temperature

All the identified parameters are listed in Table 13. It can be observed that the identified single phase heat exchange coefficients C are very different. This is explained by the simplified modeling approach: the identified correlations not only account for the heat exchange, but also for pressure drops and ambient heat losses (mainly in the evaporator). This leads, for example, to a very low Nusselt in the vapor zone of the evaporator because the vapor undergoes high ambient heat losses at that point.

Condenser	Evaporator
$\mathrm{Nu}_w = 0.72 \cdot \mathrm{Re}^{0.7} \cdot Pr^{1/3}$	$\mathrm{Nu}_a = 0.101 \cdot \mathrm{Re}^{0.7} \cdot Pr^{1/3}$
$\mathrm{Nu}_v = 0.84 \cdot \mathrm{Re}^{0.7} \cdot Pr^{1/3}$	$\mathrm{Nu}_v = 0.063 \cdot \mathrm{Re}^{0.7} \cdot Pr^{1/3}$
$\mathrm{Nu}_l = 0.4 \cdot \mathrm{Re}^{0.7} \cdot Pr^{1/3}$	$\mathrm{Nu}_v = 1.29 \cdot \mathrm{Re}^{0.7} \cdot Pr^{1/3}$
$h_{tp} = 1.98 \cdot h_l \cdot Bo^{0.5}$	$h_{tp} = 23.7 \cdot h_l \cdot \left(75 \cdot Bo^{0.75} + 0.25 \cdot Co^{-0.45} \cdot Fr_l^{0.25}\right)$

Table 13: Identified heat exchanger model parameters

Sizing model

In the model described and validated above, the parameters are imposed to the model, which calculate the resulting working conditions (*outputs*) for given *inputs*.

However, when designing a thermodynamic cycle, it is often useful to impose the working conditions and have the heat exchanger parameters recalculated. This type of model is called *sizing model*.

For a given corrugation pattern (amplitude, chevron angle, and enlargement factor), two degrees of freedom are available when sizing a plate heat exchanger: the length and the total flow width. The total flow width is given by the plate width multiplied by the number of channels:

$$W_{tot} = W_{hx} \cdot \frac{N_p - 1}{2} \tag{37}$$

The two degrees of freedom are fixed by the heat exchange area requirement and the limitation on the pressure drop on the working fluid side:

- Increasing the total width decreases the Reynolds number. This leads to a lower pressure drop and to a higher required heat transfer area, since the heat transfer coefficient is also decreased.
- Increasing the plate length leads to a higher pressure drop.

Therefore, by imposing a pinch point and a pressure drop, it is possible to define the total width and the length of the plate heat exchanger. The flow chart of the sizing process is shown in Figure 46.

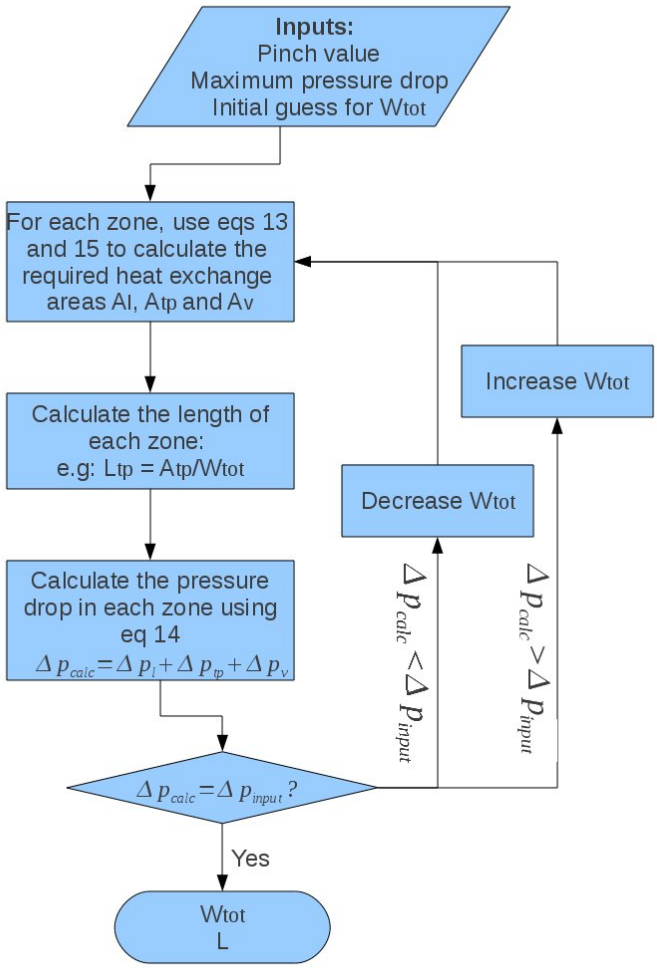

Figure 46: Heat exchanger sizing process

2.3 Pump

The positive-displacement pump is characterized by its swept volume and its global isentropic effectiveness (η_{pp}). The latter lumps the internal irreversibility of the pumping process with the electromechanical losses of the electric motor. It can be identified from experimental data or using typical efficiency curves for volumetric pumps. The pump electrical consumption is given by:

$$\dot{W}_{el,pp} = \frac{\dot{W}_{pp,s}}{\eta_{pp}} = \frac{\dot{M}_f \cdot (h_{ex,pp,s} - h_{su,pp})}{\eta_{pp}} = \frac{\dot{M}_f \cdot v_{su,pp} \cdot (p_{ex,pp} - p_{su,pp})}{\eta_{pp}} \quad (38)$$

The mass flow rate displaced by the pump is computed as a function of its capacity fraction X_{pp}:

$$\dot{M}_f = \frac{\dot{V}_{s,pp}}{v_{su,pp}} = \frac{X_{pp} \cdot \dot{V}_{s,pp,max}}{v_{su,pp}} \quad (39)$$

The capacity fraction X_{pp} is defined as the ratio between the actual volume flow rate and the maximum volume flow rate of the pump. This variable is an

input of the model; it is actually tuned by modifying the swept volume of the pump or its rotating speed.

Model validation

Figure 22 shows a good correlation between pump efficiency and isentropic compression power. The following empirical law is used, predicting the measured efficiency with a maximum error of 2.1%:

$$\varepsilon_{pp} = 0.2673 + 0.259 \cdot \dot{W}_{pp,s} - 0.000744 \cdot \dot{W}_{pp,s}^2 \quad (40)$$

The prediction of the refrigerant flow rate using Eq. 39 gives good results, but only for the working points without pump cavitation: for these points (26 out of 39) a maximum error of 5.4% is stated. For the points with a too low liquid level, a gas phase appears during the suction process which leads to lower measured flow rate than the predicted one.

2.4 Cycle model

The global model of the cycle is built by interconnecting the models of the different sub-components described above, as shown in Figure 47.

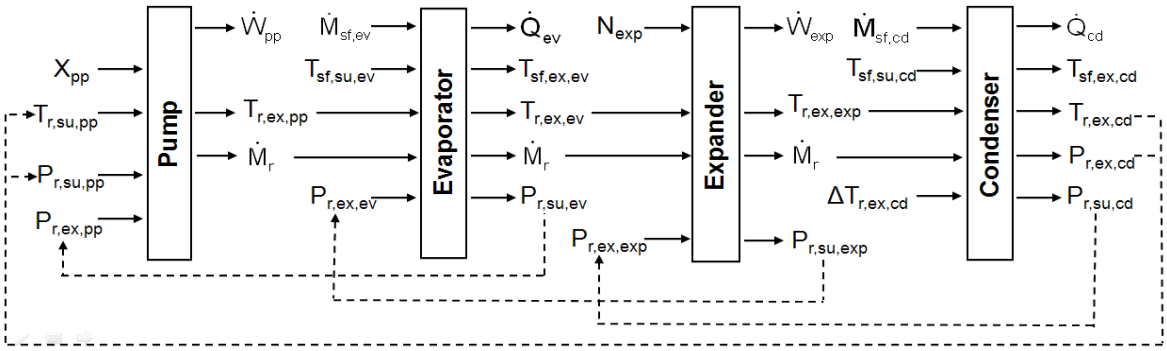

Figure 47: Interconnection of the submodels leading to the global cycle model

The modeling highlights the following constraints:

a) For a given displacement, the pump imposes the refrigerant mass flow rate.

b) The evaporator imposes the fluid superheating and the pump exhaust pressure.

c) Provided its rotational speed is fixed, the expander imposes the evaporator exhaust pressure.

d) For given secondary fluid mass flow rate and supply temperature, the condenser imposes the pressures at expander exhaust and pump supply.

This simulation model is not fully predictive, because liquid subcooling at the condenser exhaust is defined as a model input. To predict this subcooling, a refrigerant charge model should be introduced. In the scope of this work, it was decided not to implement such a model because the subcooling was mainly influenced by the presence of non-condensing gases (whose total mass is unknown) in the cycle during the experimental campaign.

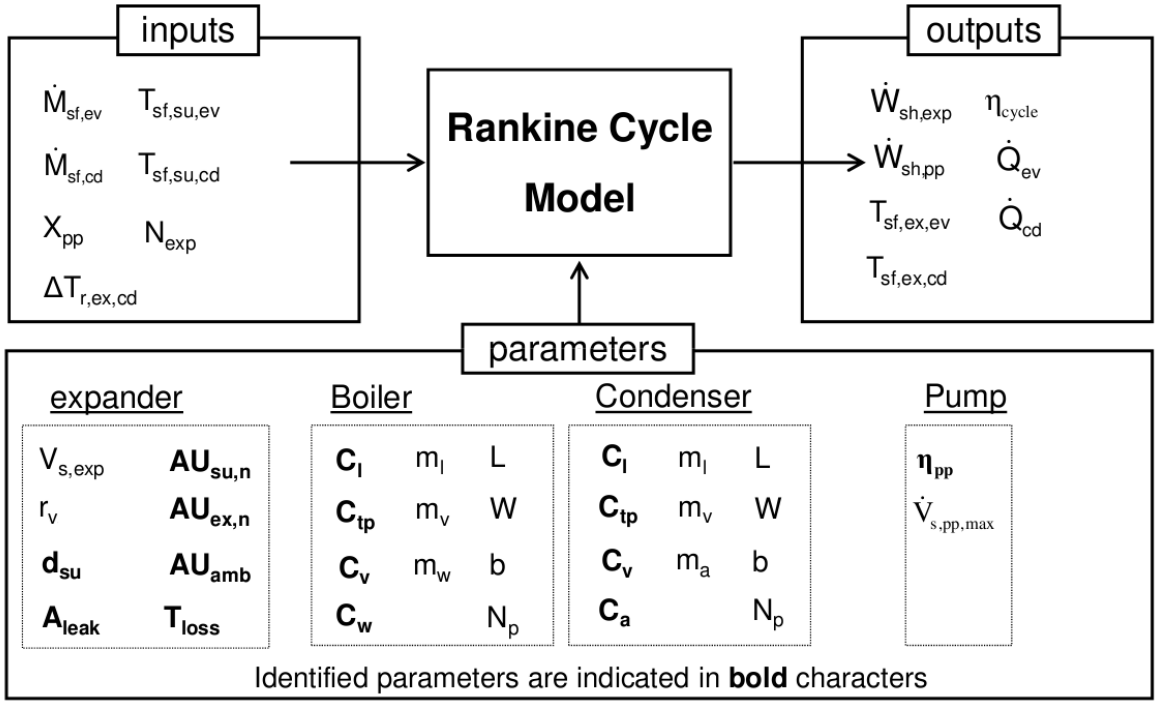

Figure 48: Global ORC model

The information diagram of the Rankine cycle simulation model is given in Figure 48. The inputs of the model are the mass flow rates and supply temperatures of the secondary fluids in the evaporator and in the condenser, the capacity fraction of the pump and its rotational speed. The main outputs are the expander shaft power and the cycle efficiency. The parameters to identify with experimental data are indicated in bold. All other parameters are measured or imposed.

Model validation

Taking into account the different submodel parameters identified in the previous sections, the predicted expander shaft power is compared to the measured one. Figure 49 shows that all measurements are predicted within 10% error. The error is higher for the global cycle model because of the cumulated errors of the subcomponent models.

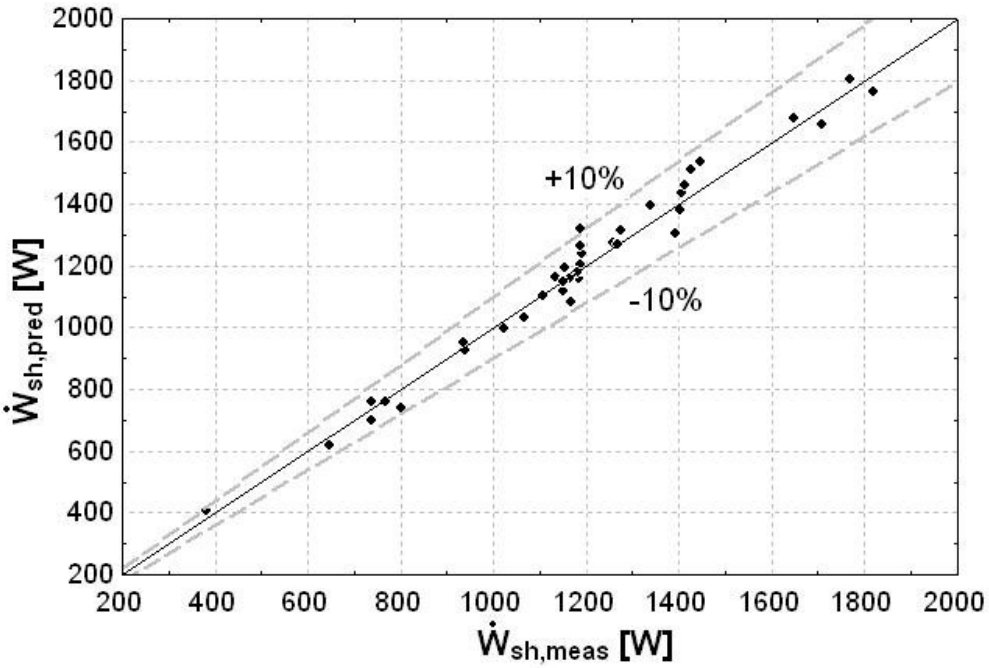

Figure 49: Predicted vs. measured shaft power with the global model of the cycle

2.5 Model exploitation

This section illustrates how the simulation models established and validated in the previous sections can be used to optimize the working conditions of the system.

ORC test rig

The global validated model of the ORC test rig allows understanding its behavior under various operating conditions. It can also be used to estimate the potential of performance improvement. The increase of the system performance following this optimization is evaluated hereafter for one of the 39 measured performance points, characterized by $P_{su,exp}$ = 7.91 105 Pa, $P_{ex,exp}$ = 1.84 105 Pa, $T_{su,exp}$ = 133°C and N_{exp}=2660 rpm.

Figure 50 shows the T-s diagram of this working point, with superposition of the secondary fluids temperature profiles. Large vapor superheating at the evaporator exhaust and liquid subcooling at the condenser exhaust are observed.

A first improvement consists in reducing the apparent liquid subcooling. As detailed in chapter 3.2.3 , this subcooling is mainly due to the presence of a non-condensable gas in the condenser. It is estimated that if the non-condensable gas are removed, the subcooling can be reduced from 27 K (measured value) down to 5 K. The increase in performance can be explained by the location of the pinch point at the condenser exhaust (on the refrigerant side), which prevents the condensing pressure to be lowered.

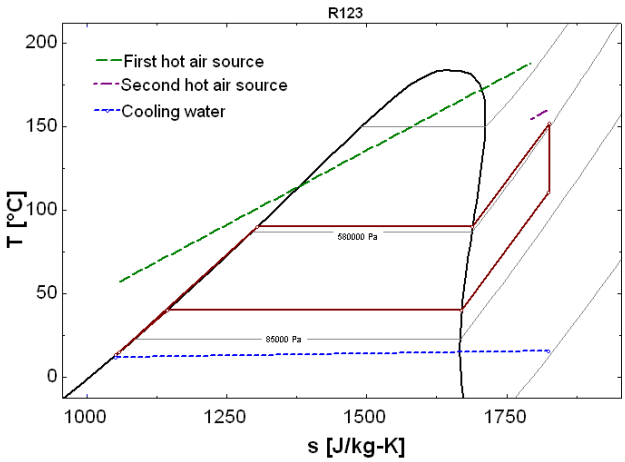

Figure 50: T-s diagram of the measured, non-optimized working point

A second improvement is the selection of a more efficient pump. The effectiveness of the pump installed on test bench is 15%. A higher effectiveness should obviously be achieved. A pump effectiveness of 60% is assumed in this simulation.

The third parameter to be optimized is the evaporator exhaust superheating. (Yamamoto et al., 2001) showed that for a working fluid with a low latent heat such as HCFC-123, the saturated vapor at the turbine supply would give the best performance. This can be achieved in two ways, as shown in Figure 51:

1. Modification of the pump flow rate: Increasing the fluid mass flow rate will lead to a higher pressure at the expander supply, since the latter has to "increase" the density of the fluid to absorb the total amount of mass flow rate imposed by the pump. Increasing the pressure will lead to a higher evaporation temperature and hence to a lower temperature difference between the two heat sources. The mean logarithmic temperature difference being smaller, the heat flow rate across the evaporator will be reduced and the superheating will be reduced. Figure 52 gives the evolution of the cycle efficiency and of the expander effectiveness with the flow rate, and shows that a higher flow rate indeed increases the performance.
2. Modification of the expander rotational speed: If the expander rotational speed is decreased, the absorbed volumetric flow rate is decreased, and, for a given mass flow rate, the pressure is increased. Figure 51 shows that lowering the expander speed indeed increases the performance, but only until a certain point (around 1000 rpm), where the expander effectiveness is reduced to a prohibitive value because of internal leakage.

Therefore, reducing the expander rotational speed and increasing the pump mass flow rate both have a similar effect: they yield a higher evaporating pressure and a reduced superheating.

Since the reduction of the superheating can be achieved in two ways, it is important to determine which combination of mass flow rate / rotational speed optimizes the cycle performance.

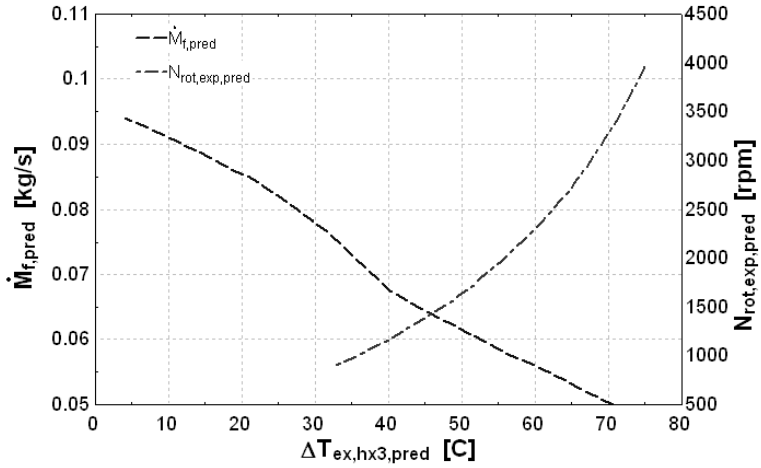

Figure 51: Required flow rate and speed to achieve a given superheating

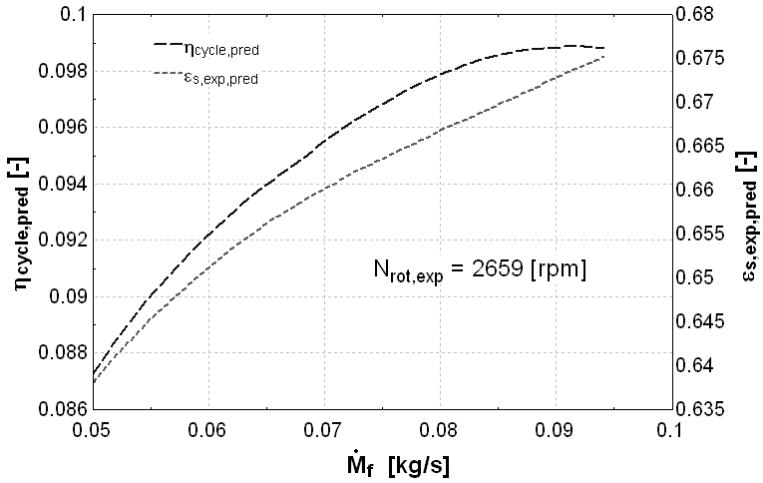

Figure 52: Cycle efficiency and expander effectiveness vs. flow rate

The following observations should be taken into account while trying to optimize the working conditions:

- A higher mass flow rate increases the heat transfer in the evaporator and thus the output power (at constant cycle efficiency).
- There exists a rotational speed that maximizes the expander effectiveness. This is due to the antagonist effects of the rotational speed on the internal leakages and on friction losses and supply pressure drop.
- A higher pressure in the evaporator may decrease the heat transfer (because of the lower logarithmic mean temperature difference), and increase the under-expansion losses in the expander.

To determine the optimal working condition, a map of the cycle efficiency is drawn in Figure 53: the cycle efficiency is plotted as a function of the two

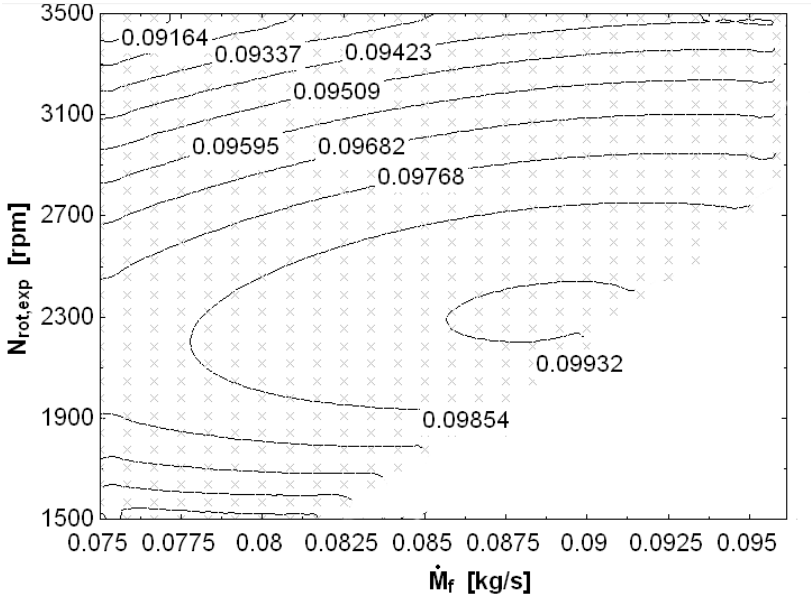

Figure 53: Efficiency mapping

working conditions. Each gray cross in the background represent one point calculated by the model and used to establish the isometric curves. These curves should only be read in the area defined by the crosses.

The lower right part of the map corresponding to high mass flow rate and low rotational speed is undefined, because superheating is reduced to zero, which would correspond to a two-phase state at the evaporator exhaust.

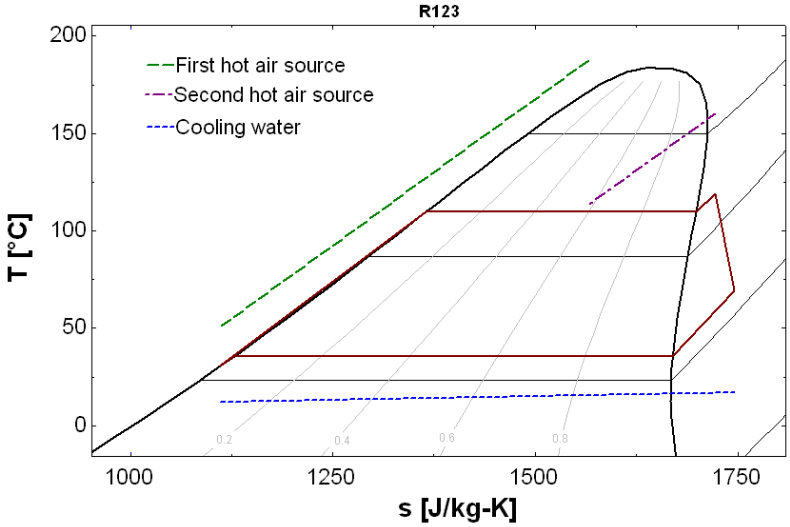

Figure 54: T-s diagram and secondary fluid temperatures

Figure 53 shows that an optimum working point is obtained around a value of 0.09 kg/s and 2300 rpm. The optimum is very close to the saturation zone, which confirms that superheating should be as small as possible in an ORC.

The T-s diagram of this new, optimized working point is presented in Figure 54. This new cycle is much closer to the theoretical Carnot cycle than the original cycle. Its efficiency has been increased from 5.1% to 9.9%.

Scroll expander

The validated simulation model of the scroll expander can be used to evaluate the impact of the different losses on its overall performance. Starting from a model that assumes a fully isentropic expansion, the different losses are introduced one after another. Results for the hermetic expander are shown in Figure 55. The simulation is performed for a supply pressure of 12.61 bar

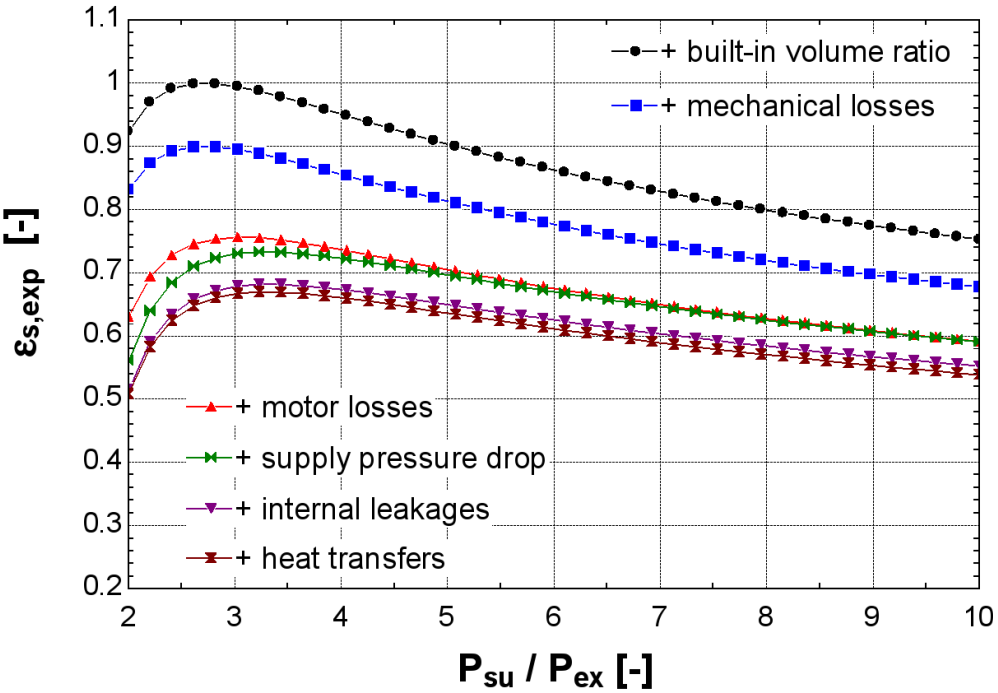

Figure 55: Isentropic effectiveness vs. pressure ratio

(which corresponds to a saturation temperature of 100°C) and a supply temperature of 110°C. A pressure ratio of 10 corresponds to a saturation temperature close to 20°C at the exhaust pressure. These conditions are representative of those of the envisioned ORC application.

It can be observed that the electromechanical losses are significant. Further investigation should indicate in which extent these losses could be reduced by selecting a better adapted induction motor. Figure 56 shows the evolution of the motor efficiency and overall electromechanical efficiency with the electrical power produced by the expander.

Internal leakages were also found to be non negligible. However, the impact of these losses is largely reduced in comparison with the previously tested kinematically rigid configuration. This is due to both the axial and radial compliance mechanisms.

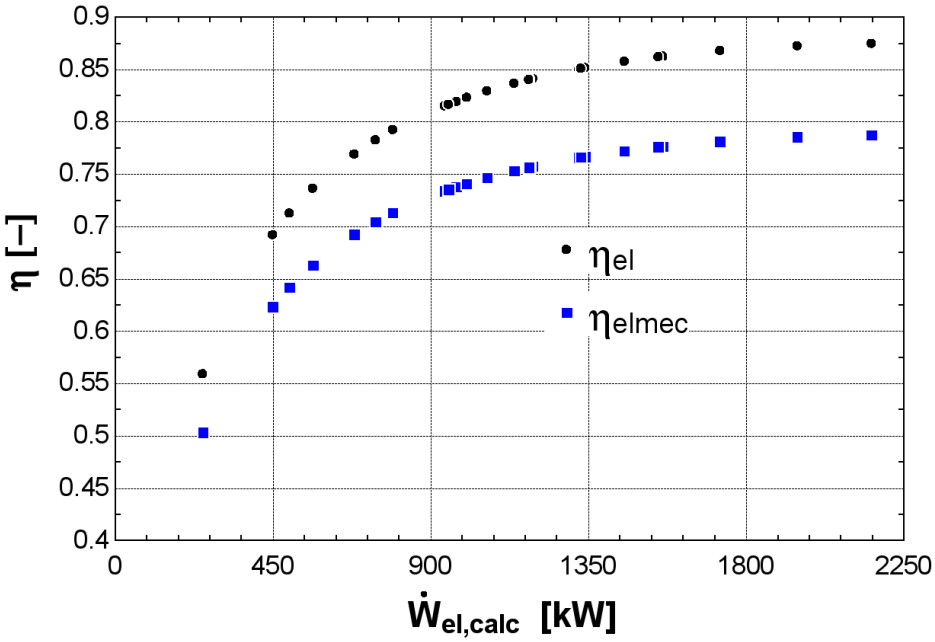

Figure 56: Motor efficiency and electro-mechanical losses

For the high pressure ratios, the under-expansion losses have a significant impact on the overall performance. A machine with a larger built-in volume ratio would yield better performance for pressure ratios higher than 3.

3 Dynamic models

This section describes the dynamic modeling of different components involved in a waste heat recovery ORC. The models are implemented in Modelica and the fluid properties are computed using the TILMedia library coupled to Refprop.

Solving a dynamic system simulation consists in two consecutive steps: the *initialization* phase, in which a consistent set of values is assigned to all the model variables, and the *simulation* phase, in which a trajectory is computed. The values calculated during the initialization phase are used for the initial step (t=0) of the simulation process (Dynasim, 2011).

As in Engineering Equation Solver, the equations and the connections in Modelica are acausal, which allows stating the model equations in a neutral form without considering a computational order (Jensen, 2003).

In addition to the model themselves (described in the next sections), an interface has been written in Matlab to visualize the temporal evolution of the temperature profiles in the heat exchanger and of the T-s, p-h and p-v diagrams of the cycle. This interface is described in Appendix E.

3.1 Heat exchangers model

Dynamic models of heat exchanger can be subdivided into two main categories: moving boundaries models and discretized models. The moving boundary formulation is characterized by several zones whose boundaries vary in time according to the current conditions. In a discretized model, most commonly a finite volume model, the 1D flow is subdivided into several equal control volumes. According to (Satyam Bendapudi et al., 2008), moving boundaries models are about three times faster than finite volume models, but they are also less robust through start-up and load-change transients, and are less accurate for refrigerant charge calculation.

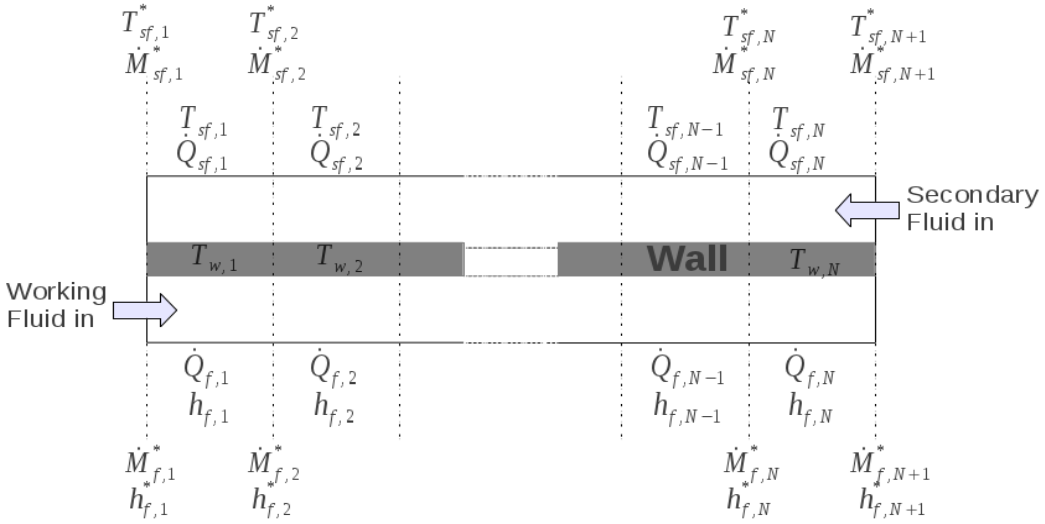

Figure 57: Discretized heat exchanger model

In this work, a finite volume model is preferred, mainly because of the robustness. The heat exchanger is discretized into N cells in which the energy and mass conservation equations are applied (see Figure 57). The momentum balance is neglected. The secondary fluid is a single phase-fluid. It can therefore be modeled only by its mass flow rate, its average heat capacity and its density. The proposed model is a 1-D model, i.e. the fluid properties are assumed to vary only in the flow direction.

Two types of variables can be distinguished in Figure 57: cell variables and node variables. The latter are indicated by a "star" superscript (*). To compute the node values, the following acausal equations are used:

$$h_i = \frac{h^*_{i+1} + h^*_i}{2} \;\; ; \;\; T_i = \frac{T^*_i + T^*_{i+1}}{2} \tag{41}$$

For each cell, a heat exchange area, a wall mass and a fluid volume are defined:

$$A_i = \frac{A}{N} \;\; ; \;\; V_i = \frac{V}{N} \;\; ; \;\; M_{w,i} = \frac{M_w}{N} \tag{42}$$

For both sides, the mass balance is written:

$$A \cdot \frac{\partial \rho}{\partial t} + \frac{\partial \dot{M}}{\partial x} = 0 \tag{43}$$

In the present model, the selected state variables are p and h. These variables should be the ones to be differentiated with respect to time. The density derivative appearing in Eq. (43) is therefore expressed as:

$$\frac{\partial \rho}{\partial t} = \frac{\partial \rho}{\partial h} \cdot \frac{dh}{dt} + \frac{\partial \rho}{\partial p} \cdot \frac{dp}{dt} \tag{44}$$

where $\partial \rho / \partial h$ and $\partial \rho / \partial p$ can be considered as thermodynamic properties and are derived from the considered fluid equation of state.

The discrete form of the mass balance is finally written:

$$\frac{dM_i}{dt} = V_i \cdot \left(\frac{\partial \rho}{\partial h} \cdot \frac{dh}{dt} + \frac{\partial \rho}{\partial p} \cdot \frac{dp}{dt} \right) = \dot{M}^*_i - \dot{M}^*_{i-1} \tag{45}$$

The energy balance is written:

$$\frac{dU_i}{dt} = \dot{M}^*_{i-1} \cdot h^*_{i-1} - \dot{M}^*_i \cdot h^*_i + \dot{Q}_i + \dot{W}_i - p \cdot \frac{dV_i}{dt} \tag{46}$$

recognizing that $U_i = H_i - p \cdot V_i$ and that the internal work $\dot{W}_i$ is null, equation (46) becomes:

$$V_i \cdot \frac{\partial \rho_i}{\partial t} \cdot h_i + V_i \cdot \rho_i \cdot \frac{\partial h_i}{\partial t} - V_i \cdot \frac{dp}{dt} = \dot{M}^*_{i-1} \cdot h^*_{i-1} - \dot{M}^*_i \cdot h^*_i + \dot{Q}_i \tag{47}$$

Combining Eqs 45 and 47 yields:

$$V_i \cdot \rho_i \cdot \frac{\partial h_i}{\partial t} = \dot{M}^*_{i-1} \cdot (h^*_{i-1} - h_i) - \dot{M}^*_i \cdot (h^*_i - h_i) + \dot{Q}_i + V_i \cdot \frac{dp}{dt} \tag{48}$$

In the case of the secondary fluid, since a constant heat capacity is assumed and since the fluid is incompressible, Eq. (48) simplifies into:

$$V_i \cdot \rho_i \cdot \bar{c_p} \cdot \frac{\partial T_i}{\partial t} = \dot{M} \cdot \bar{c_p} \cdot (T^*_{i-1} - T^*_i) + \dot{Q}_i \tag{49}$$

The energy balance over the wall is written:

$$c_w \cdot M_{w,i} \cdot \frac{dT_{w,i}}{dt} = \dot{Q}_{sf,i} - \dot{Q}_{f,i} \tag{50}$$

Heat transfer

When using traditional dynamic simulation tools, it is generally difficult to use correlations for the heat transfers and the pressure drops, since they slow down the calculation process and can even lead to numerical instabilities and simulation failures.

To propose a heat exchanger model that is robust and fast, the following methodology is proposed:

1. A complete model of the heat exchanger is developed in steady-state, with the proper heat transfer and pressure drop correlations, as described in section 2.2 .
2. A nominal heat transfer coefficient is identified with the steady-state model for the nominal conditions.
3. The heat transfer correlations are simplified and a simple law is proposed to compute the variation of the nominal heat transfer coefficient with the most relevant working conditions.

In total, four different heat transfer coefficients are calculated: one on the secondary fluid side and three (vapor, two-phase, liquid) on the refrigerant side.

For single-phase heat transfer, Eq. 30 can be rewritten:

$$U = \frac{Nu \cdot k}{L} = \frac{k}{L} \cdot \left(\frac{\dot{M} \cdot L}{A \cdot \mu} \right)^m \cdot Pr^n = \dot{M}^m \cdot \frac{L^{(m-1)}}{A} \cdot \frac{k \cdot Pr^n}{\mu^m} \tag{51}$$

The second factor ($L^{(m-1)}/A$) in Eq. (51) is related to the geometry and is therefore constant for a given heat exchanger. The third factor ($k\,Pr^n/\mu^m$) contains transport properties of the working fluid. This factor varies in a narrow range if the working fluid remains unchanged and if the operating pressure and temperature levels are kept more or less constant, which is the case in an ORC evaporator/condenser. The main term influencing the heat transfer coefficient being the mass flow rate, the following approximation can be written:

$$U = U_n \cdot \left(\frac{\dot{M}}{\dot{M}_n} \right)^m \tag{52}$$

where U_n is a nominal heat transfer determined by the complete steady state model (section 2.2) for the nominal flow rate $\dot{M}_n$. m is the Reynolds exponent and is equal to 0.8 for turbulent flows.

For the boiling and condensing heat transfer coefficients, such a simplification is trickier since the latter also depends on the heat flux through the heat exchanger. However, in order to keep the model as simple as possible and since two-phase heat transfer coefficients are generally high compared to the secondary fluid heat transfer coefficient, it is decided to assume the boiling number constant to simplify equations (32) and (34). Another non-negligible influence is the vapor quality. However, since an average heat transfer coefficient is assumed for the whole two-phase zone, this influence is not taken into account.

The evaporation heat transfer is evaluated from a correlation provided by (Y.-Y. Yan & Lin, 1999). In this correlation, the Nusselt number depends on the Prandlt, Reynolds and Boiling numbers. The exponent of the Reynolds number being 0.5, the following relation can be written:

$$U_{ev} = U_{ev,n}\left(\frac{\dot{M}}{\dot{M}_n}\right)^{0.5} \tag{53}$$

For the condensation heat transfer, (Yi-Yie Yan & Lin, 1999) found a 0.4 Reynolds exponent. The following relation is therefore obtained:

$$U_{cd} = U_{cd,n}\left(\frac{\dot{M}}{\dot{M}_n}\right)^{0.4} \tag{54}$$

To avoid any inconsistency, the transition between two different heat exchange coefficients is performed on a non-null quality width by interpolating between the two coefficients. An interpolation function is defined, selected to be smooth at the first order (i.e. the heat transfer coefficient as a function of the vapor quality h(x) and its first derivative are continuous). This continuity avoids negative effects in the solution process. The value of the heat transfer coefficient is provided in Eq 55.

$$U = \begin{cases} U_l & for \quad x < -\Delta x \\ U_l + \frac{(U_{tp} - U_l)}{2} \cdot \left(1 + \sin\left(\frac{\pi \cdot x}{2 \cdot \Delta x}\right)\right) & for \quad -\Delta x < x < \Delta x \\ U_{tp} & for \quad \Delta x < x < 1 - \Delta x \\ U_{tp} + \frac{(U_v - U_{tp})}{2} \cdot \left(1 + \sin\left(\frac{\pi \cdot (x-1)}{2 \cdot \Delta x}\right)\right) & for \quad 1 - \Delta x < x < 1 + \Delta x \\ U_v & for \quad 1 + \Delta x < x \end{cases} \tag{55}$$

where x the vapor quality, defined by an enthalpy ratio not limited to the [0,1] interval:

$$x = \frac{h - h_l}{h_v - h_l} \tag{56}$$

Δx is a transition width, imposed to 0.05 for the present work.

The transitions between the different heat transfer coefficients in Eq 55 are surrounded by the Modelica "noevent" instruction to avoid triggering a breakpoint ("event") in the simulation.

Pressure drops

In the reference steady-state model, pressure drops are computed for each zone of the heat exchanger. In a discretized model, pressure drop should be computed in each cell. However, this causes a multiplication of the number of pressure states, which are often the "fastest" states in thermo-fluid systems (i.e. the eigenvalues of the Jacobian differ by a factor comprised between 10^4 and 10^6). This leads to stiff models, which necessitate small time steps and can increase dramatically the simulation time (Richter, 2008).

In the scope of this work, this is solved by assuming that the entire pressure drop is concentrated at the end of the vapor phase since this is the region where the fluid density is lowest. The pressure drop is lumped into a single orifice pressure drop, whose diameter is identified with the detailed model (section 2.2). The fluid flow is assumed to be incompressible and the pressure drop is computed by:

$$\Delta p = \frac{\dot{M}^2}{2 \cdot \rho \cdot A^2} \tag{57}$$

where A is the equivalent pressure drop orifice diameter, identified with Eqs 31 and 34.

Numerical issues

Initialization

Failures in dynamics simulations involving discretized heat exchangers can occur during the *initialization* phase or during the *simulation* phase.

The initial Differential Algebraic Equations (DAE) system[2] is underspecified for a number x of variables, x being the number of differentiated equations in the DAE system (Dynasim, 2011). Without information, the solver sets these variables to a default value of 1. This usually leads to the non-convergence of the solution process. Two types of values must be set when modeling dynamic systems:

- *Start values* are values used to start the Newton resolution process. A start value should be assigned to each state variable.
- *Initial values* are imposed to the solver. Their maximum number is equal to the number of differentiated variable. If the initial system is underspecified, the solver uses start values as initial values to reach the

[2] In the present context, "algebraic" refers to a variable that is free of derivative, not to an algebraic variable. DAE systems are distinguished from Ordinary Differential Equation (ODE) systems, in which all the variables can be differentiated.

same number of equations and unknowns. An example of initial value assignment is the steady-state hypothesis: in this case, all the time derivatives are set to zero and the simulation starts in steady-state.

Even with correctly-assigned start and initial values, highly non-linear systems might still fail to converge during initialization. To improve the convergence, a strategy similar to the one proposed by (P. Li et al., 2010) is applied. In this approach, the initial system is simplified: heat transfer coefficients and pressure drops are set to constant values during a certain amount of time. When the system stabilizes after a few seconds of simulation, the heat transfer and pressure drop equations are activated one by one. The activation is performed by an interpolation function similar to the one proposed in Eq (55) between the constant value and the value computed by the model. The activation time and length are set as model parameters. This strategy makes the initialization problem faster and much easier to solve.

Phase transitions

Simulation failures during the integration phase often occur in the heat exchangers. Most of the time, these failures are due to a phase transition (liquid to two-phase) which involves a discontinuity in the first derivative of the density. This is illustrated in Figure 58: the discontinuity appears at x=0, and the numerical integration leads to unsteadinesses (chattering) in the calculation of the mass balance for each cell.

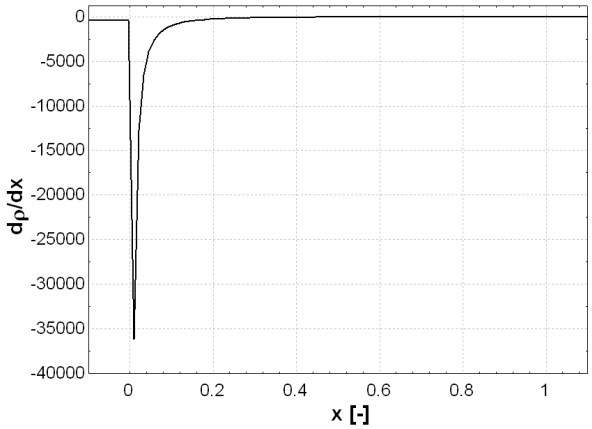

Figure 58: First derivative of the density as a function of the vapor quality

Figure 59 is an example of such chattering. The simulation is performed for one heat exchanger with a two-phase flow under highly transient conditions. The red curve corresponds to the case with a 20-cells discretization, while the blue curve corresponds to a 100-cells discretization. Each oscillation on the flow rate prediction between t=13s and t=18s corresponds to a phase transition in one of the cell: the high density derivative is applied to a cell with a non-negligible working fluid mass. High flow rates transitions are therefore generated between cells and spread trough the heat exchanger.

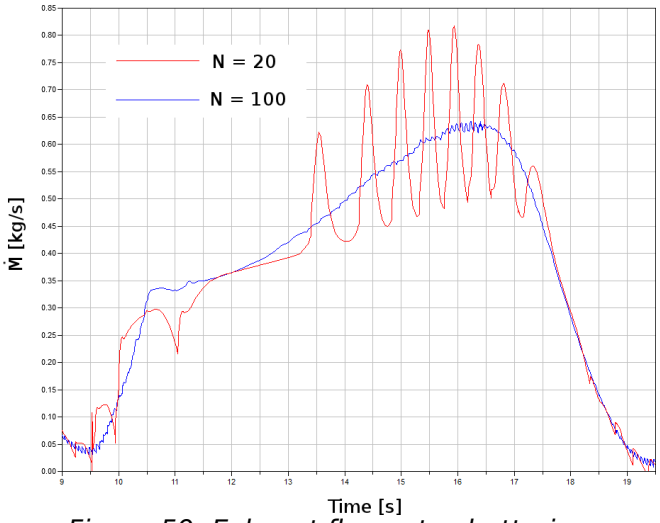

Figure 59: Exhaust flow rate chattering

The case with N=100 also generates oscillations, but since the density transition is applied to a much smaller cell, the oscillations are relatively smaller and occur at a higher frequency.

It should be noted that these oscillations only occur for "stressed systems", i.e. systems under highly transient conditions and with a high ratio between heat exchanger internal volume and mass flow rate. The underlying reason is derived mathematically in Appendix F.

In the scope of this work, special attention is paid to the model robustness, even in extreme conditions. Several methods are therefore developed and tested to avoid these oscillations:

1. Constant node flow rate: the flow rate variations are reported on the last node, while a constant flow rate is assumed for all the other nodes.
2. Truncated density derivative: $d\rho/dx$ (Figure 58) is truncated to limit the instabilities generated during a phase transition. The parametric value of the maximum value of $d\rho/dt$ must be provided by the user. This is internally converted into maximum values for $\partial\rho/\partial h$ and $\partial\rho/\partial p$ using arbitrary typical values for the derivatives of the state variables.
3. Filtered density derivative: the phase transition is smoothed by applying a first order filter on the time derivative of the density. The time constant of the filter must be provided by the user.
4. High number of cells: even though the occurrence of phase changes is higher with highly discretized models, their impact is lower, as shown in Figure 59.

A thorough description of these 4 methods is provided in appendix F, with the comparison of their accuracy, and simulation speed. A significant increase of the simulation robustness is stated with these different methods. This increase is however achieved at the cost of a small decrease of the simulation accuracy.

Model parameters

Figure 60 presents the Modelica interface for the model parameter. These include the heat exchanger internal volumes, the heat transfer area, the metallic wall mass and specific heat, the number of cells and the nominal heat transfer coefficients. Boolean parameters are added to allow the user to select between numerical methods: "Mdotconst", "Max_drhodt", "filter_dMdt" correspond to the constant node flow rate, truncated density derivative and the filtered density derivative strategies, respectively. "average_Tcell" corresponds to the application of Eq. (41). False corresponds to the upwind scheme, true corresponds to the central-difference scheme.

The default number of cells selected for all the dynamic heat exchanger models used in this work is set to 20, since it turned out to be a good tradeoff between accuracy and computation time. This number is higher than the one recommended by (S. Bendapudi et al., 2005), who found that a minimum of four elements were necessary in the evaporator to detect superheat while 15 were needed for accurate simulation of a dynamic chiller model.

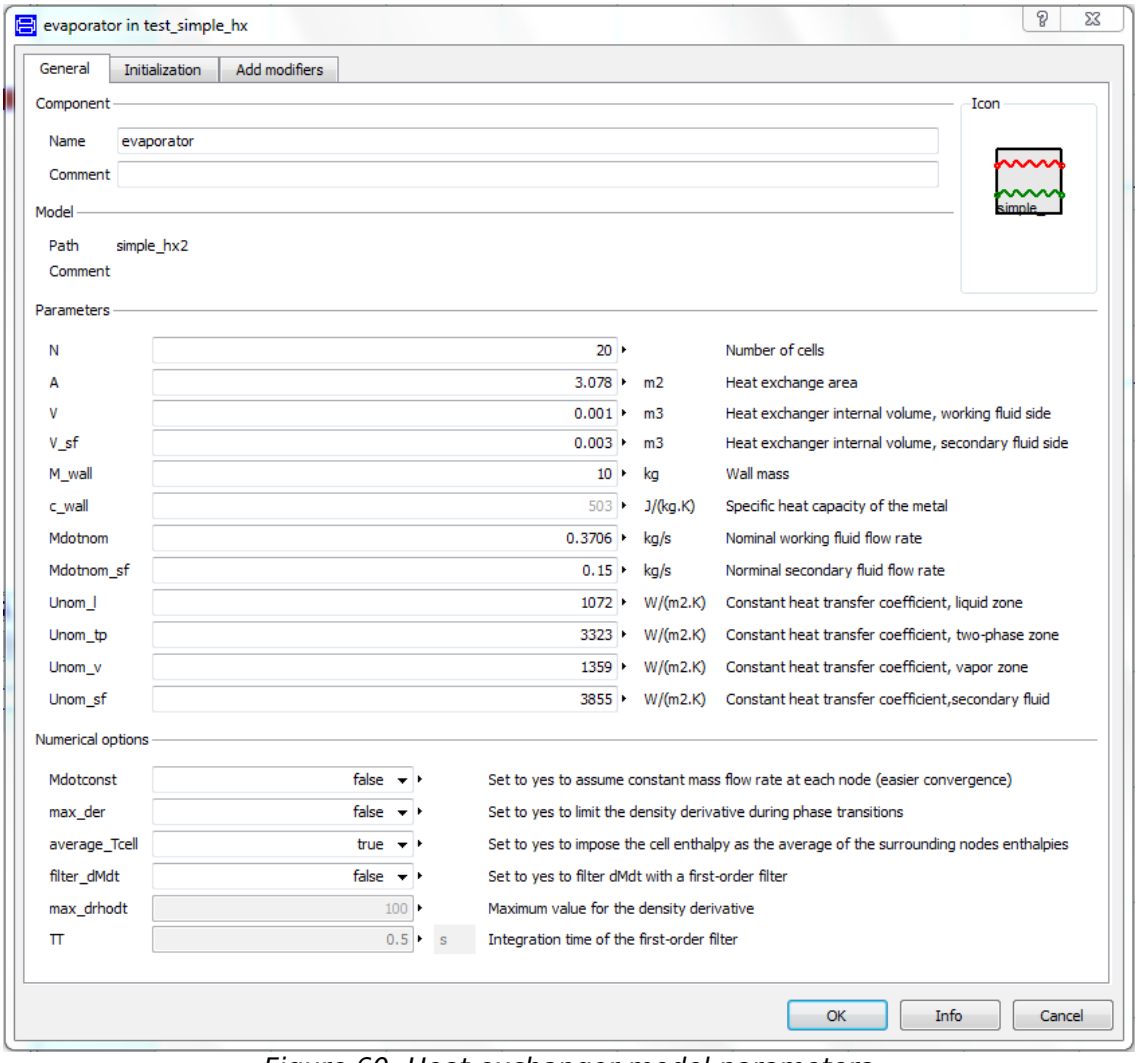

Figure 60: Heat exchanger model parameters

3.2 Pump/expander models

The time constants involved when using positive displacement-machines such as the pump or a scroll expander are low compared to that of the heat exchangers. (Guangbin et al., 2011) showed, through simulations, that the typical response time of scroll expanders is not higher than 2 to 3 seconds. This is very small compared to the time constants involved in dynamic heat exchanger models and can therefore be neglected.

To keep the simulation model as effective and fast as possible, detailed thermodynamic model of the expansion process such as the one presented in previous sections are not implemented. Instead, the simplified polynomial models developed in section 2.1 are implemented: the machine is entirely defined by its filling factor and its isentropic effectiveness, which are computed using a limited number of inputs. The model parameters are presented in Figure 61: in all cases the expander swept volume must be defined. Three options are then available: "hermetic scroll expander" and "open-drive scroll expander" correspond to the polynomial laws relative to each type of expander, while "User defined" allows imposing constant values for these two parameters.

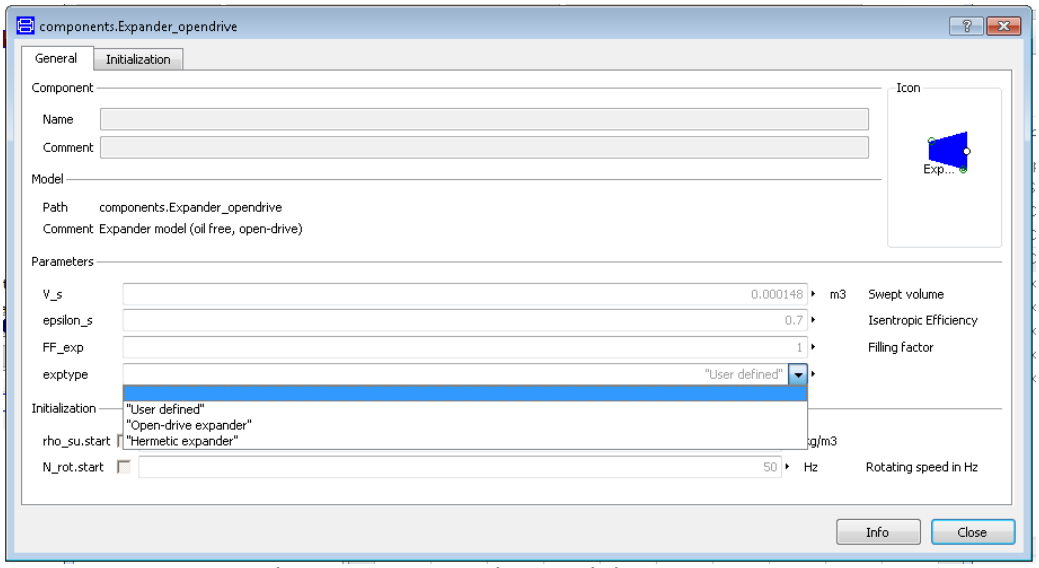

Figure 61: Expander model parameters

3.3 Liquid receiver model

The liquid receiver is assumed to be in thermodynamic equilibrium at all times, i.e. the vapor and liquid are saturated at the given pressure.

It is modeled by the same energy and mass conservation laws as in the discretized heat exchanger (Eqs 42 and 48). The exhaust flow rate is defined as saturated liquid while the supply flow rate coming from the condenser can be either subcooled (in which case the receiver pressure is going to decrease), saturated (in which case the receiver pressure remains constant) or two-phase (in which case the receiver pressure is going to increase).

For the initialization phase, two options are left to the user:

1. Imposed initial tank level: this allows a good control of the initial refrigerant charge in the cycle since the latter is mainly defined by the volume of liquid in each cycle component.
2. Imposed initial pressure: this can make the initialization process less iterative and easier to solve.

The only parameter of the liquid receiver model is its internal volume. It should be noted that, the higher this volume, the easier the solving process since the tank acts as a damper and reduces the pressure fluctuations.

3.4 Valve model

The pressure drop in the valve is modeled by a quadratic expression using the incompressible flow hypothesis. This is typically written:

$$\dot{M} = X_{open} \cdot A_{full} \cdot \sqrt{(2 \cdot \rho \cdot \Delta p)} \tag{58}$$

where $X_{open} \cdot A_{full}$ is the actual valve cross-sectional area.

This formulation may cause numerical issues when $\dot{M}$ and Δp are small because the derivative $d\dot{M}/d\Delta p$ tends to infinity. The actual physical flow characteristic does not show this singularity because the flow becomes laminar (Casella et al., 2006). To avoid numerical issues, Eq 58 is replaced by the following expression, proposed by (Richter, 2008), ensuring the continuity of both the pressure drop function and its first derivative:

$$\dot{M} = \begin{cases} A \cdot \sqrt{(2 \cdot \rho \cdot \Delta p)} & for \quad \Delta p > \Delta p_0 \\ -A \cdot \sqrt{(2 \cdot \rho \cdot \Delta p)} & for \quad \Delta p < -\Delta p_0 \\ A \cdot \sqrt{(\Delta p_0)} \cdot \frac{\Delta p}{4 \cdot \Delta p_0} \cdot \left(5 - \left(\frac{\Delta p}{\Delta p_0}\right)^2\right) & for \quad -\Delta p_0 < \Delta p < \Delta p_0 \end{cases} \tag{59}$$

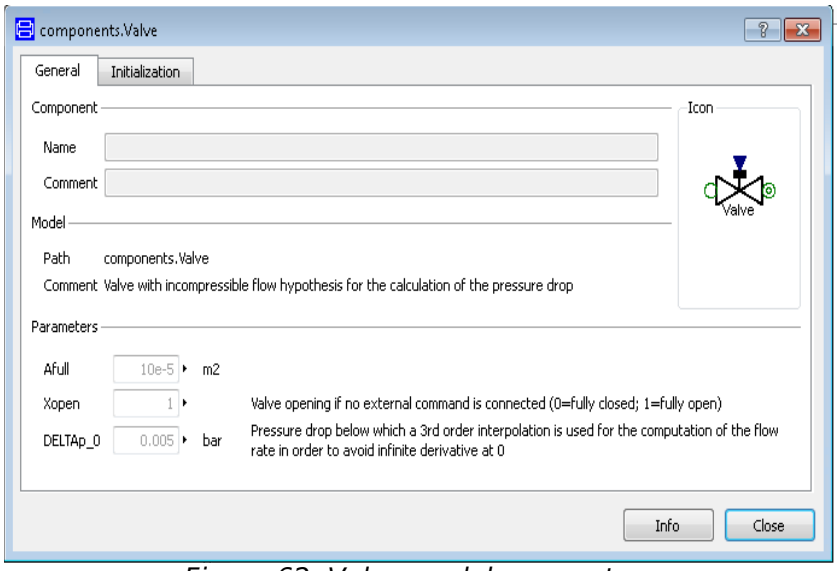

Figure 62: Valve model parameters

where Δp_0 is the minimum pressure drop below which the polynomial is applied instead of the quadratic law. The final model parameters are presented in Figure 62.

4 Conclusions

In this chapter, different models have been proposed, developed and validated.

The experimental campaigns on the different test rigs allowed quantifying the main thermo-physical phenomena influencing the performance of ORC systems and their components. They also allowed pointing out different auxiliary or parasitic phenomena decreasing the cycle efficiency. Starting from that experience, semi-empirical steady-state models have been proposed. These models do not pretend to represent all the phenomena in a deterministic way, but propose a more empirical approach: a single parameter lumps one type of irreversibility in one particular location, even though this irreversibility occurs in the whole component. One parameter is defined for each type of irreversibility. These parameters should then be identified with the experimental results, which was successfully achieved.

The model of the global ORC cycle was obtained by interconnecting the submodels of each component. It was shown that this approach leads to an acceptable error on the prediction of the output power, lower than 10%.

An illustration of the utility of such a global ORC model was then proposed to optimize the working conditions of one particular working point. Efficiency maps were generated to evaluate the performance of the components in part-load conditions.

Steady state models are useful for cycle optimization problems, but they cannot be used to evaluate the cycle performance under highly transient conditions, nor can they be utilized for defining a proper control strategy. Dynamic models of each component have therefore been developed, based on the steady-state models. To ensure the robustness of the simulation, the models have however been simplified: the expanders were model by efficiency curves and the heat transfer and pressure correlations have been simplified. The numerical issues linked to the development of such models have been described and strategies have been developed to propose component models that are robust and efficient enough to be integrated into a more general/complex model of an ORC system.

Chapter 5:

Fluid selection and cycle optimization

Where we cannot invent, we may at least improve

Charles Caleb Colton

Summary. Starting from the experience gained in the experimental campaigns and the steady-state models developed in Chapter 4, this chapter provides more general guidelines for fluid selection and cycle optimization. The first part presents general rules for optimizing ORC cycles within imposed constraints (generally related to the heat source and sink). The second part presents three different fluid selection methodologies. The discussion that follows compares these methodologies and provides guidelines and conditions for their optimal usage. The analysis proposed in this chapter is not constrained to the small-scale ORC systems described in the previous sections.

---

1 Introduction

Selection of working fluids has been treated in a large amount of scientific publications. Most of the time, these works propose a comparison between a set of candidate working fluids in terms of thermodynamic performance and based on a thermodynamic model of the cycle.

Since the optimal working conditions are closely linked to the selected working fluid, an optimization must be performed for each screened medium. The first part of this chapter thus aims at defining guidelines for optimizing the working conditions.

In the second part, state of the art literature regarding working fluid selection is summarized. Two new fluid selection methodologies are then proposed, in an attempt to go one step further: the operating map approach and the thermoeconomic approach.

When selecting the most appropriate working fluid, the following guidelines and indicators should be taken into account:

1. *Thermodynamic performance*: the efficiency and/or output power should be as high as possible for given heat source and heat sink temperatures. This performance depends on a number of interdependent thermodynamic properties of the working fluid: critical point, acentric factor, specific heat, density, etc. It is uneasy to define

an optimum for each specific thermodynamic property independently. The solution consists in simulating the cycle with a thermodynamic model and compare the fluids in terms of cycle efficiency and/or output power.

2. *Positive or isentropic saturation vapor curve*. As previously detailed in the case of water, a negative saturation vapor curve (“Wet” fluid) leads to droplets at the end of the expansion. The vapor must therefore be superheated at the turbine inlet to avoid turbine damages. In the case of positive saturation vapor curve (“Dry” fluid), a recuperator can be used in order to increase cycle efficiency. This is illustrated in Figure 63 with isopentane, R11 and R12.
3. *High vapor density*: this parameter is of key importance, especially for fluids showing a very low condensing pressure (e.g. silicon oils). A low density leads to a higher volume flow rate: the pressure drops in the heat exchangers are increased, and the size of the expander must be increased. This has a non-negligible impact on the cost of the system. It should however be noted that larger volume flow rates might allow the design of turboexpanders, for which the size is not a crucial parameter.
4. *Low viscosity*: a low viscosity both in the liquid and vapor phases is required to maintain high heat transfer coefficients and low friction losses in the heat exchangers.
5. *High conductivity* is required to obtain a high heat transfer coefficient in the heat exchangers.
6. *Acceptable evaporating pressure*: as already stated with water, high pressures usually lead to higher investment costs and increased complexity.
7. *Positive condensing gauge pressure*: the low pressure should be higher than the atmospheric pressure in order to avoid air infiltration in the cycle.
8. *High stability temperature*: unlike water, organic fluids usually suffer chemical deteriorations and decomposition at high temperatures. The maximum heat source temperature is therefore limited by the chemical stability of the working fluid.
9. *The melting point* should be lower than the lowest ambient temperature through the year to avoid the freezing of the working fluid.
10. *High safety level*: Safety includes two main parameters: the toxicity and the flammability. The ASHRAE Standard 34 classifies refrigerants in safety groups and can be used for the evaluation of a fluid[3].
11. *Low Ozone Depleting Potential (ODP)*: The ozone depleting potential is measured with comparison to the ODP of the R11, set to the unity. The ODP of current refrigerants is either null either very close to zero, since

[3] It contains a character (A: Lower Toxicity; B: Higher Toxicity) and a number (1: No flame propagation; 2: Lower flammability; 3: Higher Flammability). For example, HCFC-123 is classified as B1, i.e. higher toxicity – no flame propagation.

non-null ODP fluids are progressively being phased out by the Montreal Protocol.

12. *Low Greenhouse Warming Potential (GWP)*: GWP is measured with comparison to the GWP of CO_2, set to the unity. Although some refrigerants can reach a GWP value as high as 1000, there is no legislation restricting the use of high GWP fluids.
13. *Good availability and low cost*: Fluids already used in refrigeration or in the chemical industry are easier to obtain and more cost-effective.

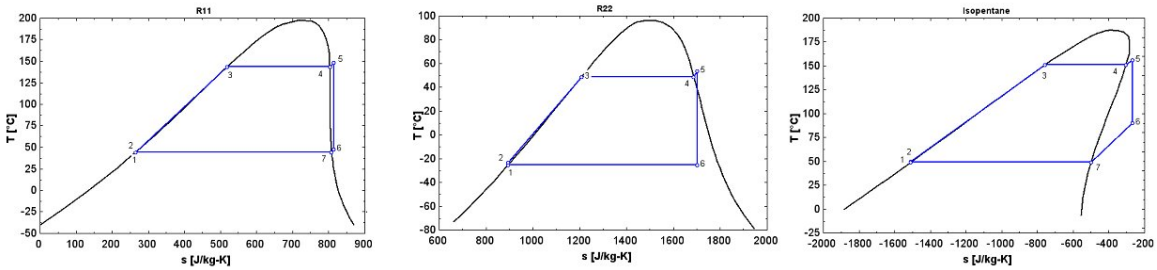

Figure 63: Examples of isentropic, wet and dry fluids

While fluid selection studies in the scientific literature cover a broad range of working fluids, only a few fluids are actually used in commercial ORC power plants. These fluids are the following, classified in terms of critical temperature (Sylvain Quoilin & Lemort, 2009):

HFC-134a:	Used in geothermal power plants or in very low temperature waste heat recovery.
HFC-245fa:	Low temperature working fluid, mainly used in waste heat recovery
n-pentane:	Used in the only commercial solar ORC power plant in Nevada. Other applications include waste heat recovery and medium temperature geothermy.
Solkatherm:	Waste heat recovery
OMTS:	CHP power plants
Toluene:	Waste heat recovery

In general, the selected fluid shows a critical temperature slightly higher than the target evaporation temperature: if the evaporation is taken too far away from the critical temperature – for example if toluene (Tc = 319°C) is evaporated at 100°C – the vapor density is very low in both the high and low pressure sides, which causes high pressure drops and the need for bigger components.

2 Thermodynamic optimization

When optimizing the design of a cycle, it is necessary to list the degrees of freedom available in the system and link them (at least qualitatively) to the operating conditions of the cycle. This topic has already been covered in Chapter 4, by showing the influence of each degree of freedom.

The components thermodynamic interactions highlighted in the case of the ORC prototype using volumetric pump and expander are summarized hereunder:

Mass flow rate. Since the pump is a positive displacement machine, it imposes the volume flow rate. The fluid being incompressible, the mass flow rate is also determined by the pump. It can be adjusted by modifying the swept volume of the pump or varying its rotational speed.

Evaporating pressure. In the case of a positive displacement machine, the absorbed volume of fluid at each revolution is fixed. Since the volume flow rate is imposed by the expander rotating speed, and since the mass flow rate is imposed by the pump, the vapor density is modulated to maintain continuity at steady state. Modulating the density can be achieved by varying the temperature or the pressure. However, in usual working conditions, the relative variation of the temperature (expressed in Kelvin) is small compared to the relative variation of the pressure. The expander supply pressure is thus imposed by the expander rotating speed for a given pump flow rate: reducing the expander rotating speed leads to a higher evaporating pressure. In the case of a turbomachine, the relation is similar: the high pressure is fixed by the opening of the guiding vanes. When these vanes are mobile, the smaller the opening, the higher the evaporating pressure.

Evaporator exhaust superheating. Flow rate and evaporating pressure being set by the pump and the expander, the total heat transfer across the evaporator is determined by the evaporator configuration and by the temperature and flow rate of the hot stream. This heat flux also imposes the superheating at the evaporator exhaust.

Condenser supply temperature. In the absence of recuperator, the condenser supply temperature is the temperature of the fluid leaving the expander. This temperature is imposed by the expander efficiency and by the ambient heat losses of the expander.

Condenser exhaust subcooling. In an ORC cycle, the mass of the fluid in vapor state is negligible compared to that of the liquid. Adding more fluid to the circuit increases the amount of liquid, and increases the level of liquid in the heat exchangers. If the evaporating conditions (pressure, overheating) are fixed, the liquid level in the evaporator remains more or less the same because the fluid requires a fixed heat exchanger area to get evaporated and overheated. In this case, increasing the refrigerant charge will increase the liquid level in the condenser only and increase the subcooling zone in the heat exchanger. The fluid will therefore have more exchange area to become

subcooled. It can then be concluded that the condenser exhaust subcooling is imposed by the refrigerant charge. It should be noted that in most ORC systems, saturation conditions (null subcooling) are obtained by the addition of a liquid receiver after the condenser, which absorbs the refrigerant charge fluctuations.

Condensing pressure. The condenser supply temperature and subcooling are imposed by the expander and by the refrigerant charge, respectively. The condenser heat flow rate is thus imposed. The condensing temperature is fixed by the pinch value (reflecting the heat exchanger effectiveness) and the cooling fluid temperature at the pinch point: decreasing the pinch will lead to lower condensing temperature pressure. The same effect is stated if the cooling fluid temperature is decreased.

Pressure drops. Pressure drops are mainly a function of the heat exchanger geometrical characteristics and of the flow rate.

Optimal operating conditions

The operating conditions and the thermodynamic state of the organic Rankine cycle can be defined by four variables: the evaporating temperature, the superheating at the evaporator exhaust, the condensing temperature and the subcooling at the condenser exhaust. In addition to these variables, supplementary parameters accounting for the irreversibilities in the cycle can be added: expander and pump efficiencies, pressure drops, pinch points.

As a general rule, the following criteria should be fulfilled:

- The condensing pressure should be maintained as low as possible.
- The superheating at the evaporator exhaust should be as low as possible.
- The subcooling at the condenser exhaust should be null or as low as possible.
- The optimal evaporation temperature results of an optimization of the overall efficiency (see below).

Consequently, the main control variable in the cycle is the evaporating temperature since the condensing pressure, the superheating and the subcooling should be maintained as low as possible. Two cases can be distinguished while optimizing the evaporation temperature: a sensible heat source, or a constant-temperature heat source.

Sensible heat source

In this work "sensible heat source" refers to a thermal heat source that is fully exploited if its temperature is decreased down to the ambient (or reference) temperature. This is typically the case for waste heat sources or ICE exhaust gases: the full potential of the heat source is recovered if the temperature of the hot stream is minimum after the heat recovery process. For example, if a hot air heat source at 200°C is recovered by means of an ORC, and if its temperature after heat recovery is 50°C, the ambient temperature being 20°C,

the last 30°C are not exploited, which represents more than 16% of the heat source potential.

This is illustrated in Figure 64, showing the T-s diagram of the cycle in four different cases: Case A corresponds to a small heat source temperature glide, without recuperator; case B corresponds to a high temperature glide in the evaporator, without recuperator ; case C corresponds to a small temperature glide, with recuperator; Case D corresponds to a high temperature glide, with recuperator.

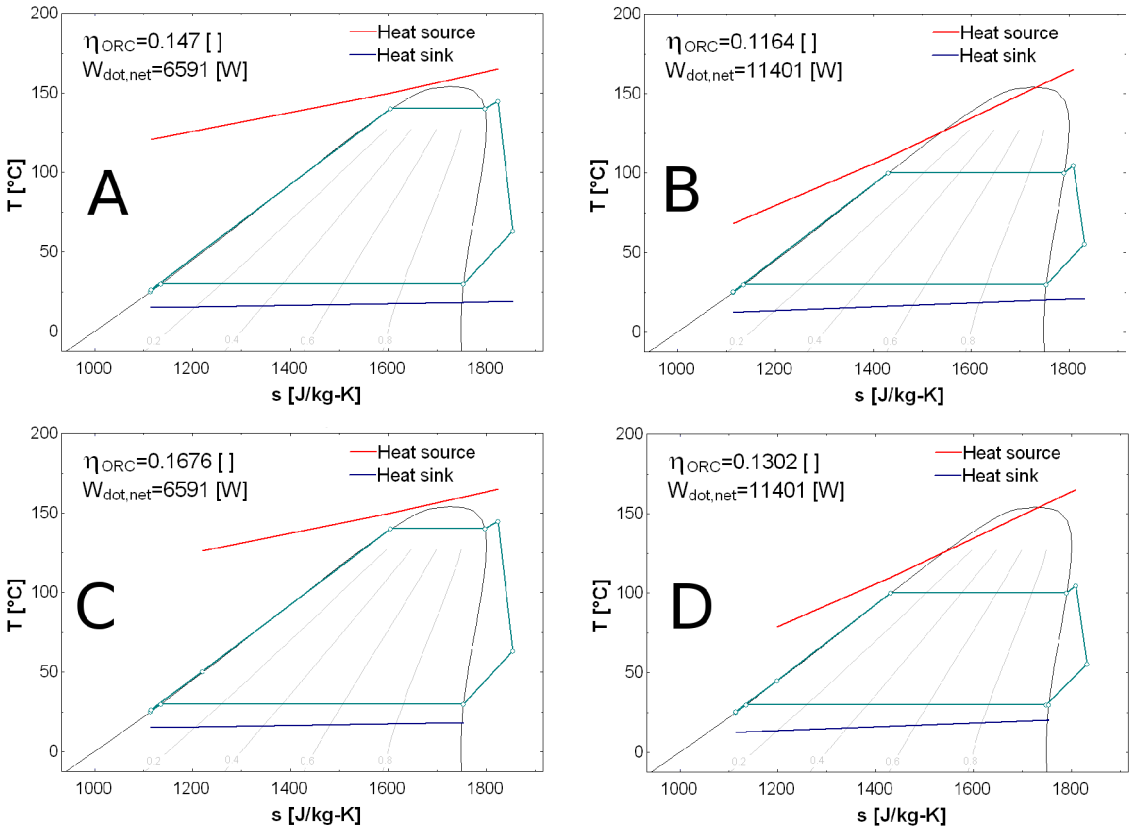

Figure 64: Cycle efficiency and output power for a given heat source and varying working conditions

For the purpose of the example, a heat source consisting of hot air at a temperature of 160°C and characterized by a flow rate of 1 kg/s is imposed. The heat sink is also assumed to be air, whose supply temperature is 10°C, and whose flow rate is adapted to maintain the imposed condensing temperature. The considered working fluid is HFC-245fa. The superheating at the evaporator exhaust is set to 10K, and the subcooling at the condenser exhaust is set to 5K. The pinch points are set to 10K.

In case A, the heat capacity flow rate in the heat exchangers is high. This allows high evaporating and low condensing pressures. Increasing the pressure ratio leads to a higher efficiency. In case B, the temperature glide of the heat source is important and more heat is recovered from the heat stream. The pinch point limitation leads to a lower evaporating pressure and thus to a lower cycle efficiency (11.6% instead of 14.7%), but the amount of heat

recovered is higher and the output power is increased (11.8 KW instead of 6.6 KW).

As a consequence, there exists an optimum evaporating temperature, resulting of a tradeoff between cycle efficiency and heat recovery efficiency. This optimum evaporating temperature is generally much lower than the heat source temperature.

Comparison of cases A,B with cases C, D indicates that the recuperator increases the cycle efficiency, but has almost no impact on the output power. This is explained by the higher working fluid temperature at the inlet of the evaporator, which reduces the amount of heat recovered.

In summary, in heat recovery applications, the output power, and not the efficiency should be maximized; the evaporating temperature should be much lower than the heat source temperature, and a recuperator is not necessary (Case B in Figure 64).

Constant-temperature heat source

In this section, "constant-temperature heat source" refers to a high thermal energy source, such as solar radiative energy or the chemical energy of biomass (combustion). In this case, there is no constraint on the heat source cooling down: there is no need to decrease the temperature of the heat stream in the evaporator, since the total energy content of the heat source flows "through" the ORC cycle. Therefore, optimizing the output power is equivalent to optimizing the cycle efficiency, which can be achieved by selecting a high evaporating temperature, and by installing a recuperator (Case C in Figure 64).

However, the conversion efficiency of the heat source itself can be affected by the temperatures in the evaporator. Depending on the nature of this heat source, an optimal temperature might exist. A solar ORC system is a typical example of such optimum: increasing the temperature leads to higher collector ambient heat losses, but also to a higher conversion efficiency. The choice of the optimum temperature in the collectors/evaporator therefore results of a tradeoff between collector and cycle efficiency.

Degrees of freedom

As stated in the previous section, the condensing temperature is imposed by the heat sink, and the subcooling is imposed by the charge of working fluid or by the liquid receiver. These two parameters can hardly be controlled since the charge is generally not modified in operation and the heat sink conditions are usually imposed by the ambient conditions.

The evaporating temperature and the superheating are controlled by the pump and by the expander: for a given heat source, by imposing a certain pump speed and an inlet volume flow rate on the expander, it is possible to determine both the evaporating temperature and the superheating. In other words, if one of the parameters cannot be controlled (e.g. the turbine inlet

volume flow rate), one cycle working condition (e.g. the superheating) will be floating.

The pump speed is the most commonly controlled parameter in an ORC. The control of the turbine inlet volume flow rate, when present, is defined either by the guiding vane position or by the volumetric expander speed.

3 Working fluid selection: The screening approach

The screening method is by far the most used method for fluid selection in the scientific literature: it consists in building a steady-state simulation model of the ORC cycle and run it with different working fluids. The proposed model can be more or less detailed, and the selected cycle performance indicators can vary from one publication to another.

Table 14 summarizes the scientific literature in the field of working fluid selection for ORC systems: to compare the different papers, three characteristics are taken into account: the target application, the considered condensing temperature and the considered evaporating temperature range. The papers comparing the working fluid performance as a function of the turbine inlet pressure (for example (Hung, 2001)) and not the temperature are excluded since the main limitation in the ORC technology is the heat source temperature and not the high pressure.

Table 14 shows that, despite the multiplicity of the working fluid studies, no single fluid has been identified as optimal for the ORC. This is due to the different hypotheses required to perform the fluid comparison:

- Some authors consider the environmental impact (ODP, GWP), the flammability, the toxicity of the working fluid, while some others don’t.
- Different working conditions (e.g. the considered temperature ranges) have been assumed, leading to different optimal working fluids.
- The objective functions of the optimization might vary depending on the target application: in CHP or solar application the cycle efficiency is usually maximized, while in WHR applications, the output power should be maximized.

It follows that, since no working fluid can be flagged as optimal, the study of the working fluid candidates should be integrated into the design process of any ORC system.

In many studies ((Badr et al., 1990); (W. Gu et al., 2009); (Hung, 2001); (V. Maizza & Maizza, 2001); (Drescher & Brüggemann, 2007); (V. Lemort et al., 2007); (Mago et al., 2008); (Façao et al., 2008); (Desai & Bandyopadhyay, 2009); (Aljundi, 2011) (Vaja & Gambarotta, 2010); (E. H. Wang et al., 2011); (Roy et al., 2011)) , it appears that the recommended fluid is the one with the highest critical temperature, i.e. the plant efficiency could be further improved by selecting even higher critical point working fluids (B.-T. Liu et al., 2004). However, a high critical temperature also involves working at specific vapor

densities much lower than the critical density. This reduced density shows a high impact on the design of the cycle, since the components need to be oversized for two practical reasons:

- Low densities involve high fluids velocities and therefore higher pressure drops. The fluid velocity must therefore be reduced by increasing the hydraulic diameter of the pipes and heat exchangers.
- The size of the expansion machine must be increased to absorb a higher volume flow rate.

This leads to the conclusion that additional criteria must be added to the sole thermodynamic efficiency when comparing working fluids.

Very few studies include additional parameters taking into account the practical design of the ORC system, mainly because of the difficulty to define a proper function for the multi-objective optimization of the cycle. (Lakew & Bolland, 2010) carried out a fluid selection taking into account the required heat exchange area and turbine size. They conclude that the final choice should be driven by economical considerations. It is also worthwhile to note that such studies, when they take into account additional fluid properties, don't lead to the selection of unrealistic working fluids such as a very high critical temperature working fluid for a low-temperature heat source.

Author(s)	Application	Cond. Temp.	Evap. Temp.	Considered fluids	Recommended fluids
(Badr et al., 1990)	WHR	30-50°C	120	R11, R113, R114	R113
(V. Maizza & Maizza, 2001)	n/a	35 – 60°C	80-110	Unconventional working fluids	HCFC-123, R124
(B.-T. Liu et al., 2004)	Waste heat recovery	30°C	150 – 200°C	HCFC-123, iso-pentane, HFE7100, Benzene Toluene, p-xylene	Benzene, Toluene, HCFC-123
(El Chammas & Clodic, 2005)	ICE	55°C (100°C for water)	60 - 150°C (150 – 260°C for water)	Water, HCFC-123, isopentane, R245ca, HFC-245fa, butane, isobutene and R-152a	Water, R245-ca and isopentane
(Drescher & Brüggemann, 2007)	Biomass CHP	90°C *	250 - 350°C*	ButylBenzene, Propyl-benzene, Ethylbenzene, Toluene, OMTS	ButylBenzene
(Hettiarachchi et al., 2007)	Geothermal	30°C*	70 – 90°C	Ammonia, n-Pentane, HCFC-123, PF5050	Ammonia
(V. Lemort et al., 2007)	Waste heat recovery	35°C	60 – 100°C	HFC-245fa, HCFC-123, HFC-134a, n-pentane	HCFC-123, n-pentane
(Saleh et al., 2007)	Geothermal	30°C	100°C	alkanes, fluorinated alkanes, ethers and fluorinated ethers	RE134, RE245, R600, HFC-245fa, R245ca, R601
(Borsukiewicz-Gozdur & Nowak, 2007)	Geothermal	25°C	80 – 115°C	propylene, R227ea, RC318, R236fa, ibutane, HFC-245fa	Propylene, R227ea, HFC-245fa
(Mago et al., 2008)	WHR	25°C	100-210°C	R113, 123, R245ca, Isobutane	R113
(Tchanche et al., 2009)	Solar	35°C	60 – 100°C	Refrigerants	R152a, R600, R290
(Façao et al., 2008)	Solar	45°C	120°C/230°C	Water , n-pentane HFE 7100, Cyclohexane, Toluene , HFC-245fa , n-dodecane, Isobutane	n-dodecane
(Dai et al., 2009)	WHR	25°C	145°C *	water , ammonia , butane, isobutane R11 , HCFC-123, R141B, R236EA , R245CA , R113	R236EA
(Desai & Bandyopadhyay, 2009)	WHR	40°C	120°C	Alcanes, Benzene, R113 , HCFC-123 , R141b, R236ea, R245ca , HFC-245fa , R365mfc, Toluene	Toluene, Benzene
(W. Gu et al., 2009)	WHR	50°C	80-220°C	R600a, HFC-245fa, HCFC-123, R113	R113, HCFC-123
(D. Mikielewicz & Mikielewicz, 2010)	CHP	50°C	170°C	R365mfc, Heptane, Pentane, R12, R141b, Ethanol	Ethanol
(Vaja & Gambarotta, 2010)	ICE WHR	35 °C	96-221 °C	HFC-134a, R11, Benzene	Benzene
(Aljundi, 2011)	n/a	30°C	50-140°C	RC-318, R-227ea, R-113, iso-butane, n-butane, n-hexane, iso-pentane, neo-pentane, R-245fa, R-236ea, C5F12, R236fa	n-hexane
(E. H. Wang et al., 2011)	WHR	27-87 °C	327 °C *	HFC-245fa , R245ca ,R236ea, R141b , HCFC-123,R114, R113, R11, Butane	R11, R141b, R113, HCFC-123, HFC-245fa, R245ca
(Roy et al., 2011)	WHR	n/a	277 °C *	R12, HCFC-123, HFC-134a, R717	HCFC-123

* Max/min temperature of the heat source/sink instead of evaporating or condensing temperature
** The part of the study evaluating supercritical working fluids has not been taken into account.

Table 14: Summary of different working fluid studies

4 Working fluid selection: The operating map approach

In most cases, the selection of the working fluid is linked to that of the expansion machine: selecting a certain type of expander makes the use of a series of working fluids possible while others must be rejected. In the same manner, when a working fluid is selected, not all types of expansion machines are suitable for the imposed working conditions.

Selecting a working fluid and an expansion machine should therefore be performed in the same process.

This method aims at providing a preselection tool for selecting the most suitable combinations of working fluid / expansion machine for a wide range of working conditions typical of ORC systems.

This is achieved by building an operating map of each combination in terms of condensing and evaporating temperatures, taking into account the practical limitations of each expansion machine. The power ranges suitable to each combination are then evaluated.

4.1 Limitations of volumetric expanders

As detailed in chapter 2.4, volumetric expanders are characterized by a built-in volume ratio, which corresponds to the volumetric increase of the pocket in which the fluid is trapped after the suction process. As shown in 4.2.1, over and under-expansion losses can easily be computed by summing an isentropic expansion and a constant-volume expansion:

Isentropic expansion:

$$w_1 = h_{su} - h_{in} \tag{60}$$

h_{in} being the isentropic enthalpy at pressure p_{in}.

Constant volume expansion:

$$w_2 = v_{in} \cdot (p_{in} - p_{ex}) \tag{61}$$

w_2 is positive in case of under-expansion, and negative in case of over-expansion. The total expansion work is then obtained by summing w_1 and w_2.

The internal expansion isentropic efficiency is therefore given by:

$$\varepsilon_{in} = \frac{w_1 + w_2}{\Delta h_s} \tag{62}$$

The maximum internal built-in volume ratio of positive-displacement expander is usually not higher than 5. It is limited by the length of the rotor (bending stresses) in the case of a screw expander and by the number of spiral revolutions in the case of a scroll expander. This is an important limitation since most ORCs operate at much higher volume ratios.

However, allowing a small under-expansion can substantially increase the volume ratio over the expander with a limited penalty on the efficiency. It is

therefore economically viable for volumetric expanders to operate at a slightly lower internal built-in volume ratio than the ideal one.

For this analysis an under-expansion leading to an internal expansion isentropic efficiency of 0.9 is considered as acceptable.

The second main limitation of volumetric expanders is the swept volume. This swept volume is linked to the maximum rotor diameter in the case of screw expanders (about 400mm) or to the maximum spiral height and diameter in the case of a scroll expander.

To determine the boundary working conditions of volumetric expander, it seems reasonable to take profit of the experience acquired for volumetric compressors in the refrigeration field and assume that the absorbed volumetric flow rates of the machine should be similar.

After a screening of the available scroll and screw compressors on the market, the boundaries provided in Table 15 are adopted.

	$\dot{V}_{cp,min}$	$\dot{V}_{cp,max}$	$r_{v,\mathrm{in},max}$	$\varepsilon_{\mathrm{in}}$
Scroll	1.1 l/s	49 l/s	4	> 0.9
Screw	25 l/s	1100 l/s	5	> 0.9

Table 15: Boundary working conditions for the volumetric expanders

The boundary volume flow rates are given in compressor mode, which corresponds to the exhaust volumetric flow rates of the expander.

Since positive displacement machines can absorb a limited flow rate, it is not advisable to run them with low vapor density fluids: the mass flow rate through the expander being low, the output power is reduced. The limitation on the vapor density results of an economical trade-off that is out of the scope of this work. However, the experience gained in the compressor market can be used and transposed to the expander technology.

A new performance indicator, the volume coefficient, is defined as the ratio between the expander volume flow rate and the output power:

$$VC = \frac{\dot{V}_{su,\exp}}{\dot{W}} = \frac{v_{su,\exp}}{\Delta h} \quad [m^3/MJ] \tag{63}$$

A screening of the refrigeration and heat pump applications shows that for a compressor, this ratio (defined with the exhaust volume flow rate) is roughly comprised between 0.25 and 0.6 m³/MJ. For the present work, a maximum value of 0.5 is selected.

4.2 Limitations of the turbine technology

The following developments are applied to the particular case of a 90° IFR radial-inflow turbine, but a similar analysis could easily be transposed to alternatives turbine designs, such as single-stage axial turbines.

It is uneasy to define a firm limit for each turbine parameter since these parameters are sometimes set empirically by the turbine manufacturers, stating that exceeding a certain values reduces the efficiency. Moreover, these boundary values sometimes vary from one manufacturer to another. For the purpose of this work, the selected boundary values are extracted from the scientific literature and from discussions with turbine manufacturers. They should not, however, be considered as absolute constraints. In particular, the current experience and textbooks regarding turbine design do not cover the case of high-expansion ratios with organic working fluids. The ongoing scientific works aiming at addressing this gap (see for example Harinck, Turunen-Saaresti, Colonna, Rebay, & van Buijtenen, 2010) might displace the current boundaries.

A first important limitation of turbines is the maximal allowable tip speed U_2, given by:

$$U_2 = \pi \cdot N \cdot D_2 \tag{64}$$

D_2 being the wheel diameter and N the rotating speed.

As a general rule, a high tip speed is always preferred since it increases the stage specific work. It is however limited by the strength of materials at the wheel periphery. A maximum value of 370 m/s is chosen.

The maximum turbine efficiency is generally well described by its specific speed N_s, given by:

$$N_S = 2 \cdot \pi \cdot N \cdot \frac{\sqrt{(\dot{V}_{ex})}}{\Delta h_s^{0.75}} \quad [rad] \tag{65}$$

Where $\dot{V}_{ex}$ is the exhaust volume flow rate and Δh_s is the isentropic enthalpy drop. Figure 7 in Chapter 2.4.1 shows a typical wheel efficiency curve based on manufacturer data: the given efficiency is the maximum efficiency for a given specific speed, i.e. the efficiency obtained when the ratio U_2/C_s is optimized for the given working conditions, where C_s is the isentropic speed, given by:

$$C_s = \sqrt{(2 \cdot \Delta h_s)} \tag{66}$$

For the present analysis a minimum wheel efficiency of 84% is assumed, which corresponds to a specific speed varying roughly between 0.3 and 0.9 (Figure 7).

This value is in good agreement with Dixon's recommended optimal boundaries for radial turbines, comprised between 0.3 and 1 (Dixon, 2005).

An important limitation of single stage radial inflow turbines is the maximum Mach numbers in both the turbine nozzle and rotor.

The turbine speed triangles are calculated with the following assumptions:

- The degree of reaction is set to 50%
- The ratio between inner and outer wheel diameters is set to 0.3

Choked flow should be avoided in the whole rotor, the critical part being the rotor exhaust (point 3). The Mach number is calculated by:

$$M_3 = \frac{W_3}{C_{sound,3}} \tag{67}$$

W_3 being the relative speed at the rotor exhaust and $C_{sound,3}$ the sound speed at the same place. A maximum Mach number of 0.85 is generally recommended in order to avoid any local choking of the flow in the rotor.

The maximum Mach number in the turbine nozzle constraints the maximum allowable pressure/volume ratio over the turbine. Most turbine manufacturers allow the nozzle flow to be supersonic, but a too high Mach number might decrease the efficiency and should be avoided. For the present analysis, a maximum value of 1.8 is selected.

$$M_2 = \frac{C_2}{C_{sound,2}} \tag{68}$$

The order of magnitude of the tip speed U_2 is usually quite independent from the size of the turbine (Persson, 1990). Micro-scale turbines therefore show a very high rotational speed since D_2 is low in Eq 64. Decreasing the nominal turbine power therefore increases the bearing losses, which can become prohibitive compared to the output power. A maximum rotational speed can therefore be defined: (De Vlaminck, 1988) recommends a maximum speed of 50,000 rpm, while (Sauret & Rowlands, 2011) selected a number of 24,000 rpm. For the present work a value of 50,000 rpm is selected.

Turbines can usually absorb a much higher flow rate than volumetric expanders for a given machine size (i.e. wheel diameter). A limitation on the volume factor, as set for the scroll and screw technologies, is therefore not taken into account for this technology.

A summary of the turbine boundaries is provided in Table 16.

	Minimum Value	*Maximum value*
U_2		*370 m/s*
N_s	*0.30*	*0.89*
M_2		*1.8*
M_3		*0.85*
N		*50000 rpm*

Table 16: Boundary conditions for the radial inflow turbine

4.3 Operating maps

The limitations described in the previous sections can be used to build a map of the allowable working conditions in a T_{ev}/T_{cd} diagram. Figure 65 and Figure 66 show the envelope mapping of the scroll and screw technologies respectively for a few typical ORC working fluids.

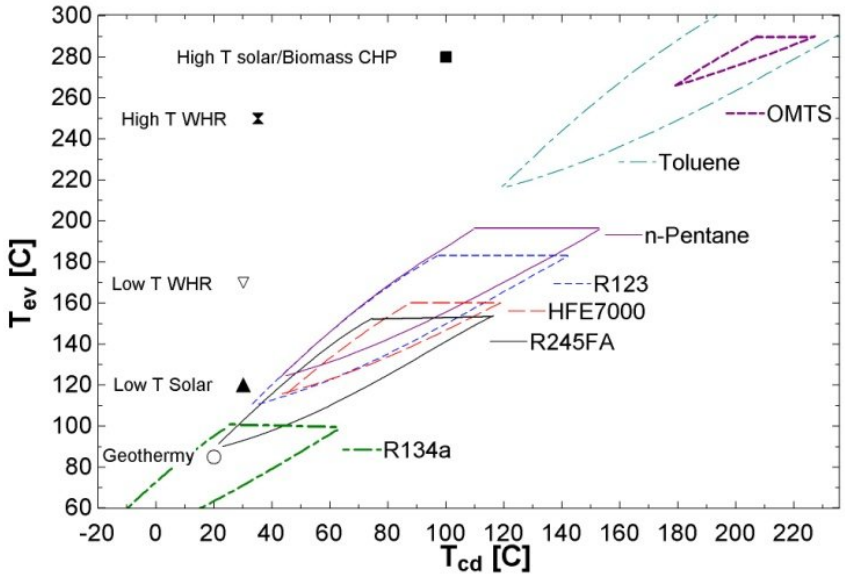

Figure 65: Scroll expander operating map (the top left-hand corner corresponds to a too high expansion ratio, while the down right-hand corner corresponds to a too high volume flow rate)

Five typical ORC applications have been overlaid on the operating maps in the form of dots. They illustrate how the map can be exploited: if a single-stage scroll expander can be used for a low-temperature geothermal application (90/20°C) or even for a low temperature solar application (120°C/30°C), it is not suitable for applications working with higher evaporating temperatures, such low or higher temperature waste heat recovery, or biomass CHP.

It can be noted that the maps of the screw expander are wider than that of the scroll expander. This is due to a higher maximum volume ratio.

The upper left curve of each map is defined by the limitation on the under-expansion losses. The down right curve is defined by the limitation on the volume coefficient, and the upper line is given by the critical temperature of the fluid.

Figure 65 and Figure 66 also show that both volumetric expander types are not adapted to the three higher temperature applications because of a too high volume ratio. The obvious solution in this case would be to assemble several expanders in series.

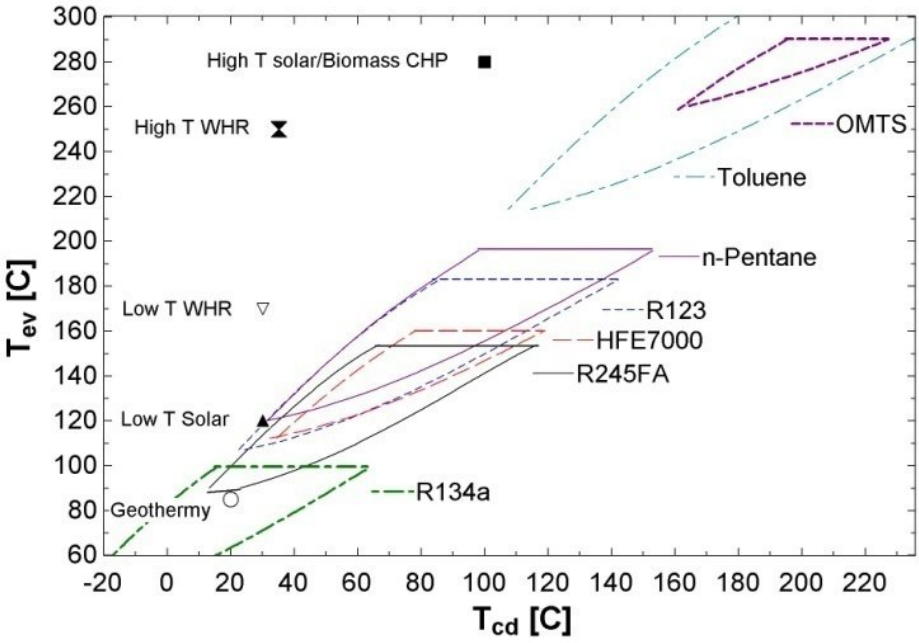

Figure 66: Screw expander operating map

It should be mentioned that no restriction has been defined regarding the maximum allowable temperature at the expander inlet. Refrigeration compressors are usually not operated over a temperature of 150°C. Volumetric expanders using toluene or OMTS might therefore not be feasible due to too high thermal expansion or stresses.

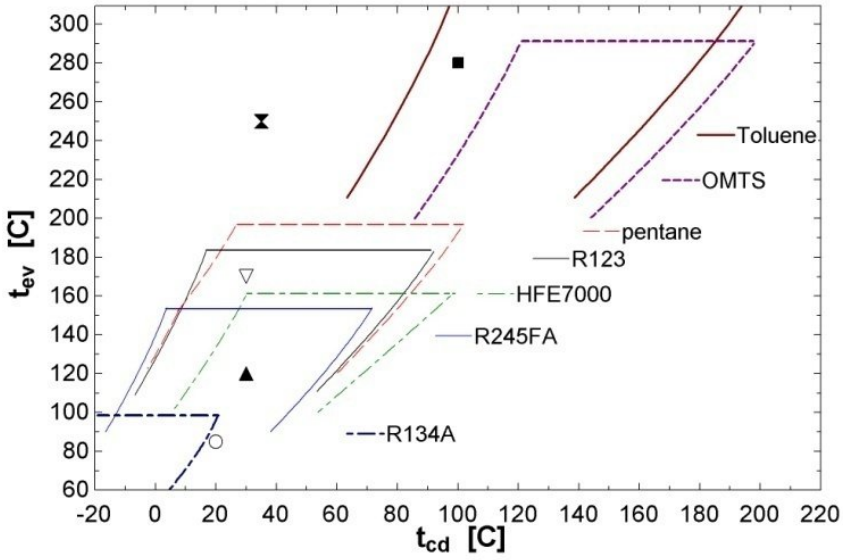

Figure 67: Radial inflow turbine operating map

The mapping of the radial inflow turbine is presented in Figure 67. The right curve of each map corresponds to the maximum specific speed of the turbine. The upper line is defined by the critical temperature since this works only

focuses on subcritical ORCs. The left curve is the limitation on the maximum Mach number at point 2 for Toluene, OMTS and HFE7000 but corresponds to the minimum specific speed for HFC-134a, HFC-245fa, and HCFC-123 and n-pentane.

For all fluids except n-pentane, the maximum Mach number at point 3 was reached before reaching the maximum tip speed U_2. This situation usually occurs with high molecular weight fluids, while the maximum tip speed is usually reached before the maximum Mach number when using air or steam. In the case of pentane, the minimum specific speed curve is split into a lower part (below 150°C) corresponding to M_3=0.85 and higher part corresponding to U_2=370 m/s.

It can be stated that the capabilities of the radial inflow turbine are broader than that of the volumetric expander, since only one of the typical applications is outside the defined maps. For those special conditions corresponding to very high volume ratios, a multi-stage axial turbine technology should be selected.

Each expansion machine technology is adapted to a specific power range. The maximum and minimum volume flow rates as well as the maximum turbine speed can be used to define a power range for each application. This involves selecting a fluid for each one of these applications. Taking into account the previous analysis, the following association is selected: HFC-134a for the geothermal cycle, HFC-245fa for the low temperature solar application and HCFC-123 for the low temperature WHR cycle.

Figure 68 shows the obtained power range for the low temperature application and each expander technology. It is obvious that the scroll technology is the one allowing the lowest output power (a few hundred watts), while the radial inflow is the technology with the highest output power.

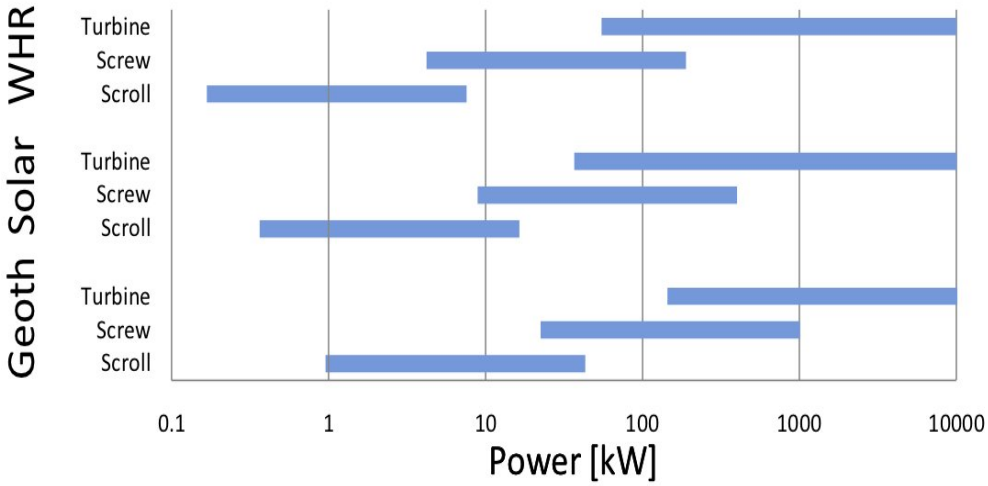

Figure 68: Allowed power range for the low temperature applications and each type of expansion machine

5 Working fluid selection: The thermoeconomic approach

The literature review regarding the "screening" fluid selection method highlighted the need to consider additional criteria to the sole thermodynamic efficiency. This section addresses this statement by proposing a fluid selection based on thermo-economic considerations, rather than on a simple thermodynamic objective function. This approach allows taking into account, through their cost, the effects of working fluid properties, such as the effect of the vapor density on the equipment size.

This method will be described through a practical example. A first thermodynamic optimization will be performed according to the recommendations of Chapter 5.2. The same practical example will then be optimized with the thermoeconomic approach and the results of both methods will be compared.

5.1 Considered WHR ORC

The simple ORC system integrates four basic components: an evaporator, an expander/alternator unit, a condenser and a working fluid pump. In this example, no recuperator is considered since it was shown above that this is not suitable for waste heat to power applications.

The waste heat can be recovered by means of two different setups:

1. Direct heat exchange between waste heat source and working fluid.
2. A heat transfer fluid loop is integrated to transfer the heat from the waste heat side to the evaporator.

In the present study, the heat source is considered to be a generic heat source recovered by a heat transfer fluid (HTF) loop. The considered system with its boundaries is shown in Figure 69.

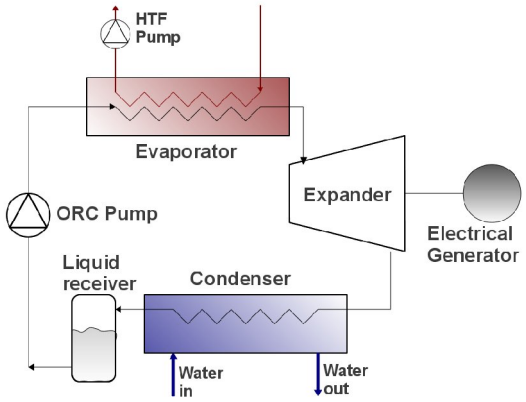

Figure 69: Considered WHR system

The system boundary is the HTF loop (including its circulating pump) and the heat sink, considered to be cold water. Since the methodology proposed in this

work aims at being as generic as possible, the HTF heat exchanger is not considered because this component depends on the application: in some cases, the heat exchanger can already be present in the process, and its size and configuration can vary, depending on the nature of the heat source.

All the heat exchangers are plate heat exchangers. The pump is assumed to be volumetric and the expander is a positive-displacement expander (e.g. scroll, screw).

For the present study, the following assumptions are made:

- The heat source is exhaust gas at 180 °C, with a mass flow rate of 0.3 kg/s. The heat transfer fluid is TherminolVP-1.
- The condenser is cooled with cold water at 15 °C, and a flow rate of 0.5 kg/s.
- The superheating at the expander inlet is 5 K
- The subcooling after the condenser is 5 K

5.2 Considered Working fluids

This method involves performing a numerical optimization for each working fluid. To compare a reasonable amount of working fluids a pre-screening of the fluid candidates is necessary.

According to the previous sections, a certain number of working fluids characteristics can be outlined. Fluids with high critical temperature or high boiling point such as toluene and silicone oils are usually used with high temperature heat sources (typically close to 300°C). Hydrocarbons such as pentanes or butanes and refrigerants such as R227ea, HCFC-123, HFC-245fa, and HFE7000 are good candidates for moderate and low temperatures (typically lower than 200°C).

The pre-selection is performed according to the following criteria:

- The working fluid should have a critical temperature lower than 200°C, since to high critical temperatures lead to low vapor densities.
- The selection criteria described in 5.1 should be fulfilled in an acceptable way. For instance, fluids with a very high ODP (close to 1) are rejected.
- It should be a well-known working fluid in the ORC field, i.e. a fluid that has been previously studied in the scientific literature (cfr. Table 14) or fluids that are used in commercial ORC power plants.

It should be noted that HFC-134a is currently being replaced by HFO-1234yf because of its high Global Warming Potential (GWP). HFE7000 and Solkatherm are announced as replacements for HCFC-123 due to its non-null Ozone Depleting Potential (ODP): the latter is already or will be phased out at the latest in 2030 depending on national legislations. For the present work, it is decided to include the replacement fluids in the analysis as well as the traditional ones to compare their respective performance.

The final selection of working fluid candidates is described in Table 17.

	ASHRAE 34*	GWP	ODP	T_c (ºC)	P_c (bar)
HFO-1234yf	A2	4	0	94.75	33.7
HFC-134a	A1	1300	0	101.1	40.6
HC-600	A3	20	0	152	37.96
HFC-245fa	B1	950	0	154.1	36.4
HFE-7000	n/a	370	0	165	24.8
SES36	n/a	n/a	0	177.6	28.5
HCFC-123	B1	77	0.02	183.7	36.68
HC-601	A3	20	0	196.5	33.64

*ASHRAE Standard 34 – Refrigerant safety group classification. 1: No flame propagation; 2: Lower flammability; 3: Higher Flammability; A: Lower Toxicity; B: Higher Toxicity

Table 17: List of considered working fluids

5.3 Thermodynamic model parameters

To predict the cycle performance, the steady-state models developed in Chapter 4 are used. However, some models are simplified to get rid of some characteristics linked to specific technologies and propose an analysis as generic as possible.

Heat exchangers. In this model, the working conditions are imposed as inputs and the cycle parameters are computed. Therefore, the sizing heat exchanger model developed in section 4.2.2 is used. In single phase, the heat transfer and the pressure are computed according to Thonon's correlation for corrugated plate heat exchangers (Thonon B., 1995). The boiling heat transfer coefficients and friction factors are estimated by the Hsieh correlation (Hsieh & Lin, 2002), established for the boiling of refrigerant R410a in a vertical plate heat exchanger. The condensation heat transfer coefficient is estimated by the Kuo correlation (Kuo et al., 2005), established in the case of a vertical plate heat exchanger fed with R410A.

The imposed parameters of the model are presented in Table 18. All the other parameters are recalculated.

Parameter	Description	Value
D_h	Hydraulic diameter	2 mm
β	Chevron angle	45°

Table 18: Heat exchanger model parameters

Volumetric expander. Losses inside expansion machines mainly include under and over-expansion, friction, leakage, heat transfers and pressure drops. The relative magnitude of each loss type depends on the volumetric expander technology (scroll, screw, reciprocating, etc.). However one type of losses is common to all these technologies, namely the under and over-expansion losses since they all present an internal built-in volume ratio ($r_{v,\text{in}}$).

Therefore, in the expander model developed in chapter 4, only the over and under expansion losses are conserved. The other sources of losses are lumped into one constant electromechanical efficiency η_{mech} :

$$\dot{W}_{\exp} = \dot{M} \cdot (w_1 + w_2) \cdot \eta_{mech} \tag{69}$$

where w_1 and w_2 are the isentropic and constant volume expansion works, respectively.

Since the expansion is assumed adiabatic, the exhaust enthalpy is computed by:

$$h_{ex} = h_{su} - \frac{\dot{W}_{\exp}}{\dot{M}} \tag{70}$$

Since this is a sizing model, for given rotational speed and fluid flow rate, the expander swept volume is recalculated with the following equation:

$$\dot{M} = \frac{\rho_{su} \cdot V_s \cdot N_{rot}}{60} \tag{71}$$

The imposed parameters of the model are presented in Table 19. All the other parameters are recalculated.

Parameter	Description	Value
$r_{v,\text{in}}$	Internal built-in volume ratio	3.4
η_{mech}	Electromechanical efficiency	70%

Table 19: Heat exchanger model parameters

Pumps. Two pump consumptions are taken into account: the heat transfer fluid pump and the working fluid pump. They are modeled by a constant isentropic efficiency. For the HTF pump, the pressure difference is given by the pressure drop in the evaporator while for the ORC pump, it is given by the difference between evaporating and condensing pressures. A constant, realistic value of 60% is assumed for both pump efficiencies (C. Lin, 2008).

Cycle model. The global model of the system is obtained by interconnecting all subcomponent models. Several performance indicators are defined.

The overall heat recovery efficiency:

$$\varepsilon_{hr} = \frac{\dot{Q}_{ev}}{\dot{Q}_{ev,max}} = \frac{\dot{M}_{htf} \cdot \bar{c}_{p,htf} \cdot (T_{htf,su,ev} - T_{htf,ex,ev})}{\dot{M}_{htf} \cdot \bar{c}_{p,htf} \cdot (T_{htf,su,ev} - T_{amb})} \tag{72}$$

The net electrical output power:

$$\dot{W}_{net} = \dot{W}_{\exp} - \dot{W}_{pp} - \dot{W}_{pp,htf} \tag{73}$$

The ORC cycle efficiency:

$$\eta_{ORC} = \frac{\dot{W}_{net}}{\dot{Q}_{ev}} \tag{74}$$

The overall system efficiency:

$$\eta_{overall} = \frac{\dot{W}_{net}}{\dot{M}_{htf} \cdot \bar{c}_{p,htf} \cdot (T_{htf,su,ev} - T_{amb})} = \varepsilon_{hr} \cdot \eta_{ORC} \quad (75)$$

5.4 Thermodynamic optimization

In the present case of an ORC designed for a waste heat recovery application, the thermodynamic optimization should maximize the net power output. This is equivalent to maximizing the overall efficiency since the flow rate and the temperature of the heat source are fixed in Eq. 75. For the purpose of this optimization, the pinch points on the heat exchangers must be imposed. A value of 10K is selected for both the condenser and the evaporator. The pressure drop is set to 100 mbar on the evaporator and to 200 mbar on the condenser.

The optimization is performed in agreement with the guidelines developed in section 4.2 : superheating and condensing temperature are kept as low as possible while the evaporating temperature is optimized. Increasing the evaporation temperature implies several antagonist effects:

- The under-expansion losses in the expander are increased, and its efficiency is decreased
- The heat recovery efficiency is decreased since the heat source is cooled down to a higher temperature. This is shown in Figure 70: the dashed cycle operates at a lower evaporating temperature, and more heat is recovered from the heat source.
- The expander specific work is increased since the pressure ratio is increased.

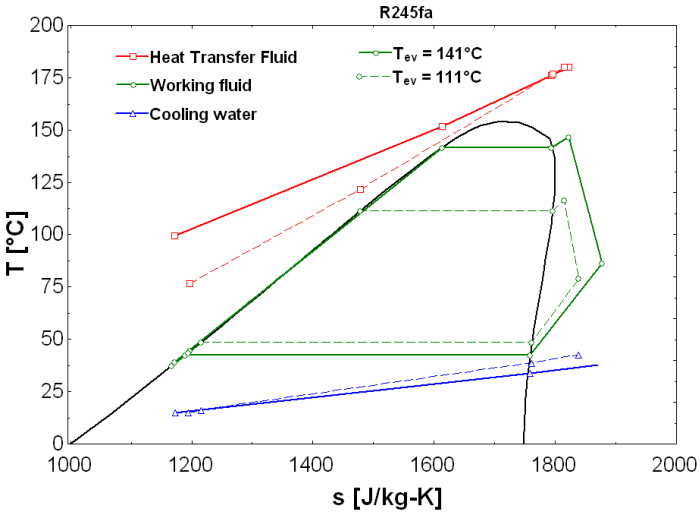

Figure 70: T-s diagram of the cycle for two different T_{ev}

These influences are illustrated for HFC-245fa in Figure 71. For this particular steady-state working point, an optimum evaporation temperature of 113 °C is obtained.

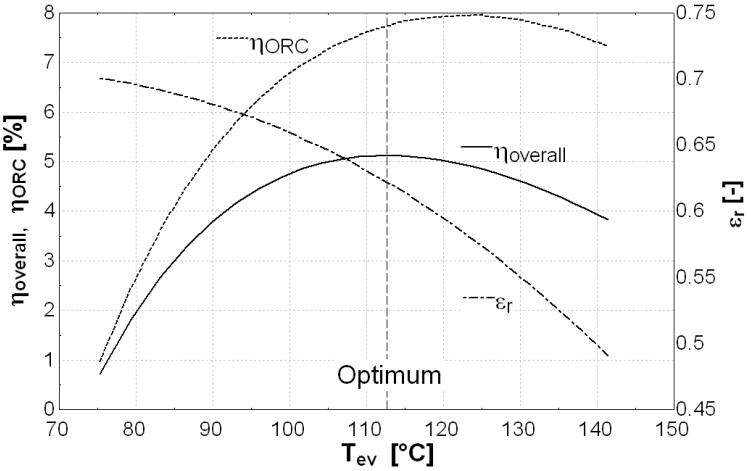

Figure 71: Influence of T_{ev} on the performance indicators

This analysis can be conducted for each candidate working fluid to define their respective optimum evaporation temperatures. The results of this optimization are presented in Table 20. n-butane is the fluid showing the highest overall efficiency, followed by HFC-245fa and HCFC-123. It should be noted that, in the case of HFC-134a and HFO-1234yf, the optimization lead to increase the evaporating temperature up to the critical point. It is therefore obvious that these two fluids are not suitable for the present heat source temperature.

Fluid	T_{ev} [°C]	$\eta_{overall}$ [%]	η_{ORC} [%]	$\dot{W}_{net}$ [W]
HCFC-123	111.8	5.004	8.412	4648
n-butane	114.4	5.222	7.977	4851
SES36	110.4	4.803	7.357	4462
HFE-7000	111.6	4.928	6.857	4577
HFC-245fa	113.5	5.128	7.779	4764
n-pentane	111.6	4.933	8.071	4583
HFC-134a	100.9	3.919	5.193	3640
HFO-1234yf	91.34	2.734	3.616	2540

Table 20: Performance of the different working fluids

5.5 Thermoeconomic optimization

The goal of this section is to propose an alternative optimization for the ORC working conditions: instead of the system efficiency, the selected objective function for this optimization is the specific investment cost (SIC) expressed in €/KWe:

$$SIC = \frac{Cost_{Labor} + Cost_{Components}}{\dot{W}_{net}} \quad (76)$$

Since WHR sources are cost-free by definition, optimizing this parameter is equivalent to optimizing the profitability of the system if maintenance and insurance annual costs are neglected.

In order to obtain the total investment cost, a cost correlation is used for each component of the system and is given in Table 21.

Component	Dependent variable	Cost [€]
Expander	Volume flow rate $\dot{V}_{su,\exp}$ (m³/s)	$1.5 \cdot (225 + 170 \cdot \dot{V}_{su,\exp})$
Heat exchangers	Heat exchange area A (m²)	$190 + 310 \cdot A$
Working fluid pump	Electrical power $\dot{W}_{pp}$ (W)	$900 \cdot (\dot{W}_{pp}/300)^{0.25}$
HTF pump	Electrical power $\dot{W}_{pp}$ (W)	$500 \cdot (\dot{W}_{pp}/300)^{0.25}$
Liquid receiver	Volume Vol (l)	$31.5 + 16 \cdot Vol$
Piping	Pipe diameter d_{pipe} (mm)	$(0.9 + 0.21 \cdot d_{pipe}) \cdot L_{pipe}$
Working fluid	Mass M (kg)	$20 \cdot M$
Miscellaneous hardware	/	300
Control system	/	500
Labor	Total component costs (€)	$0.3 \cdot TCC$

Table 21: Component costs

The cost of the expander is based on the cost of hermetic compressors with the same swept volume. To take into account the lower maturity of the expander technology, the cost of the compressor is multiplied by a factor 1.5. The costs used to establish the correlations for the compressor and the heat exchangers are based on the Belgian prices in 2010.

The pump cost correlation is an exponential expression, proposed by (Bejan et al., 1996). It shows the advantage of requiring cost data for only one pump, and assumes that this cost can be correlated to the nominal power as single input. For the present analysis, the capacity of the liquid receiver is assumed to be constant at 5 liters. The pipe diameter is calculated by imposing the fluid speed to the values recommended in refrigeration applications: $V_{ex,pp} = V_{ex,cd} = 0.6$ m/s; $V_{ex,ev} = 10$ m/s; $V_{ex,exp} = 12$ m/s (Noack, 1999). The lengths of the liquid, low vapor pressure and high vapor pressure lines are assumed to be 3 meters, 1 meter and 1 meter respectively. The total mass of working fluid in the system is calculated by assuming that the two-phase zone in the heat exchangers is half-filled with liquid, and by assuming that one third of the liquid receiver is filled with liquid.

Influence of the working conditions

Contrary to the thermodynamic optimization, the thermoeconomic optimization allows defining more cycle parameters than the sole evaporating temperature: the pressure drops and the pinch points on the heat exchangers

also result from an economic optimum. The influences of these two parameters are straightforward:

- Decreasing the pressure drop requires increasing the total width W_{tot} of the heat exchanger, and therefore its cost. On the other hand, the cycle efficiency is increased which decreases the Specific Investment Cost (SIC).
- A lower pinch point requires a higher heat exchange area, which also increases the cost of the system. On the other hand, the evaporating and condensing pressures are respectively increased and decreased, which increases the output power.

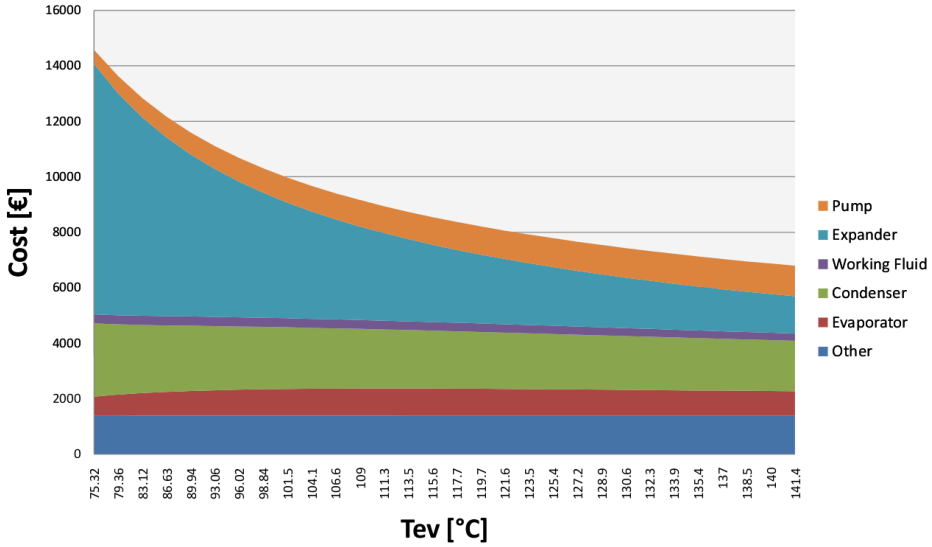

Figure 72: Influence of Tev on the component costs

The influence of the evaporating temperature on the cost is manifold. In general, increasing this parameter increases the vapor density which reduces the pressure drops in the heat exchangers and the required swept volume of the expander. This is illustrated in Figure 72: the cost of the expander decreases with the evaporation temperature, but the cost of the working fluid pump increases since the pressure difference increases. The influence on the cost of the other components is more limited.

Figure 73 shows the evolution of the SIC with the evaporating temperature. A minimum value for the SIC is observed around 136°C for the particular case of HFC-245fa. However, this minimum does not coincide with maximum output power of 4325 W obtained at 128°C. This observation can be extended to other fluids used in this investigation.

The five parameters (P_{ev}, $pinch_{cd}$, $pinch_{ev}$, ΔP_{cd}, ΔP_{ev}) are therefore optimized with the objective of minimizing the SIC. This is done using the simplex algorithm (Kiefer, 1953). Table 22 shows the results of the thermoeconomic optimization for each fluid. As for the thermodynamic optimization, HFC-134a and HFO-1234yf were limited by their critical temperature. For the other fluids, the optimization leads to a much higher optimal evaporating temperature than in the first case (about 25K higher). The optimal pinch point

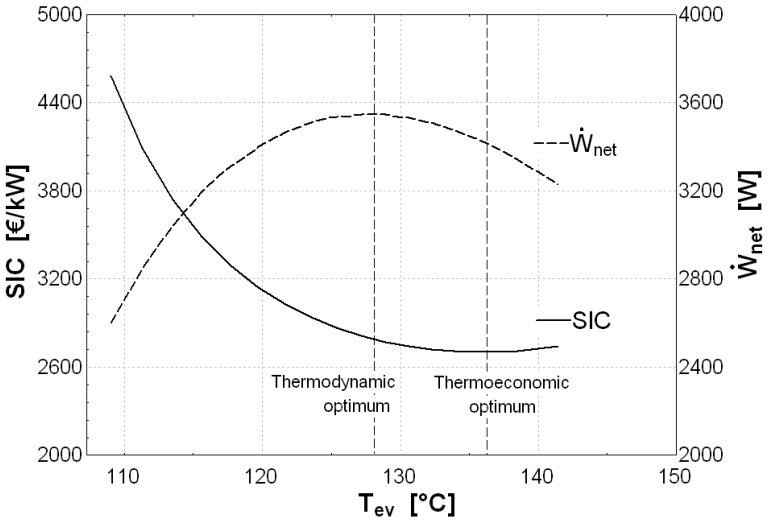

Figure 73: Thermodynamic and thermoeconomic optimums for HFC-245fa

on the evaporator is always below 10K, except for HFC-134a and HFO-1234yf, again because of the critical temperature limitation. It is however much higher on the condenser, with values comprised between 20 and 30K, due to the lower density of the fluid and to higher pressure drops in the low pressure vapor. It is interesting to note that the optimum fluid (n-butane) is the same as in the thermodynamic optimization.

Fluid	T_{ev}	$\eta_{overall}$	η_{ORC}	$pinch_{cd}$	$pinch_{ev}$	ΔP_{cd}	Δp_{ev}	SIC
	°C	-	-	K	K	mbar	mbar	€/kW
HFC-245fa	135.9	3.687	6.964	28.33	7.834	449	261	2700
n-butane	133.2	4.474	7.686	18.31	7.506	357	69	**2136**
HFE-7000	142.4	3.349	6.123	31.84	6.164	297	807	3069
n-pentane	139.9	3.878	8.369	21.81	4	172	146	2505
HCFC-123	141.4	3.427	8.298	30.28	4.967	268	507	2916
HFC-134a	101.1	3.017	5.796	13.47	51.68	527	12	3432
HFO-1234yf	94.42	2.404	5.12	12.1	62.14	398	8	4260
SES36	141.6	3.461	7.137	31.47	4	154	127	2659

Table 22: Results of the thermoeconomic optimization

5.6 Discussion

The thermodynamic optimization leads to the selection of the following working fluids, sorted by overall efficiency (highest efficiency first): n-butane, HFC-245fa, HCFC-123, n-pentane, HFE7000, SES36, HFC-134a, HFO-1234yf. The thermoeconomic optimization leads to the selection of the following working fluids, sorted by Specific Investment Cost (lowest first): n-butane, n-pentane, SES36, HFC-245fa, HCFC-123, HFE7000, HFC-134a, HFO-1234yf. The economical optimum is obtained with a specific cost of 2136 €/kW and an overall efficiency of 4.47%, while the thermodynamic optimum is obtained

with an overall efficiency of 5.22%, corresponding to a higher specific cost of 2448 €/kW.

The following statements can be formulated:

- When optimizing the thermodynamic performance of a WHR ORC, an optimum evaporating temperature exists that maximizes the output power (or the overall efficiency). The optimal evaporating temperature is usually far below the heat source temperature.
- The thermoeconomic optimization leads to the selection of a higher evaporating temperature, because it increases the high-pressure vapor density and decreases the cost of the expander and of the evaporator.
- For the particular working conditions selected for the work, both optimizations lead to the selection of n-butane as optimal fluid. However, the “second-best fluid” differs for both optimization, as well as the next ones. Therefore, if the thermodynamic optimization can give a good idea of the best fluids, it won’t necessarily lead to the selection of the optimal working fluid in terms of economical profitability.

It should be noted that the present work mainly describes a methodology, rather than an accurate economic study for small-scale WHR ORCs: the cost taken into account correspond to the retail price for Belgium, but a large-scale commercialization of such systems could dramatically reduce those costs. On the other hand, some costs were not taken into account, such as the cost of the HTF heating system, because it depends on the target application.

6 Conclusions

This chapter showed how the working conditions of ORC systems can be optimized in different cases. The optimization of the main degree of freedom (the evaporating temperature) was detailed for different applications types.

Despite the large amount of working fluid studies for ORC applications, their conclusions do not lead to one single optimal fluid for a given temperature level and a given application. This is mainly due to the diversity of the selected objective functions when screening working fluids.

Three approaches for fluid selection have been discussed in this chapter:

- Screening of working fluids is by far the most common approach in the scientific literature. A thermodynamic model is built and the working fluid performances are compared in terms of first-law efficiency, output power or generated irreversibilities. The main issue linked to this approach is the objective function, which does not take into account additional fluid properties influencing the practical design of the cycle. This can lead to recommendation of unrealistic working fluids, such as toluene or benzene for a very low temperature heat source.
- The operating map approach focuses on the interaction between expansion machine and working fluid. It provides operating maps of acceptable conditions, i.e. leading to acceptable efficiencies and

acceptable component sizes. Compared to the screening method, it shows the advantage of setting limits on the component size and therefore does not lead to unrealistic working fluids. However, the operating maps of different working fluids are often overlapping. This method must therefore be considered as preselection tool only. It must be followed by a more accurate fluid selection procedure, such as the one proposed by the thermoeconomic approach.

- The thermoeconomic approach is the most efficient method for working fluid selection since it optimizes the economics of the system. However, its implementation is more complex than the two previous methods: a cost function must be assigned to each component and multiparameter optimization algorithms must be used. Due to the high computational effort involved, this analysis can only be performed for a few working fluids. A preselection must therefore be performed.

The advantages and drawbacks of each method are summarized in Table 23.

	Recommended field of application	**Advantages/drawbacks**
Screening	Preselection of working fluids Selection of the working fluid when the cycle layout is already defined	Difficulty to take into account additional factors than the sole thermodynamic efficiency Easy to implement
Operating maps	Preselection of working fluids Co-selection of the pair ORC fluid/Expansion machine	Acceptable boundaries for the working conditions (e.g. expander rotational speed) are set arbitrarily.
Thermoeconomic optimization	Final fluid selection and component sizing	Requires a cost function for each component Multiparameter optimizations are uneasy to implement and time-consuming.

Table 23: Different approaches for working fluid selection

Chapter 6:

Case studies

All technology should be assumed guilty until proven innocent

David Brower

Summary. This chapter illustrates how the models previously developed and validated can be used to predict the performance of different ORC systems. For this purpose, two different prospective ORC units are considered. The first one is a small-scale concentrating solar power system, designed for rural electrification of remote areas. The second is a waste heat recovery system running under transient heat source conditions.

---

1 Prospective study n°1: Solar ORC

1.1 Introduction

Concentrating Solar Power (CSP) systems have been implemented with a variety of collector technologies such as the parabolic trough, the solar dish, the solar tower or the Fresnel linear collector. However, most of the currently installed CSP plants are coupled to a steam Rankine cycle as power block. This technology requires a minimum power of a few MWe to be competitive and involves high collector temperatures.

Solar ORCs have been studied both theoretically (Davidson, 1977; Probert et al., 1983) and experimentally (Monahan, 1976) as early as in the 70s and with reported overall efficiencies varying between 2.52 and 7% (Davidson, 1977, Monahan, 1976, Probert et al., 1983).

Recent studies emphasize optimization of fluid selection for different cycle architectures and collecting temperatures (Bruno et al., 2008, Agustín Manuel Delgado-Torres & García-Rodríguez, 2007, Agustín M. Delgado-Torres & García-Rodríguez, 2010, McMahan, 2006, X. D. Wang et al., 2010, Wolpert J.L. & Riffat S.B., 1996).

Experimental data regarding the performance of solar ORC prototypes are scarcer: M. Kane et al. (2003) studied the coupling of linear Fresnel collectors with a cascaded 9-kWe ORC, using HCFC-123 and HFC-134a as working fluids. An overall efficiency (solar to electricity) of 7.74% was obtained, with a collector efficiency of 57%. X. D. Wang et al. (2010) studied a 1.6 kWe solar ORC using a rolling piston expander. Overall efficiencies of 4.2 % and 3.2%

were obtained with evacuated tube and flat plate collectors respectively. The difference in efficiency was explained by lower collector efficiency (71% for the evacuated tube vs. 55% for the plate technology) and lower collection temperature.

Detailed models of such systems are also rare in the scientific literature: (McMahan, 2006) proposed a detailed model and an optimization of the ORC cycle for solar applications, but this model was not coupled to a solar collector model; (Forristall, 2003) proposed a model of the solar collectors validated with the SEGS plants data, independent of a power cycle model. (Jing, Gang, & Jie, 2010b) developed a model of an ORC cycle using HCFC-123 as working fluid and coupled to CPC collectors: the predicted overall efficiency was about 7.9% for a solar insolation of 800 W/m² and an evaporating temperature of 147°C. E. H. Kane (2002) developed a model of a cascaded ORC using scroll expanders and coupled to a collector model. This model was used to conduct a thermoeconomic optimization on the system.

Most of the above mentioned studies show that the ORC efficiency is significantly improved by inclusion of a recuperator, of cascaded cycles, or of reheating (E. H. Kane, 2002, McMahan, 2006, Prabhu, 2006).

At present, only one commercial solar ORC power plant is reported in the technical literature: the 1 MWe Saguaro Solar ORC plant in Arizona, USA. This plant uses n-pentane as working fluid and shows an overall efficiency of 12.1%, for a collector efficiency of 59% (Canada, 2004).

If medium-scale solar ORCs are already commercially available, work remains to be done for very small-scale units (a few kWe), especially to reduce the specific investment costs and to control the system to avoid the need of an on-site operator.

1.2 System description

Researchers at MIT and University of Liège have collaborated with the non-governmental organization STG International for the purpose of developing and implementing a small scale solar thermal technology utilizing medium temperature collectors and an ORC. A first unit was installed by STG in 2007 (Figure 74).

The goal is to provide rural areas of developing countries with a system that can be manufactured and assembled locally (unlike PV collectors) and can replace or supplement Diesel generators in off grid areas, by generating clean power at a lower levelized cost (Orosz et al., 2010).

At the core of this technology is a solar thermal power plant consisting of a field of parabolic solar concentrating collectors and a vapor expansion power block for generating electricity. An electronic control unit is added for autonomous operation as sub-megawatt scale plants cannot justify the staffing of on-site personnel. Operating at a lower cycle temperatures (<200 °C) is an example of a design tradeoff for maintaining low cost at small scales. For a given level of output power, lower temperatures enable cost savings in the

Figure 74: First solar ORC prototype, installed by STG in Lesotho, 2007

materials and manufacture of the absorber units, heat exchangers, fluid manifolds and parabolic troughs.

Because no thermal power blocks are currently manufactured in the kilowatt range, a small-scale ORC has to be designed for this application. The design is based on modified commercially available components e.g. HVAC scroll compressors (for the expander), and industrial pumps and heat exchangers. It should be noted that the main challenge for ORC development is the high cost of specially designed expander-generator equipment.

The goal of this work is to design and dimension an improved solar ORC unit to be installed in a rural clinic in Berea District of Lesotho and to evaluate its performance with different working fluids. The main characteristics of this unit are the following:

- Target net output power: 3kWe
- Collector field: 75m^2 single-axis parabolic trough, using Miro aluminum reflectors and a Heat Collection Element (HCE) with selective coating and air-filled annulus between absorber pipe and glazing.
- ORC: One or two stage expansion of HFC-245fa using modified commercial HVAC compressors, brazed plate heat exchangers for high pressure heat transfer, and commercial HVAC tubes-and-fins air condenser for heat rejection.
- Heat transfer fluid (HTF): Monoethylene glycol (MEG) with thermal buffering in a thermal storage tank with a 2m^3 packed bed of 19mm quartzite.

The heat transfer fluid is heated up in the collector field and driven to the evaporator by the heat transfer fluid pump. A thermal storage is installed to attenuate the fast fluctuations of solar irradiation during the day and to maintain stable operation of the ORC engine (Figure 75).

In an ORC with a ‘dry’ fluid, recuperation from the superheated exhaust to the subcooled liquid is typically achieved with a recuperator interposed between

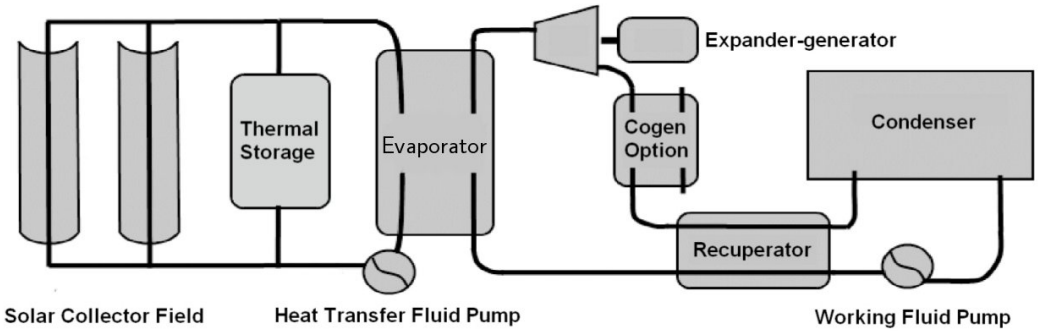

Figure 75: Conceptual scheme of the solar ORC (Orosz, 2010)

the expander exhaust and the pump outlet. This superheated exhaust is also readily exploitable for cogeneration, requiring an additional heat exchanger which can be positioned in series with or parallel to the recuperator.

In the proposed system the cycle heat exchangers (evaporator, recuperator and condenser) are sized to obtain the required pinch point and pressure drop. The working fluid is condensed in an air condenser to avoid unnecessary water consumption (but at the expense of non-negligible fan consumption) and then repressurized in a piston pump. The expansion process is performed by one or two modified HVAC hermetic scroll machines assembled in series. Cogeneration is obtained with the additional plate heat exchanger installed between the expander and the recuperator to produce hot water in addition to electricity, depending on the local demand.

1.3 Modeling

In this section, a steady-state model of the system presented in Figure 75 is developed, for the rating and sizing of the different components and to optimize the working conditions on a nominal point. The transient behavior of the solar source is not taken into account here and an average insolation is utilized. It is assumed that the storage is sized in such a way to maintain almost constant heat transfer fluid flow rate and temperature during the operating time of the system: the ORC engine is assumed to stand by in case of insufficient solar insolation to meet temperature requirements and to avoid part load conditions that might reduce the cycle efficiency. In practice this means that during periods of low insolation, the time to charge the storage to the set operational point is longer than the operating time of the ORC engine. In light of this steady state hypothesis, the storage tank is not modeled. The water heating heat exchanger is also neglected, since the main goal of the model is to evaluate the electricity generation potential of the system.

The solar ORC is modeled within the EES environment: the models developed in Chapter 4 are exploited for the ORC components, a new model is developed for the parabolic trough.

Since a nominal size (or power) must be set, the proposed model is a hybrid between a simulation model and a sizing model: on one hand, the design, the size and the parameters of the collector are set according to the collector

technology developed by STG International and installed in Lesotho. On the other hand, the size of the ORC cycle and of its components is recalculated by the model to obtain a good match between collector power and ORC engine power.

Parabolic Trough Model

The trough module, largely adapted from (Forristall, 2003), is a one-dimensional energy balance model around a Heat Collection Element (HCE) of user specified dimensions and materials: Radiation impinges on a reflector element with user-input focal length, reflective coefficient, and aperture. The energy is correspondingly reduced (e.g. due to a reflective coefficient < 1) and concentrated onto a nodal area of the HCE, where it is transmitted through a glass envelope and a gas annulus, and finally absorbed or reflected at the surface of the HCE.

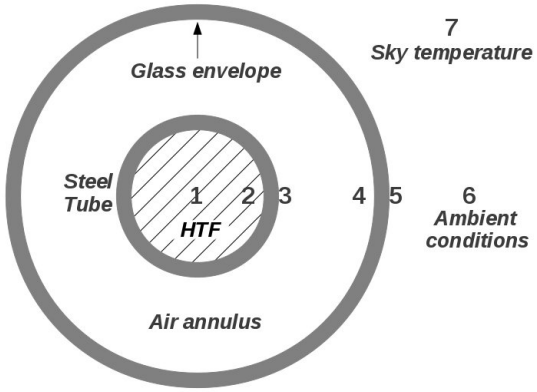

Figure 76: Heat transfer in the absorber

Depending on the absorptivity and emissivity characteristics of the selective coating and the temperature of the HTF flowing through the HCE at a given node, some amount of absorbed energy is transferred through the HCE wall into the HTF (process 2-1 in Figure 76) with a heat exchange coefficient calculated from the fluid thermal properties and flow regime parameters. The remaining absorbed heat is lost at the HCE outer surface, via convection and radiation back through the annulus (3-4), conduction through the envelope (4-5), radiation between the envelope and the sky (5-7) and convection to the ambient air (5-6).

This process is repeated for each node, where the input is the output of the previous node, resulting in an overall enthalpy and temperature gain for the focal line length specified by the user. The collector module thus derives a thermal efficiency and outputs a heat flux and temperature gain for the HTF at the user specified flow rate and initial temperature.

The different heat transfer relations used to compute the heat flows are provided in Table 24.

	Heat transfer type	Heat transfer law
1-2	Convection	Gnielinski correlation for turbulent heat transfer in pipes (Incropera & DeWitt, 2001)
2-3	Conduction	$q_{23}=2\pi k_{23}\frac{T_2-T_3}{\ln(D_3/D_2)}$ q_{23} is the assumed-to-be-constant steel conductivity
3-4	Convection	Hollands correlation for natural convection in an annular space between horizontal cylinders (Hollands et al., 1975).
	Radiation	$q_{34,rad}=\sigma\pi D_3\frac{(T_3^4-T_4^4)}{\frac{1}{\varepsilon_3}+\frac{1-\varepsilon_4 D_3}{\varepsilon_4 D_4}}$
4-5	Conduction	$q_{45}=2\pi k_{45}\frac{T_4-T_5}{\ln(D_5/D_4)}$
5-6	Free convection	Churchill and Chu correlation for laminar convection from a horizontal cylinder (Incropera & DeWitt, 2001).
5-6	Forced convection	Zhukauskas' correlation for external forced convection flow normal to an isothermal cylinder (Incropera & DeWitt, 2001)
5-7	Radiation	$q_{57,rad}=\sigma\pi D_5(T_5^4-T_7^4)$ T_7 is taken 8 degrees below the ambient temperature.

Table 24: Absorber heat transfer model

The amounts of radiation absorbed by the collector and by the glass envelope are respectively given by (Forristall, 2003):

$$q_{sun,3}=q_{sun}\cdot\eta_{opt}\cdot\tau_{env}\cdot\alpha_{coating} \quad (77)$$

$$q_{sun,5}=q_{sun}\cdot\eta_{opt}\cdot\alpha_{env} \quad (78)$$

where $q_{sun}=S\cdot W_{col}[W/m]$ is the linear beam insolation

and:

$$\eta_{opt}=\rho_{mirror}\cdot\eta_{tracking}\cdot\eta_{shadowing}\cdot\eta_{geometry}\cdot\eta_{unaccounted} \quad (79)$$

is the optical efficiency, lumping different sources of losses such as mirror reflectivity (ρ_{mirror}), tracking losses ($\eta_{tracking}$), shadowing ($\eta_{shadowing}$), geometrical effects ($\eta_{geometry}$) and other unaccounted losses ($\eta_{unaccounted}$). The values of the different efficiencies are the ones recommended by Forristall (2003), except for $\eta_{tracking}$ and $\eta_{geometry}$, where a significantly lower efficiency is selected. This conservative hypothesis is made to account for the relatively lower optical intercept factor (~0.9) resulting from the low-cost design of the collector, which could reduce the performance of the system.

To reduce the magnitude of $q_{34,rad}$, a selective coating is applied on the collector tube, maximizing the solar absorptivity and minimizing the infra-red emissivity. This emissivity is calculated according to Forristall recommendation for a "Solar UAV cermet" coating:

$$\varepsilon_{coating} = 2.249 \cdot 10^{-7} \cdot T_3^2 + 1.039 \cdot 10^{-4} \cdot T_3 + 5.599 \cdot 10^{-2} \quad (80)$$

For each cell of the discretized collector (having a length equal to the total focal line length divided by the number of cells) the different energy balance equations can be applied:

$$T_{ex,cell} = T_{su,cell} + \frac{q_{12} \cdot \Delta x}{\dot{M}_{htf} \cdot \bar{cp}_{htf}} \quad (81)$$

$$q_{45} = q_{34,conv} + q_{34,rad} \quad (82)$$

$$q_{56,conv} = q_{45} + q_{sun,5} - q_{57} \quad (83)$$

$$q_{12,conv} = q_{23} \quad (84)$$

$$q_{23} + q_{34,conv} + q_{23,rad} - q_{sun,3} = 0 \quad (85)$$

The pressure drop on the heat transfer fluid can be computed in each cell using the following equation:

$$\Delta p_{cell} = \frac{f \cdot \Delta L \cdot G_{htf}^2}{2 \cdot D_2 \cdot \rho} \quad (86)$$

where f is the friction factor, calculated with the Gnielinski correlation (Incropera & DeWitt, 2001).

Parameter	Description	Value
ρ_{mirror}	Mirror reflectivity	0.94
$\eta_{tracking}$	Tracking error	0.92
$\eta_{shadowing}$	Shadowing error	0.98
$\eta_{geometry}$	Geometry error	0.93
$\eta_{unaccounted}$	Unaccounted losses	0.96
D_2	Absorber tube inner diameter	66 mm
D_3	Absorber tube outer diameter	70 mm
D_4	Envelope inner diameter	80 mm
D_5	Envelope outer diameter	88 mm
L_{col}	Total collector length	46 m
W_{col}	Collector width	2.5 m
τ_{env}	envelope transmissivity	0.96
α_{env}	envelope absorbtivity	0.04
$\alpha_{coating}$	coating absorbtivity	0.96
ε_{env}	envelope emissivity	0.86
N	Number of node	15

Table 25: Collector model parameters

The different parameters used for the modeling of the solar collector are summarized in Table 25.

ORC cycle model

Plate heat exchangers. The plate heat exchangers installed on the system include the evaporator and the condenser. The sizing heat exchanger model developed in Chapter 4.2.2 is used. In single phase, the heat transfer and the pressure are computed according to Thonon's correlation for corrugated plate heat exchangers (Thonon B. 1995). The boiling heat transfer coefficients and friction factors are estimated by the Hsieh correlation (Hsieh & T. F. Lin 2002), established for the boiling of refrigerant R410a in a vertical plate heat exchanger.

The imposed parameters of the model are the hydraulic diameter ($D_h = 2\,mm$) and the chevron angle ($\beta = 45°$).

Scroll expander. The expander selected for the prototype is the hermetic, lubricated scroll expander tested in Chapter 3 and modeled in Chapter 4. However, the present model is a sizing model, i.e. the expander swept volume is recalculated for the imposed working conditions. For that reason, the detailed semi-empirical expander model cannot be used. The polynomial model developed in Chapter 4.2.1 is therefore selected (Eq. 26).

Double-stage scroll expander. As mentioned above, volumetric expanders are optimized for a given specific volume ratio. Specific volume ratios involved in refrigeration for which the scroll compressors are designed is typically much lower than the specific volume ratios involved in ORC cycles. When the expander is obtained from a modified scroll compressor, under-expansion losses can therefore become prohibitive for high specific volume ratios (typically higher than 10). A possible solution consists in using two expanders assembled in series, as shown in Figure 77.

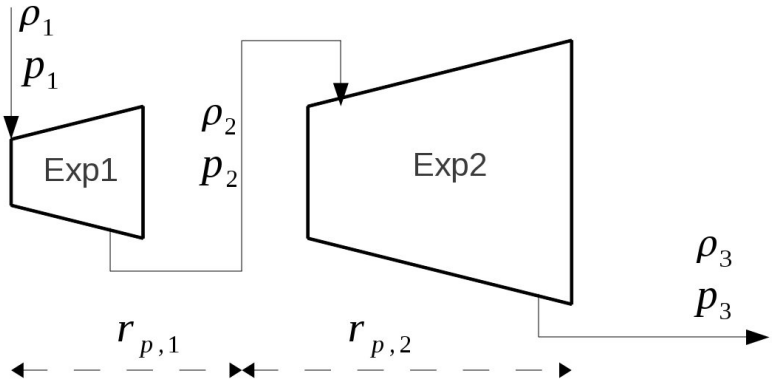

Figure 77: Two-stage expander

When sizing a double-stage expander, it is important to define carefully the two swept volumes in order to optimize the intermediate pressure p_2. If the expander efficiency was only dependent on the pressure ratio, the optimal single-stage pressure ratio would be defined as the square root of the overall

pressure ratio ($r_{p,1}=r_{p,2}=\sqrt{(r_p)}$). However, the efficiency also depends on the flow rate flowing through the expander because a higher flow rate entails a higher output power and makes the constant losses (e.g. friction losses) relatively smaller. In the polynomial correlations, the influence of the flow rate is reflected by the dependence in terms of supply vapor density or pressure.

To determine the optimal first-stage pressure ratio, the overall isentropic efficiency is maximized using the following equation:

$$\frac{d\,\varepsilon}{dr_{p,1}}=\frac{d}{dr_{p,1}}\left[\frac{h_1-h_3}{h_1-h_{3s}}\right]=0 \tag{87}$$

This can be done numerically or analytically. For the latter solution, ε must be expressed in terms of $r_{p,1}$, which can be achieved using the ideal gas hypothesis. The analytical solution of Eq. 87 is obviously more efficient than the numerical one in terms of computational effort. It is derived in Appendix G.

Pumps. Two pump consumptions are taken into account: the heat transfer fluid pump and the working fluid pump. They are modeled by a constant isentropic efficiency. For the HTF pump, the pressure difference is given by the pressure drop in the evaporator and in the collector while for the ORC pump, it is given by the difference between evaporating and condensing pressures. A constant, realistic value of 70% is assumed for both pump efficiencies.

Condenser model. Since air condensers are well-known components in HVAC applications, a simplified model based on manufacturer data (Witt, 2004) is used to compute the condenser performance and fan consumption.

The two inputs are the pinch point, defined as the difference between the condensing temperature and the ambient temperature, and the condensing power.

Special attention is paid to the fan consumption since it can amount for a non-negligible share of the generated power. The fan consumption is computed as a function of the heat transfer power and of the pinch point with the following relation (Witt, 2004) :

$$\dot{W}_{fan,cd}=54.5+0.0185\cdot\dot{Q}_{cd}\cdot\frac{8.33}{pinch_{cd}} \tag{88}$$

Cycle model. The global model of the system is obtained by interconnecting each subcomponent model according to Figure 78.

Several performance indicators can be defined.

The overall collector efficiency:

$$\eta_{col}=\frac{\dot{M}_{htf}\cdot\bar{cp}_{htf}\cdot(T_{htf,ex,col}-T_{htf,su,col})}{S_{beam}\cdot L_{col}\cdot W_{col}} \tag{89}$$

The net electrical output power:

$$\dot{W}_{net}=\dot{W}_{\exp}-\dot{W}_{pp}-\dot{W}_{fans}-\dot{W}_{pp,htf} \tag{90}$$

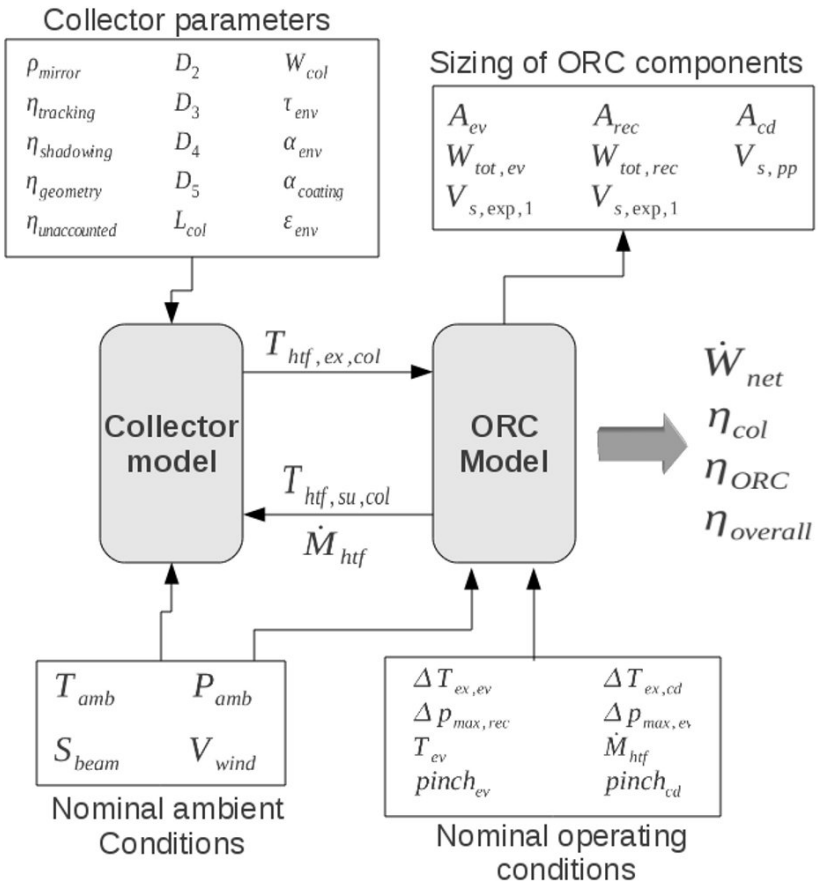

Figure 78: Global model parameters, inputs and outputs

The ORC cycle efficiency:

$$\eta_{ORC} = \frac{\dot{W}_{net}}{\dot{Q}_{ev}} \tag{91}$$

The overall system efficiency:

$$\eta_{overall} = \frac{\dot{W}_{net}}{S_{beam} \cdot L_{col} \cdot W_{col}} = \eta_{col} \cdot \eta_{ORC} \tag{92}$$

In this work, the pinch points are set to 8K, the superheating at the expander inlet is set to 10K, the subcooling at the condenser outlet is set to 5K, and the maximum pressure drop on the refrigerant side of each heat exchanger is set to 75 mbar.

1.4 System performance and fluid comparison

This section aims at understanding the influence of different cycle parameters on the system and to compare several working fluids and cycle architectures. For that purpose, nominal ambient conditions are imposed and kept constant for all the simulations performed below:

- $T_{amb} = 15\,°C$

- $p_{amb} = 0.83\,\text{bar}$
- $S_{beam} = 800\,W/m^2$
- $V_{wind} = 2\,m/s$

These conditions are typical of the mid-season or winter time conditions in the highlands of Lesotho.

Three main degrees of freedom are available to control the working conditions of the cycle: the heat transfer fluid flow rate, the working fluid flow rate and the expander swept volume or rotational speed. Since the superheating should be maintained as low as possible, two working conditions remain to be optimized: evaporating temperature and collector temperature glide.

Influence of the temperature glide in the collector

Modifying the heat transfer fluid flow rate entails different antagonist effects:

- The overall temperature level in the collector is modified (Figure 79), which will impact its thermal efficiency via the various heat loss mechanisms.
- Changing the fluid flow rate affects the heat transfer coefficient between the heat transfer fluid and the absorber, which also impacts the collector efficiency.
- The HTF pump consumption is modified.

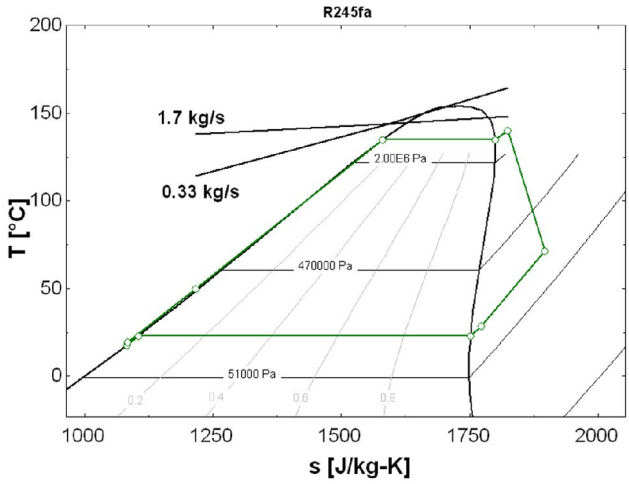

Figure 79: T-s diagram of the ORC process

Figure 80 shows that the second effect is predominant: For very low temperature glides, the overall efficiency is reduced because of the very high HTF fluid pumping consumption. For high temperature glides, the overall efficiency is lowered by the low heat transfer coefficient in the collector. An optimum is obtained for a temperature glide of 15K, corresponding to a heat transfer fluid flow rate of 1.2 kg/s.

In the following parametric studies, the temperature glide value will always be set to its optimal value for each computed working point. This value is obtained with the "Golden Section Search" algorithm.

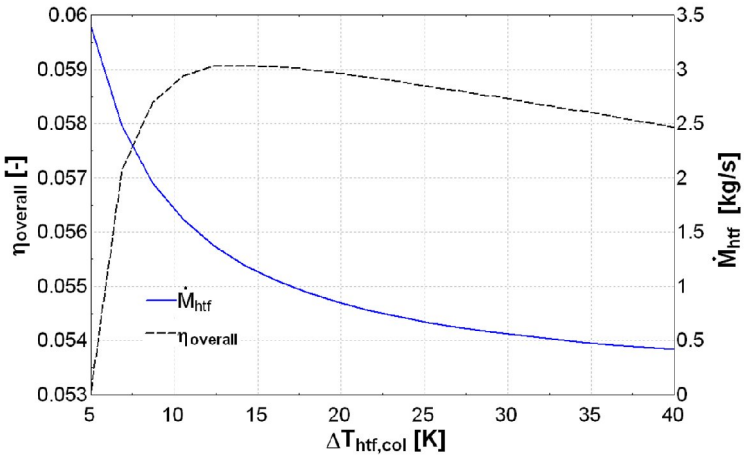

Figure 80: Influence of the HTF temperature glide

Influence of the evaporating pressure

The selection of the optimal evaporating temperature results in a tradeoff between collector efficiency and cycle efficiency. In the particular case of an ORC using volumetric expanders, increasing the evaporation temperature also increases the under-expansion losses and reduces the cycle efficiency, which constitutes an additional influence.

The goal of this section is to illustrate the influence of the evaporating temperature on different cycle parameters and performance indicators. For

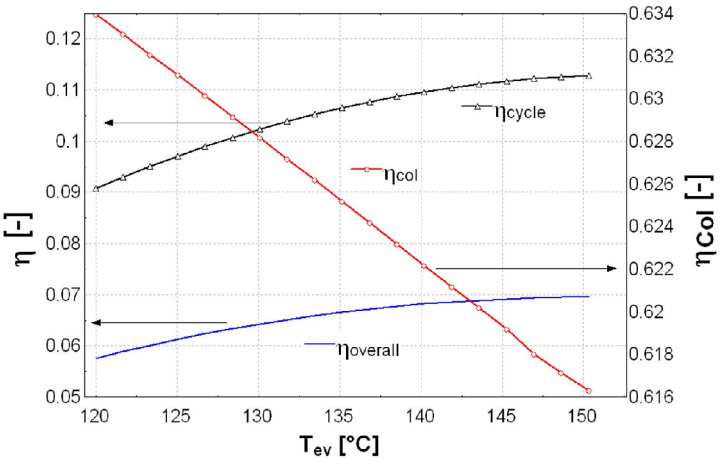

Figure 81: Influence the evaporation temperature on the performance.

that purpose, an arbitrary working point is selected: the selected working fluid is HFC-245fa, with a two-stage expander, an optimized heat transfer fluid temperature glide, a superheating of 5K, and a subcooling of 5K.

As shown in Figure 81, increasing the evaporating temperature leads to higher cycle efficiency and to lower collector efficiency. An optimal overall efficiency is stated around 150°C, which is just below the critical point (154°C for HFC-245fa).

The evaporating temperature also has an impact on the size of the different components. Figure 82 shows that with high evaporating temperature levels, smaller swept volumes are needed for both expanders since the inlet densities are higher. This is an appreciable advantage since the cost of the expanders is reduced.

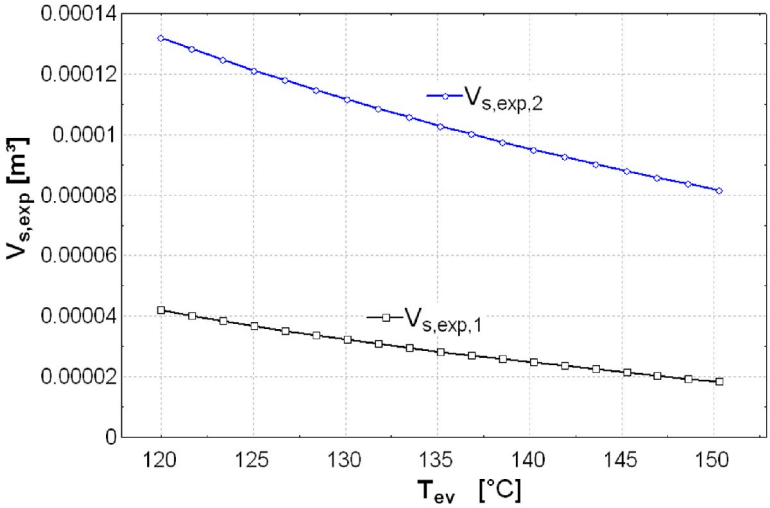

Figure 82: Required swept volumes vs. evaporating temperature.

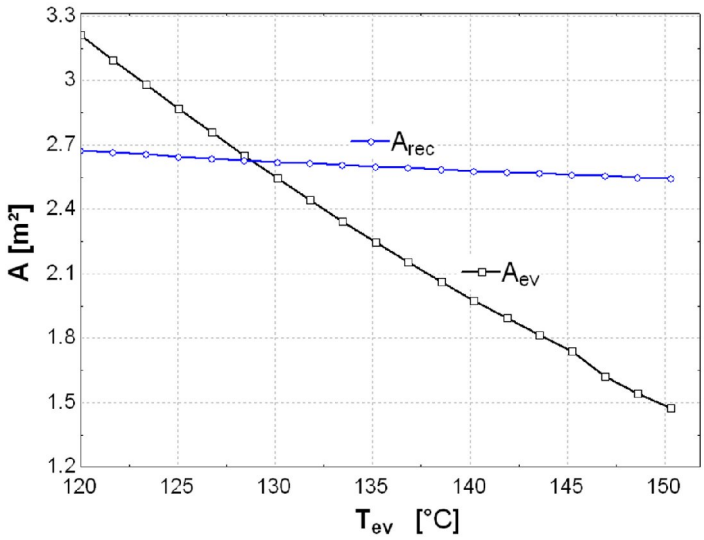

Figure 83: Required heat transfer area vs. evaporation temperature.

A similar effect is stated for the heat transfer area of the evaporator (Figure 83): for a given pressure drop, a higher vapor density allows reducing the

passage area, which in turn reduces the required area. Figure 83 also shows that a modification of the evaporating temperature has a very limited effect on the required recuperator area. Although those calculations were performed for HFC-245fa, a similar behavior is stated for alternative working fluids.

Working fluid and architecture comparison

To compare a reasonable amount of working fluids, a pre-screening is performed. Four fluids are selected for the comparison: HFC-134a, HFC-245fa, Solkatherm (SES36) and n-Pentane.

One of the main influences of the working fluid on the cycle architecture lies in the specific volume ratio: generally speaking, the higher the critical temperature, the higher the specific volume ratio over the expander. The scroll expanders considered in this work are designed for a volume ratio close to 3. As discussed above, when used at much higher specific volume ratios,

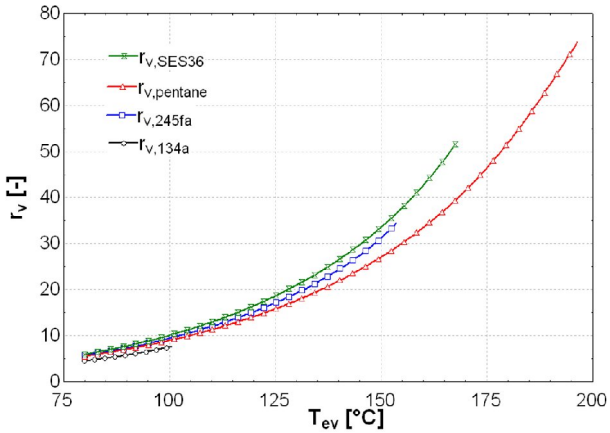

Figure 84: Specific volume ratio vs. evaporation temperature.

their effectiveness is reduced. Figure 84 shows that the specific volume ratio remains acceptable for single stage expansion only for HFC-134a and HFC-245fa (at low evaporating temperature). In the simulations, HFC-134a is therefore used with single-stage expansion architecture. Solkatherm and n-pentane are simulated with a double-stage expansion. HFC-245fa is simulated with both architectures.

Figure 85 shows the overall efficiency of the system with the four different fluids. A maximum appears in terms of evaporating temperature when the single-stage architecture is selected. This is explained by the very high under-expansion losses, which reduce the expander effectiveness at high evaporating temperature. On the contrary, when using a two-stage expansion, the efficiency is limited by the critical temperature or by unrealistic working conditions such as very high specific volume ratios.

Solkatherm is the highest-efficiency fluid, with a maximum close to 8%. It should however be noted that refrigeration compressors are not designed for temperatures higher than 150°C, which might reduce their lifetime. If this

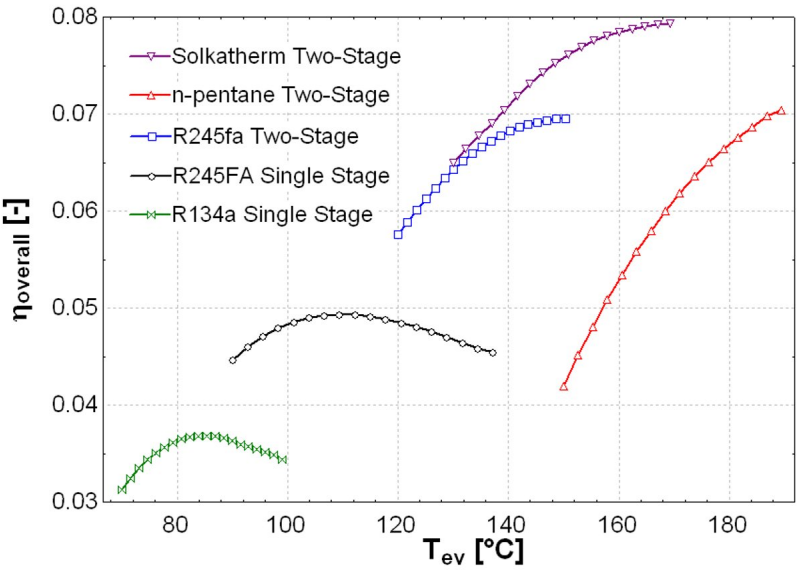

Figure 85: Overall efficiency for different working fluids.

limit is applied, the maximum overall efficiency is 7.5% for Solkatherm and 7% for HFC-245fa.

Additional parameters to the sole efficiency must be taken into account when comparing working fluids. Table 26 shows the more relevant cycle parameters for a few selected optimal points. The bold characters indicate the most advantageous value for each column. If Solkatherm is the most efficient fluid, it is also the one requiring the biggest expander, with a suction swept volume (in expander mode) of 180.7 cm³ for the second stage of expansion and an evaporating temperature of 150°C. HFC-245fa on the contrary shows very advantageous swept volumes, which could reduce the cost of the system. n-pentane must be run at very high temperature to show a good efficiency. Its required evaporator area is advantageous, but the required recuperator area is very high due to the low density and the very high pressure drops in the low-pressure vapor.

	T_{ev}	Δt_{htf}	η_{col}	η_{ORC}	$\eta_{overall}$	ε_{exp}	$V_{s,1}$	$V_{s,2}$	A_{ev}	A_{rec}
	°C	°C	%	%	%	%	cm³	cm³	m²	m²
n-pentane	189	31.6	59.1	11.9	7.0	47.2	22.2	98.9	**0.95**	3.53
SES36	169	19.5	60.4	**13.1**	**7.9**	54.9	27.1	137.3	1.1	**1.24**
SES36	150	14.0	61.6	12.3	7.5	55.0	44.9	180.7	1.71	1.29
HFC-245fa	150	22.9	61.6	11.2	6.9	58.7	**20.8**	**92.8**	1.48	2.54
HFC-245fa	109	12.8	**63.9**	7.7	4.9	50.3	59.9	0	4.02	2.73
HFC-134a	**85**	17.1	65.1	5.6	3.6	**59.7**	37.2	0	2.7	1.53

Table 26: Simulations results for the different working fluids.

Influence of the operating conditions

The developments proposed above were conducted for nominal conditions. However, the selection of these working conditions can have a non-negligible influence on the simulation results.

A parametric study is therefore performed to evaluate the influence of the nominal working conditions on the overall efficiency: this study is performed for the SES36 working fluid and an evaporating temperature imposed at 150°C (third line in Table 26). Figure 86 shows the influence of the wind speed, of the

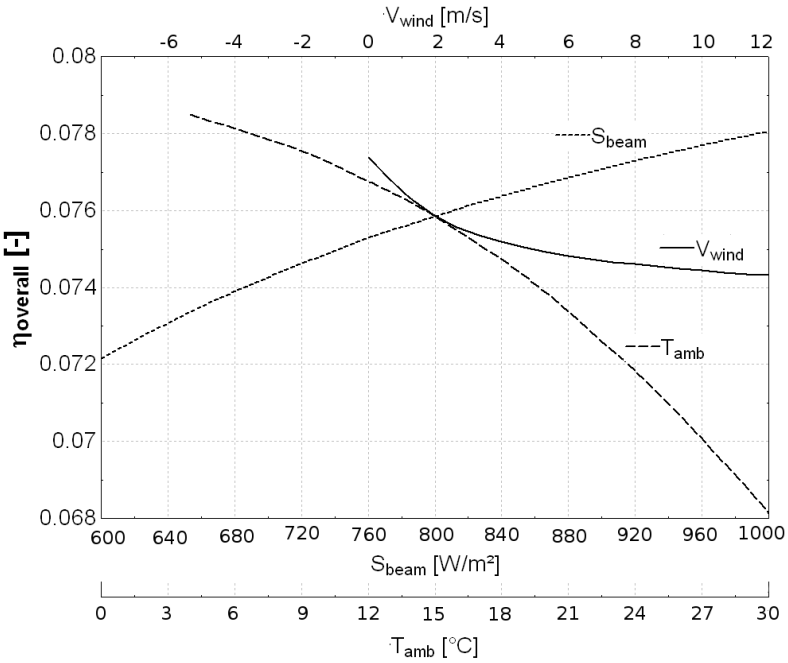

Figure 86: Influence of the working conditions on the efficiency.

ambient temperature and of the solar beam insolation on the system performance. The influence of the wind speed is straightforward: the higher the speed, the lower the overall efficiency since the heat transfer coefficient from the collector to the ambient is increased. The same trend is stated for the beam insolation: a higher value makes the ambient losses of the collector proportionally smaller, and the overall efficiency is increased. The ambient temperature influences the cycle performance in two different ways: the ambient heat losses of the collector are increased with a lower ambient temperature, and the cycle efficiency is increased because of a lower condensing temperature. Figure 86 shows that this second influence is predominant: for a 3 to 30°C variation of the ambient temperature, the collector efficiency is increased by 2%, while the ORC cycle efficiency is decreased by 15%, resulting in a 13% decrease of the overall efficiency.

1.5 Conclusions

Small-scale solar Organic Cycles are well adapted for remote off-grid areas of developing countries. Compared to the main competitive technology, the PV collector, Solar ORCs have the advantage of being manufacturable locally. They are also more flexible and allow the production of hot water as a by-product.

This section focused on the evaluation of the thermodynamic performance of the system. With conservative hypotheses, and real expander efficiency curves, it was shown that an overall electrical efficiency between 7 and 8 % can be reached. This efficiency is a steady-state efficiency at a nominal working point. To evaluate the yearly energy output, a dynamic simulation is needed. In particular, the behavior of the storage tank should be modeled to perform a one-year simulation.

It should be noted that these calculations were performed for off-the-shelf components, especially the expander, whose combined electro-mechanical efficiency did not exceed 60%. Components specifically developed for the target applications (e.g. a high volume ratio expander, optimized for the ORC working fluid) could significantly increase the system performance.

The comparison between working fluids showed that the most efficient fluid is Solkatherm. However, it is also the fluid requiring the highest expander swept volumes, which increases the cost of the system. HFC-245fa also shows a good efficiency and has the advantage of requiring much smaller equipment.

Even though part-load conditions were not simulated in the present work, the proposed model allows computing the performance of the system for a wide range of working and ambient conditions.

2 Transient Waste Heat Recovery Organic Rankine Cycle

2.1 Introduction

The potential for exploiting waste heat sources from engine exhaust gases or industrial processes is particularly promising (J. Wang, Dai, et al., 2009), but these can vary in terms of flow rate and temperature over time, which complicates the regulation of waste heat recovery (WHR) devices.

This section describes a small scale ORC used to recover energy from a variable flow rate and temperature waste heat source. A traditional static model is unable to predict transient behavior in a cycle with a varying thermal source, whereas this capability is essential for simulating an appropriate cycle control strategy during part-load operation and start and stop procedures. A dynamic model of an ORC using volumetric expander is therefore proposed, focusing specifically on the time-varying performance of the heat exchangers, the dynamics of the other components being of minor importance.

This model is then used to optimize the working conditions and to address the issue of the control strategy for variable waste heat sources.

2.2 System description and methodology

Figure 88 shows the conceptual scheme of the considered system. Even though the goal of this section is not to describe a system in particular, but to propose a methodology for optimizing and controlling waste heat recovery ORCs, the parameters selected for the models proposed in the next section correspond to realistic components, typical of small-scale ORCs: The expander is the oil-free scroll expander, described in Chapter 3, the heat exchanger parameters are typical of plate heat exchangers. The pump is a volumetric pump (e.g. a diaphragm pump), whose speed is controlled by means of an inverter. The expander speed is also controlled by an inverter and varies within a reasonable range specified by the manufacturer.

The selected working fluid is HFC-245fa. As aforementioned, fluid selection is an important and preliminary issue in ORC design. However, this selection was already discussed in Chapter 5 and is out of the scope of this section. It is therefore assumed that the study of the optimal working fluid was previously carried out.

The present work focuses on ORCs operating with variable heat sources. A generic variable heat source is thus defined and will be used to validate and to compare different control strategies. This heat source is considered to be hot water under pressure with variable temperature and flow rate, and is described in Figure 87. This heat source could typically correspond to the profile of an internal combustion engine exhaust gases, via an intermediary heat transfer fluid loop.

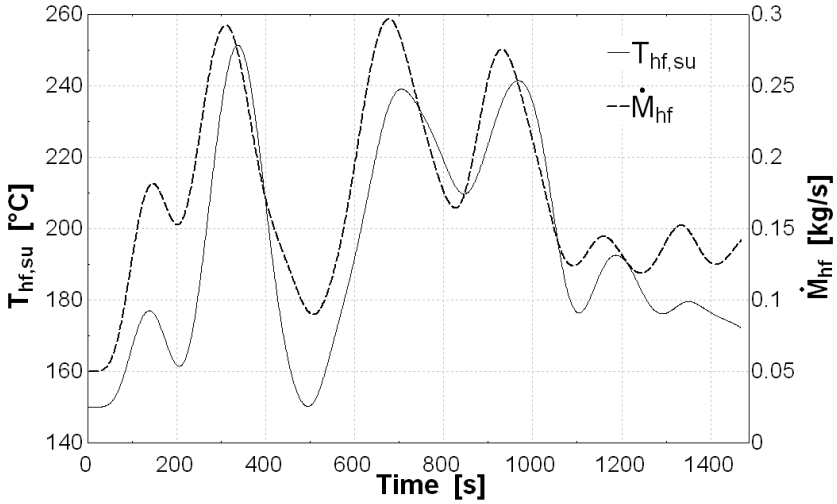

Figure 87: Heat source mass flow rate and temperature

In a real system, heat sink conditions are likely to vary as well, but in a more limited scale. This is simulated by assuming a heat sink with a constant flow rate, but variable temperature:

$$T_{cf,su} = 15 - 5 \cdot \cos\left(\frac{4 \cdot \pi \cdot t}{t_{tot}}\right) \quad [°C] \tag{93}$$

where t_{tot} is the total simulation time, in this case 1469 seconds.

To maximize the amount of energy recovered from this heat source, the working conditions of the ORC should constantly be adapted to the heat source temperature and flow rate. A proper control strategy must therefore be developed. The following methodology is proposed:

1. Static and dynamic models of the cycle are developed (cfr. Chapter 4). The static model analogous to the dynamic model, but with all the time derivatives set to zero.
2. The static model is used to optimize the working conditions of the cycle for a wide range of heat source and heat sink conditions.
3. The optimized working points are used to define a model-based control strategy.
4. The control strategy is implemented in the dynamic model and simulated with the random variable heat source. Its performance is finally compared to alternative control strategies.

In addition to the objective of maximizing the recovered energy, the formation of droplets at the evaporator outlet must be avoided, since it can damage certain types of expanders. A positive superheating must therefore always be maintained by the control strategy.

2.3 Dynamic model

The different subcomponents dynamic models are described in Chapter 4.3. The overall model is obtained by interconnecting them, by connecting pressure, temperature and flow rate sensors and by adding a control unit. The subcomponents models are validated in steady-state (thus with all time derivatives set to zero), however, neither the overall model, nor its dynamics were validated with experimental data. This model is presented in Figure 88. The red lines are used for the secondary fluids (in this case pressurized water), refrigerant lines are presented in green and electrical connection and control wires are presented by dashed, thinner lines.

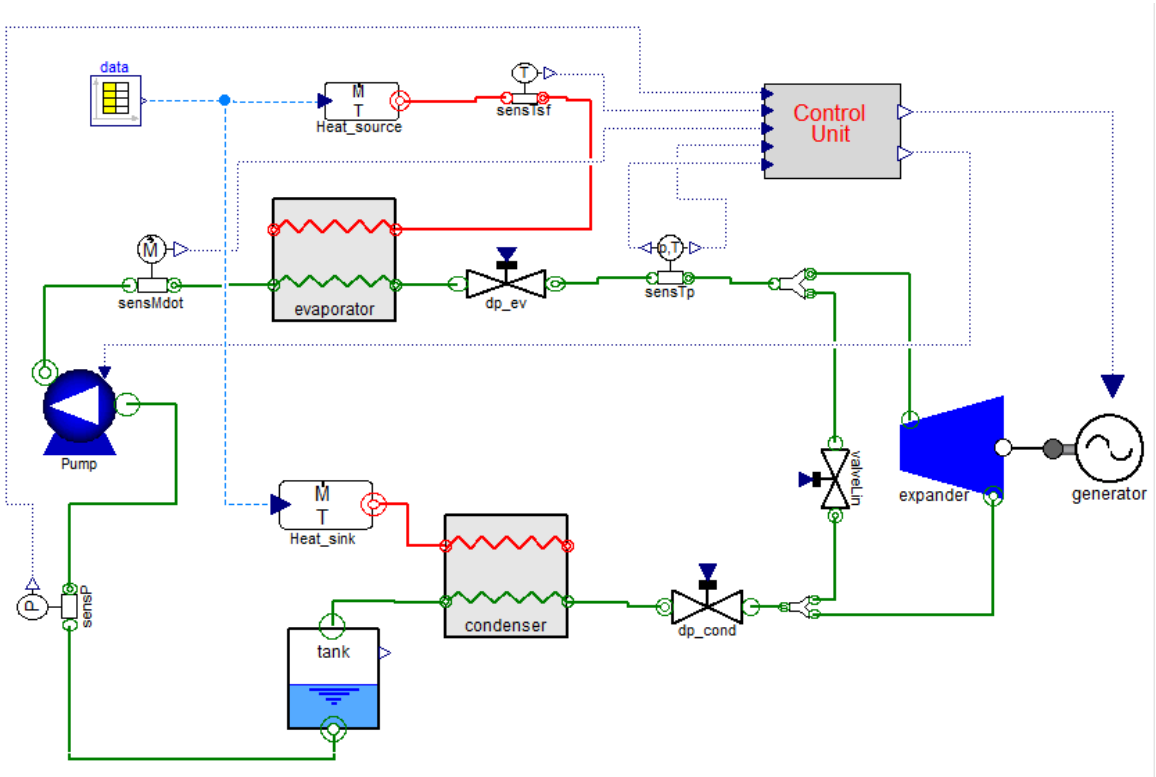

Figure 88: Modelica interface of the dynamic WHR ORC

The different components are:

Evaporator:	Heat exchanger model (cfr section 4.3.1)
dp_ev:	Evaporator equivalent pressure drop (modeled by an equivalent orifice.
sensTp:	Pressure and temperature sensors
ValveLin:	By-pass valve
Expander:	Open-drive expander model (cfr section 4.3.2)
dp_cond:	Condenser equivalent pressure drop
Tank:	Liquid receiver model (cfr section 4.3.3)
sensP:	Pressure sensor
Pump:	Pump model (cfr section 4.3.2)

SensMdot:	Mass flow rate sensor (e.g. coriolis flow meter).
data:	temperature and flow rate data for the heat source and heat sink (Figure 87 and Eq 93)
Heat_source:	Definition of the hot fluid mass flow rate, temperature, specific heat and density as a function of *data*
SensTsf:	Hot fluid temperature sensor.
Control Unit:	Control of the pump capacity fraction and expander speed (detailed in Figure 90)
Heat_sink:	Definition of the cold fluid mass flow rate, temperature, specific heat and density as a function of *data*
Generator:	Ideal synchronous generator. The frequency is set by the Control Unit.

Because of the transient character of the simulation, the performance indicators must be expressed as integrated values.

The net work output:

$$W_{net} = \int_{t_1}^{t_2} (\dot{W}_{\exp} - \dot{W}_{pp})\, dt \tag{94}$$

The cycle efficiency η_{ORC} :

$$W_{net} = \eta_{ORC} \cdot \int_{t_1}^{t_2} \dot{Q}_{ev}\, dt \tag{95}$$

The heat recovery efficiency ε_{hr} :

$$\int_{t_1}^{t_2} \dot{Q}_{ev}\, dt = \varepsilon_{hr} \cdot \int_{t_1}^{t_2} \dot{M}_{htf} \cdot (h_{htf,su} - h_{htf,ref})\, dt \tag{96}$$

$h_{htf,ref}$ being the heat transfer fluid reference enthalpy at 25°C.

The overall energy conversion efficiency is finally defined by:

$$\eta_{overall} = \eta_{ORC} \cdot \varepsilon_{hr} \tag{97}$$

The final cycle parameters are summarized in Table 27.

Parameter	***Description***	***Value***	***Parameter***	***Description***	***Value***
	Evaporator			***Condenser***	
N	*Number of cells*	*20*	N	*Number of cells*	*20*
A	*Heat exchanger area*	*3.078 m²*	A	*Heat exchanger area*	*7.63 m²*
V	*Internal volume*	*3.3 l*	V	*Internal volume*	*9.56 l*

Parameter	Description	Value	Parameter	Description	Value
V_{sf}	Internal volume, secondary fluid	3.3 l	V_{sf}	Internal volume, secondary fluid	9.56 l
M_{wall}	Mass	13 kg	M_{wal}	Mass	30 kg
$\dot{M}_{nom}$	Nominal mass flow rate	0.37 kg/s	$\dot{M}_{nom}$	Nominal mass flow rate	0.37 kg/s
$\dot{M}_{nom,sf}$	Nominal secondary fluid mass flow rate	0.15 kg/s	$\dot{M}_{nom,sf}$	Nominal secondary fluid mass flow rate	2 kg/s
$U_{nom,l}$	Nominal liquid heat transfer coefficient	1072 W/m²K	$U_{nom,l}$	Nominal liquid heat transfer coefficient	425 W/m²K
$U_{nom,tp}$	Nominal two-phase heat transfer coefficient	3323 W/m²K	$U_{nom,tp}$	Nominal two-phase heat transfer coefficient	1453 W/m²K
$U_{nom,v}$	Nominal vapor heat transfer coefficient	1359 W/m²K	$U_{nom,v}$	Nominal vapor heat transfer coefficient	477 W/m²K
$U_{nom,sf}$	Secondary fluid heat transfer coefficient	3855 W/m²K	$U_{nom,sf}$	Secondary fluid heat transfer coefficient	5199 W/m²K
Strategy	Numerical methods	Max der, average _Tcell	Strategy	Numerical methods	Max der, average_ Tcell
A_{dp}	Equivalent pressure drop diameter	3.07 cm²	A_{dp}	Equivalent pressure drop diameter	5.6 cm²
	Tank			**Expander**	
V	Volume	15 l	type	Selected polynomial	Open-drive
	Pump		V_s	Swept volume	1.1e-4 m³
η_{pp}	Pump efficiency	0.7			

Table 27: Dynamic ORC model parameters

2.4 Control strategy

The goal of this work is to define a control strategy for a small-scale ORC working with a heat source that varies in terms of temperature and mass flow.

The first step is to optimize the working conditions of the cycle for a given static heat source. This is done according to the recommendations of section 5.2 : the subcooling and the superheating are reduced to a minimum, and the

evaporating temperature is optimized numerically for given working conditions.

To achieve the optimal working conditions, two degrees of freedom are available, i.e. the pump speed and the expander speed.

It should be noted that the action of these two parameters have very different time constants. A modification of the pump flow rate alters the working conditions of the evaporator and therefore induces a change in the evaporating temperature and/or in the amount of superheating, but with a delay due to the thermal and fluid dynamics of the heat exchanger. In contrast, a modification of the expander speed induces an almost immediate change in the evaporating pressure: the volumetric flow rate absorbed by the device is modified, while the mass flow rate is kept constant; the two flow rates are reconciled through a change in fluid density, mediated via a shift in vapor pressure.

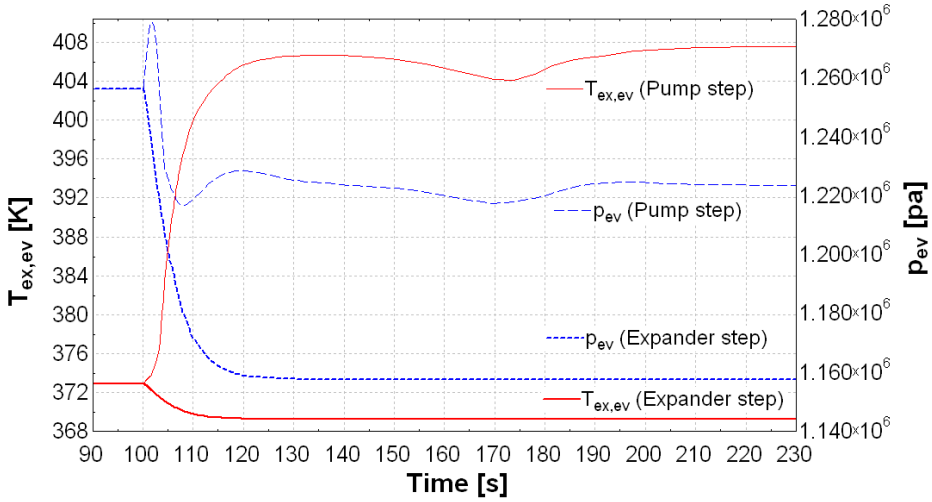

Figure 89: Response of the evaporator exhaust temperature and pressure to a step on the pump speed and on the expander speed

This is confirmed by two simulations whose results are provided in Figure 89: in the first simulation, the ORC model presented in Figure 88 is submitted to a step on the pump flow rate (from 0.55 to 0.44 kg/s) at t=100s. In the second one, the expander speed is submitted to a step (from 3000 to 3600 rpm). Figure 89 shows that the system submitted to an expander step reaches a steady state after 30 seconds. The system under a pump step undergoes major variations during the first 30-40 seconds and then secondary effects appear: the modification of the pump flow rates entails a modification of the temperature, which in turns affects the pressure, etc. This system reaches the steady state after a much longer time period of about 120 seconds.

The evaporating temperature being a more critical working condition than the superheating, it is decided to control the evaporating temperature with the expander speed and the superheating with the pump flow rate.

PI controllers are used to maintain the desired working conditions. The choice of PI controllers over PID controllers is justified by their satisfactory behavior in

the simulations and by the higher sensitivity of PID controllers to measurement noise. The control signal is described by the equation:

$$CS = K_p \cdot \left(b \cdot e + \frac{1}{t_i} \cdot \int (e + track) \cdot dt \right) \quad (98)$$

where e is the error between the present value and the set point, both scaled between 0 and 1, b is the set point weight on the proportional action, K_p is the proportional gain, and t_i is the integral time constant.

The control signal (CS) saturates at 0 and at 1. The variable "track" is defined as the difference between CS and its saturated value, in order to avoid integral windup. K_p, b and t_i are parameters to be tuned. This is done manually, with the aim of minimizing the stabilization time towards a steady state of the system. The following parameters are obtained:

Parameter	Pump PI controller	Expander PI controller
K_p	0.7	2
b	1	1
t_i	2 s	3 s

Table 28: Parameters of the PI controllers

The detailed view of the Control Unit Modelica interface is provided in Figure 90. The different components are described hereunder:

Tev_sp:	Computes the optimal evaporating temperature as a function of the condensing pressure, fluid mass flow rate and heat source temperature
DELTAT:	Computes the saturation temperature and the superheating of the current working fluid using polynomial laws
DELTAT_SP:	Constant value for the set point of the superheating
Initialisation:	Smooth switching between a constant value and the actual control value to facilitate the initialization process (cfr section 4.3.1). Takes as parameter the starting time and the length of the transition.
Const_exp:	Constant initial value for the expander rotating speed
Const_pump:	Constant initial value for the pump flow fraction.
PID:	PID controller (cfr Eq. 98)
CS_freq:	Control signal for the expander frequency
CS_Xpp:	Control signal for the pump flow fraction

Two different control strategies are defined and are described below.

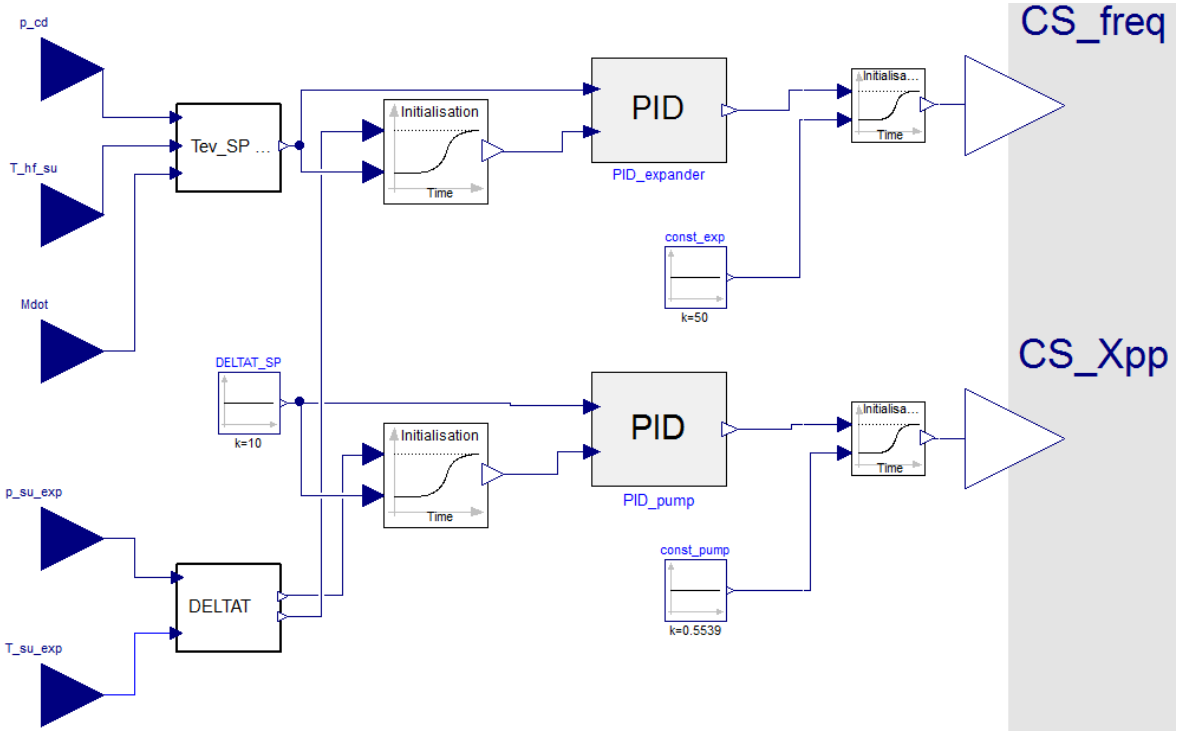

Figure 90: Control Unit of the ORC system

Constant evaporating temperature

The most common control strategy is to define a constant evaporating temperature and superheating. In this case, it is not possible to know a priori which constant evaporating temperature will be optimal for the process. This regulation strategy requires two measurements: $\Delta T_{ex,ev}$ and T_{ev} (Figure 91).

Optimum evaporating temperature

As shown in section 5.2 , an optimum evaporating temperature can be determined for given working conditions. Three inputs are sufficient to determine this evaporating temperature: the condensation temperature, the heat source temperature and the heat source flow rate.

However, it is important to base the control system on variables that are easily measurable. In the systems under consideration, the mass flow rate of the

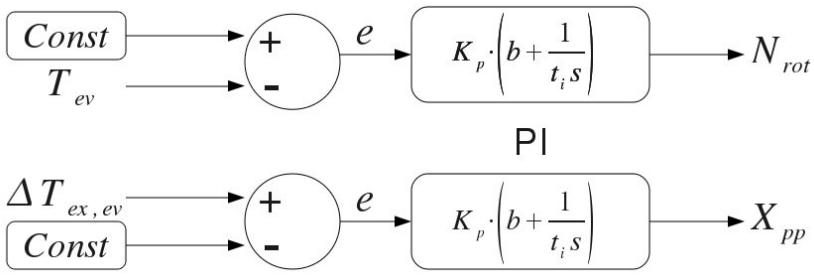

Figure 91: First regulation strategy: constant evaporating temperature.

heat source is difficult to measure in a cost-effective way. On the other hand, the working fluid flow rate is easily accessible, either by direct measurement, or by relation to the pump speed. Since the superheating is fixed, $\dot{M}_{hf}$ can be directly correlated to $\dot{M}_f$, provided that the evaporating temperature and the heat source temperature are known.

The optimal evaporating temperature can therefore be correlated to the heat source temperature, to the condensing temperature and to the working fluid mass flow rate.

To determine this optimum over a broad range of working conditions the dynamic model described above is implemented in steady-state in Engineering Equation Solver (Klein, 2011). The optimum evaporating temperature is determined using the Golden Section Search method for 38 working points and for working conditions varying in the following range:

$$20 \leq T_{cd}\ (°C) \leq 40 \tag{99}$$

$$0.1 \leq \dot{M}_f (kg/s) \leq 0.3 \tag{100}$$

$$150 \leq T_{htf,su,ev} (°C) \leq 250 \tag{101}$$

This range of working conditions is typical of a kW-scaled waste heat recovery ORC working with a heat source varying from 150 to 250°C.

A linear regression is then performed to predict $T_{ev,optim}$. A first order polynomial is preferred to higher order expressions in order to avoid the Runge phenomenon. Due to the quadratic character of the relationship between $T_{ev,optim}$ and $T_{htf,su,ev}$, $\ln(T_{htf,su,ev})$ is used instead. The following relationship is obtained, predicting the optimal evaporating temperature with R^2=93.7%:

$$T_{ev,optim} = 77.6 + 4.93 \cdot 10^{-05} \cdot p_{cd} + 23.8 \cdot \ln(\dot{M}) + 7.65 \cdot \ln(T_{htf,su,ev}) \tag{102}$$

The principle of this regulation is presented in Figure 92.

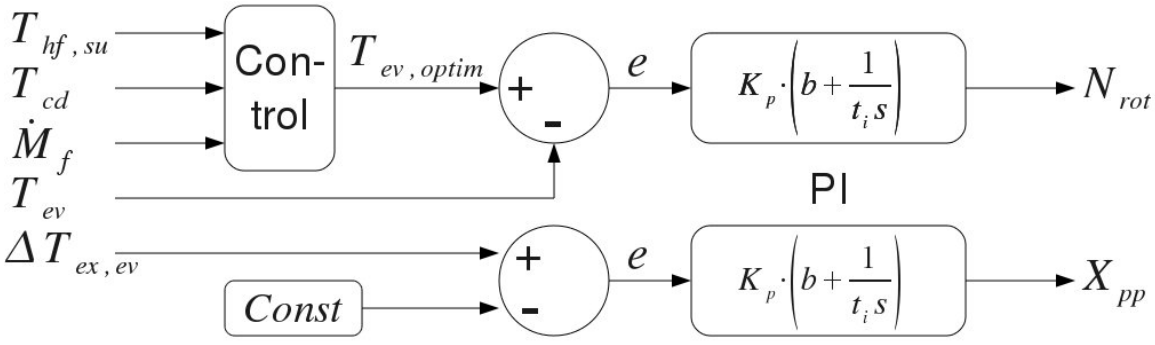

Figure 92: Second regulation strategy: optimal evaporating temperature

2.5 Simulation results

Figure 93 and Figure 94 show the superheating and the evaporating temperatures with their set point for the second regulation strategy. As expected, the evaporating temperature matches its set point temperature

better than the superheating due to the delayed action of a pump flow rate modification.

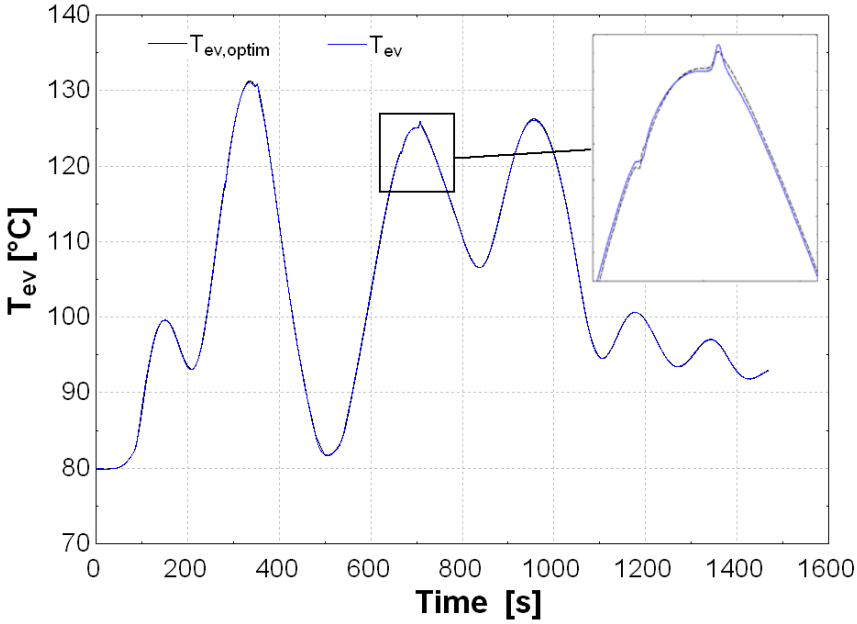

Figure 93: Optimal/actual evaporating temperatures (2nd strategy)

Figure 94 shows however that the control system is able to maintain a positive superheating and therefore avoid the formation of liquid droplets that could damage the expander.

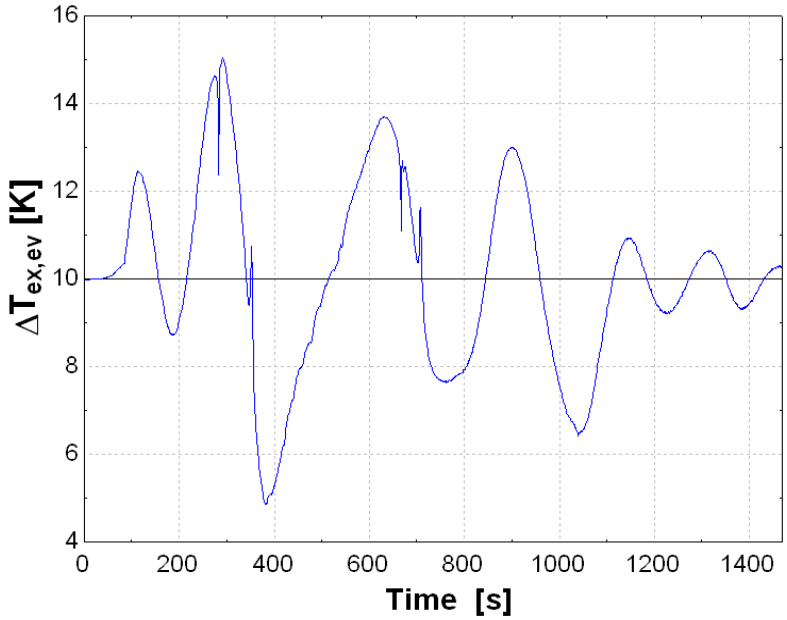

Figure 94: Evolution of the superheating over time (2nd strategy).

Figure 95 shows the expander speed for the different controls strategies. It can be noted than for low evaporating temperatures, the expander speed saturates to its maximum allowed value: the evaporating temperature can no longer be maintained at its set point value by the control system. For T_{ev}=120°C, the expander speed reaches its minimum value during three different time intervals. The optimal evaporating temperature strategy does not load to the extreme values of the rotational speed, and the expander operates in more favorable conditions.

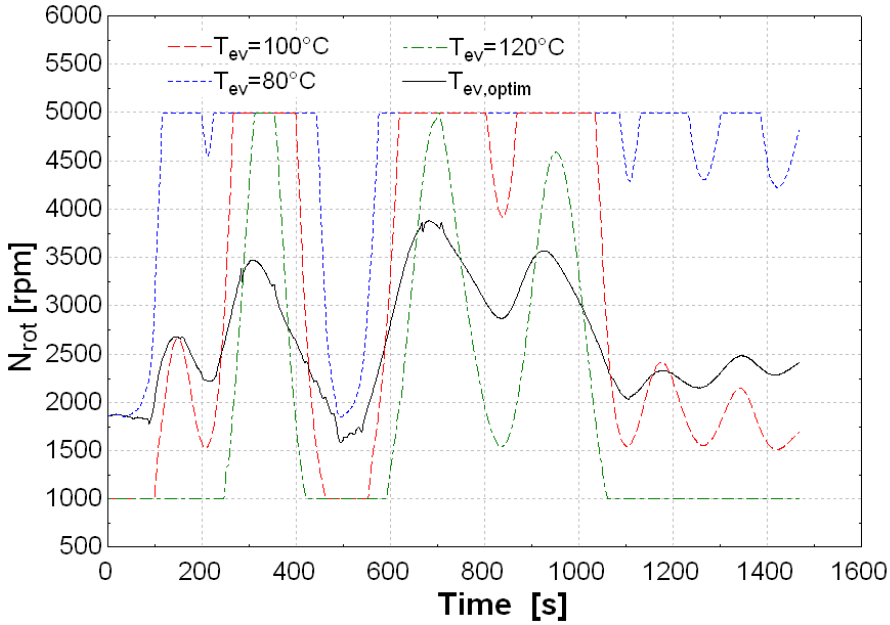

Figure 95: Expander speed for different control strategies.

2.6 Comparison between control strategies

The performance indicators are presented in Table 29 for each control strategy.

T_{ev}	ε_{hr}	$\eta_{overall}$	η_{ORC}
80	0.74	0.0632	0.0856
90	0.73	0.0662	0.0908
100	0.72	0.0665	0.0926
110	0.70	0.0645	0.0916
120	0.69	0.0629	0.0908
$T_{ev,optim}$	0.72	0.0695	0.0970

Table 29: Cycle performance

The optimized evaporating temperature strategy is the one yielding the highest overall efficiency (6.95%). The constant evaporating temperature strategy also shows a good efficiency for 90<T_{ev}<100, but this efficiency decreases sharply for different evaporating temperatures (Figure 96).

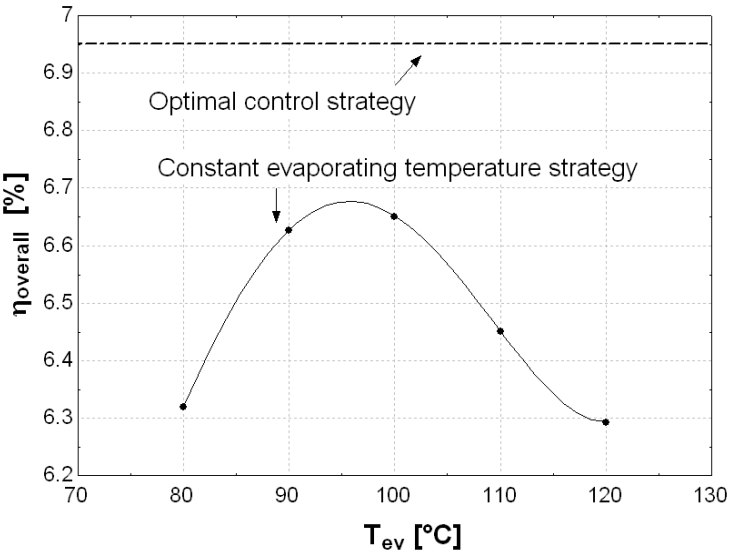

Figure 96: Overall efficiency vs. temperature.

2.7 Conclusions

The simulation results show that small scale ORCs are well adapted to waste heat recovery with variable heat source flow rate and temperature. A proper control strategy must however be defined because cycle performance can drop rapidly. An overall waste heat recovery efficiency of 6.95 % was obtained for the defined heat source.

The control of both the expander and the working fluid pump is required to take the best profit of variable heat sources. Two different control strategies were tested: a constant evaporating temperature and an optimized evaporating temperature depending on the actual working conditions. The best results are obtained with the optimized evaporating temperature regulation. This regulation makes use of a steady state optimization of the system run over a wide range of parameters bracketing the possible working conditions. The drawback of a non-optimized constant evaporating temperature regulation strategy mainly lays in the fact that the ideal evaporating temperature cannot be known a priori.

Chapter 7:

Conclusions

The design of a small-scale ORC system often relies on an optimization process, including a series of tradeoffs regarding the selection of the working fluid, the optimal working conditions or the cycle configuration. This is a non-negligible difference with traditional steam power plants, where the boundaries often result of practical limitations of the materials. The number of degrees of freedom is also higher, among others because of the variety of available working fluids.

This work proposes a step-by-step, multifactorial approach to the design, the modeling, and the optimization of small-capacity low temperature ORC power systems.

As a first step, different prototypes have been developed (an ORC test bench and two scroll expander prototypes). They allowed gaining the necessary experience for the practical operation of such a cycle and pointed out the main issues arising when designing this kind of systems. Reached performance is higher than the one reported in the scientific literature regarding small-scale ORC systems and scroll expanders.

Both the open-drive and the hermetic scroll expanders were tested with a maximum mechanical isentropic effectiveness higher than 71%. However this effectiveness is an electrical effectiveness for the hermetic machine, i.e. including the generator losses. It can be concluded that the hermetic scroll expander is more efficient, mainly because of reduced internal leakage and supply pressure drop. It is also more cost-effective because of its generalized use in HVAC systems. On the contrary, the open-drive machine shows the advantage of not requiring oil in the ORC loop. The main drawback is the necessity to develop a casing to avoid leakages.

A complete model of an ORC cycle has then been developed and validated component by component. This model is suitable for small-scale ORC systems using volumetric expanders. To our knowledge, this work is the first in the scientific literature to propose an entire set of experimental results and the corresponding validated model. A maximum error of 10% was stated between predicted and measured values. The range of validity of the model corresponds to the range of variation of the operating conditions during the experimental campaign. However, the model being based on physically meaningful parameters, the predicted trends outside of the validity range can be trusted with a certain amount of confidence.

The component models illustrate the main interactions in an ORC cycle and thus the main available control variables/degrees of freedom. They are used to size, evaluate the performance and simulate ORC systems. They are also useful to compare working fluids and optimize the thermodynamic conditions. In this work, special attention has been paid to the optimization of the cycle design and of the operating conditions. This optimization can be conducted with different objective functions (e.g. economic profitability, thermodynamic efficiency), or by taking into account practical limitations on the component side, such as the volume ratio imposed to the expander or the component size.

Two prospective studies have finally been proposed to illustrate the utility of the developed model and of the practical guidelines provided in this work. The first one is a small-scale low cost solar ORC to be installed in rural area of developing countries. Using the performance data of the experimental campaigns, it was shown, with conservative hypotheses, that an overall solar-to-electricity efficiency of 8% is reachable.

The second prospective study aimed at addressing the issue of heat recovery with variable heat sources. At the present time, there is indeed no commercially-available ORC system optimized for transient heat recovery. A control strategy involving a limited number of sensors has been proposed and successfully compared to current state-of-the-art control strategies.

The developments presented in this work open a whole area of further research. The models and methods can be adapted to alternative ORC configurations or advanced cycle designs, such as:

- Transcritical or supercritical cycles
- ORCs using zeotropic substances
- Two-phase expansion cycles
- Multiple evaporation pressure cycles
- Superposed cycles

The models themselves could be further refined:

- The influence of the lubrication on the expander and on the heat exchanger should be integrated into the steady-state models
- The turbine model and boundaries should be refined
- The operating maps should be extended to more expansion machines and working fluids
- The dynamic models should be validated in transient conditions

In the same order of idea, the optimal control strategies developed for the particular case of a waste heat recovery system could be further improved, validated and proof-tested on other applications, such as a highly transient solar ORC (i.e. without storage).

Chapter 7: Conclusions

Finally, the different results proposed in this work show that small-scale ORCs are feasible in a technical point of view. The reached efficiencies are low (typically lower than 10%) but this is counterbalanced by the "free" nature of the heat source (e.g. solar radiation, waste heat in industrial process) and by the low cost of the system. More work is needed to evaluate the economic profitability of such small-scale systems, as well as their potential contribution to the current general effort towards sustainable energy conversion.

A Experimental Data

Due to the large amount of Experimental data, the latter is available in electronic form only.

The spreadsheets can be downloaded on the following web page:

http://www.labothap.ulg.ac.be/staff/squoilin/

Or by e-mail request at the following address:

squoilin@ulg.ac.be

The web page also includes a copy of the main models described in Chapter 4, as well as a pdf version of this thesis.

B Adaptation of a hermetic scroll compressor in expander mode

Summary. This appendix describes the practical steps for the conversion of a hermetic scroll compressor into an expander. The scroll machine is an axially and radially compliant device with a floating seal system.

The eccentric motion and the design of scroll machines (Figure 97) allows them to run as a compressor or as an expander without major design adaptation. The main interventions performed on the device are listed below.

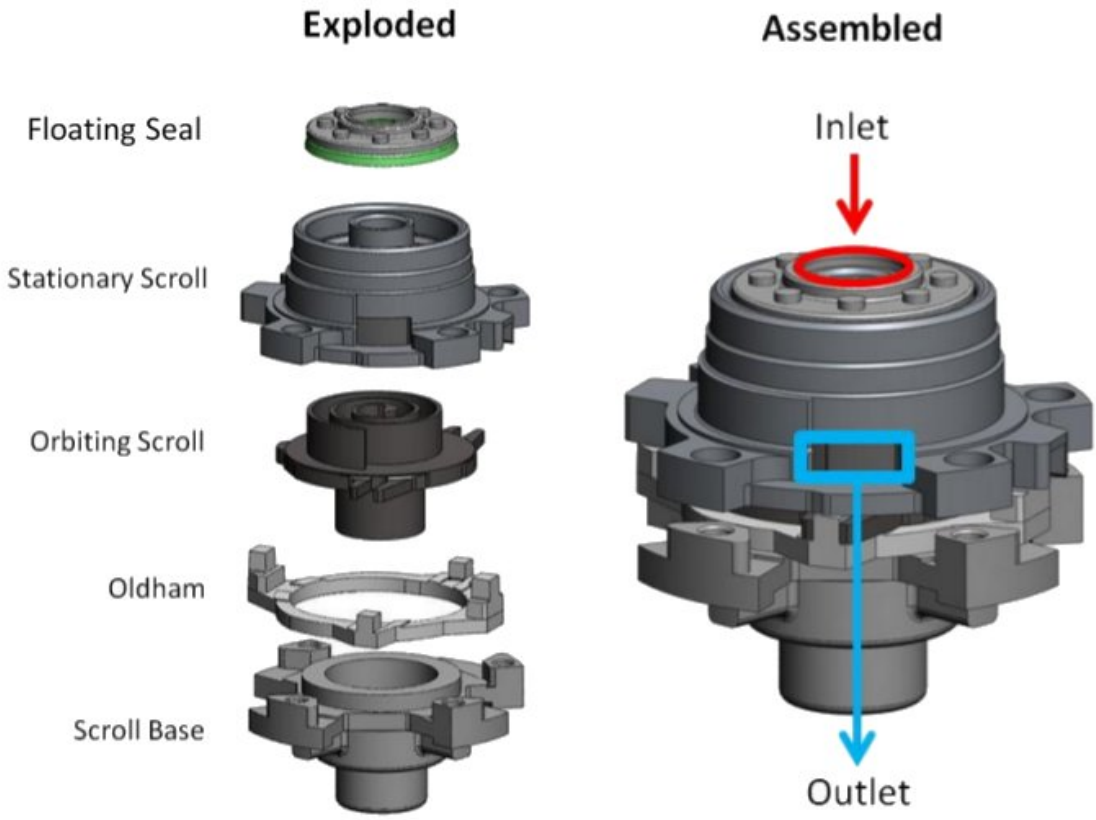

Figure 97: Exploded and assembled view of the scroll elements (Adapted from Harada, 2010)

Installation of flanges

To perform the required modifications, the compressor casing is opened (below the inlet port), and flanges are welded on both parts. The flanges are connected with bolts and the tightness is ensured by an O-ring seal (Figure 98).

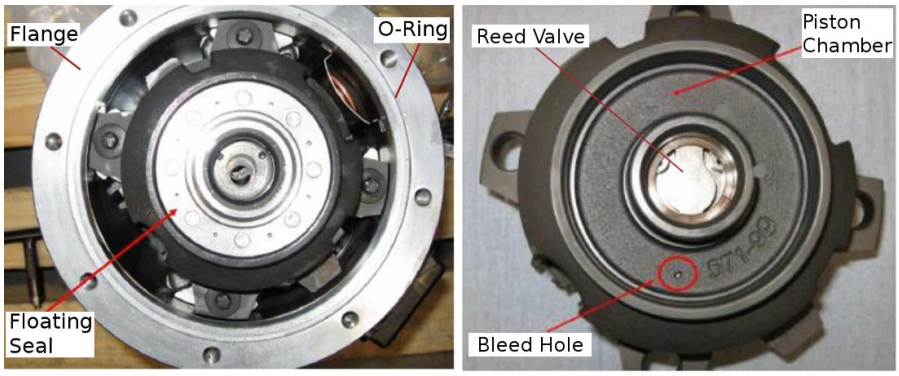

Figure 98: Stationary scroll. Left: inside the casing with the floating seal. Right: without floating seal

Removal of the check valves.

Two check valves are removed:

- The check valve in the compressor outlet (expander inlet in Figure 99).
- The reed valve in the discharge port (in compressor mode) of the stationary scroll (Figure 98).

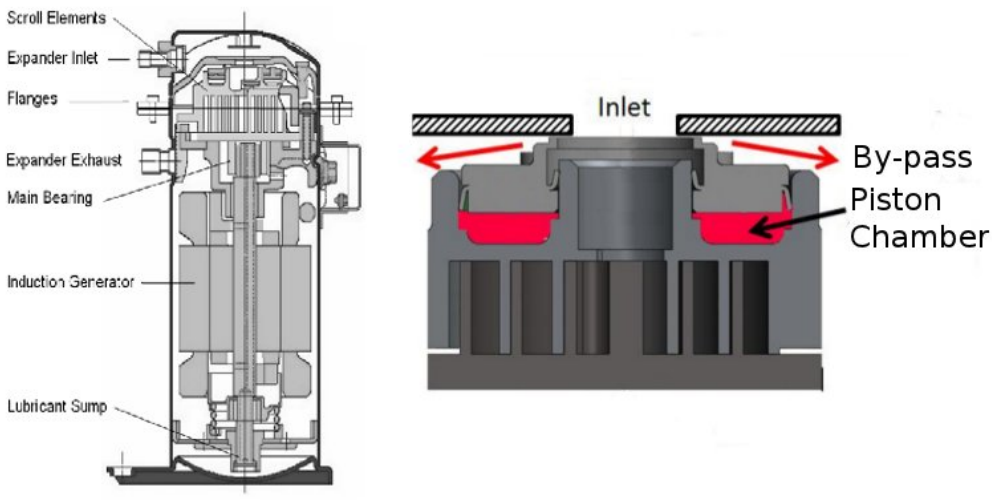

Figure 99: Schematic view of a hermetic scroll machine (left); Detailed view of the floating seal system (right). (Adapted from Harada, 2010)

Floating Seal

The floating seal (Figure 97, 98 and 99) is used to by-pass the working fluid at the beginning of the compression. This system is designed to avoid

overheating in the electrical motor at start-up. A bleed hole (Figure 98) is drilled in the stationary scroll, connecting the compression pockets to an intermediary piston chamber. At rest, the pressure in the piston chamber is equal to the exhaust pressure; the force equilibrium maintains the floating seal in its lower position and most of the fluid is by-passed. The compression then leads to a pressure increase in the piston chamber, the floating seal lifts up and the by-pass is closed.

In expander mode, the pressure difference between inlet and outlet is low at start-up, leading to an over-expansion of the working fluid. The pressure in the bleed hold can therefore be lower than the exhaust pressure (Figure 100, left), which maintains the floating seal in its lower position, the by-pass remaining open.

In order to address this issue and maintain the floating seal in its upper position, three springs are inserted in the piston chamber (Figure 100).

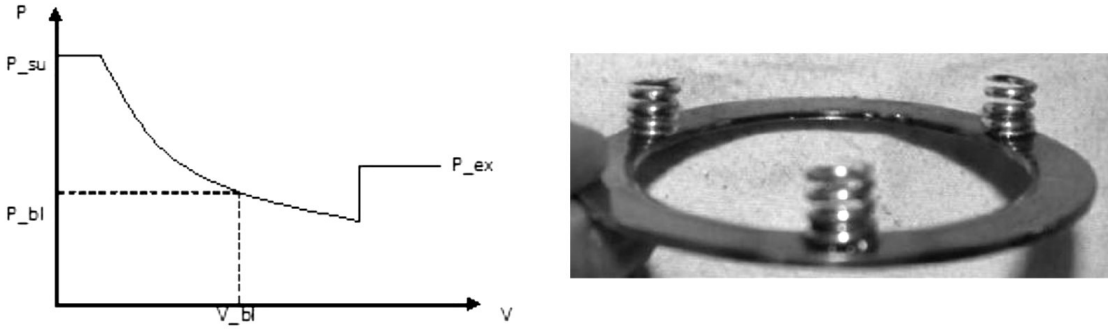

Figure 100: Left : Expansion profile corresponding to a bleed hole pressure inferior to the exhaust pressure. Right : Springs inserted underneath the floating seal in the piston chamber

The selection of the spring constant and of the spring length must be carefully performed:

- A too high spring constant/length leads to an increased pressure between both scrolls and excessive friction (due to the axial compliance mechanism).
- A too low spring constant/length does not ensure a correct sealing of the by-pass.

In this work, the selected spring length is 9.5 mm for a chamber height of 9 mm. Spring constant was selected empirically by successive increases until reaching proper expander start-up conditions (i.e. without excessive by-pass).

Lubrication

Beyond providing a medium to transfer power, the shaft in the compressor also acts as a rudimentary centrifugal oil pump: the oil is driven up through an off centered hole in the motor shaft. This supplies two journal bearings with oil

and helps lubricate the scroll assembly. The bottom journal bearing is lubricated by pooled oil at the bottom of the compressor (Harada, 2010).

The pumping driving principle being mainly based on centrifugal forces (due to the off centered hole in the shaft), the lubrication is ensured in expander mode as well as in compressor mode. Therefore, no modification is brought to the lubrication system.

The scroll components themselves are lubricated with oil entrained in the refrigerant. A small oil fraction of about 1% must therefore be maintained in the inlet refrigerant at all times.

Induction Generator

In compressor mode, the electrical consumption is given by:

$$\dot{W}_{cp} = \frac{\dot{M} \cdot \Delta h_s}{\varepsilon_s} \tag{103}$$

In expander mode, the electrical output is given by:

$$\dot{W}_{\text{exp}} = \varepsilon_s \cdot \dot{M} \cdot \Delta h_s \tag{104}$$

If the isentropic power and the overall isentropic effectiveness are assumed equal in these two equations, the following relation between compression and expansion electrical power can be written:

$$\dot{W}_{\text{exp}} = \varepsilon_s^2 \cdot \dot{W}_{cp} \tag{105}$$

This leads to the conclusion that the induction generator (that was designed for the compressor mode) is oversized: if the overall isentropic effectiveness is assumed to be 70%, the induction generator should be two times smaller than the one installed on the original machine. This is confirmed by the test-rig measurements: the maximum achieved output power is 2 kWe, while the maximum power of the electrical motor is about 5 kWe. Operating at such partial loads reduces the generator efficiency and should therefore be avoided.

However, due to practical constraints, the replacement of the electrical generator could not be performed on the tested machine, this task being left for future works and investigations.

C Polynomial laws

Summary. This appendix provides the polynomial laws of the isentropic effectiveness and of the filling factor for the two tested expanders. These laws are not provided in the form of an array, but directly in their analytical form in order to allow the interested reader to easily copy and paste them.

Hermetic expander.

Validity range (for the working fluid HFC-245fa):

$$1.8 \cdot 10^5 < p_{su} < 35.9 \cdot 10^5 \quad ; \quad 1.7 < r_p < 20 \tag{106}$$

Polynomial arguments:

$\alpha = \ln(r_p)$

$\beta = \ln(p_{su}[Pa])$

Polynomials (phi is the filling factor and epsilon the isentropic effectiveness):

```
phi=4.97108293E+00 - 5.27064860E-02*alpha - 5.04681859E-03*alpha^2 - 6.50892012E-01*beta + 2.63129696E-
02*beta^2 + 5.98837743E-03*alpha*beta

epsilon= - 2.87173728E+03 + 2.44443715E+03*alpha - 2.57532748E+03*alpha^2 + 1.25755504E+03*alpha^3 -
2.16811406E+02*alpha^4 + 7.18905239E-02*alpha^5 + 9.35443246E+02*beta - 1.21737770E+02*beta^2 +
7.87961830E+00*beta^3 - 2.52714006E-01*beta^4 + 3.20018368E-03*beta^5 - 7.16372155E+02*alpha*beta +
7.92355110E+01*alpha*beta^2 - 3.90043332E+00*alpha*beta^3 + 7.19343942E-02*alpha*beta^4 +
7.67983172E+02*alpha^2*beta - 8.61015725E+01*alpha^2*beta^2 + 4.28450197E+00*alpha^2*beta^3 -
7.97424498E-02*alpha^2*beta^4 - 3.76024800E+02*alpha^3*beta + 4.22096747E+01*alpha^3*beta^2 -
2.10123991E+00*alpha^3*beta^3 + 3.91129453E-02*alpha^3*beta^4 + 6.47012110E+01*alpha^4*beta -
7.25177711E+00*alpha^4*beta^2 + 3.60364465E-01*alpha^4*beta^3 - 6.69631843E-03*alpha^4*beta^4
```

Open-drive expander.

Validity range (for the working fluid HCFC-123):

$$1000 < N_{rot} < 5000 \quad ; \quad 20 < \rho_{su} < 240 \quad ; \quad 1.2 < r_p < 20 \tag{107}$$

Polynomial arguments:

$$\alpha = \ln(r_p)$$
$$\beta = \ln(N_{rot}[rpm])$$
$$\gamma = N_{rot}[rpm]$$
$$\delta = \rho_{su}[kg/m^3]$$

Polynomials (phi is the filling factor and epsilon the isentropic effectiveness):

```
phi=7.89735259E+00 - 1.29473957E+00*beta + 5.41680549E-02*beta^2 + 5.95345527E-04*delta - 6.03120996E-
06*delta^2

epsilon= - 2.16329421E+00 + 6.78008871E-04*gamma - 5.54407717E-07*gamma^2 + 8.03956432E-11*gamma^3 -
2.24146877E-15*gamma^4 + 2.91161840E-03*delta + 1.12613000E-06*delta^2 + 8.49777454E-08*delta^3 -
4.50090810E-10*delta^4 + 4.67781024E+00*alpha - 3.55789871E+00*alpha^2 + 1.16705018E+00*alpha^3 -
1.38101959E-01*alpha^4 + 2.37728921E-07*gamma*delta - 3.25174455E-09*gamma*delta^2 + 7.85764846E-
12*gamma*delta^3 - 6.05137025E-04*gamma*alpha + 4.49229123E-04*gamma*alpha^2 - 9.99328287E-
05*gamma*alpha^3 + 3.75965704E-11*gamma^2*delta + 4.39606024E-13*gamma^2*delta^2 - 8.61198734E-
16*gamma^2*delta^3 + 6.95577624E-07*gamma^2*alpha - 4.20590506E-07*gamma^2*alpha^2 + 8.24820738E-
08*gamma^2*alpha^3 + 3.34903471E-15*gamma^3*delta - 7.54325941E-17*gamma^3*delta^2 + 8.13185576E-
20*gamma^3*delta^3 - 9.33650022E-11*gamma^3*alpha + 5.77554418E-11*gamma^3*alpha^2 - 1.14741098E-
11*gamma^3*alpha^3 + 7.45493269E-03*delta*alpha - 5.32817717E-03*delta*alpha^2 + 9.48009166E-
04*delta*alpha^3 - 9.67639285E-05*delta^2*alpha + 5.34409340E-05*delta^2*alpha^2 - 8.76813140E-
06*delta^2*alpha^3 + 2.69821471E-07*delta^3*alpha - 1.37299471E-07*delta^3*alpha^2 + 2.18231218E-
08*delta^3*alpha^3
```

D Steady-state moving-boundaries heat exchanger model

Summary. This appendix describes the practical implementation of a three-zone steady-state heat exchanger model. A formalism is set up to avoid numerical failures during the iterations of the Newton solver.

When simulating steady state thermodynamic cycles with acausal equations, e.g. using "Engineering Equation Solver" (EES), non-convergence often occurs in the heat exchanger models, particularly when three-zones, moving boundaries model are used. This is particularly true in the case of low pinch point (i.e. relatively high heat transfer coefficients or exchange area): the iteration process can lead to a superposition of both temperature profiles, as illustrated in Figure 101.

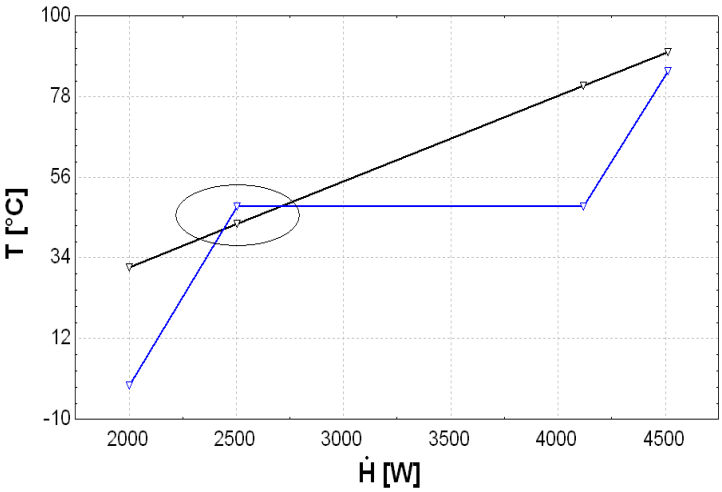

Figure 101: Simulation failure due to non-physical temperature profiles during the iterations

To avoid this issue, the iterative process should not be left to the solver, and most of the heat exchanger model should be written using causal equations, allowing conditional statements. The iteration scheme of the proposed heat exchanger model is the following:

1. The complete temperature profile is defined as an initial value. The heat transfer coefficients are set as parameters or calculated with heat transfer correlations.
2. Using these heat transfer coefficients, the required heat transfer area for each zone (liquid, two-phase, vapor) is calculated with causal equations only. This implies using the LMTD method instead of the $\varepsilon - NTU$ method. The required total heat transfer area is then obtained by summing the computed values for each zone.

3. The calculated heat transfer area is compared to the actual heat transfer area. If it is higher, the temperature profile is updated to increase the pinch point. If it is lower, the temperature profile is updated to decrease the pinch point.

Failure occurs if:

1. The initial conditions are poorly defined, leading the situation of Figure 101.
2. The update of the temperature profile during iterations leads to a negative pinch point.

To avoid failures when these cases occur, the LMTD equations are slightly modified to avoid logarithms of negative numbers. A penalty is assigned in terms of required area when this is the case. The code below corresponds to the case of a moving boundaries counterflow condenser model and is applied for each of the three zones:

```
if T_sf,su < T_r,ex - 1 then
      if T_sf_ex < T_r,su - 1 then
```

$$\Delta T_{\log} = \frac{\left(T_{sf,su} - T_{r,ex}\right) - \left(T_{sf,ex} - T_{r,su}\right)}{\ln\left(\frac{T_{sf,su} - T_{r,ex}}{T_{sf,ex} - T_{r,su}}\right)}$$

```
      else
```

$$\Delta T_{\log} = \frac{T_{sf,su} - T_{r,ex} + 1}{\ln\left(T_{r,ex} - T_{sf,su}\right)} \cdot \frac{1}{1 + \xi \cdot \left(T_{sf,ex} - T_{r,su} + 1\right)}$$

```
else
      if T_sf,ex < T_r,su - 1 then
```

$$\Delta T_{\log} = \frac{T_{sf,ex} - T_{r,su} + 1}{\ln\left(T_{r,su} - T_{sf,ex}\right)} \cdot \frac{1}{1 + \xi \cdot \left(T_{sf,su} - T_{r,ex} + 1\right)}$$

```
      else
```

$$\Delta T_{\log} = \frac{1}{\left(1 + \xi \cdot \left(T_{sf,su} - T_{r,ex} + 1\right)\right) \cdot \left(1 + \xi \cdot \left(T_{sf,ex} - T_{r,su} + 1\right)\right)}$$

```
      endif
endif
```

$$A = \frac{\dot{Q}}{U \cdot \Delta T_{\log}}$$

ξ is the penalty factor. It is set arbitrarily to 10^4.

When the difference between the secondary fluid temperature profile and the refrigerant temperature profile is lower than 1K, the expression of the LMTD is "freezed" to that temperature difference and divided by a penalty term proportional to the difference between refrigerant and secondary fluid temperatures. By doing this, the calculation of A is artificially impacted and leads to very high required heat transfer areas when the temperature

difference is negative, without causing a numerical error linked to the logarithm of a negative number. This high area leads the iteration process to increase the pinch point and escape the "non-physical" temperature profiles area.

E Display of the simulation results.

Summary. This appendix describes the Matlab interface developed to read the result files of Modelica simulations. Two animated graphs are proposed: the first one displays the temperature profiles in each heat exchanger (secondary fluid, wall and working fluid) while the second displays the thermodynamic states in three different diagrams (T-s, p-h or p-v).

When debugging or interpreting simulation results, raw temporal data is generally not sufficient. It is for example very useful to have a display of the system thermodynamic state at a given time. This allows quickly detecting states causing a simulation error, or graphically identifying where the main irreversibilities occur in the cycle.

To that end, an analysis tool is developed to process and display the raw data. The proposed interface is shown in Figure 102. This interface is specific to the models developed in section 4.3, i.e. it cannot work with alternative Modelica simulation libraries.

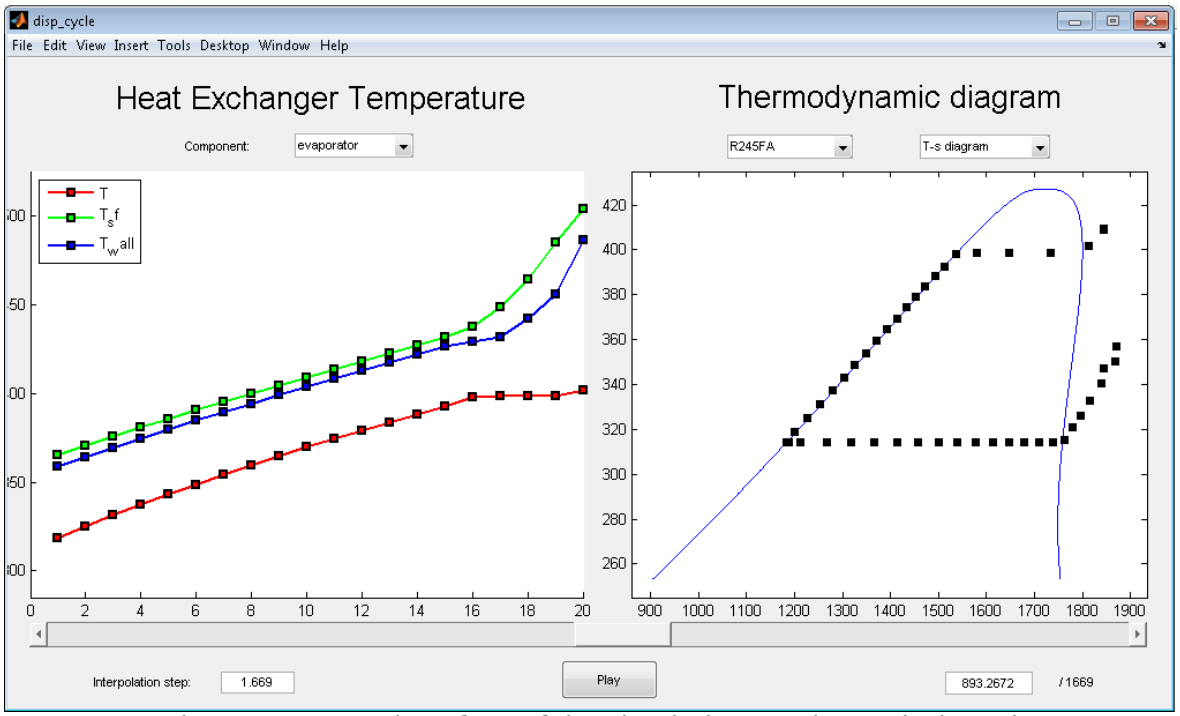

Figure 102: User interface of the simulation results analysis tool

Modelica raw data does not always come with constant time steps, because of simulation events (a breakpoint in the simulation due e.g. to a "if" statement) or variable step-size integration algorithms. To standardize the raw data, the latter is interpolated using a user-defined time-step, set by default to the total simulation time divided by 1000 (the defaults can be edited in the *def_cycle.m* Matlab file).

E Display of the simulation results.

The left figure displays the temperature profiles for each cell of the heat exchanger. The user selects the component of interest in a drop-down list box among all the first-level components of the Modelica model. If the selected component is recognized as a valid heat exchanger model (see chapter 4.3.1), the temperature profiles are interpolated and displayed.

The right figure displays each computed thermodynamic state of the model:

- The user selects a type of thermodynamic diagram (T-s, p-h or p-v)
- The user selects a working fluid, which allows the software to compute the saturation curve. Saturation data for all Refprop pure fluids is stored in the *sat.mat* file.
- The analysis tool scans the simulation result file to discover all the thermodynamic states corresponding to the defined working fluid. It interpolates them and displays them.

The scroll bar allows traveling in the simulation. A specific simulation time can also be provided in the corresponding text box. The *Play* button allows animating the results, the animation speed being defined in the *def_cycle.m* Matlab file.

F Numerical issues in dynamic heat exchanger models.

Summary. This appendix describes the practical implementation of the different numerical methods developed to ensure the robustness of the dynamic heat exchanger models during phase transitions.

The phenomenon of chattering (Figure 103) may occur when discontinuities in the model variables are present (Jensen, 2003). This phenomenon can lead the computed variables to exceed acceptable boundaries, causing simulation failures.

In a discretized heat exchanger model, the main discontinuity is often the density derivative on the liquid saturation curve (Figure 104). Simulation failure occurs if the cell-generated (and purely numerical) flow rate due to this discontinuity is of the same order of magnitude as the working fluid flow rate in the cycle. Therefore, a numerical stability criteria can be expressed as follows:

$$\dot{M}_{su} \gg V_i \cdot \frac{d\rho_i}{dt} \tag{108}$$

where $\dot{M}_{su}$ is the heat exchanger supply flow rate, V_i is the cell volume and ρ_i is the cell density.

This equation can be rewritten in the following form:

$$\dot{M}_{su} \gg \frac{V}{N} \cdot \left[\frac{\partial \rho_i}{\partial h} \cdot \frac{dh_i}{dt} + \frac{\partial \rho_i}{\partial p} \cdot \frac{dp}{dt} \right] \tag{109}$$

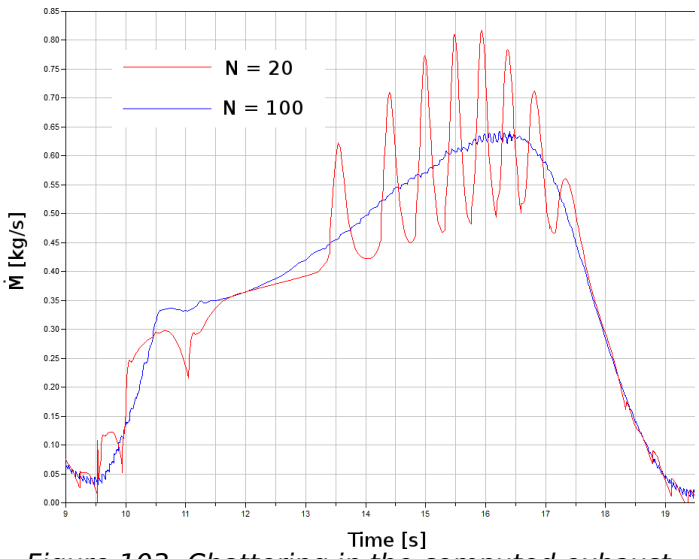

Figure 103: Chattering in the computed exhaust mass flow rate

As stated in Eq. 109, chattering and simulations failures are likely if:

- The number of cells is low (Figure 103)
- The cycle working fluid flow rate is low
- The heat exchanger internal volume is high
- The working conditions are highly transient (i.e. dh_i/dt and dp/dt are high)

In order to compare the efficiencies of different numerical methods aiming at addressing this issue, a so-called "stressed" system is defined: this system is a heat exchanger (evaporator) submitted to very transient operating conditions and to a low working fluid flow rate. The following boundary conditions are defined:

- Heat source: Water, 0.15 kg/s, 200°C
- Supply conditions: HFC-245fa, 0.37 kg/s, 50°C
- Heat exchanger parameters: N=20, V=3l (For the other parameters, see Figure 60)
- Evaporating pressure: $p = 12 + 5 \cdot \sin(0.2 \cdot \pi \cdot t) \quad [\text{bar}]$

The internal heat exchanger volume of 3l is selected by increasing its value until reaching a simulation failure. The highly transient character of the operating conditions is ensured by a sine wave on the pressure, with an amplitude of 5 bars and a frequency of 0.1 Hz. The period of 10s is smaller than the natural response time of the heat exchanger, resulting in pressure and enthalpy derivatives much higher than in traditional ORC simulations.

Robustness strategies

Constant node flow rates. This strategy avoids the generation of a high node flow rate in one particular cell by applying the mass conservation equation between the inlet and the outlet of the whole heat exchanger instead of every cell. The mass variations inside the cells are summed and reported on the last node flow rate. This is written:

$$\dot{M}_i^* = \dot{M}_{su} \tag{110}$$

$$\dot{M}_{ex} = \dot{M}_{su} - V_i \cdot \sum_1^N \frac{d\rho_i}{dt} = \dot{M}_{su} - V_i \cdot \sum_1^N \left[\frac{\partial \rho_i}{\partial h} \cdot \frac{dh_i}{dt} + \frac{\partial \rho_i}{\partial p} \cdot \frac{dp}{dt} \right] \tag{111}$$

Maximum density derivative. In this strategy, the peak in the density derivative occurring after the transition from liquid to two-phase is truncated, as shown in Figure 104.

This strategy allows conserving the mass balance equation in each cell. The simulation is therefore not affected, except when a phase transition occurs. In this case, the mass balance is not respected and a mass default can appear. Figure 104 shows however that the truncated area is relatively small, which should reduce the mass unbalance.

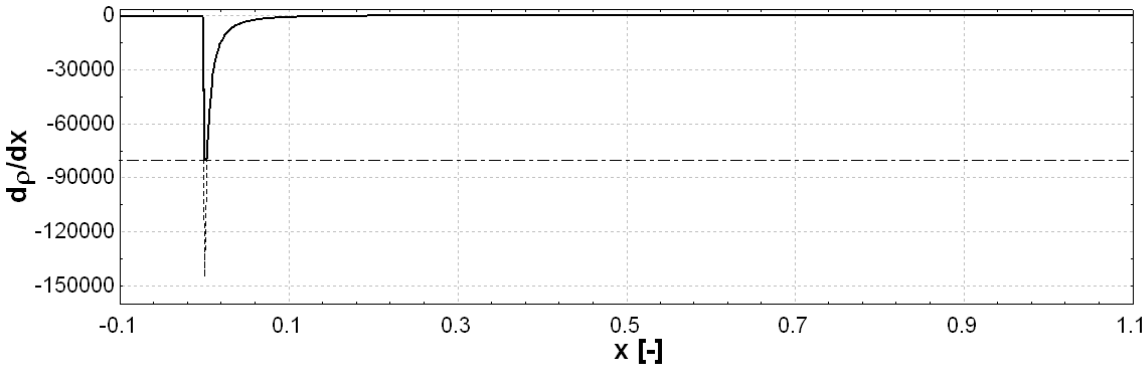

Figure 104: Truncature of the density derivative

The maximum value of the density derivative (with respect to time) is a model input. It is converted into maximum values for $\partial\rho_i/\partial h$ and $\partial\rho_i/\partial p$ with the following relation:

$$\frac{d\rho^{max}}{dt} = \frac{\partial\rho^{max}}{\partial h} \cdot \frac{dh^{ref}}{dt} + \frac{\partial\rho^{max}}{\partial p} \cdot \frac{dp^{ref}}{dt} \tag{112}$$

where the reference enthalpy and pressure time derivatives are set to typical values, namely:

$$\frac{dh^{ref}}{dt} = -4000\ [J/kg\,s]\ ;\ \frac{dp^{ref}}{dt} = 10^5\ [Pa/s] \tag{113}$$

The maximum partial derivatives are then calculated by assuming that the time derivative of the second parameter is null (i.e. dp/dt is set to 0 to calculate $\partial\rho/\partial h$ and dh/dt is set to 0 to calculate $\partial\rho/\partial h$.

Filtered density derivative. In this strategy , a first order filter is applied to the fast variations of the density with respect to time. This filter acts as "mass damper" and avoids transmitting abrupt variations to the node flow rates. The filtered mass accumulation in each cell is written:

$$\frac{dM_i^2}{dt^2} = \frac{V_i \cdot \left[\frac{\partial\rho_i}{\partial h} \cdot \frac{dh_i}{dt} + \frac{\partial\rho_i}{\partial p} \cdot \frac{dp}{dt}\right] - \frac{dM_i}{dt}}{T_i} \tag{114}$$

where T_i is the filter time constant, set as model input.

This strategy displaces the mass variations in time but does not generate mass defaults. However the energy balance is affected because the cell density is not exactly the one corresponding to the actual node flow rates.

High number of cells. As shown in Figure 103, increasing the number of cells reduces the refrigerant mass on which the non-continuous density derivative is applied, which reduces the node mass flow rate fluctuations. This method is the most accurate, but also requires a large number non-linear equations and increases computational times. To avoid simulation failures on the stressed system, a number of cells close to 100 was necessary.

Results and Discussion

For the purpose of the comparison, the stressed system is simulated on a time period of 70 seconds with each method.

Table 30 summarizes the simulation results and compares them with a reference case. This reference case is the stressed system described above, but with an internal volume of 1 liter instead of 3 liters. This volume difference is sufficient to avoid the simulation failure.

The mass and energy unbalances are computed with the following equations:

$$\begin{aligned} error_{ener} = & \int_t cp_{sf} \cdot \dot{M}_{sf} \cdot (T_{sf,su,hx} - T_{sf,ex,hx}) dt \\ & - \int_t (\dot{M}_{ex} \cdot h_{ex} - \dot{M}_{su} \cdot h_{su}) dt \\ & - V_i \cdot \sum_{i=1}^{N} (\rho_{i,final} \cdot u_{i,final} - \rho_{i,init} \cdot u_{i,init}) \end{aligned} \quad (115)$$

$$error_{mass} = \int_t (\dot{M}_{ex} - \dot{M}_{su}) - \sum_{i=1}^{N} V_i (\rho_{i,final} - \rho_{i,init}) \quad (116)$$

Eqs 115 and 116 are absolute errors. The errors provided in Table 30 are relative errors, i.e. they have been divided by the total mass/energy transfer.

	Reference case	***Constant flow rate***	***Maximum derivative***	***Filtering***	***High number of cells***
Simulation Time	*64.5 s*	*19.8 s*	*33.2 s*	*41.1 s*	*419 s*
Number of non-linear equations	*20*	*20*	*20*	*40*	*100*
Error on the mass balance	*0.8 ‰*	*3.3 ‰*	*3.0 ‰*	*0.87 ‰*	*3.8 ‰*
Error on the energy balance	*1.1 ‰*	*20 ‰*	*3.5 ‰*	*16 ‰*	*3 ‰*

Table 30: Simulation results with the different strategies

Figure 105 shows the predicted exhaust enthalpy with each strategy. The enthalpy profile is best predicted with the "high number of cells strategy", followed by the "filtered density" strategy and by the "maximum derivative strategy". The enthalpy is always under-predicted by the "constant flow rate" strategy, which should therefore be avoided.

The following conclusions can be drawn:

- The constant flow rate strategy is optimal in terms of computation time. However, it is also the one with the highest error on the energy balance.
- The maximum derivative strategy shows a slight increase on the mass and energy unbalances. These errors remain however limited, considering that the simulated system is highly transient compared to traditional systems and thus undergoes a higher number of phase transitions.
- As expected, the filtering strategy shows a good mass balance, but an energy unbalance higher than 1%. It is also slightly slower due to an additional state variable in each cell (the second derivative of the density).
- Surprisingly, the simulation with 100 cells shows a lower accuracy than that with 20 cells. This is most likely due to truncation errors. It is also very slow due to the 100 non-linear equations.

For the simulations performed in this work, the "maximum derivative" strategy was selected, as a good tradeoff between simulation accuracy, computational time and robustness.

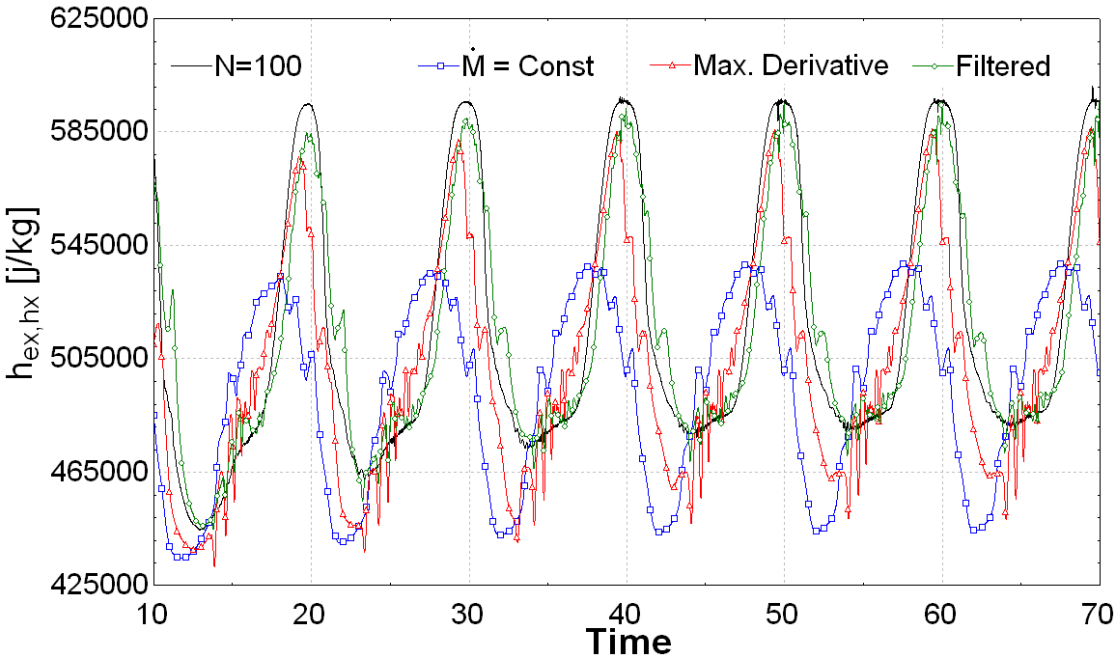

Figure 105: Predicted exhaust enthalpy with the different strategies

G Compounding two scroll expanders in series.

Summary. This appendix derives an analytical expression of the optimal intermediate pressure between two expanders assembled in series. This expression is useful while designing and optimizing ORC cycles with two-stage expansion in an effective way.

If the expander efficiency was only dependent on the pressure ratio, the optimal first-stage pressure ratio would be defined as the square root of the overall pressure ratio ($r_{p,1}=r_{p,2}=\sqrt{r_p}$). However, the efficiency also depends on the flow rate through the expander since a higher flow rate entails a higher output power and makes the constant losses (e.g. friction losses) relatively smaller.

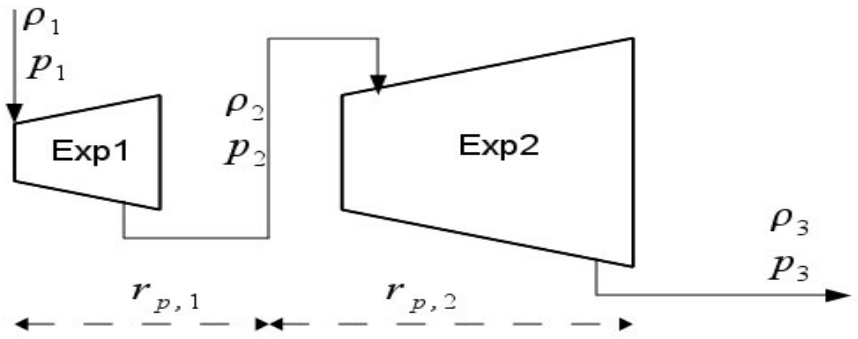

Figure 106: Two-stage expander

In the polynomial correlations proposed in section 4.2.1, the influence of the flow rate is reflected by the dependence in terms of supply vapor density or pressure. The present analysis corresponds to the case where pressure ratio and density are the two input variables. However, the same method could easily be extended to the case in which the two inputs of the polynomial laws are the pressure ratio and the supply pressure.

The following developments aim at determining the optimal pressure ratio $r_{p,1}$ that maximizes the overall expansion efficiency for the two expansion stages.

If the vapor is treated as an ideal gas, the isentropic overall effectiveness for the two expanders can be written:

$$\frac{h_{3s}}{h_1}=r_p^{\left[\frac{1-\gamma}{\gamma}\right]} \tag{117}$$

where the enthalpy reference is taken at 0K.

The different expansion efficiencies are defined as follows:

$$\varepsilon=\frac{h_1-h_3}{h_1-h_{3s}}=\frac{h_1-h_3}{\beta\cdot h_1}\ ;\ \varepsilon_1=\frac{h_1-h_2}{h_1-h_{2s}}=\frac{h_1-h_2}{\beta_1\cdot h_1}\ ;\ \varepsilon_2=\frac{h_2-h_3}{h_2-h_{3ss}}=\frac{h_2-h_3}{\beta_2\cdot h_2} \tag{118}$$

Where the factors β are defined by:

$$\beta_i=1-r_{p,i}^{(\frac{1-\gamma}{\gamma})} \tag{119}$$

Rearranging Eq 118, the overall efficiency can be expressed as a function of the individual expander efficiencies and of the β factors:

$$\varepsilon=\frac{\varepsilon_1\cdot\beta_1+\varepsilon_1\cdot\beta_2-\varepsilon_1\cdot\varepsilon_2\cdot\beta_1\cdot\beta_2}{\beta} \tag{120}$$

This efficiency is the one to be maximized. To that end, the derivatives of each factor on the right side of the equation must be calculated.

The derivative of β_1 is straightforward and is given by:

$$\frac{d\beta_1}{dr_{p,1}}=\left[\frac{\gamma-1}{\gamma}\right]\cdot r_{p,1}^{\left[\frac{1-2\cdot\gamma}{\gamma}\right]} \tag{121}$$

Recognizing that $r_p=r_{p,1}\cdot r_{p,2}$, the derivative of β_2 is calculated in that same manner:

$$\frac{d\beta_2}{dr_{p,1}}=\left[\frac{\gamma-1}{\gamma}\right]\cdot r_p^{\left[\frac{1-\gamma}{\gamma}\right]}\cdot r_{p,1}^{\left[\frac{-1}{\gamma}\right]} \tag{122}$$

As shown in section 4.2.1 , the individual efficiencies can be expressed as a function of the pressure ratios and of the supply density in the form of:

$$\varepsilon_1=\sum_{i=0}^{n-1}\sum_{j=0}^{n-1}a_{ij}\cdot\ln(r_{p,1})^i\cdot\rho_1^j+a_{n0}\cdot\ln(r_{p,1})^n+a_{0n}\cdot\rho_1^n=f(r_{p,1},\rho_1) \tag{123}$$

$$\varepsilon_2=\sum_{i=0}^{n-1}\sum_{j=0}^{n-1}a_{ij}\cdot\ln(r_{p,2})^i\cdot\rho_2^j+a_{n0}\cdot\ln(r_{p,2})^n+a_{0n}\cdot\rho_2^n=f(r_{p,2},\rho_2) \tag{124}$$

ρ_1 being independent of $r_{p,1}$, the derivative of ε_1 is straightforward:

$$\frac{d\varepsilon_1}{dr_{p,1}}=\frac{\partial\varepsilon_1}{\partial r_{p,1}}=\frac{1}{r_{p,1}}\sum_{i=1}^{n-1}\sum_{j=0}^{n-1}a_{ij}\cdot i\cdot\ln(r_{p,1})^{(i-1)}\cdot\rho_1^j+a_{n0}\cdot n\cdot\ln(r_{p,1})^{n-1} \tag{125}$$

On the contrary, for ε_2, $r_{p,2}$ and ρ_2 both depend on $r_{p,1}$. In good approximation, the density ρ_2 can be assimilated to the density at the same pressure calculated as if the first expansion was isentropic:

$$\rho_2\simeq\rho_1\cdot r_{p,1}^{\left[-\frac{1}{\gamma}\right]} \tag{126}$$

The derivative of ε_2 can then be calculated by:

$$\frac{d\varepsilon_2}{dr_{p,1}}=-\frac{r_p}{r_{p,1}^2}\frac{\partial\varepsilon_2}{\partial r_{p,2}}-\frac{\rho_{su,\exp}}{\gamma}\cdot r_{p,1}^{\left[-\frac{\gamma+1}{\gamma}\right]}\cdot\frac{\partial\varepsilon_2}{\partial\rho} \tag{127}$$

with:

$$\frac{\partial \varepsilon_2}{\partial r_{p,2}} = \frac{1}{r_{p,2}} \sum_{i=1}^{n-1} \sum_{j=0}^{n-1} a_{ij} \cdot i \cdot \ln(r_{p,2})^{(i-1)} \cdot \rho_2^j + a_{n0} \cdot n \cdot \ln(r_{p,2})^{n-1} \quad (128)$$

and:

$$\frac{\partial \varepsilon_2}{\partial \rho} = \frac{1}{\rho_2} \cdot \sum_{i=0}^{n-1} \sum_{j=1}^{n-1} a_{ij} \cdot j \cdot \ln(r_{p,2})^i \cdot \rho_2^{(j-1)} + a_{0n} \cdot n \cdot \rho_2^{(n-1)} \quad (129)$$

The derivative of each factor in Eq 127 being calculated, the maximum is obtained by equaling the derivative of the efficiency to zero ($d\varepsilon/dr_{p,1}=0$).This implies:

$$\xi = \varepsilon_1' \beta_1 + \varepsilon_1 \beta_1' + \varepsilon_2' \beta_2 + \varepsilon_2 \beta_2' - \varepsilon_1' \beta_1 \varepsilon_2 \beta_2 - \varepsilon_1 \beta_1' \varepsilon_2 \beta_2 - \varepsilon_1 \beta_1 \varepsilon_2' \beta_2 - \varepsilon_1 \beta_1 \varepsilon_2 \beta_2' = 0 \quad (130)$$

where the ' indicate the derivative of the given variable with respect to $r_{p,1}$

The optimal first stage pressure ratio is therefore the one that nullifies ξ, as defined in Eq 130.

The above equations are developed in the hypothesis of an ideal gas. This hypothesis is not verified for most organic fluids in vapor state close to the vapor saturation curve. However, Eq 130 can also be applied to real gases with very good results by calculating an equivalent isentropic expansion factor derived from Eq. 117:

$$\gamma_{eq} = \left[1 + \frac{\ln(1 - \frac{h_1}{h_{3s}})}{\ln(r_p)} \right]^{-1} \quad (131)$$

where $h_{3s} = \boldsymbol{h}(p = p_3, s = s_1)$

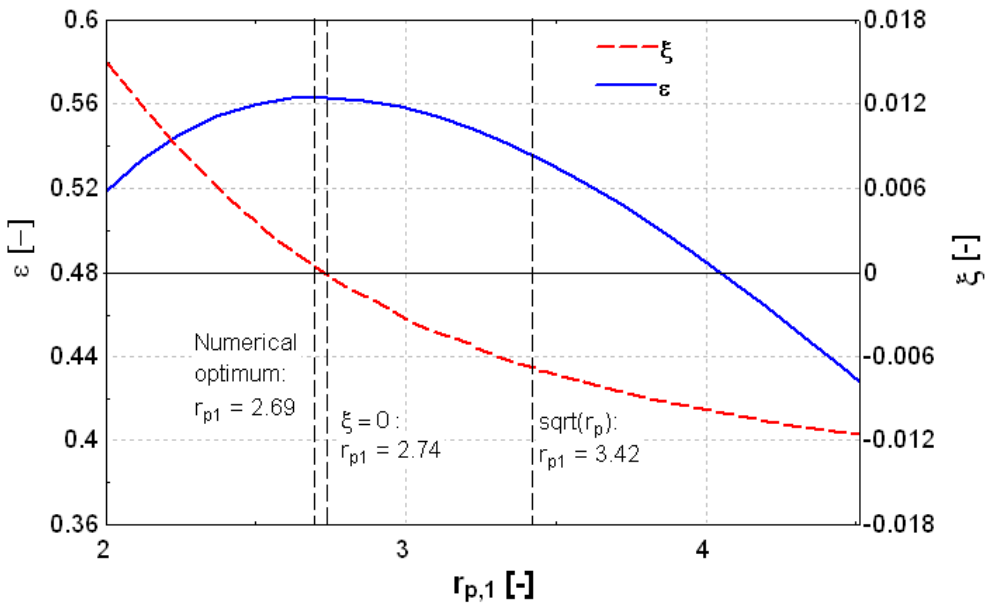

Figure 107: Optimal first-stage pressure ratio calculated numerically (left) analytically (middle) or by assuming equal first and second stage pressure ratios

G Compounding two scroll expanders in series.

The result of the optimization is illustrated in Figure 107 for the following working conditions: HFC-245fa working fluid; $p_{su,\exp}=23.4\,bars$; $p_{ex,\exp}=2.0\,bars$; $T_{su,\exp}=140°C$. The selected expander is the hermetic scroll expander. For these working conditions, the pressure ratio is 11.7. Setting the pressure ratio over expander 1 to the square root of the overall pressure ratio would lead to $r_{p,1}=3.42$. However, when plotting the overall efficiency, the optimum is obtained for $r_{p,1}=2.69$. When the above-proposed method is applied, ξ is null for $r_{p,1}=2.74$. The error relative to the simplifying hypothesis (Eqs 126 and 131) is therefore very limited, which validates the method.

Bibliography

Aljundi, I. H. (2011). Effect of dry hydrocarbons and critical point temperature on the efficiencies of organic Rankine cycle. *Renewable Energy*, *36*(4), 1196-1202. doi:16/j.renene.2010.09.022

Aoun, B., & Clodic, D. (2008). Theoretical and experimental study of an oil-free scroll type vapor expander. *Proceedings of the International Compressor Engineering Conference at Purdue: paper* (Vol. 1188).

Badr, O., O'Callaghan, P. W., & Probert, S. D. (1990). Rankine-cycle systems for harnessing power from low-grade energy sources. *Applied Energy*, *36*(4), 263-292. doi:16/0306-2619(90)90002-U

Bailey, O., & Worrell, E. (2005). Clean Energy Technologies: A Preliminary Inventory of the Potential for Electricity Generation.

Bejan, A., Tsatsaronis, G., & Moran, M. J. (1996). *Thermal design and optimization*. Wiley-IEEE.

Bendapudi, S., Braun, J. E., & Groll, E. A. (2005). Dynamic Model of a Centrifugal Chiller System-Model Development, Numerical Study, and Validation. *ASHRAE Transactions*, *111*(Part 1), 132–148.

Bendapudi, Satyam, Braun, J. E., & Groll, E. A. (2008). A comparison of moving-boundary and finite-volume formulations for transients in centrifugal chillers. *International Journal of Refrigeration*, *31*(8), 1437-1452. doi:16/j.ijrefrig.2008.03.006

Borsukiewicz-Gozdur, A., & Nowak, W. (2007). Comparative analysis of natural and synthetic refrigerants in application to low temperature Clausius-Rankine cycle. *Energy*, *32*(4), 344-352. doi:16/j.energy.2006.07.012

Bruno, J. C., López-Villada, J., Letelier, E., Romera, S., & Coronas, A. (2008). Modelling and optimisation of solar organic rankine cycle engines for reverse osmosis desalination. *Applied Thermal Engineering*, *28*(17-18), 2212-2226. doi:16/j.applthermaleng.2007.12.022

Bundela, P. S., & Chawla, V. (2010). Sustainable Development through Waste Heat Recovery. *American Journal of Environmental Sciences*, *6*.

Canada, S. (2004). Parabolic Trough Organic Rankine Cycle Solar Power Plant. *DOE Solar Energy Technologies*. Presented at the NREL.

Casella, F., Otter, M., Proelss, K., Richter, C., & Tummescheit, H. (2006). The Modelica Fluid and Media library for modeling of incompressible and compressible thermo-fluid pipe networks. *Conference Proceedings, Modelica Conference* (pp. 4–5).

Dai, Y., Wang, J., & Gao, L. (2009). Parametric optimization and comparative study of organic Rankine cycle (ORC) for low grade waste

heat recovery. *Energy Conversion and Management*, *50*(3), 576-582. doi:16/j.enconman.2008.10.018

Davidson, T. A. (1977). *Design and analysis of a 1 kw Rankine power cycle, employing a multi-vane expander, for use with a low temperature solar collector.* Massachusetts Institute of Technology.

Delgado-Torres, Agustín Manuel, & García-Rodríguez, L. (2007). Comparison of solar technologies for driving a desalination system by means of an organic Rankine cycle. *Desalination*, *216*(1-3), 276-291. doi:16/j.desal.2006.12.013

Delgado-Torres, Agustín M., & García-Rodríguez, L. (2010). Analysis and optimization of the low-temperature solar organic Rankine cycle (ORC). *Energy Conversion and Management*, *51*(12), 2846-2856. doi:16/j.enconman.2010.06.022

Desai, N. B., & Bandyopadhyay, S. (2009). Process integration of organic Rankine cycle. *Energy*, *34*(10), 1674-1686. doi:16/j.energy.2009.04.037

De Vlaminck, M. (1988). Turbines axiales, turbines radiales et machines de détente à vis: domaines d'utilisation dans des installations ORC. *Revue générale de thermique*, *27*, 18-27.

Dixon, S. L. (2005). *Fluid mechanics, thermodynamics of turbomachinery*. Butterworth-Heinemann.

Drescher, U., & Brüggemann, D. (2007). Fluid selection for the Organic Rankine Cycle (ORC) in biomass power and heat plants. *Applied Thermal Engineering*, *27*(1), 223-228. doi:16/j.applthermaleng.2006.04.024

Dynasim. (2011). Dymola. User's Manual. Version 7.4. Dynasim AB.

El Chammas, R., & Clodic, D. (2005). Combined cycle for hybrid vehicles. *SAE Technical Paper*, 01–1171.

Endo, T., Kojima, Y., Takahashi, K., Baba, T., Ibaraki, S., Takahashi, T., & Shinohara, M. (2007). Study on Maximizing Exergy in Automotive Engines. *SAE*.

Enertime. (2011). *The Organic Rankine Cycle and its applications*. Retrieved from http://www.cycle-organique-rankine.com

Engin, T., & Ari, V. (2005). Energy auditing and recovery for dry type cement rotary kiln systems--A case study. *Energy Conversion and Management*, *46*(4), 551-562. doi:16/j.enconman.2004.04.007

European Climate Foundation. (2010). *EU Roadmap 2050*. Retrieved from http://www.roadmap2050.eu/

Façao, J., Palmero-Marrero, A., & Oliveira, A. C. (2008). Analysis of a solar assisted micro-cogeneration ORC system. *International Journal of Low-Carbon Technologies*, *3*(4), 254.

Ford, G. (2008). CSP: bright future for linear fresnel technology? *Renewable Energy Focus*, *9*(5), 48-49, 51. doi:16/S1755-0084(08)70029-2

Forristall, R. (2003). *Heat transfer analysis and modeling of a parabolic trough solar receiver implemented in engineering equation solver*. Citeseer.

Freymann, R., Strobl, W., & Obieglo, A. (2008). The Turbosteamer: A System Introducing the Principle of Cogeneration in Automotive Applications. *MTZ*, *69*, 20–27.

Frick, S. (2009). *Design Approach for Geothermal Binary Power Plants, Low-Bin project*. Retrieved from http://www.lowbin.eu/documentation.php

García-Cascales, J. R., Vera-García, F., Corberán-Salvador, J. M., Gonzálvez-Maciá, J., & Fuentes-Díaz, D. (2007). Assessment of boiling heat transfer correlations in the modelling of fin and tube heat exchangers. *International Journal of Refrigeration*, *30*(6), 1004-1017. doi:16/j.ijrefrig.2007.01.006

Guangbin, L., Yuanyang, Z., Yunxia, L., & Liansheng, L. (2011). Simulation of the dynamic processes in a scroll expander–generator used for small-scale organic Rankine cycle system. *Proceedings of the Institution of Mechanical Engineers, Part A: Journal of Power and Energy*, *225*(1), 141-149. doi:10.1177/09576509JPE1036

Gu, W., Weng, Y., Wang, Y., & Zheng, B. (2009). Theoretical and experimental investigation of an organic Rankine cycle for a waste heat recovery system. *Proceedings of the Institution of Mechanical Engineers, Part A: Journal of Power and Energy*, *223*(5), 523–533.

Harada, K. J. (2010). *Development of a small scale scroll expander* (Master Thesis). Oregon State University.

Harinck, J., Turunen-Saaresti, T., Colonna, P., Rebay, S., & van Buijtenen, J. (2010). Computational Study of a High-Expansion Ratio Radial Organic Rankine Cycle Turbine Stator. *Journal of Engineering for Gas Turbines and Power*, *132*(5), 054501-6. doi:10.1115/1.3204505

Hettiarachchi, H. D., Golubovic, M., Worek, W. M., & Ikegami, Y. (2007). Optimum design criteria for an Organic Rankine cycle using low-temperature geothermal heat sources. *Energy*, *32*(9), 1698-1706. doi:16/j.energy.2007.01.005

Hollands, K. G. T., Raithby, G. D., & Konicek, L. (1975). Correlation equations for free convection heat transfer in horizontal layers of air and water. *International Journal of Heat and Mass Transfer*, *18*(7-8), 879–884.

Hsieh, Y. Y., & Lin, T. F. (2002). Saturated flow boiling heat transfer and pressure drop of refrigerant R-410A in a vertical plate heat exchanger. *International Journal of Heat and Mass Transfer*, *45*(5), 1033-1044. doi:16/S0017-9310(01)00219-8

Hung, T.-C. (2001). Waste heat recovery of organic Rankine cycle using dry fluids. *Energy Conversion and Management*, *42*(5), 539-553. doi:16/S0196-8904(00)00081-9

Incropera, F. P., & DeWitt, D. P. (2001). *Fundamentals of Heat and Mass Transfer, 5th Edition* (5th ed.). Wiley.

Jackson, T., McKibben, B., Robinson, M., & Sukhdev, P. (2011). *Prosperity without Growth: Economics for a Finite Planet* (Reprint.). EarthScan.

Jensen, J. M. (2003). *Dynamic modeling of Thermo-Fluid Systems-With focus on evaporators for refrigeration* (PhD Thesis). Department of Mechanical Engineering, Technical University of Denmark, Lyngby (Dänemark).

Jing, L., Gang, P., & Jie, J. (2010a). Optimization of low temperature solar thermal electric generation with Organic Rankine Cycle in different areas. *Applied Energy*, *87*(11), 3355-3365. doi:10.1016/j.apenergy.2010.05.013

Jing, L., Gang, P., & Jie, J. (2010b). Optimization of low temperature solar thermal electric generation with Organic Rankine Cycle in different areas. *Applied Energy*, *87*(11), 3355-3365. doi:16/j.apenergy.2010.05.013

Jing, L., Pei, G., Li, Y., & Ji, J. (2011). Evaluation of external heat loss from a small-scale expander used in Organic Rankine Cycle. *Applied Thermal Engineering*, *In Press, Accepted Manuscript*. doi:10.1016/j.applthermaleng.2011.04.039

Jones, G. J., & Thompson, G. (1996). Renewable energy for African development. *Solar Energy*, *58*(1-3), 103-109. doi:16/0038-092X(96)00057-6

Kane, E. H. (2002). *Intégration et optimisation thermoéconomique & environomique de centrales thermiques solaires hybrides*. PhD Thesis, Laboratoire d'Energétique Industrielle, Ecole polytechnique Fédérale de Lausanne, Suisse.

Kane, M., Larrain, D., Favrat, D., & Allani, Y. (2003). Small hybrid solar power system. *Energy*, *28*(14), 1427-1443. doi:16/S0360-5442(03)00127-0

Karytsas, C. (2007). *Efficient Low Temperature Geothermal Binary Power – Low-Bin Project*. Retrieved from http://www.lowbin.eu/documentation.php

Kiefer, J. (1953). Sequential minimax search for a maximum. *Proc. Amer. Math. Soc* (Vol. 4, pp. 502–506).

Klein, S. (2011). *Engineering Equation Solver*. F-Chart Software.

Kranz, S. (2007). *Market Survey – Germany, Low-Bin project*. Retrieved from http://www.lowbin.eu/documentation.php

Kuo, W. S., Lie, Y. M., Hsieh, Y. Y., & Lin, T. F. (2005). Condensation heat transfer and pressure drop of refrigerant R-410A flow in a vertical plate heat exchanger. *International Journal of Heat and Mass Transfer*, *48*(25-26), 5205-5220. doi:16/j.ijheatmasstransfer.2005.07.023

Lakew, A. A., & Bolland, O. (2010). Working fluids for low-temperature heat source. *Applied Thermal Engineering*, *30*(10), 1262-1268. doi:16/j.applthermaleng.2010.02.009

Lemort, V. (2009). *Contribution to the characterization of scroll machines in compressor and expander modes*. University of Liège, Liège.

Lemort, V., Cuevas, C., Lebrun, J., & Teodorese, I. V. (2007). Contribution à l'étude des cycles de Rankine de récupération de chaleur. *VIIIème Colloque Interuniversitaire Franco-Québécois sur la Thermique des Systèmes*. Presented at the VIIIème Colloque Interuniversitaire Franco-Québécois sur la Thermique des Systèmes, Montreal.

Lemort, V., Quoilin, S., Cuevas, C., & Lebrun, J. (2009). Testing and modeling a scroll expander integrated into an Organic Rankine Cycle. *Applied Thermal Engineering*, *29*(14-15), 3094-3102. doi:10.1016/j.applthermaleng.2009.04.013

Lin, C. (2008). *Feasibility of using power steering pumps in small-scale solar thermal electric power systems*. [39] Dept. of Mechanical Engineering, MIT.

Li, P., Li, Y., & Seem, J. E. (2010). Dynamic Modeling and Consistent Initialization of systems of Differential-Algebraic equations for centrifugal chillers. *Fourth National Conference of IBPSA*. Presented at the Fourth National Conference of IBPSA.

Liu, B.-T., Chien, K.-H., & Wang, C.-C. (2004). Effect of working fluids on organic Rankine cycle for waste heat recovery. *Energy*, *29*(8), 1207-1217. doi:16/j.energy.2004.01.004

Liu, H., Qiu, G., Shao, Y., Daminabo, F., & Riffat, S. B. (2010). Preliminary experimental investigations of a biomass-fired micro-scale CHP with organic Rankine cycle. *International Journal of Low-Carbon Technologies*, *5*(2), 81 -87. doi:10.1093/ijlct/ctq005

Mago, P. J., Chamra, L. M., Srinivasan, K., & Somayaji, C. (2008). An examination of regenerative organic Rankine cycles using dry fluids. *Applied Thermal Engineering*, *28*(8-9), 998-1007. doi:16/j.applthermaleng.2007.06.025

Maizza, V., & Maizza, A. (2001). Unconventional working fluids in organic Rankine-cycles for waste energy recovery systems. *Applied Thermal Engineering*, *21*(3), 381-390. doi:16/S1359-4311(00)00044-2

Manolakos, D., Kosmadakis, G., Kyritsis, S., & Papadakis, G. (2009). On site experimental evaluation of a low-temperature solar organic Rankine

cycle system for RO desalination. *Solar Energy*, *83*(5), 646-656. doi:10.1016/j.solener.2008.10.014

Manzagol, J., d' Harboulle, P., Claudet, G., & Baguer, G. G. (2002). Cryogenic scroll expander for claude cycle with cooling power of 10 to 100 Watts at 4.2 K. (M. Adams, M. DiPirro, S. Breon, D. Glaister, J. R. Hull, P. Kittel, V. Pecharsky, et al., Eds.)*AIP Conference Proceedings*, *613*(1), 267-274. doi:10.1063/1.1472030

McMahan, A. C. (2006). Design & Optimization of Organic Rankine Cycle Solar-Thermal Powerplants. *Master's Thesis, University of Wisconsin-Madison*.

Mikielewicz, D., & Mikielewicz, J. (2010). A thermodynamic criterion for selection of working fluid for subcritical and supercritical domestic micro CHP. *Applied Thermal Engineering*, *30*(16), 2357-2362. doi:16/j.applthermaleng.2010.05.035

Monahan, J. (1976). Development of a 1-kW, Organic Rankine Cycle Power Plant for remote applications. Presented at the Intersociety Energy Conversion Engineeing Conference, New York.

Muley, A., & Manglik, R. M. (1999). Experimental Study of Turbulent Flow Heat Transfer and Pressure Drop in a Plate Heat Exchanger With Chevron Plates. *Journal of Heat Transfer*, *121*(1), 110-117. doi:10.1115/1.2825923

Müller-Steinhagen, H., & Trieb, F. (2004). Concentrating solar power—a review of the technology. *Quarterly of the Royal Academy of Engineering Ingenia*, *18*, 43–50.

Noack, H. (1999). *Pratique des installations frigorifiques*. Pyc Livres.

Oomori, H., & Ogino, S. (1993). *Waste Heat Recovery of Passenger Car Using a Combination of Rankine Bottoming Cycle and Evaporative Engine Cooling System* (No. 930880). Warrendale, PA: SAE International. Retrieved from http://papers.sae.org/930880

Orosz, M., Quoilin, S., & Hemond, H. (2010). SORCE: A design tool for solar organic Rankine cycle systems in distributed generation applications. Presented at the SolarPaces.

Patel, P. S., & Doyle, E. F. (1976). Compounding the Truck Diesel Engine with an Organic Rankine-Cycle System. *Society of Automotive Engineers (SAE)*.

Pei, G., Li, J., Li, Y., Wang, D., & Ji, J. (2011). Construction and dynamic test of a small-scale organic rankine cycle. *Energy*, *36*(5), 3215-3223. doi:10.1016/j.energy.2011.03.010

Persson, J. G. (1990). Performance mapping vs design parameters for screw compressors and other displacement compressor types. *VDI Berichte*.

Peterson, R. B., Wang, H., & Herron, T. (2008). Performance of a small-scale regenerative Rankine power cycle employing a scroll expander.

Proceedings of the Institution of Mechanical Engineers, Part A: Journal of Power and Energy, *222*(3), 271-282. doi:10.1243/09576509JPE546

Prabhu, E. (2006). *Solar trough organic rankine electricity system (stores) stage 1: Power plant optimization and economics*. NREL/SR-550-39433.

Probert, S. D., Hussein, M., O'Callaghan, P. W., & Bala, E. (1983). Design optimisation of a solar-energy harnessing system for stimulating an irrigation pump. *Applied Energy*, *15*(4), 299-321. doi:16/0306-2619(83)90059-4

Quadrelli, R., & Peterson, S. (2007). The energy-climate challenge: Recent trends in CO2 emissions from fuel combustion. *Energy Policy*, *35*(11), 5938-5952. doi:16/j.enpol.2007.07.001

Quoilin, Sylvain, & Lemort, V. (2009, April). Technological and Economical Survey of Organic Rankine Cycle Systems. Retrieved from http://hdl.handle.net/2268/14609

Rentizelas, A., Karellas, S., Kakaras, E., & Tatsiopoulos, I. (2009). Comparative techno-economic analysis of ORC and gasification for bioenergy applications. *Energy Conversion and Management*, *50*(3), 674-681. doi:16/j.enconman.2008.10.008

Richter, C. (2008). *Proposal of new object-oriented equation-based model libraries for thermodynamic systems*. Braunschweig.

Roy, J. P., Mishra, M. K., & Misra, A. (2011). Performance analysis of an Organic Rankine Cycle with superheating under different heat source temperature conditions. *Applied Energy*, *88*(9), 2995-3004. doi:16/j.apenergy.2011.02.042

Saleh, B., Koglbauer, G., Wendland, M., & Fischer, J. (2007). Working fluids for low-temperature organic Rankine cycles. *Energy*, *32*(7), 1210-1221. doi:16/j.energy.2006.07.001

Sauret, E., & Rowlands, A. S. (2011). Candidate radial-inflow turbines and high-density working fluids for geothermal power systems. *Energy*, *In Press, Corrected Proof*. doi:16/j.energy.2011.03.076

Tchanche, B. F., Papadakis, G., Lambrinos, G., & Frangoudakis, A. (2009). Fluid selection for a low-temperature solar organic Rankine cycle. *Applied Thermal Engineering*, *29*(11-12), 2468-2476. doi:16/j.applthermaleng.2008.12.025

Thonon B. (1995). Recent research and developments in plate heat exchangers. *Fuel and Energy Abstracts*, *36*, 361. doi:10.1016/0140-6701(95)96878-G

Vaja, I., & Gambarotta, A. (2010). Internal Combustion Engine (ICE) bottoming with Organic Rankine Cycles (ORCs). *Energy*, *35*(2), 1084-1093. doi:16/j.energy.2009.06.001

Wang, E. H., Zhang, H. G., Fan, B. Y., Ouyang, M. G., Zhao, Y., & Mu, Q. H. (2011). Study of working fluid selection of organic Rankine cycle

(ORC) for engine waste heat recovery. *Energy*, *36*(5), 3406-3418. doi:16/j.energy.2011.03.041

Wang, H., Peterson, R. B., & Herron, T. (2009). Experimental performance of a compliant scroll expander for an organic Rankine cycle. *Proceedings of the Institution of Mechanical Engineers, Part A: Journal of Power and Energy*, *223*(7), 863-872. doi:10.1243/09576509JPE741

Wang, J., Dai, Y., & Gao, L. (2009). Exergy analyses and parametric optimizations for different cogeneration power plants in cement industry. *Applied Energy*, *86*(6), 941-948. doi:16/j.apenergy.2008.09.001

Wang, X. D., Zhao, L., Wang, J. L., Zhang, W. Z., Zhao, X. Z., & Wu, W. (2010). Performance evaluation of a low-temperature solar Rankine cycle system utilizing R245fa. *Solar Energy*, *84*(3), 353-364. doi:16/j.solener.2009.11.004

Wei, D., Lu, X., Lu, Z., & Gu, J. (2008). Dynamic modeling and simulation of an Organic Rankine Cycle (ORC) system for waste heat recovery. *Applied Thermal Engineering*, *28*(10), 1216-1224. doi:10.1016/j.applthermaleng.2007.07.019

Winandy, E., Saavedra, C., & Lebrun, J. (2002). Experimental analysis and simplified modelling of a hermetic scroll refrigeration compressor. *Applied Thermal Engineering*, *22*(2), 107-120. doi:10.1016/S1359-4311(01)00083-7

Witt. (2004). *Air Cooled Condenser 550 RPM/Flying Bird 2*. Retrieved from http:// www.witthtp.com/literature.html

Wolpert J.L., & Riffat S.B. (1996). Solar-powered rankine system for domestic applications. *Applied Thermal Engineering*, *16*, 281-289. doi:10.1016/1359-4311(95)00032-1

Xiaojun, G., Liansheng, L., Yuanyang, Z., Pengcheng, S., & Shen, J. (2010). Research on a scroll expander used for recovering work in a fuel cell. *International Journal of Thermodynamics*, *7*(1), 1–8.

Yamamoto, T., Furuhata, T., Arai, N., & Mori, K. (2001). Design and testing of the organic Rankine cycle. *Energy*, *26*(3), 239–251.

Yanagisawa, M. T., Fukuta, M., Ogi, Y., & Hikichi, T. (2001). Performance of an oil-free scroll-type air expander. *International Conference on Compressors and their Systems, 9-12 September 2001, City University, London, UK*. John Wiley and Sons.

Yan, Yi-Yie, & Lin, T.-F. (1999). Condensation heat transfer and pressure drop of refrigerant R-134a in a small pipe. *International Journal of Heat and Mass Transfer*, *42*(4), 697-708. doi:16/S0017-9310(98)00195-1

Yan, Y.-Y., & Lin, T.-F. (1999). Evaporation Heat Transfer and Pressure Drop of Refrigerant R-134a in a Plate Heat Exchanger. *Journal of Heat Transfer*, *121*(1), 118-127. doi:10.1115/1.2825924

Zanelli, R., & Favrat, D. (1994). Experimental Investigation of a Hermetic Scroll Expander–Generator. Retrieved from http://infoscience.epfl.ch/record/53238